In presenting this dissertation as a partial fulfillment of the requirements for an advanced degree from Emory University, I agree that the Library of the University shall make it available for inspection and circulation in accordance with its regulations governing materials of this type. I agree that permission to copy from, or to publish, this dissertation may be granted by Professor Craig L. Hill, or, in his absence, by the Dean of the Graduate School when such copying or publication is solely for scholarly purposes and does not involve potential financial gain. It is understood that any copying from, or publication of, this dissertation that involves potential financial gain will not be allowed without written permission.

_____

Rui Cao

Late Transition Metal Oxo Complexes.
The Use of Polyoxometalate as a Stabilizing Ligand

By

Rui Cao
Doctor of Philosophy

Department of Chemistry

_____
Craig L. Hill
Advisor

_____
Dale E. Edmondson
Committee Member

_____
Michael C. Heaven
Committee Member

Accepted:

_____
Lisa A. Tedesco, Ph.D.
Dean of the Graduate School

_____
Date

Late Transition Metal Oxo Complexes. The Use of Polyoxometalate as a Stabilizing Ligand

By

Rui Cao
B.S.; Peking University, Beijing, China, 2003

Advisor: Professor Craig L. Hill

An Abstract of
A dissertation submitted to the Faculty of the Graduate School of
Emory University in partial fulfillment of
The requirements for the degree of
Doctor of Philosophy

Department of Chemistry / Graduate School of Arts and Sciences
2008

Abstract

The use of polyoxometalate (POM) as stabilizing ligands for the synthesis and isolation of late-transition metal oxo (LTMO) complexes is addressed. Metal-oxo species, in particular terminal metal-oxo (O^{2-}) complexes of the late-transition-metal elements have long been thought to exist as transient intermediates in systems ranging from Cu oxidase enzymes to the surfaces of noble metal oxidation catalysts. However, despite decades of speculation and attempted synthesis, no terminal metal-oxo complexes of any element to the right of Ru in the periodic table had been reported prior to 2004 with the exception of the d^4 $(mesityl)_3Ir^V$-oxo complex of G. Wilkinson and co-workers. A current bonding paradigm argues that terminal metal oxo groups are stabilized at metal centers with no more than four d electrons.

This dissertation reports several isolated and fully characterized molecular terminal oxo complexes of the group 10 and 11 elements with the use of polytungstate ligand environments. Polytungstates, which share many structural and reactivity features in common with the metal oxides of broad importance in catalytic technologies (TiO_2, CeO_2, others), are both good σ-donating and π-accepting ligands that may facilitate stabilization and isolation of terminal late transition metal-oxo units. A total of four structural types of LTMO complexes are presented in this study: (1) $M(O)(OH_2)\{A\text{-}PW_9\}_2$ with one bridging octahedral metal unit between two $[A\text{-}\alpha\text{-}PW_9O_{34}]^{9-}$ ligands (M = Pt and Au); (2) $M(O)(OH)W(O)(OH_2)\{A\text{-}PW_9\}_2$ with two linkages between $\{A\text{-}PW_9\}$ units, a metal and a tungsten atom (M = Pd); (3) $M(O)(OH_2)(O{=}WOH_2)_2\{A\text{-}PW_9\}_2$ with the terminal M = O group incorporated in a clam shell-like monovacant polytungstate ligand formed by the fusion of two $\{A\text{-}PW_9\}$ units by two tungsten atoms (M = Pd and

Au); and (4) $(O{=}MOH_2)_2W(O)(OH_2)\{A\text{-}PW_9\}_2$ (M = Pd), which represents the unique example having two terminal M=O groups coordinated in one molecule. All these molecular LTMO complexes have been carefully studied by geometric and electronic structure methods, including single crystal X-ray diffraction, neutron diffraction, extended X-ray absorption fine structure methods, ^{31}P and ^{17}O NMR spectroscopy, and other chemical and physicochemical methods.

Importantly, the counterion effect in the controlled speciation of the late transition metal substituted polytungstates is discussed. By strongly interacting with the polyanion unit, Cs^+ countercations can prevent the hydrolytic decomposition of the tri-metal sandwich structure in solution. As a result, the formation of conventional d^8 Pd(II)-substituted polytungstates and unprecedented terminal Pd=O complexes can be controlled.

Reactivity studies are conducted on $M(O)(OH_2)(O{=}WOH_2)_2\{A\text{-}PW_9\}_2$ (M = Pd and Au), a structure that is quite stable in both aqueous and organic solution. The stoichiometric oxo transfer from terminal M=O to other substrates and subsequent reoxidization of the deoxygenated form by air are confirmed by spectroscopy methods. Furthermore, the deoxygenated product, $[Pd^{II}(O{=}WOH_2)_2(A\text{-}\alpha\text{-}PW_9O_{34})_2]^{8-}$, can be isolated as crystalline plates, and X-ray diffraction confirms the existence of a four-coordinate square-planar Pd(II) center. These results and subsequent catalytic oxidation studies strongly suggest the involvement of terminal M=O species in noble metal-based homogenous and heterogenous catalysts in O_2-based green organic oxidations.

Late Transition Metal Oxo Complexes.
The Use of Polyoxometalate as a Stabilizing Ligand

By

Rui Cao
B.S.; Peking University, Beijing, China, 2003

Advisor: Professor Craig L. Hill

A dissertation submitted to the Faculty of the Graduate School of
Emory University in partial fulfillment of
The requirements for the degree of
Doctor of Philosophy

Department of Chemistry / Graduate School of Arts and Sciences
2008

Acknowledgment

I would like to acknowledge many people for their help during my doctoral work. First of all, I especially wish to thank my advisor, Professor Craig L. Hill, for offering me the opportunity to work with him in such a productive group and in such an interesting area of chemistry. Few advisors give their students more trust and freedom than Craig has given to me. With his great support, I have obtained exceptional achievements in my academic career. It is really fortunate for me to present this work with the contributions from an outstanding scholar and teacher like him.

I also would like to thank Dr. Kenneth I. Hardcastle, the director of the X-ray center at Emory. During my two-year service as the assistant in the X-ray laboratory, Kenneth has been giving me great help and expert advice on crystallography. It is always a pleasure for me to work with him as a top crystallographer.

I am very grateful for the support, advice and encouragement I have received from my research committee, Professor Dale E. Edmondson and Professor Michael C. Heaven. Their suggestions are really helpful in my research. Professors Cora Macbeth and Karl S. Hagen are also appreciated, and I would like to particularly thank Cora for her advice on my career development.

I extend my many thanks to my colleagues who collaborate on these projects. I thank Dr. Travis M. Anderson, Dr. Xikui Fang and Dr. Yurii V. Geletii in Hill's group for their friendship and help on my research; I thank Dr. Kenneth I. Hardcastle in the X-ray center at Emory University and Dr. Joseph H. Reibenspies in the X-ray Crystallography Laboratory at Texas A&M University for their help on crystallography; I thank Dr. Elena Slonkina, Dr. Britt Hedman and Dr. Keith O. Hodgson in the Department

of Chemistry and Stanford Synchrotron Radiation Laboratory at Stanford University for the collection and analysis of X-ray absorption spectroscopy; I thank Dr. Paula M. B. Piccoli, Dr. Arthur J. Schultz and Dr. Thomas F. Koetzle at Intense Pulsed Neutron Source, Argonne National Laboratory for the neutron diffraction studies; I thank Dr. Martin L. Kirk and Dr. Sushilla Knottenbelt at The University of New Mexico for low-temperature optical spectroscopy; I thank Dr. Djamaladdin G. Musaev and Dr. Keiji Morokuma in the Cherry L. Emerson Center for Scientific Computation at Emory University for theoretical studies; I thank Dr. Paul Kögerler at Ames Laboratory and Iowa State University for temperature-dependent magnetic studies; and I thank Dr. Masashi Takahashi at Toho University for providing ^{197}Au Mössbauer data.

Finally, I would like to thank all previous and current Hill group members. Particular thanks go to Dr. Travis M. Anderson, Dr. Xikui Fang, Dr. Yurii V. Gueletti, Dr. Wade Neiwert, Dr. Ira Weinstock, Dr. Jongwoo Han, Zhen Luo and Daniel A. Hillesheim. I would like to thank Leslie Chauvin who is very helpful organizing the group.

Table of Contents

ABSTRACT ..... **IV**

ACKNOWLEDGMENT ..... **VII**

CHAPTER 1 INTRODUCTION **1**

1.1 Terminal Transition Metal Oxo Units 2

1.2 Supported Noble Metal Catalysis 5

1.3 Bridging Noble Metal-oxo Species 8

1.4 Polyoxometalates – Metal-oxide Clusters 13

1.5 Use of Polyoxometalates as stabilizing ligand for M=O 22

References 24

CHAPTER 2 [$MO(OH_2)(PW_9O_{34})_2$] (M = PT OR AU) **35**

2.1 Abstract 36

2.2 Introduction 37

2.3 Experimental Section 39

General Methods and Materials *39*

*Synthesis of $K_7Na_9[PtO(OH_2)(PW_9O_{34})_2]\cdot 21.5H_2O$ (**1**)* *40*

*Synthesis of $K_{15}H_2[AuO(OH_2)(PW_9O_{34})_2]\cdot 25H_2O$ (**2**)* *41*

X-ray Crystallographic Studies *42*

Neutron Diffraction Studies *43*

Electrochemistry *46*

X-ray Absorption Spectroscopy Studies *47*

^{17}O NMR Studies *49*

Computational Methods *50*

2.4 Results and Discussion 51

*Synthesis of Terminal Pt-oxo (**1**) and Au-oxo (**2**) complexes* *51*

*Purity of Complexes, **1** and **2*** 52

*X-ray crystal structures of **1** and **2*** 53

Neutron Diffraction Studies 58

Optical Spectroscopy 68

Electrochemistry 70

X-ray Absorption Spectroscopy Studies 74

^{17}O NMR studies 77

Computational Studies 78

REFERENCES 85

CHAPTER 3 [MO(OH)WO(OH$_2$)(PW$_9$O$_{34}$)$_2$] (M = PD) **96**

3.1 ABSTRACT 97

3.2 INTRODUCTION 97

3.3 EXPERIMENTAL SECTION 99

General Methods and Materials 99

Synthesis of $H_{5.6}K_{7.6}Na_{1.4}[Pd_{0.3}\{WO(OH_2)\}_{0.7}(PW_9O_{34})_2]$ 99

*Synthesis of $K_{10}Na_3[PdO(OH)WO(OH_2)(PW_9O_{34})_2]\bullet 16H_2O$ **(3)*** 100

Crystallographic Studies 101

Titration Studies 102

Electronic Absorption Studies 103

^{17}O NMR Studies 103

X-ray Absorption Studies 105

Electrochemistry 106

Computational Procedures 107

3.4 RESULTS AND DISCUSSION 107

*Synthesis of $K_{10}Na_3[PdO(OH)WO(OH_2)(PW_9O_{34})_2]\bullet 16H_2O$ **(3)*** 107

Crystallographic Studies 112

X-ray Absorption Studies 116

Titration Studies 119

^{17}O NMR Studies ... *120*

Electronic Absorption Studies ... *124*

Electrochemistry ... *125*

Pd(IV) oxidation state assignment ... *127*

Computational Results ... *128*

REFERENCES ... 129

CHAPTER 4 $[MO(OH_2)(WO(OH_2))_2(PW_9O_{34})_2]$ (M = PD OR AU) ... **134**

4.1 ABSTRACT ... 135

4.2 INTRODUCTION ... 136

4.3 EXPERIMENTAL SECTION ... 138

General Methods and Materials ... *138*

*Synthesis of $K_8[Pd^{IV}O(OH_2)P_2W_{20}O_{70}(OH_2)_2]\cdot 22H_2O$ (**4**)* ... *140*

*Synthesis of $K_7H_2[Au^{III}O(OH_2)P_2W_{20}O_{70}(OH_2)_2]\cdot 27H_2O$ (**5**)* ... *141*

X-ray Crystallographic Studies ... *142*

X-ray Absorption Spectroscopy Studies ... *143*

Ultra-Low-Temperature Electronic Absorption Spectroscopy ... *145*

pH Dependent UV-vis and ^{31}P NMR Titrations ... *146*

Electrochemistry ... *146*

Chemical Titrations ... *147*

^{17}O NMR Studies ... *148*

4.4 RESULTS AND DISCUSSION ... 150

Synthesis ... *150*

*Magnetism of Au LTMO complexes, **2** and **5*** ... *151*

X-ray Crystallographic Studies ... *152*

X-ray Absorption Spectroscopy Studies ... *155*

Ultra-Low-Temperature Electronic Absorption Spectroscopy ... *160*

pH Dependent UV-vis and ^{31}P NMR Titrations ... *162*

Electrochemistry ... *164*

Chemical Titrations ... *169*

^{17}O NMR Studies ... *172*

Atomic Occupancy at the Au Position ... *174*

Au Oxidation State ... *175*

4.5 CONCLUSIONS ... 177

REFERENCES ... 178

CHAPTER 5 $[(MO(OH_2))_2WO(OH_2)(PW_9O_{34})_2]$ (M = PD) ... 185

5.1 ABSTRACT ... 186

5.2 INTRODUCTION ... 187

5.3 EXPERIMENTAL SECTION ... 188

General Methods and Materials ... *188*

*Synthesis of $Cs_{3.5}K_3Na_{3.5}[(O=Pd^{IV}(OH_2))_2P_2W_{19}O_{68}(OH)_2]\bullet 20H_2O$ (**6**)* ... *189*

Crystallography Studies ... *190*

X-ray Absorption Spectroscopy ... *191*

Reduction of 6 with Na_2SO_3 and $(CH_3)_2S$ ... *192*

Computational Studies ... *193*

5.4 RESULTS AND DISCUSSION ... 196

Synthesis ... *196*

Thermogravimetric Analysis (TGA) ... *198*

Structural Studies ... *198*

Pd(IV) Oxidation State Assignment ... *200*

*Reduction of **6*** ... *200*

Computational Studies ... *204*

REFERENCES ... 206

CHAPTER 6 COUNTERCATION EFFECT ... 210

6.1 ABSTRACT ... 211

6.2 INTRODUCTION ... 212

6.3 Experimental Section 216
General Methods and Materials *216*
*Synthesis of $K_{12}[Pd^{II}_3(PW_9O_{34})_2]\cdot 18H_2O$ (K**9**)* *216*
*Synthesis of $Cs_8Na_4[Pd^{II}_3(PW_9O_{34})_2]\cdot 18H_2O$ (CsNa**9**)* *217*
*Synthesis of $Cs_9Na_5[Pd^{II}_3(SiW_9O_{34})_2]\cdot 16H_2O$ (**10**)* *218*
*Synthesis of $Cs_5K_3Na_4[Pd^{II}_2WO(OH_2)(SiW_9O_{34})_2]\cdot 16H_2O$ (**11**)* *218*
Crystallographic Studies *219*
6.4 Results and Discussion 223
*Synthesis of K**9** and CsNa**9*** *223*
*Effect of Cs Countercation in the Synthesis, Controlled Speciation of **10** and **11*** *226*
*Crystallographic Studies of K**9**, CsNa**9**, **10** and **11*** *227*
6.5 Conclusion 229
References 230
CHAPTER 7 REACTIVITY STUDIES 232
7.1 Abstract 233
7.2 Introduction 234
7.3 Experimental Section 235
General Methods and Materials *235*
*Stoichiometric Oxo Transfer of Au-oxo Complex **5*** *237*
*Stoichiometric Oxo Transfer of Pd-oxo Complex **4*** *238*
*Crystallography Studies of the Deoxygenated Product **12*** *239*
*Reoxygenation of Pd(II) Complex **12*** *241*
*Catalytic Properties of Pd-oxo Complex **4*** *241*
Comparative Reaction: $[Pd^{II}Br_4]^{2-} + Ph_3P$ *242*
7.4 Results and Discussion 243
*Stoichiometric Oxo Transfer of Au-oxo Complex **5*** *243*
*Stoichiometric Oxo Transfer of Pd-oxo Complex **4*** *247*
*Crystallography Studies of **12*** *250*

*Reoxygenation of Pd(II) Complex **12*** *252*

*Catalytic Oxidation by Pd-oxo Complex **4*** *256*

Comparative Reactions *262*

REFERENCES 262

List of Figures

FIGURE 1.1 SCHEMATIC PRESENTATION OF THE MOLECULAR ORBITALS FOR A SIX-COORDINATE LOCAL C_{4V} M=O UNIT, SHOWING EACH D ELECTRON ABOVE THE D^2 CONFIGURATION (REPRESENTED IN RED) ADDED TO THE METAL CENTER OCCUPIES ANTIBONDING ORBITALS. 3

FIGURE 1.2 SUCCESSFULLY SYNTHESIZED AND FULLY CHARACTERIZED MOLECULAR COMPLEXES CONTAINING STABLE TERMINAL OXO OXYGEN AT METAL CENTERS WITH FOUR OR MORE D ELECTRONS. 4

FIGURE 1.3 SCHEMATIC REPRESENTATION OF THE EARLY STAGES OF THE OXIDATION OF CARBON MONOXIDE AT THE PERIPHERY OF AN SUPPORTED ACTIVE GOLD PARTICLE.[69] 7

FIGURE 1.4 MOLECULAR STRUCTURE OF A BRIDGING PD-OXO CONTAINING COMPLEX. THE BOND DISTANCES AND ANGLES OF THE CENTRAL $Pd_4(\mu_4\text{-}O)$ ARE: PD-O 2.020(1), 2.028(2) Å, PD-O-PD 98.6-118.0°. 9

FIGURE 1.5 STRUCTURE DIAGRAM OF TWO BRIDGING HETERO-NOBLE-METAL (PD AND AU) OXO COMPLEXES. 9

FIGURE 1.6 STRUCTURE DIAGRAM OF A BRIDGING PT-OXO COMPLEX. ANION BF_4^- CONNECTS TO THE $[(PH_3P)_2Pt(\mu\text{-}O)]_2$ UNIT THROUGH A Li^+ CATION. 10

FIGURE 1.7 SCHEMATIC REPRESENTATION OF THE REACTION BETWEEN A $Au_2(\mu\text{-}O)_2$ COMPLEX AND NORBORNENE. A TERMINAL AU-OXO CONTAINING INTERMEDIATE (**I**) IS PROPOSED IN THE REACTION MECHANISM.[81] 11

FIGURE 1.8 MOLECULAR EXAMPLES OF BRIDGING AU-O CONTAINING COMPLEXES WITH GOLD IN OXIDATION STATE +1 (LEFT) AND +3 (RIGHT). 12

FIGURE 1.9 KEGGIN-BASED LACUNARY POLYTUNGSTATES AND THEIR CHEMISTRY. 16

FIGURE 1.10 WELLS-DAWSON BASED LACUNARY POLYTUNGSTATES AND THEIR CHEMISTRY 20

FIGURE 1.11 SCHEMATIC REPRESENTATIONS OF THE TERMINAL METAL-OXO UNITS IN THE COORDINATION SPHERES OF POLYOXOMETALATE (LEFT) AND METALLOPORPHYRIN (RIGHT), SHOWING THE VERY SIMILAR LIGAND ENVIRONMENTS AFFORDED BY BOTH POM AND PORPHYRIN. 23

FIGURE 2.1 COMBINATION POLYHEDRAL/BALL-AND-STICK REPRESENTATIONS OF POLYANIONS **1** AND **2** (TOP LEFT) AS WELL AS THERMAL ELLIPSOID PLOTS AND NUMBERING SCHEME FOR **2** (RIGHT). THE WO_6 (OR W ATOM) AND PO_4 POLYHEDRA ARE SHOWN IN GRAY AND PINK. THE AU, O ATOMS AND AQUA (H_2O) LIGANDS ARE SHOWN IN YELLOW, RED, AND BLUE, RESPECTIVELY. AT THE BOTTOM LEFT IS X-RAY STRUCTURE AROUND THE AU ATOM IN **2**. A SHORT AU-O_{OXO} (1.763(17) Å) BOND IS *TRANS* TO A LONGER AU-OH_2 (2.29(4) Å) BOND, AND THE CENTRAL AU ATOM IS DISPLACED OUT OF THE EQUATORIAL O_4 PLANE TOWARD THE TERMINAL OXO BY 0.31(1) Å. 54

FIGURE 2.2 F_{OBS} FOURIER MAPS DERIVED FROM SINGLE CRYSTAL NEUTRON TOF LAUE DIFFRACTION DATA TAKEN AT 30K ON **1**. DATA WERE COLLECTED ON THE SINGLE CRYSTAL DIFFRACTOMETER AT THE INTENSE PULSED NEUTRON SOURCE, ARGONNE NATIONAL LABORATORY. ATOM POSITIONS IN THE MODEL ARE MARKED WITH A + AND ARE LABELED WITH THEIR NAMES. IN THIS SAMPLE, ALL NON-HYDROGEN ATOMS HAVE POSITIVE SCATTERING LENGTHS (SOLID CONTOUR LINES) AND ONLY HYDROGEN 60

FIGURE 2.3 F_{OBS} FOURIER MAP SECTIONS DERIVED FROM SINGLE CRYSTAL NEUTRON TOF LAUE DIFFRACTION DATA TAKEN AT 30 K ON **2**. ATOM POSITIONS ARE LABELED. IN THESE SECTIONS, ALL63

FIGURE 2.4 ELECTRONIC ABSORPTION SPECTRUM OF **1**. THREE ABSORPTION BANDS AT 574 NM (BAND 1), 502 NM (BAND 2), AND 428 NM (BAND 3) ARE CONSISTENT TO THE d^6 PT(IV) OXIDATION STATE ASSIGNMENT. 69

FIGURE 2.5 CYCLIC VOLTAMMOGRAMS OF 2.85 MM **2** AND 2.0 MM **5** (THE OTHER AU-OXO POLYTUNGSTATE, SEE CHAPTER 4) IN SODIUM CHLOROACETATE BUFFER (0.4 M, PH 3.0) SOLUTION. THE INITIAL POTENTIAL WAS SET AT +800 MV. ROOM TEMPERATURE, SCAN RATE 100 MV/S 70

FIGURE 2.6 CORRECTED NUMBER OF ELECTRONS, $\mathbf{n} = (\mathbf{C}\text{-}\mathbf{C_B})/FN$, PASSED DURING BULK ELECTROLYSIS UNDER CONTROLLED POTENTIALS AS A FUNCTION OF TIME. (A) 3.37 MM $(NH_4)AuCl_4$, 50 MM SODIUM SULFATE BUFFER, PH ~2, 0.4 M NACL, E = 320 MV; (B) 2.0 MM **2**, 50 MM SODIUM SULFATE BUFFER, PH ~2, 0.4 M NACL, E = 300 MV; (C) 4.2 MM **5** (SEE CHAPTER 4), 0.2 M SODIUM CHLOROACETATE BUFFER, PH ~3, E = 350 MV. 73

FIGURE 2.7 AU L_2 NEAR-EDGE X-RAY ABSORPTION SPECTRA OF $Au^{III}(CH_3COO)_3$ (BLACK), **2** (ORANGE), **5** (BLUE), $Na_3Au^{I}(S_2O_3)_2$ (MAGENTA), $KAu^{I}(CN)_2$ (GREEN), AND Au^0 FOIL (GREY). THE EDGE REGION

IS MAGNIFIED IN THE INSET. SPECTRA WERE MEASURED AT THE STANFORD SYNCHROTRON RADIATION LABORATORY (SSRL) ON BEAM LINES 2-3 AND 9-3. 75

FIGURE 2.8 ^{17}O NMR SPECTRA OF TETRA-*N*-BUTYLAMMONIUM (TBA) SALT OF AU-OXO COMPLEX **2** IN 50:50 (V:V) $CH_3CN:CDCL_3$. 78

FIGURE 2.9 SIMPLE MOLECULAR ORBITAL DIAGRAM FOR THE PT(IV)-OXO PORTION OF **1** ILLUSTRATING THE STABILIZATION RESULTING FROM PT $D_{XZ,YZ}$-W $D_{XZ,YZ}$ INTERACTION AND EFFECTIVE DONATION OF ELECTRON DENSITY FROM THE FORMAL PT-OXO π^* ORBITALS TO DELOCALIZED ORBITALS ON THE POLYTUNGSTATE LIGANDS. THE D ORBITALS OF THE METAL-OXO UNIT ARE SHOWN WITH THEIR CORRESPONDING C_{4V} SYMMETRY LABELS. ENERGY ORDERING FOR THE UNPERTURBED PT-OXO ORBITALS (LEFT) ARE THOSE APPROPRIATE FOR *TYPICAL* METAL-OXO SPECIES AND INDICATE THE LARGE 79

FIGURE 2.10 SCHEMATIC PRESENTATION OF THE MO-CORRELATION DIAGRAM FOR THE $^2\prod$ ELECTRONIC STATE OF THE DIATOMIC AUO MOLECULE. 81

FIGURE 3.1 COMBINATION POLYHEDRAL/BALL-AND-STICK REPRESENTATION OF POLYANION **3** (TOP LEFT) AS WELL AS THERMAL ELLIPSOID PLOTS AND NUMBERING SCHEME FOR **3** (RIGHT). THE WO_6 (OR W ATOM) AND PO_4 POLYHEDRA ARE SHOWN IN GRAY AND PINK. THE PD AND O ATOMS ARE SHOWN IN 108

FIGURE 3.2 ATOMIC ARRANGEMENT IN THE CENTRAL BELT OF THE POLYANION IN **3** ILLUSTRATING THE BRIDGING $[O=W^{VI}(OH_2)]^{4+}$ UNIT, W19, IS DISORDERED BETWEEN TWO SITES, COMPONENT 1 (LEFT, 90%) AND COMPONENT 2 (RIGHT, 10%). 113

FIGURE 3.3 PD *K*-EDGE EXAFS DATA (BLACK), FIT (RED), AND THE CORRESPONDING NON-PHASE SHIFT CORRECTED FOURIER TRANSFORMS FOR **3**. 117

FIGURE 3.4 PH-DEPENDENT UV-VIS TITRATION OF **3** WITH HCL AND THE BACK TITRATION WITH NAOH, SHOWING THE REVERSIBLE CHANGES IN THE D-D BANDS AT 444 NM UPON LOWERING AND INCREASING THE PH OF THE SOLUTION. 119

FIGURE 3.5 ^{17}O NMR SPECTRA OF PD-OXO COMPLEX **3** AND ITS ISOSTRUCTURAL ALL-TUNGSTEN COMPLEX, $[P_2W_{20}O_{70}(OH_2)_2]^{10-}$ (**P_2W_{20}**). TWO PEAKS AT 330 AND 570 PPM (RELATIVE TO D_2O AT 0 PPM) ARE

ATTRIBUTABLE TO THE HYDROXO AND OXO LIGANDS OF PD, RESPECTIVELY. THE TWO PEAKS ARE ASSIGNED BASED ON THE ESTABLISHED CORRELATION BETWEEN DOWNFIELD CHEMICAL SHIFT 122

FIGURE 3.6 ULTRA-LOW-TEMPERATURE (5 K) ELECTRONIC ABSORPTION SPECTRUM OF **3** SHOWING TWO WEAK ABSORPTION BANDS IN THE VISIBLE REGION AT 19,750 CM^{-1} (506 NM; BAND 1) AND 22,700 CM^{-1} (441 NM; BAND 2). 124

FIGURE 3.7 CYCLIC VOLTAMMOGRAM OF **3**. THE RESULTS INDICATE THAT **3**, ITS PD(II)-PRECURSOR ($PDSO_4$), AND PD(II) CONTAINING POLYTUNGSTATES HAVE DISTINCT ELECTROCHEMICAL BEHAVIOURS. 126

FIGURE 3.8 MOLECULAR ORBITAL DIAGRAM OF THE MODEL $[O=Pd^{IV}(OH)]^{1-}$. HERE WE HAVE PRESENTED ONLY IMPORTANT ORBITALS OF THIS MODEL. ALL ENERGETICS ARE IN A.U. 128

FIGURE 4.1 COMBINATION POLYHEDRAL/BALL-AND-STICK REPRESENTATIONS OF POLYANIONS **5** (TOP LEFT) AND $[P_2W_{20}O_{70}(H_2O)_2]^{10-}$ (**P_2W_{20}**, TOP RIGHT), THE STABILIZING LIGAND OF **5**. THERMAL ELLIPSOID PLOTS AND NUMBERING SCHEME FOR POLYANIONS **5** (BOTTOM LEFT) AND **P_2W_{20}** (BOTTOM RIGHT). THE WO_6 (OR W ATOM) AND PO_4 POLYHEDRA ARE SHOWN IN GRAY AND PINK. THE AU, O ATOMS AND AQUA (H_2O) LIGANDS ARE SHOWN IN YELLOW, RED, AND BLUE, RESPECTIVELY. THE COORDINATION SPHERE AROUND THE AU ATOM IN **5** (AU-O_{OXO}, 1.77(4) Å; AU-OH_2, 2.32(6) Å; DOMING DISTANCE OF THE AU ATOM, 0.32(1) Å) IS ALMOST IDENTICAL TO THAT TRIPLY DETERMINED, DISORDER FREE STRUCTURES OF AU-OXO COMPLEX **2** (A SHORT AU-O_{OXO} (1.763(17) Å) BOND IS 154

FIGURE 4.2 ^{31}P NMR SPECTRA OF PD-OXO COMPLEX **4** (TOP) AND AU-OXO COMPLEX **5** (BOTTOM) WITH THE ADDITION OF AUTHENTIC SAMPLES OF THE STARTING POLYTUNGSTATE LIGAND $[P_2W_{20}O_{70}(H_2O)_2]^{10-}$ (**P_2W_{20}**) AS WELL AS THE ISOSTRUCTURAL ALL-TUNGSTEN COMPLEX $[P_2W_{21}O_{71}(H_2O)_3]^{6-}$ (**P_2W_{21}**). . 158

FIGURE 4.3 PD *K*-EDGE EXAFS DATA AND THE CORRESPONDING NON-PHASE SHIFT CORRECTED FOURIER TRANSFORMS FOR PD-OXO COMPLEXES **3** (BLACK) AND **4** (RED). 159

FIGURE 4.4 LOW TEMPERATURE (17 K) ELECTRONIC ABSORPTION SPECTRUM OF **5** IN A 1:3 WATER:GLYCEROL GLASS WITH BAND DECONVOLUTION. 160

FIGURE 4.5 PH-DEPENDENT UV-VIS TITRATION OF **5** WITH NAOH AND THE BACK TITRATION WITH HCL, SHOWING THE REVERSIBLE CHANGES IN THE D-D BANDS AT 410 NM UPON INCREASING AND LOWERING THE PH OF THE SOLUTION. 163

FIGURE 4.6 CYCLIC VOLTAMMOGRAM OF **4** IN A PH 4.5 MEDIUM, SHOWING DISTINCT ELECTROCHEMICAL BEHAVIORS FROM CONVENTIONAL PD(II)-SUBSTITUTED POLYTUNGSTATES AND FREE PD(II) ($PdSO_4$). 165

FIGURE 4.7 CYCLIC VOLTAMMETRY (CV) CHARACTERIZATION OF A THICK FILM OF **4** IN ITS PREPARATION MEDIUM (2 X 10^{-4} M OF **4** + (0.4 M CH_3COONa + CH_3COOH) PH = 4.5 BUFFER). WORKING ELECTRODE: GLASSY CARBON; REFERENCE ELECTRODE: SCE; SCAN RATE: 2 MV S^{-1}. IT SHOWS THE CHARACTERISTIC "TWO STEP OXIDATION" OF THE SURFACE OF THICK PD(0) FILMS. 167

FIGURE 4.8 CHANGES IN THE REDUCTION POTENTIAL OF THE $SiW_{12}O_{40}^{5-}/SiW_{12}O_{40}^{4-}$ SOLUTION (INITIAL CONCENTRATION 0.87 MM $SiW_{12}O_{40}^{5-}$) UPON ADDITION OF **5** (1 MM IN STOCK SOLUTION). 170

FIGURE 4.9 ^{17}O NMR SPECTRA OF PD-OXO **4** AND AU-OXO **5** COMPLEXES IN 50:50 (V:V) $CH_3CN:CDCl_3$. (A) TETRA-*N*-BUTYLAMMONIUM (TBA) SALT OF **4**. (B) K⊂*CIS*-DICYCLOHEXANO-18-CROWN-6 SALT OF **5** ENRICHED IN AQUEOUS SOLUTION. (C) K⊂*CIS*-DICYCLOHEXANO-18-CROWN-6 SALT OF **5** ENRICHED IN ACETONITRILE. 173

FIGURE 5.1 COMBINATION POLYHEDRAL/BALL-AND-STICK REPRESENTATION OF POLYANION **6** (TOP RIGHT) AND ITS THERMAL ELLIPSOID PLOTS AND NUMBERING SCHEME (LEFT). THE WO_6 (OR W ATOM) AND PO_4 POLYHEDRA ARE SHOWN IN GRAY AND PINK. THE PD, O ATOMS AND AQUA (H_2O) LIGANDS ARE SHOWN IN YELLOW, RED, AND BLUE, RESPECTIVELY. THE VERY SHORT PD-O BOND ON THE AXIAL POSITION IS 1.66(3) Å, AND IS TRANS TO A LONGER PD-OH_2 BOND (2.199(18) Å). THE CENTRAL PD ATOM IS DISPLACED OUT OF THE EQUATORIAL O_4 PLANE TOWARD THE TERMINAL OXO BY 0.30(2) Å. ^{31}P NMR SPECTRUM OF 6 IN AQUEOUS SOLUTION (BOTTOM RIGHT), SHOWING ONE SINGLE PEAK AT -12.00 PPM, A RESULT CONSISTENT TO THE CRYSTALLOGRAPHIC STUDIES. 193

FIGURE 5.2 TOP: THERMOGRAVIMETRIC ANALYSIS (TGA) OF PD-OXO COMPLEX **6** (BLACK) AND ALL-TUNGSTEN COMPLEXES, $\mathbf{P_2W_{19}}$ (BLUE) AND $\mathbf{P_2W_{20}}$ (RED). BOTTOM: THERMOGRAVIMETRIC ANALYSIS (TGA) OF AU-OXO COMPLEXES **2** (BLACK) AND **5** (RED) COMPARED TO THEIR ISOSTRUCTURAL ALL-TUNGSTEN COMPLEXES, $\mathbf{P_2W_{19}}$ (BLUE) AND $\mathbf{P_2W_{21}}$ (PURPLE), RESPECTIVELY. 197

FIGURE 5.3 REDUCTIVE TITRATION OF PD(IV) CENTER IN **6** FOLLOWED BY ELECTRONIC ABSORPTION SPECTROSCOPY, SHOWING THE INCREASED ABSORPTION BANDS AT THE RANGES OF 350-450 NM WHEN THE PD(IV) CENTER IS REDUCED. 201

FIGURE 5.4 THERMAL ELLIPSOID PLOTS AND NUMBERING SCHEME FOR THE TWO REDUCED PRODUCTS **8** (LEFT) AND **7** (RIGHT). 202

FIGURE 5.5 THE **6M-XL$_N$** MODEL USED IN THE CALCULATIONS. FOR SIMPLICITY, WE HAVE PRESENTED ONLY CASE WITH **XL$_N$** = SMe_2. 204

FIGURE 5.6 SCHEMATIC PRESENTATION OF THE CHANGES TO THE TOTAL ENERGIES OF **6M-XL$_N$** AS A FUNCTION OF PD-X DISTANCE (BLUE LINE IS FOR **XL$_N$** = DMS, AND RED LINE IS FOR **XL$_N$** = PPH_3)... 205

FIGURE 6.1 BALL-AND-STICK REPRESENTATION OF POLYANION $[PD_3SI_2W_{18}O_{68}]^{14-}$, SHOWING THE THREE CS^+ CATIONS LOCATING AT THE CENTRAL BELT OF THE SANDWICH STRUCTURE. PD, W, SI, O AND CS ATOMS ARE SHOWN IN GREEN, GRAY, BLUE, RED AND PINK, RESPECTIVELY. THE INTERACTION BETWEEN CS^+ CATIONS AND OXO OXYGENS ON THE POLYANION IS ILLUSTRATED AS LIGHT BLUE BONDS. THESE EXTRA LINKAGES BETWEEN THE TWO $[A\text{-}\alpha\text{-}SIW_9O_{34}]^{10-}$ LIGANDS INCREASE THE SOLUTION STABILITY OF THE WHOLE SANDWICH STRUCTURE. 215

FIGURE 6.2 THERMAL ELLIPSOID PLOTS AND NUMBERING SCHEME FOR K**9** (TOP LEFT), CSNA**9** (TOP RIGHT), **10** (BOTTOM LEFT) AND **11** (BOTTOM RIGHT). 220

FIGURE 6.3 COMBINATION POLYHEDRAL/BALL-AND-STICK REPRESENTATIONS OF POLYANIONS **9** (LEFT) **10** (MIDDLE) AND **11** (RIGHT). THE WO_6 (OR W ATOM), PO_4 AND SIO_4 POLYHEDRA ARE SHOWN IN GRAY, PINK AND YELLOW, RESPECTIVELY. THE PD ATOM IS SHOWN IN GREEN. 225

FIGURE 7.1 ^{31}P NMR SPECTRA OF AU-OXO COMPLEX **5** (K⊂*CIS*-DICYCLOHEXANO-18-CROWN-6 SALT), PD-OXO COMPLEX **4** (TETRA-*N*-BUTYLAMMONIUM (TBA) SALT), PH_3P AND PH_3P=O IN 50:50 (V:V) CH_3CN:$CDCL_3$ SOLUTION. 240

FIGURE 7.2 ^{31}P NMR SPECTROSCOPY STUDIES OF OXO TRANSFER FROM AU-OXO COMPLEX **5** (K⊂*CIS*-DICYCLOHEXANO-18-CROWN-6 SALT) TO PH_3P IN 50:50 (V:V) CH_3CN:$CDCL_3$ SOLUTION. 245

FIGURE 7.3 ^{17}O NMR SPECTROSCOPY STUDIES OF OXO TRANSFER FROM AU-OXO COMPLEX **5** (K⊂*CIS*-DICYCLOHEXANO-18-CROWN-6 SALT) TO PH_3P IN 50:50 (V:V) CH_3CN:$CDCL_3$ SOLUTION, SHOWING THE SELECTIVE DISAPPEARANCE OF THE TERMINAL AU(III)=O PEAK AT 605 PPM AND THE APPEARANCE OF THE PH_3P=O PEAK AT 45 PPM. 246

FIGURE 7.4 ILLUSTRATION OF OXO TRANSFER REACTION FROM AU-OXO COMPLEX **5** TO PH_3P COMPETED WITH A DEMETALATION OF THE RESULTED AU(I) BY FREE UNREACTED PH_3P MOLECULES. 247

FIGURE 7.5 ^{31}P NMR SPECTROSCOPY STUDIES OF OXO TRANSFER FROM PD-OXO COMPLEX **4** (TETRA-*N*-BUTYLAMMONIUM (TBA) SALT) TO PH_3P IN 50:50 (V:V) CH_3CN:$CDCL_3$ SOLUTION. (A) **4** + 0.8 PH_3P; (B) **4** + 3.0 PH_3P. THE DEOXYGENATED PRODUCT, $[PD(II)P_2W_{20}O_{70}(OH_2)_2]^{8-}$ (**12**), IS STABLE IN THE PRESENCE OF EXTRA PH_3P MOLECULES AND CONFIRMS THE STOICHIOMETRIC OXO TRANSFER FROM THE TERMINAL PD(IV)=O UNIT TO PH_3P. 249

FIGURE 7.6 ^{17}O NMR SPECTROSCOPY STUDIES OF OXO TRANSFER FROM PD-OXO COMPLEX **4** (TETRA-*N*-BUTYLAMMONIUM (TBA) SALT) TO PH_3P IN 50:50 (V:V) CH_3CN:$CDCL_3$ SOLUTION, SHOWING THE SELECTIVE DISAPPEARANCE OF THE TERMINAL PD(IV)=O PEAK AT 545 PPM AND THE APPEARANCE OF THE PH_3P=O PEAK AT 45 PPM. 250

FIGURE 7.7 COMBINATION POLYHEDRAL/BALL-AND-STICK REPRESENTATION (LEFT) AND THERMAL ELLIPSOID PLOTS AND NUMBERING SCHEME (RIGHT) FOR POLYANION **12**. THE WO_6 (OR W ATOM) AND PO_4 POLYHEDRA ARE SHOWN IN GRAY AND PINK, RESPECTIVELY. THE PD ATOM IS SHOWN IN YELLOW. 251

FIGURE 7.8 ^{31}P NMR SPECTROSCOPY STUDIES OF OXO TRANSFER FROM PD-OXO COMPLEX **4** (TETRA-*N*-BUTYLAMMONIUM (TBA) SALT) TO PH_3P UNDER ARGON AS WELL AS FOLLOWED REOXYGENATION OF THE REDUCED FORM **12** UNDER AIR IN 50:50 (V:V) CH_3CN:$CDCL_3$ SOLUTION. 254

FIGURE 7.9 ELECTRONIC ABSORPTION SPECTROSCOPY STUDIES OF OXO TRANSFER FROM PD-OXO COMPLEX **4** (TETRA-*N*-BUTYLAMMONIUM (TBA) SALT) TO PH_3P UNDER ARGON AS WELL AS FOLLOWED REOXYGENATION OF THE REDUCED FORM **12** UNDER AIR IN 50:50 (V:V) CH_3CN:$CDCL_3$ SOLUTION.. 255

FIGURE 7.10 ^{17}O NMR SPECTRUM OF THE REOXYGENATION OF THE REDUCED FORM **12** WITH ^{17}O-ENRICHED DIOXYGEN ($^{17}O_2$) IN 50:50 (V:V) CH_3CN:$CDCL_3$ SOLUTION, SHOWING THE SELECTIVE BUILDING UP OF THE TERMINAL PD(IV)=O PEAK AT 545 PPM. 256

FIGURE 7.11 SCHEMATIC REPRESENTATION OF THE SYNTHESIS AND REACTIVITY (OXO TRANSFER AND REOXYGENATION BY O_2) OF THE TERMINAL PD-OXO COMPLEX **4**. THE POLYANION STRUCTURES OF THE MONOVACANT POLYTUNGSTATE LIGAND $K_{10}[P_2W_{20}O_{70}(OH_2)_2]$ (TOP LEFT), **4** (TOP RIGHT) AND THE DEOXYGENATED PRODUCT **12** (BOTTOM) ARE SHOWN AS COMBINED POLYHEDRAL/BALL-AND-STICK REPRESENTATIONS. THE WO_6 AND PO_4 POLYHEDRA ARE SHOWN IN GRAY AND PINK. THE PD, O ATOMS, AND AQUA (H_2O) LIGAND ARE SHOWN IN YELLOW, RED, AND BLUE, RESPECTIVELY. 257

FIGURE 7.12 OXIDATION OF $(MeO)_3P$ (0.55 M) TO $(MeO)_3P{=}O$ CATALYZED BY **4** (1.3 MM) IN ACETONITRILE AT 80° C WITH 1.0 ATM OF AIR (OPEN CIRCLE). A CONTROL REACTION (Δ) WAS CARRIED OUT IN THE ABSENCE OF POM. IMPORTANT NUMBERS: A YIELD OF $(MeO)_3P{=}O$ (BASED ON INITIAL $(MeO)_3P$) AFTER 30 HRS IS ~ 60%; TON = $[(MeO)_3P{=}O]/[\mathbf{4}] \geq 2x10^2$; INITIAL TOF ~ 20 H^{-1}. 258

FIGURE 7.13 THERMAL ELLIPSOID PLOTS AND NUMBERING SCHEME FOR $(PH_4P)_2PdBr_4$ (TOP LEFT), $(PH_4P)_2Pd_2Br_6$ (TOP RIGHT) AND *TRANS*-$(PH_3P)_2PdBr_2$ (BOTTOM). 259

List of Tables

TABLE 2.1 CRYSTAL DATA AND REFINEMENT PARAMETERS FOR THE X-RAY STRUCTURES OF $K_7NA_9[PTO(OH_2)(PW_9O_{34})_2]\bullet 21.5H_2O$ (**1**) AND $K_{15}H_2[AUO(OH_2)(PW_9O_{34})_2]\bullet 25H_2O$ (**2**) (DATASETS AT BOTH 173(2) K AND 96(2) K)..... 55

TABLE 2.2 ELECTRON BINDING ENERGIES FOR AU AND W[116]..... 59

TABLE 2.3 CRYSTAL DATA AND STRUCTURAL REFINEMENT FOR THE NEUTRON DIFFRACTION STRUCTURES OF $K_7NA_9[PTO(OH_2)(PW_9O_{34})_2]\bullet 21.5H_2O$ (**1**) AND $K_{15}H_2[AUO(OH_2)(PW_9O_{34})_2]\bullet 25H_2O$ (**2**) 66

TABLE 2.4 BOND DISTANCES (Å) AND ANGLES (°) FOR THE [PT-O_6] OCTAHEDRAL CORE AS DERIVED FROM NEUTRON DIFFRACTION DATA..... 67

TABLE 2.5 BOND DISTANCES (Å) AND ANGLES (°) FOR THE [AU-O_6] OCTAHEDRAL CORE AS DERIVED FROM NEUTRON DIFFRACTION DATA..... 67

TABLE 3.1 CRYSTAL DATA AND STRUCTURAL REFINEMENT FOR THE X-RAY STRUCTURES OF $K_{10}NA_3[PDO(OH)P_2W_{19}O_{69}(OH_2)]\bullet 16H_2O$ (**3**) AT THREE DIFFERENT TEMPERATURES..... 110

TABLE 3.2 CURVE FITTING RESULTS FOR THE PD *K*-EDGE EXAFS OF **3**. 118

TABLE 4.1 CRYSTAL DATA AND REFINEMENT PARAMETERS FOR THE X-RAY STRUCTURES OF $K_7H_2[AUO(OH_2)P_2W_{20}O_{70}(OH_2)_2]\bullet 27H_2O$ (**5**) AND $K_{10}[P_2W_{20}O_{70}(OH_2)_2]\bullet 22H_2O$ (**P_2W_{20}**). 157

TABLE 5.1 CRYSTAL DATA AND STRUCTURAL REFINEMENT FOR THE X-RAY STRUCTURES OF $CS_{3.5}K_3NA_{3.5}[(O{=}PD^{IV}(OH_2))_2P_2W_{19}O_{68}(OH)_2]$ (**6**), $CS_5K_3NA_3[PD^{II}{}_{2.5}P_2W_{18.5}O_{68.5}(OH_2)_{0.5}]$ (**8**) AND $CS_5K_3NA_2[PD^{II}{}_2P_2W_{19}O_{69}(OH_2)]$ (**7**)..... 194

TABLE 6.1 CRYSTAL DATA AND STRUCTURAL REFINEMENT FOR THE X-RAY STRUCTURES OF K**9**, CSNA**9**, **10** AND **11** 221

TABLE 7.1 CRYSTAL DATA AND STRUCTURAL REFINEMENT FOR THE X-RAY STRUCTURES OF $(C_2H_6NH_2)_7K[PDP_2W_{20}O_{70}(OH_2)_2]\bullet 18H_2O$ (**12**) 253

TABLE 7.2 CRYSTAL DATA AND STRUCTURAL REFINEMENT FOR THE X-RAY STRUCTURES OF $[(C_6H_5)_4P]_2[PDBR_4]$, $[(C_6H_5)_4P]_2[PD_2BR_6]$ AND $[(C_6H_5)_3P]_2PDBR_2\bullet 2CH_2CL_2$ 260

List of Abbreviations

Å	Angstrom
a, *b*, *c*	unit cell axial lengths
Ag	silver
An	actinide
Au	gold
n-Bu	*n*-butyl
°C	degrees Celsius
calcd.	calculated
CCD	charge-coupled device
CIF	crystallographic information file
cm^{-1}	reciprocal centimeter
DMS	dimethyl sulfide
DMSO	dimethyl sulfoxide
DSC	differential scanning calorimetry
equiv.	equivalent
EXAFS	extended X-ray absorption fine structure method
F.W.	formula weight
F(000)	structure factor for the unit cell; it is equal to the total number of electrons in the unit cell
FT-IR	Fourier transform infrared spectroscopy
g	grams(s)
h	hour(s)
Hz	Hertz
K	kelvin
L	ligand
Ln	lanthanide
LTMO	late transition-metal oxo complex
m	medium (FT-IR)
M	molarity
Me	methyl
mg	milligram(s)
MHz	megahertz
min	minutes(s)
mL	milliliters(s)
mmol	millimole
mol	mole
nm	nanometer
NMR	nuclear magnetic resonance spectroscopy
OAc	acetate
P	phosphorus
Pd	palladium
pH	potential of hydrogen, a measure of the acidity or alkalinity of a solution
Ph	phenyl
POM	polyoxometalate

ppm	part per million
Pt	platinum
R	discrepancy index for crystal structure refinement
s	strong (FT-IR)
sec	second(s)
sh	shoulder (FT-IR)
Si	silicon
TBA	tetrabutylammonium
TGA	thermogravimetric analysis
UV	ultraviolet
V	volume of the unit cell
vs	very strong (FT-IR)
w	weak (FT-IR)
Z	number of molecules per unit cell
α, β, γ	interaxial angles between unit cell vector **b** and **c**, **a** and **c**, and **a** and **b**, respectively
δ	chemical shift (expressed in ppm for NMR)
ε	molar extinction (or absorption) coefficient
θ	the glancing angle of the X-ray beam to the "reflecting plane"
λ	wavelength
μ	the total linear absorption coefficient (with unit of cm^{-1})

Chapter 1 Introduction

Functional Noble Metal-oxo Species and The Use of Polyoxometalates as Inorganic Ligands

1.1 Terminal Transition Metal Oxo Units

Despite the high electronegativity of oxygen, the terminal oxo ligand is a strong π electron donor, and its electrons can delocalize into vacant d orbitals on the metal.[1,2] Thus, the d-electron count on the metal center largely dictates stability and reactivity of the terminal metal-oxo unit because of repulsion between the oxygen electrons and the filled metal d orbitals: stability decreases and reactivity increases as one moves from left to right across the periodic table and electrons are added to the metal center. For the common six-coordinate local C_{4v} symmetry transition metal oxo unit, a triple bond of electron configuration ... $\sigma^2\pi^4$ with the oxo ligand acting as a π-donor to a $d^{0\text{-}2}$ metal is supported by experimental and theoretical studies; however, each d electron above the d^2 configuration added to the metal center occupies antibonding orbitals, and thus the M-O bond order decreases (**Figure 1.1**). As a result, terminal metal oxo groups are thought to be stabilized at metal centers with no more than four d electrons.[1,2]

This defines the concept of the "Metal-oxo (or Ru-oxo) Wall" which states that metal-oxo units to the right of the column 8 elements (Fe, Ru, Os) are too unstable to exist. Therefore, terminal metal-oxo units with d^0, d^1, and d^2 configurations are stable and common (lone oxygen atoms bind most stably to high valent early transition metals, such as Ti(IV), V(V), and their heavier congeners), those with d^3 and d^4 configurations like d^3 manganese-oxo and d^4 iron-oxo (ferryl) units are highly reactive (useful synthetic oxidants and arguably the most abundant highly potent oxidants in biological systems), and terminal metal-oxo species to the right of column 8 in the periodic table do not exist.[3-11]

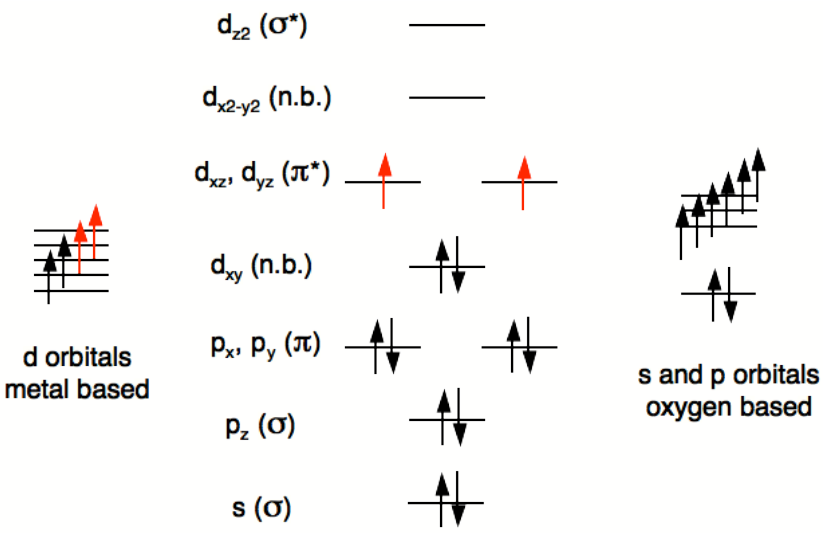

Figure 1.1 Schematic presentation of the molecular orbitals for a six-coordinate local C_{4v} M=O unit, showing each d electron above the d^2 configuration (represented in red) added to the metal center occupies antibonding orbitals.

Interestingly, recent work by synthetic chemists show that the reactive metal-oxo species with metal centers having four or more d electron counts can be stabilized and isolated (**Figure 1.2**).[7,8,11,12] There are several stable d^4 metal oxo molecular complexes, including a Ru(IV)-oxo by Che *et al.*,[13] a Ir(V)-oxo by Hay-Motherwell *et al.*,[12] and a few Fe(IV)-oxo compounds by Que and co-workers.[9,11,14] In 2000, MacBeth and Borovik reported a d^5 Fe(III)-oxo complex,[7] where the iron center has a trigonal bipyramidal coordination sphere, and the terminal oxo ligand is stabilized by surrounding hydrogen-bonds. On the other hand, a d^6 oxo, the $NaRe(O)(PhCCPh)_2$ complex, was isolated by Mayer and co-workers.[8] The stability of this Re(I)-oxo unit is largely because of the strong Re-O π* and rhenium-acetylene π backbonding, suggested by computational

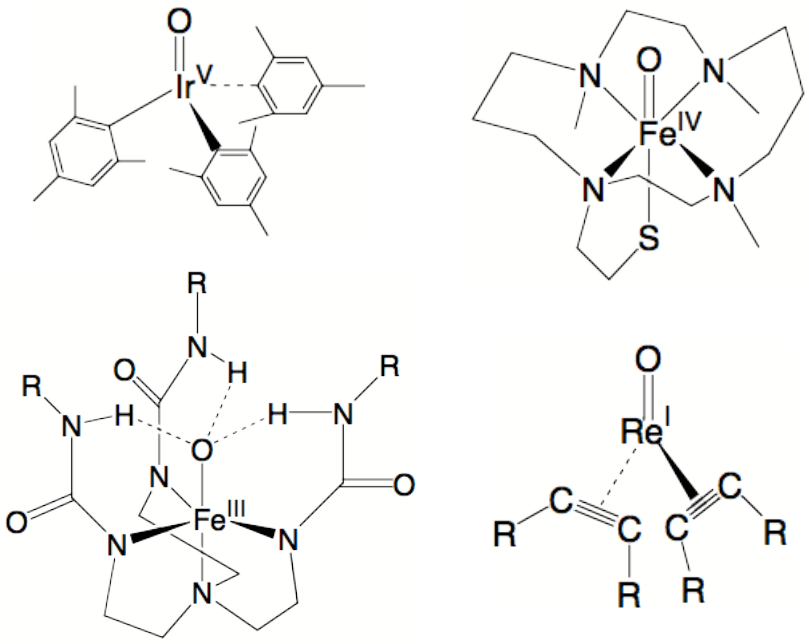

Figure 1.2 Successfully synthesized and fully characterized molecular complexes containing stable terminal oxo oxygen at metal centers with four or more d electrons.

studies. Importantly, the calculations are consistent with the experiment results: (1) the location of the sodium counter cation in the crystal lattice implies a high electron density in this orbital; (2) the short Re-C distances (average 2.006(5) Å), the long C≡C distances (average 1.316(7) Å), and the low C≡C stretching frequencies (1685 cm^{-1}) all indicate delocalization of the d electrons on the Re atom to the carbon-carbon triple bonds.

The considerable recent research on metal-oxo systems in biology, chemistry, and materials science has been mirrored by noteworthy developments involving mid- and late-transition-metal complexes with terminal multiply bonded ligands, such as carbene, imido, nitrido, phosphido, and sulfido.[14-43] All of these works, as well as the metal-oxo

studies documented above, suggest that M=E groups, where M represents the central metal atom and E is a multiply bonded terminal ligand, can be stabilized in such a ligand environment with one or more following properties. First and the most, it can delocalize the d electron counts, especially those populating the antibonding orbitals of the metal center, and as a result increase the net bonding between metal and its terminal ligand. Second, it has strong σ-donating coordination sites. Computational results show that negatively charged ligands (σ-donating) not only stabilize the high oxidation state of metal centers (low d electron counts) but also reduce the Coulomb repulsion between the positively charged M and E centers. Third, it may have non-covalent interactions with the terminal ligands, such as oxygen and nitrogen, to prevent their dissociation from the metal. One of the successful examples is the hydrogen-binding interaction used by MacBeth and Borovik in the synthesis and isolation of Fe(III)=N and Fe(III)=O species. Last but not least, the terminal ligands of M=E can also be protected sterically by a bulky ligand environment.

1.2 Supported Noble Metal Catalysis

In the last decade, a rapid growth of interest in the supported noble metal catalysis has attracted more and more attention. Highly dispersed noble metal particles, including palladium, platinum, silver and gold, on redox metal-oxide supports are catalytically active for a wide variety of important green O_2-based oxidative reactions and processes, such as CO oxidation, alkene epoxidation, methane combustion, partial oxidation of alcohol, oxidative dehydration, and so on.[44-67] Many catalytic chemists have been

involved in the development of new and extremely active supported noble metal systems, and all of these works have greatly contributed to our understanding of the importance of particle sizes and metal-oxide supports, the catalytic reaction mechanism, and the interactions between noble metal and metal-oxide support as well as oxidant (O_2) and substrates.

The ability of appropriately prepared gold nanoparticles supported on titania to catalyze CO oxidation at very moderate conditions is probably one of the greatest surprises, largely because gold has long been known to be catalytically inactive.[60,68,69] Since the discovery of its high catalytic activity for low-temperature CO oxidation to CO_2 in 1989, the research activity on the catalysis of gold has grown dramatically. Although chemists have established that the catalytic properties of gold depend on the features of the support, the deposition/preparation method, the size of gold particles, and many other factors,[51,60] the mechanism, and in particular possible gold intermediates in the oxidative catalysis is still inadequately understood. Several possible reaction mechanisms have been proposed based on many reported observations, and one is represented in **Figure 1.3**.[69] The active site contains both gold atoms and ions (Au^{III}), and the latter acts as a "chemical glue" to bind gold particles on the metal-oxide support. A gold atom with a low coordination number can chemically absorb a carbon monoxide molecule, and simultaneously a hydroxyl group on the support moves to an Au^{III} ion, leaving a vacancy on the support surface, which is then occupied by a dioxygen molecule. The further transfer of CO from gold atom to the Au^{III} site generates a carboxylate group. The inserted dioxygen group oxidizes the carboxylate group on Au^{III} center by abstracting a hydrogen atom, forming carbon dioxide. The resulting hydroperoxide anion HO_2^- can

transfer its hydroxyl group to the Au^{III} ion to start another CO oxidation and complete the catalytic cycle.

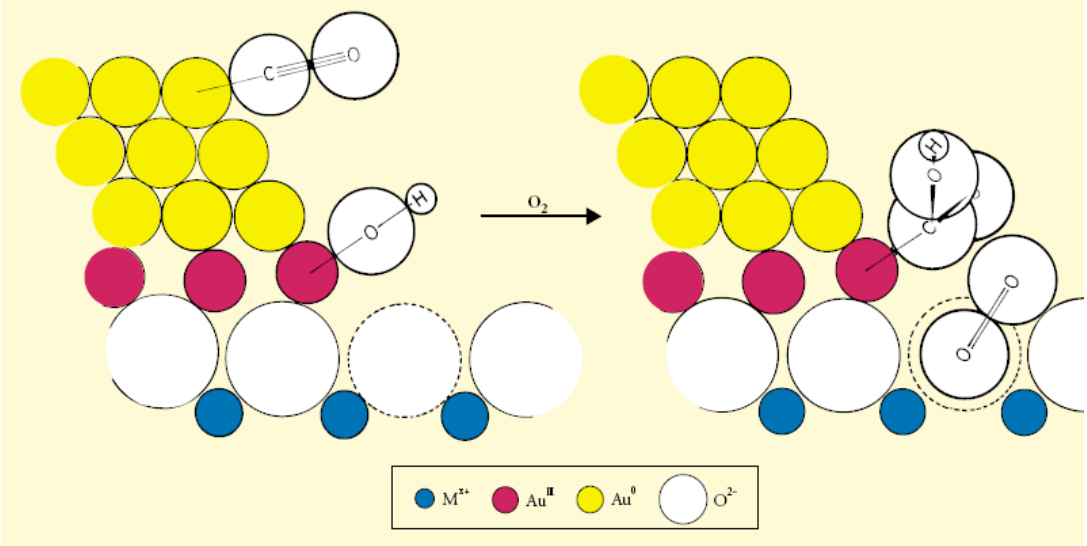

Figure 1.3 Schematic representation of the early stages of the oxidation of carbon monoxide at the periphery of an supported active gold particle.[69]

Similar to the representation above where gold oxo and particularly terminal Au-oxo species is though to be the key intermediate in the catalytic oxidation, Pd- and Pt-oxo groups have also been proposed. The interaction of dioxygen and supported noble metal surfaces/particles is complicated, and studies are difficult mainly due to insufficient techniques. As a result, many efforts have been made by synthetic chemists to synthesize and isolate molecular terminal oxo complexes of the noble metal elements, which can not only benefit our understanding of the physical and chemical properties of late transition-metal oxo groups but also serve as molecular models to study the supported noble metal

catalysts. However, these species are too unstable to be prepared and were only realized very recently by Hill and co-workers,[70-72] largely because of the maximal mismatch of metal and ligand atom (oxygen) electronegativities and orbital energies, and furthermore, the population of antibonding orbitals in the high d-electron counts metal-oxo unit.

1.3 Bridging Noble Metal-oxo Species

Because of their high electronegativity (Pd 2.20, Pt 2.28, Au 2.54) and the mismatch of the hard, basic oxygen ligand with the soft metal center, which cause a relatively weak M-O linkage, noble metal elements show low affinity for binding to oxygen. Nevertheless, a number of compounds with noble metal M-O bonds have been successfully synthesized with a variety of formal oxidation states of the metal center.[73]

There are only a few structurally characterized bridging Pd-oxo complexes in the literature. The first example is a heterometallic Pd-Cu μ_4-oxo complex $Pd_6Cu_4Cl_{12}O_4(HMPA)_4$ (HMPA = hexamethylphosphoramide) with an average Pd-μ_4-O bond distance at 2.026(5) Å, isolated by Hosokawa *et al.* in 1996.[74] The other example, $Pd_4(dpm)_4(\mu_2\text{-}Cl)_2(\mu_4\text{-}O)$ (dpm = dipivaloylmethanato), represents a $Pd_4(\mu_4\text{-}O)$ group (**Figure 1.4**).[75] The average Pd-O and Pd-μ_4-O bond lengths are 1.975(2) Å and 2.024(2) Å, respectively. Sharp and co-workers synthesized the first hetero-noble-metal oxo complexes in 2005.[76] The coordination cores of these two complexes are shown in **Figure 1.5**. In the first structure, the two Pd, two Au and two O atoms are located at the vertex sites of a pseudo octahedron; while in the second structure, the five noble metals

form a trigonal bipyramidal unit with three Pd sitting on the central plane and one Au and one Pd atom on each side of the plane.

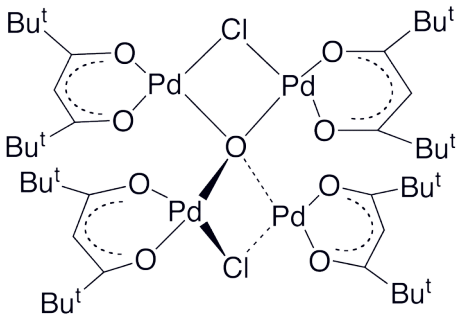

Figure 1.4 Molecular structure of a bridging Pd-oxo containing complex. The bond distances and angles of the central $Pd_4(\mu_4\text{-}O)$ are: Pd-O 2.020(1), 2.028(2) Å, Pd-O-Pd 98.6-118.0°.

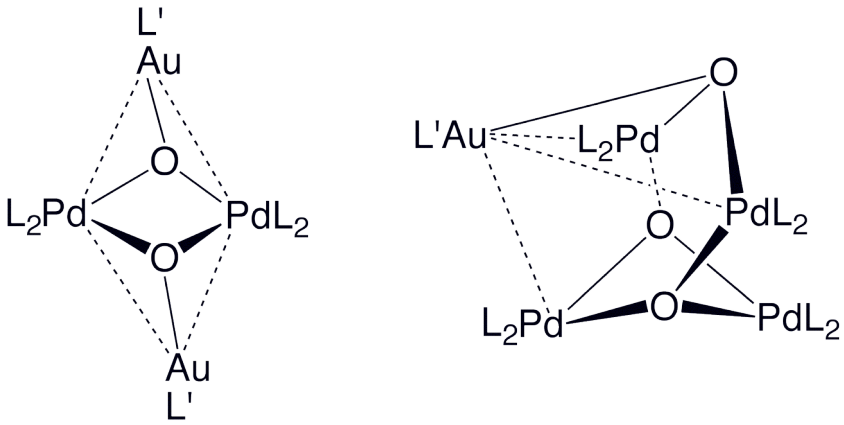

Figure 1.5 Structure diagram of two bridging hetero-noble-metal (Pd and Au) oxo complexes.

The examples of platinum oxo complexes are rare too. Sharp and co-workers have greatly expanded this chemistry, and several bridging Pt-oxo complexes are prepared and

structurally characterized.[77-79] A series of dinuclear Pt complexes have the Pt_2O_2 core unit with a butterfly structure have been made from the starting $[L_2Pt(\mu\text{-}OH)]_2^{2+}$ materials, partly because of interest in the hydrolysis chemistry of the chemotherapy drug cisplatin, *cis*-$(NH_3)_2PtCl_2$.[77,78] The phosphorus containing ligands are typically used for their flexibility and the convenience of ^{31}P NMR spectroscopy, a technique powerful not only in product characterization but also in reaction monitoring. **Figure 1.6** represents the structure of a exemplary molecule, $[(Ph_3P)_2Pt(\mu\text{-}O)]_2 \bullet LiBF_4$, with the Pt-O distances at 2.038(6) and 2.018(6) Å.

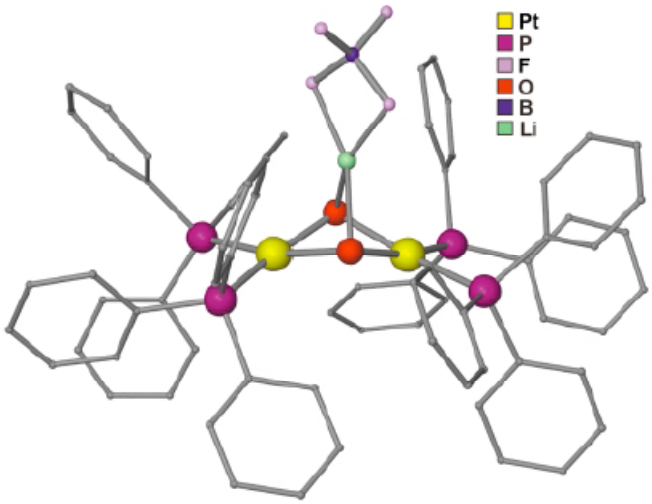

Figure 1.6 Structure diagram of a bridging Pt-oxo complex. Anion BF_4^- connects to the $[(Ph_3P)_2Pt(\mu\text{-}O)]_2$ unit through a Li^+ cation.

Unlike palladium and platinum with only a few oxo complexes and the only oxidation state +2, a number of bridging Au-O compounds have been synthesized with Au in the formal oxidation states -1, +1, and +3.[80] Although these compounds are thermally unstable in general, weak Au-O bonds are usually highly reactive and display

interesting reaction chemistry.[81] A good example is shown by Cinellu *et al.* (**Figure 1.7**).

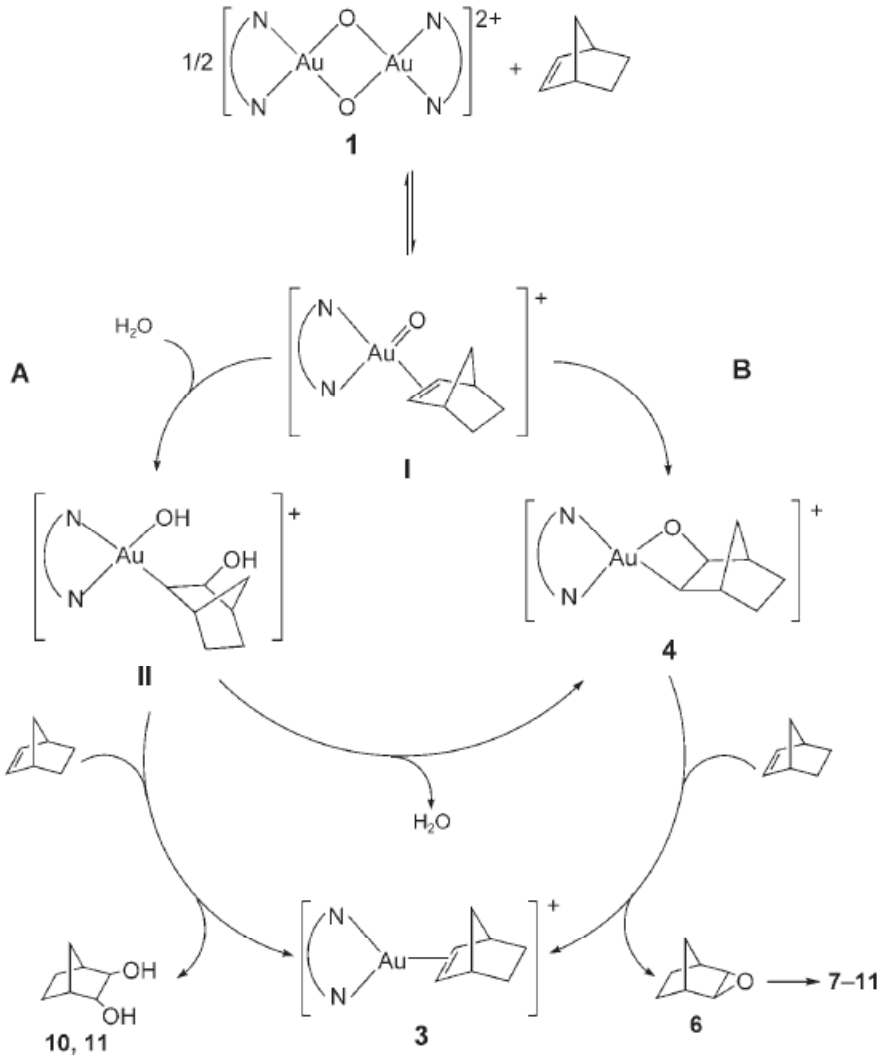

Figure 1.7 Schematic representation of the reaction between a $Au_2(\mu\text{-}O)_2$ complex and norbornene. A terminal Au-oxo containing intermediate (**I**) is proposed in the reaction mechanism.[81]

The reaction of $[Au_2(bipy^R)_2(\mu\text{-}O)_2](PF_6)_2$ with the strained cyclic alkenes norbornene (nb) gives two products, an alkene comlex $[Au(bipy^R)(nb)](PF_6)$ and an

auraoxetane [Au(bipy^{R})(κ^2-*O,C*-2-oxynorbornyl)](PF_6). The structure of the latter is fully characterized by X-ray single crystal diffraction: the gold atom has a square-planar coordination environment with bond distances 1.967(7) Å for Au-O and 2.055(8) for Au-C. Importantly, a terminal Au-oxo species is proposed to be the intermediate I in this reaction mechanism.[81]

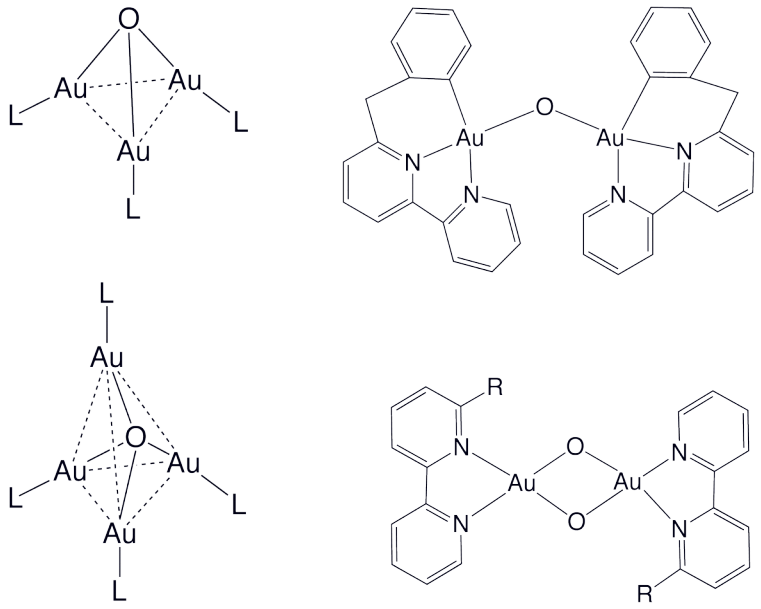

Figure 1.8 Molecular examples of bridging Au-O containing complexes with gold in oxidation state +1 (left) and +3 (right).

Gold has the highest electron affinity and electronegativity among the metals, and its oxidation state -1 was recently found in ternary oxides of the general composition M_3AuO with M = K, Rb and Cs. However, in these compounds, the Au atom does not directly bind to oxygen but is surrounded by 12 alkali metals with normal Au-M distances in the range of 3.7 to 4.2 Å.[73] Although both gold oxidation states +1 and +3

are common in Au chemistry, Au(III)-oxo complexes have been reported very recently with stabilization from chelating nitrogen ligands, while Au(I)-oxo species are well established. Structural examples of Au-O containing complexes with Au in oxidation state +1 and +3 are shown in **Figure 1.8**. All these reported Au-O bonds, including the Au_2O_2 core in the last structure representation which might be viewed as a dimer of two terminal Au=O units, vary from 1.90 to 2.1 Å, consistent with Au-O single bonds.[73,80]

1.4 Polyoxometalates – Metal-oxide Clusters

Polyoxometalate (POM for convenience) is a term used to describe the class of early transition-metal oxygen anion clusters, including both the heteropoly and isopolyanion complexes.[82] Largely because of the advances in modern high-resolution, sophisticated instrumentation and related techniques in both solid and solution state, investigations of the structural and reactivity properties of POMs have grown rapidly in the last decade. Although POMs are used as catalysts and inorganic materials, the ability to extensively and easily alter their molecular properties (structure, solubility, potential, charge, size, etc.) as well as their structural and chemical stability have made POMs highly promising in several other fields, including microelectronics and medical diagnosis.[83-90] Furthermore, lacunary POMs can act as inorganic ligands to incorporate transition metals, and this leads to a wide application of POMs in research ranging from fundamental coordination chemistry, electron transfer and ion pairing, to self-assembly, magnetism and bio-/nano-technology.[89,90] This thesis focuses on the application of lacunary POMs as inorganic ligands to incorporate noble metals, which resembles the

deposition of noble metals on redox active early transition-metal oxide surfaces used in supported catalysis. Several classical lacunary polytungstate derivatives, the most studied POM classes, and the recent development of their polydentate coordination chemistry are briefly addressed.

There are two major structural families of polytungstates, namely the Keggin[91,92] and the Wells-Dawson[93] structures with formulas $[PW_{12}O_{40}]^{3-}$ and $[P_2W_{18}O_{62}]^{6-}$, respectively. The phosphorus derivatives instead of others, like silicon, arsenic and antimony, are typically used in this thesis mainly because of (1) the phosphorus-based polytungstates have well-established solution chemistry and (2) ^{31}P NMR is a convenient and powerful technique in both product characterization and reaction monitoring. Both plenary Keggin and Wells-Dawson structures are not stable at high pH, where a series of hydrolytic decompositions/degradations occur. Controlled hydrolysis of these heteropolyanion species with base under appropriate conditions (temperature, ionic strength, etc) can specifically produce the relative lacunary structures where one or more addenda atoms (e.g. W) have been removed from the parent polyanions along with the oxygen atoms that are not shared by other addenda atoms. The generated lacunary polyanions are typically stable in a certain pH range and can generally incorporate a wide variety of transition metals to restore the parent structures or serve as building locks for constructing larger metal oxide architectures.

The commonly used Keggin-based lacunary polytungstates as well as their reaction pattern are summarized in **Figure 1.9**. The monovacant ligand $[\alpha\text{-}PW_{11}O_{39}]^{7-}$ is obtained from its parent α-Keggin $[\alpha\text{-}PW_{12}O_{40}]^{3-}$ by the loss of one $[W(VI)=O]^{4+}$ unit at pH 1.5-2.0. This lacunary polytungstate is stable in solution over a wide range of pH values and

ionic strengths, and can coordinate with most transition metal ions ($M^{2+/3+}$) to form the mono-substituted α-Keggin complexes, $[M(OH_2)PW_{11}O_{39}]^{n-}$. The tetrabutylammonium (TBA) salts of several first-row transition metal substituted $\{PW_{11}\}$ derivatives, $[(n\text{-}C_4H_9)_4N]_4H[M(OH_2)PW_{11}O_{39}]$ ($M = Mn^{II}$, Co^{II}), have been reported to be remarkably effective catalysts for many reactions, including alkene epoxidation and sulfur oxidation.[94] However, the studies of catalytic mechanisms and involved reactive intermediates are challenging largely because these $\{\alpha\text{-}MPW_{11}\}$ species resemble the parent all-tungsten α-Keggin structure and as a result usually crystallize in high symmetry cubic system. The crystallographically imposed symmetry causes the incorporated transition metal ion and the eleven tungsten atoms to be positionally disordered over the twelve heavy atom sites. As a consequence, each heavy atom position is occupied by 1/12 M and 11/12 W, which makes the absolute structural determination, including the key bond distances and angles around M center, less informative. On the other hand, reactions of $\{\alpha\text{-}PW_{11}\}$ with lanthanide (Ln) and actinide (An) ions typically lead to the Weakley-type complexes, $\{M[\alpha\text{-}PW_{11}O_{39}]_2\}^{n-}$, initially reported by Peacock and Weakley in 1971.[95] The formation of this Ln or An bridged polytungstate structures is benefited by the large coordination numbers/abilities of these f-block elements. Similarly, other large metal ions, such as Zr^{4+} and Hf^{4+}, can also form the Weakley-type (1:2) coordination compounds,[96] whose structure can be unambiguously solved by X-ray diffraction.

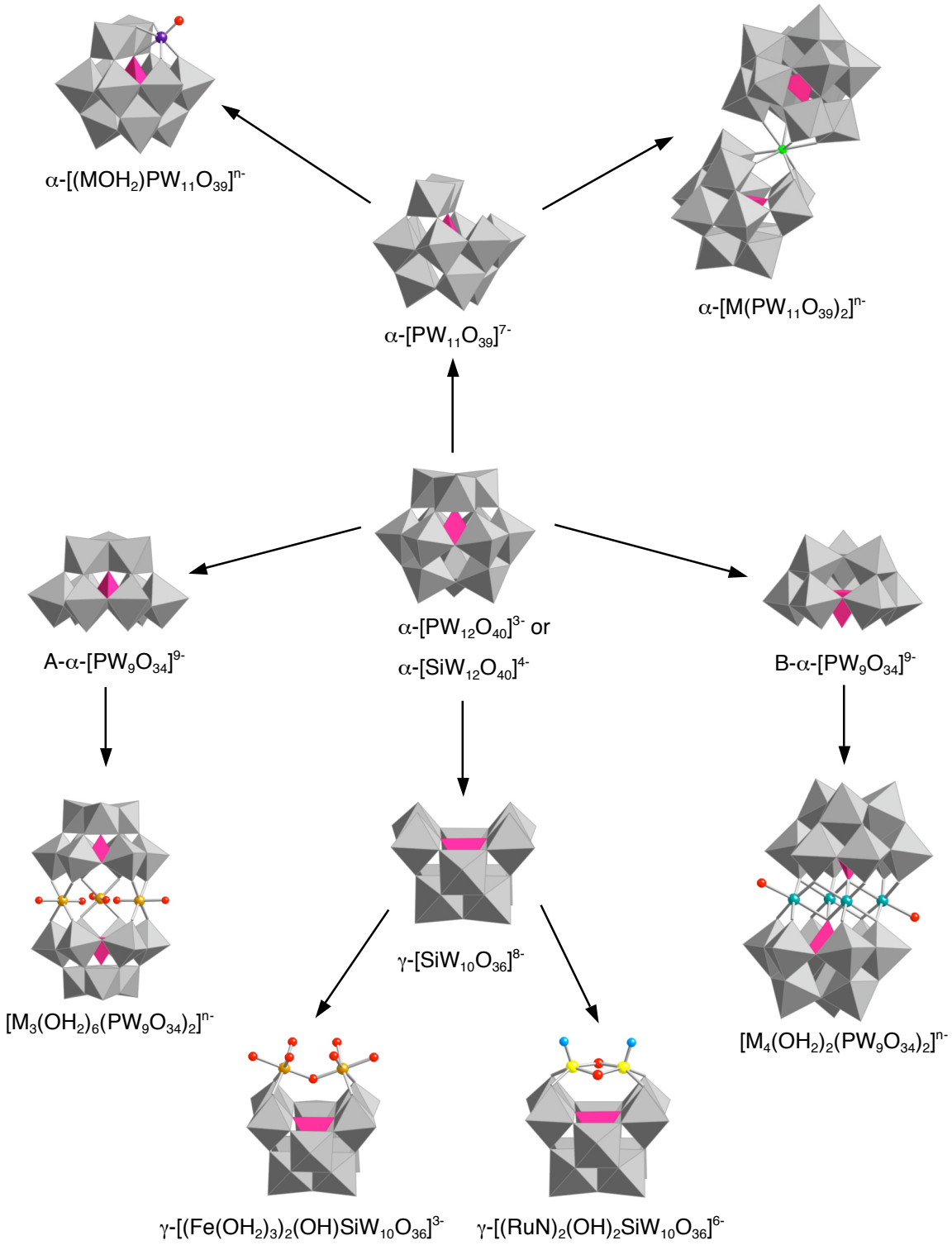

Figure 1.9 Keggin-based lacunary polytungstates and their chemistry.

The other widely used lacunary α-Keggin polytungstate is a trivacant derivative, $[A\text{-}\alpha\text{-}PW_9O_{34}]^{9-}$, formed by the removal of three corner-sharing octahedral tungsten units. Unlike the monovacant $\{\alpha\text{-}PW_{11}\}$ ligand, $\{A\text{-}\alpha\text{-}PW_9\}$ is not stable in solution: it decomposes to other polytungstate species upon dissolution, including mono tungstate (WO_4^{2-}) and $[\alpha\text{-}PW_{11}O_{39}]^{7-}$ (the existence of the latter is confirmed by its characteristic chemical shift in ^{31}P NMR spectroscopy). However, largely because of its highly reactive open coordination sites consisting of nucleophilic oxygen atoms, $\{A\text{-}\alpha\text{-}PW_9\}$ can react with most of the first-row transition metals quickly before its decomposition/isomerization in solution. The usually formed trinuclear sandwich structure, $A\text{-}[M_3(PW_9O_{34})_2]^{n-}$,[97] is stable in both aqueous and organic solution and several of them (e.g. M = Fe) are good catalysts for the alkene oxidation.[98,99] Interestingly, some small anions, such as CO_3^{2-} and NO_3^-, can be incorporated into the central cavity surrounded by the three transition metals and the polytungstate frameworks.[100] It is believed that these anions play as a template in the formation of these sandwich structures and considerably increase the stability of the whole structure in both solution and solid state.

It has been shown that $[A\text{-}\alpha\text{-}PW_9O_{34}]^{9-}$ undergoes a solid-state isomerization to form $[B\text{-}\alpha\text{-}PW_9O_{34}]^{9-}$ upon heating at 150 ºC for days.[101] The thermal transformation process can be easily monitored by FT-IR spectroscopy and it is believed that the unheated literature complex, the starting material $Na_9[PW_9O_{34}]$, is predominantly $[A\text{-}\alpha\text{-}PW_9O_{34}]^{9-}$, and the thermolyzed product is mainly $[B\text{-}\alpha\text{-}PW_9O_{34}]^{9-}$. The B-type $\{PW_9\}$ can be viewed as a trivacant α-Keggin derivatives, where the parent $[\alpha\text{-}PW_{12}O_{40}]^{3-}$ loses

one of the four edge-sharing W_3 triads. A major structural difference between A- and B-type $\{PW_9\}$ is worthy noting here. In the structure of A-α-$\{PW_9\}$, all four phosphorus oxygens of the central tetrahedral PO_4 unit are connected to tungsten atoms, while there is a free P-O oxygen in the structure of B-α-$\{PW_9\}$. This structural difference makes their coordination chemistry with transition metals quite different. Unlike A-α-$\{PW_9\}$ who usually reacts with three M to form the trinuclear sandwich complexes, B-α-$\{PW_9\}$ generally incorporates four transition metals to give the $[M_4(OH_2)_2(B\text{-}PW_9O_{34})_2]^{n-}$,[101] where two M atoms are located at the saturated internal site and the other two at the external positions. Interestingly, the sixth aqua ligand of the external M is labile and can be easily replaced by other strong σ-donating ligands.

Recently, the divacant Keggin-type polytungstate $[\gamma\text{-}SiW_{10}O_{36}]^{8-}$ has attracted much attention largely due to its application in H_2O_2 based oxidation.[102-104] Unlike the α-Keggin isomer, $[\gamma\text{-}SiW_{10}O_{36}]^{8-}$ and its di-substituted derivatives $[\gamma\text{-}M_2SiW_{10}O_{36}]^{8-}$ can crystallize in lower symmetry disorder-free space groups. There are two coordination patterns exhibited by the γ-$\{SiW_{10}\}$, namely out-of-pocket and in-pocket structures. In the out-of-pocket structure such as $\gamma\text{-}[(Fe(OH_2)_3)_2(OH)SiW_{10}O_{36}]^{3-}$, the two Fe centers are each attached to the γ-$\{SiW_{10}\}$ frameworks by two oxo oxygens and connected to each other through one bridging hydroxyl group. The coordination sphere of each Fe atom is completed by three aqua ligands, usually leading to the formation of dimer or trimer in solution.[105] On the other hand, the in-pocket structure, exemplified by $\gamma\text{-}[(RuN)_2(OH)_2SiW_{10}O_{36}]^{6-}$, has the two Ru atoms entirely inserted into the polytungstate cavities and connected to three oxo oxygens on the polyanion unit. Importantly, the two Ru centers are bridged by two hydroxyl groups, which render this structure more stable in

aqueous solution compared to the out-of-pocket structure. Furthermore, the in-pocket structure usually forms a monomer in solution, a result consistent with the considerable structural differences between these two coordination patterns.

The other well-known family of polytungstate ligands is the Wells-Dawson type lacunary species. Several commonly used ligands and their chemistry are summarized in **Figure 1.10**. The use of lacunary species derived from the plenary Wells-Dawson polyanion, $[P_2W_{18}O_{62}]^{6-}$, is similar to the Keggin series, but more diverse mainly due to their less symmetrical structure and more complex composition.

There are two monovacant isomers from hydrolytic degradation of the parent Wells-Dawson structure. The removal of a tungsten unit at the belt position leads to α_1-$[P_2W_{17}O_{61}]^{10-}$. Polytungstate α_1-$\{P_2W_{17}\}$ is not stable in solution: it will slowly convert to α_2-$\{P_2W_{17}\}$ (see below) from hydrolysis and isomerization. However, the solution stability of the α_1-$\{P_2W_{17}\}$ isomer can be considerably increased in the presence of Li^+ cation, which occupies the vacant site. Addition of transition metal ions, such as Zn^{II} and Ni^{II}, forms the 1:1 monomeric complex, α_1-$[M(OH_2)P_2W_{17}O_{61}]^{8-}$.[106,107] Reaction with Ln or An, the large f-block elements with many coordination sites, can yield a 1:2 bridging complex[108] $\{M[\alpha_1\text{-}P_2W_{17}O_{61}]_2\}^{n-}$ and a 1:1 dimeric complex[109] $\{M[\alpha_1\text{-}P_2W_{17}O_{61}]\}_2^{n-}$.

The second monovacant isomer α_2-$[P_2W_{17}O_{61}]^{10-}$ is formed by the removal of an apical tungsten unit from the plenary Wells-Dawson structure $[P_2W_{18}O_{62}]^{6-}$. Polyanion α_2-$\{P_2W_{17}\}$ is stable over a wide range of pH values and ionic strengths, and it can be isolated in several alkali salts and organic soluble forms. Similar to its α_1-$\{P_2W_{17}\}$ isomer, this monovacant polytungstate ligand can react with many transition metals to

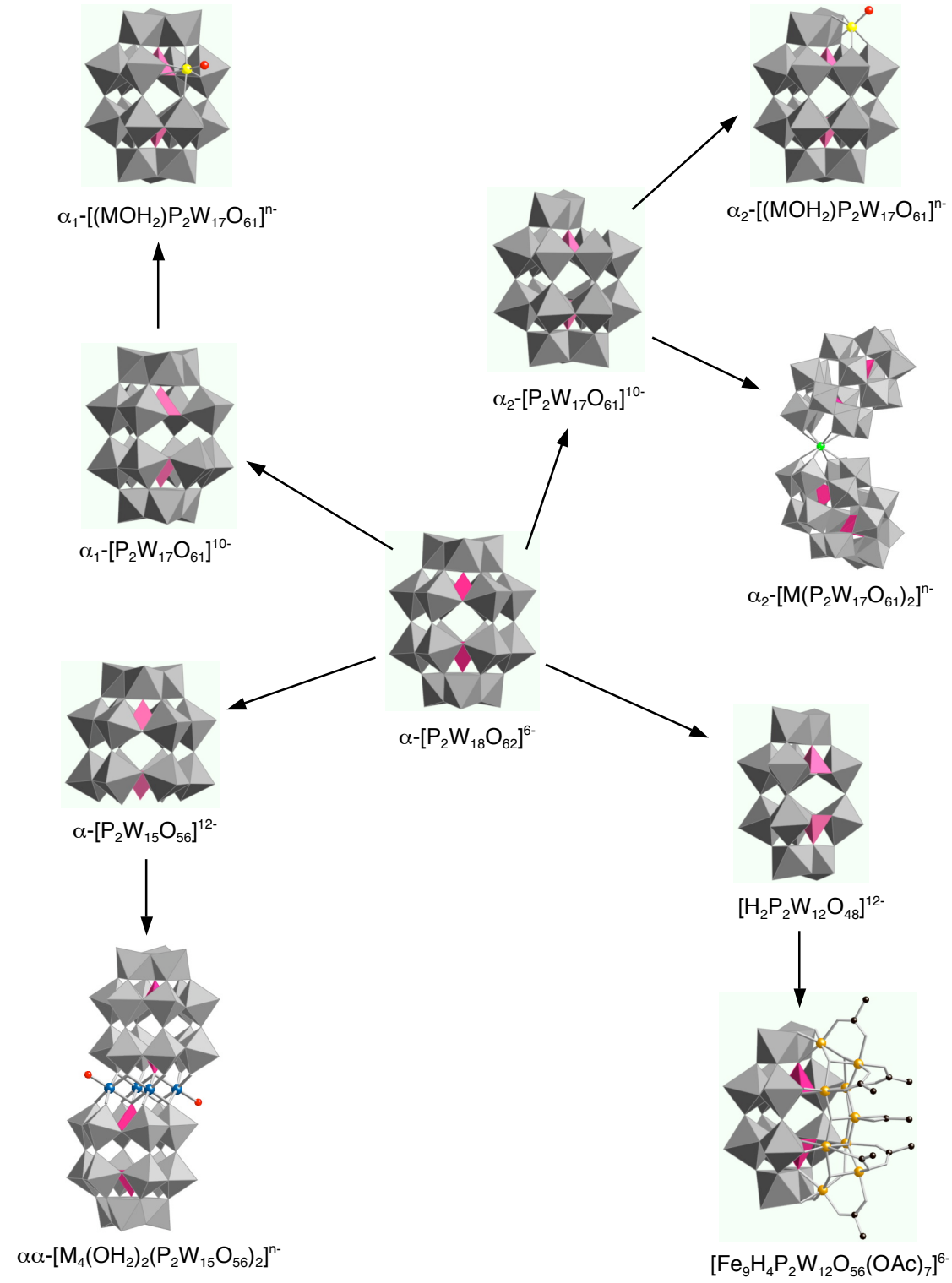

Figure 1.10 Wells-Dawson based lacunary polytungstates and their chemistry.

form one M substituted Wells-Dawson structure, α_2-$[M(OH_2)P_2W_{17}O_{61}]^{n-}$ (M = Mn^{III}, Fe^{III}, Co^{II}, Ni^{II} and Cu^{II}). The TBA salts of these complexes are highly effective oxidation catalysts in comparison with some of the best metalloporphyrin complexes.[110-112] Moreover, the 1:2 monomeric complexes[96] $\{M[\alpha_2\text{-}P_2W_{17}O_{61}]_2\}^{n-}$ and 1:1 dimeric complex[107] $\{M[\alpha_2\text{-}P_2W_{17}O_{61}]\}_2^{n-}$ have also been reported. The chemistry of both monovacant α_1-$\{P_2W_{17}\}$ and α_2-$\{P_2W_{17}\}$ isomers as well as their M substituted complexes has been extensively studied by Pope, Francesconi and their co-workers.

The trivacant Wells-Dawson polyanion, α-$[P_2W_{15}O_{56}]^{12-}$, is one of the most important polytungstate ligands used in the POM community. Its formation results from the removal of one edge-sharing W_3 cap unit from $[P_2W_{18}O_{62}]^{6-}$, thereby facilitating coordination chemistry analogous to the B-type trivacant ligand, B-α-$\{PW_9\}$. Typically, α-$\{P_2W_{15}\}$ reacts with four low valent transition metal cations $M^{2+/3+}$ to afford the normal tetranuclear sandwich structure, $[M_4(OH_2)_2(P_2W_{15}O_{56})_2]^{n-}$ (M = Mn^{II}, Mn^{III}, Fe^{III}, Co^{II}, Ni^{II}, Cu^{II} and Zn^{II}),[101,113-116] or reacts with three high valent transition metal ions to regenerate the monomeric plenary Wells-Dawson structure, $[M_3P_2W_{15}O_{62}]^{n-}$ (M = W^{VI}, Mo^{VI}, V^{V} and Nb^{V}).[117-121] Although polyanion α-$\{P_2W_{15}\}$ is not stable in solution, its structure can be deduced from the metal-ion-substituted complexes. Recently, Anderson *et al.* reported the synthesis and characterization of a di-iron(III)-substituted analogue of the tetranuclear sandwich complex, $[Fe_2(NaOH_2)_2(P_2W_{15}O_{56})_2]^{16-}$,[122-124] where the two iron(III) atoms reside at the internal positions, and the two sodium cations reside at the external sites. Importantly, the authors show that these two labile sodium cations can be replaced by other low valent transition metals to form $[Fe_2(MOH_2)_2(P_2W_{15}O_{56})_2]^{14-}$ (M = Ni^{II}, Cu^{II} and Zn^{II}). As a result, this di-iron(III) sandwich complex can serve as a very

important starting material for the preparation of many heteronuclear transition metal substituted derivatives.

The metastable polyanion α-$[H_2P_2W_{12}O_{48}]^{12-}$ is obtained from the parent Wells-Dawson structure α-$[P_2W_{18}O_{62}]^{6-}$ by the removal of six tungsten units on one side. Although the crystalline solids of this hexavacant anion are not available, its structure can be directly deduced from X-ray diffraction studies on a polyperoxo anion $[P_2W_{12}O_{56}(NbO_2)_6]^{12-}$.[125] Polyanion $\{P_2W_{12}\}$ is stable in aqueous solution at its natural pH and ionic strength. Only one single peak is observed in ^{31}P NMR spectrum, a result consistent with the crystallography studies showing the two phosphorus atoms are symmetrically equivalent. Acidification of the solution in the absence of tungstate (WO_4^{2-}) gives the dimerized product $\{P_4W_{24}\}$. Attempts to grow crystals of the dimer $\{P_4W_{24}\}$ are unsuccessful: only the tetramer $[P_8W_{48}O_{184}]^{40-}$ forms in the crystallization step, although the dimer $\{P_4W_{24}\}$ can be precipitated (by KCl) as a pure solid (its purity can be also checked by ^{31}P NMR spectroscopy).[126,127] The coordination chemistry of $\{P_2W_{12}\}$ and its oligomeric derivatives, $\{P_4W_{24}\}$ and $\{P_8W_{48}\}$, has not been extensively studied, and only a few examples are reported.[128]

1.5 Use of Polyoxometalates as stabilizing ligands for M=O

Polyoxometalates, particularly, polytungstate ligands can afford coordination spheres for the transition metals that are very similar to those in metalloporphyrin complexes. As shown in **Figure 1.11**, instead of using oxygen in polytungstates rather than nitrogen in metalloporphyrins as the coordinating atoms, both structures have the

same distorted C_{4v} local symmetry octahedral configurations. Because both oxygen and nitrogen are good σ-donating atoms and both have similar electronegativity and electronic structure, it is possible that a polytungstate ligand can act as an inorganic "porphyrin" to support terminal M=O units, especially for those mid- and late-transition metal elements whose terminal oxo ligands are not conventionally stable.

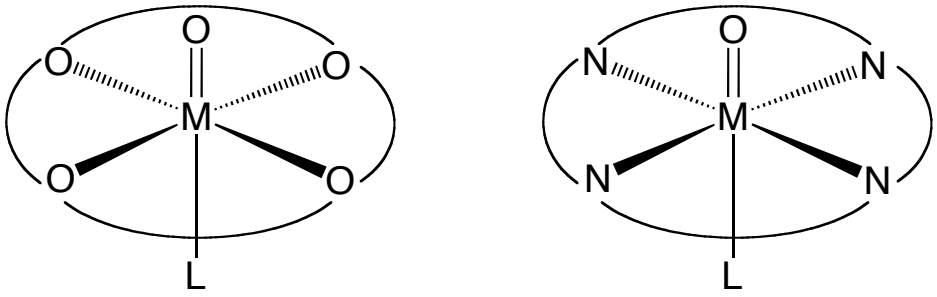

Figure 1.11 Schematic representations of terminal metal-oxo units in the coordination spheres of a polyoxometalate (left) and a metalloporphyrin (right), showing very similar ligand environments afforded by the two families of complexes.

Besides the good σ-donating properties, both polytungstates and porphyrins are good π-accepting ligands.[70,129,130] As documented above, the d-electron count on the metal center largely dictates stability and reactivity of the terminal metal-oxo unit, and as a result, in principle, the terminal oxo ligand is stabilized at metal centers with no more than four d electrons. However, the high d-electron count terminal transition metal-oxo unit can be considerably stabilized by the delocalization of those d electrons occupying the antibonding orbitals of M=O units into the ligand-based orbitals. Polytungstates have many delocalized d^0 W(VI)-based orbitals. These π character orbitals have the same

symmetry and similar energies as the π* antibonding orbitals on the M=O units, and thus they can interact effectively lowering the energy of the π* electrons on the M=O units. As a result, the net bonding between the transition metal and the terminal oxo group increases.

Based on this knowledge, it has been possible for us to stabilize the highly reactive terminal late-transition metal-oxo units in polyoxometalate ligand environments. The latter have both σ-donating and π-accepting features and are redox and hydrolytic stable metal-oxo anionic cluster units. In this thesis, the synthesis and full characterization of several terminal metal-oxo complexes of the group 10 and 11 elements (M = Pd, Pt and Au) are reported.[70-72] All these molecular complexes exhibit multiple bonding between M and oxygen, commensurate with the shortest such bond distances to date and are stabilized by electron-poor d^0 redox-active metal-oxide-like polytungstate ligands. The structural, physicochemical and other properties of these complexes are characterized by more than 10 methods.

References

(1) Holm, R. H. *Chem. Rev.* **1987**, *87*, 1401-1449.

(2) Nugent, W. A.; Mayer, J. M. *Metal-Ligand Multiple Bonds*; John Wiley & Sons, Inc.: New York, 1988.

(3) Jones, R.; Jayaraj, K.; Gold, A.; Kirk, M. L. *Inorg. Chem.* **1998**, *37*, 2842-2843.

(4) Inscore, F. E.; McNaughton, R.; Westcott, B. L.; Helton, M. E.; Jones, R.; Khawan, I. K.; Enemark, J. H.; Kirk, M. L. *Inorg. Chem.* **1999**, *38*, 1401-1410.

(5) Carducci, M. D., Brown, C., Solomon, E. I., Enemark, J. H. *J. Am. Chem. Soc.* **1994**, *116*, 11856-11868.

(6) Parkin, G. In *Prog. Inorg. Chem.*; Karlin, K. D., Ed.; Wiley: New York, 1998; Vol. 47, p 1-165.

(7) MacBeth, C. E.; Golombek, A. P.; Jr., V. G. Y.; Yang, C.; Kuczera, K.; Hendrich, M. P.; Borovik, A. S. *Science* **2000**, *289*, 938-941.

(8) Spaltenstein, E.; Conry, R. R.; Critchlow, S. C.; Mayer, J. M. *J. Am. Chem. Soc.* **1989**, *111*, 8741-8742.

(9) Rohde, J.-U.; In, J.-H.; Lim, M. H.; Brennessel, W. W.; Bukowski, M. R.; Stubna, A.; Münck, E.; Nam, W.; Que Jr., L. *Science* **2003**, *299*, 1037-1039.

(10) Green, M. T.; Dawson, J. H.; Gray, H. B. *Science* **2004**, *304*, 1653-1656.

(11) Bukowski, M. R.; Koehntop, K. D.; Stubna, A.; Bominaar, E. L.; Halfen, J. A.; Münck, E.; Nam, W.; Lawrence Jr., Q. *Science* **2005**, *310*, 1000-1002.

(12) Hay-Motherwell, R. S.; Wilkinson, G.; Hussain-Bates, B.; Hursthouse, M. B. *Polyhedron* **1993**, *12*, 2009-2012.

(13) Che, C. M.; Wong, K. Y.; Mak, T. C. W. *Chem. Commun.* **1985**, 988-990.

(14) Klinker, E. J.; Jackson, T. A.; Jensen, M. P.; Stubna, A.; Juhász, G.; Bominaar, E. L.; Münck, E.; Lawrence Que, J. *Angew Chem. Int. Ed.* **2006**, *45*, 7394 –7397.

(15) Glueck, D. S.; Wu, J.; Hollander, F. J.; Bergman, R. G. *J. Am. Chem. Soc.* **1991**, *113*, 2041-2054.

(16) Andrews, M. A.; Gould, G. L.; Voss, E. J. *Inorg. Chem.* **1996**, *35*, 5740-5742.

(17) Verma, A. K.; Lee, S. C. *J. Am Chem. Soc.* **1999**, *121*, 10838-10839.

(18) Verma, A. K.; Nazif, T. N.; Achim, C.; Lee, S. C. *J. Am Chem. Soc.* **2000**, *122*, 11013-11014.

(19) Mindiola, D. J.; Hillhouse, G. L. *J. Am. Chem. Soc.* **2001**, *123*, 4623-4624.

(20) Melenkivitz, R.; Mindiola, D. J.; Hillhouse, G. L. *J. Am. Chem. Soc.* **2002**, *124*, 3846-3847.

(21) Mindiola, D. J.; Hillhouse, G. L. *J. Am. Chem. Soc.* **2002**, *124*, 9976-9977.

(22) Artero, V.; Proust, A.; Herson, P.; Villain, F.; Moulin, C. C. d.; Gouzerh, P. *J. Amer. Chem. Soc.* **2003**, *125*, 11156-11157.

(23) Thyagarajan, S.; Shay, D. T.; Incarvito, C. D.; Rheingold, A. L.; Theopold, K. H. *J. Am. Chem. Soc.* **2003**, *125*, 4440-4441.

(24) Waterman, R.; Hillhouse, G. L. *J. Am. Chem. Soc.* **2003**, *125*, 13350-13351.

(25) Hu, X.; Meyer, K. *J. Am Chem. Soc.* **2004**, *126*, 16322-16323.

(26) MacBeth, C. E.; Thomas, J. C.; Betley, T. A.; Peters, J. C. *J. Inorg. Chem* **2004**, *43*, 4645-4662.

(27) Seo, M. S.; In, J.-H.; Kim, S. O.; Oh, N. Y.; Hong, J.; Kim, J.; Lawrence Que, J.; Nam, W. *Angew Chem. Int. Ed.* **2004**, *43*, 2417 –2420.

(28) Amisial, L. D.; Dai, X.; Kinney, R. A.; Krishnaswamy, A.; Warren, T. H. *Inorg. Chem.* **2004**, *43*, 6537-6539.

(29) Dai, X.; Warren, T. H. *J. Am Chem. Soc.* **2004**, *126*, 10085-10094.

(30) Kogut, E.; Zeller, A.; Warren, T. H.; Strassner, T. *J. Am. Chem. Soc.* **2004**, *126*, 11984-11994.

(31) Larsen, P. L.; Gupta, R.; Powell, D. R.; Borovik, A. S. *J . Am. Chem. Soc.* **2004**, *126*, 6522-6523.

(32) Rohde, J.-U.; Torelli, S.; Shan, X.; Lim, M. H.; Klinker, E. J.; Kaizer, J.; Chen, K.; Nam, W.; Lawrence Que, J. *J. Am Chem. Soc.* **2004**, *126*, 16750-16761.

(33) Rohde, J.-U.; Lawrence Que, J. *Angew Chem. Int. Ed.* **2005**, *44*, 2255 –2258.

(34) Kogut, E.; Wiencko, H. L.; Zhang, L.; Cordeau, D. E.; Warren, T. H. *J. Am Chem. Soc.* **2005**, *127*, 11248-11249.

(35) Abu-Omar, M. M.; Loaiza, A.; Hontzeas, N. *Chem. Rev.* **2005**, *105*, 2227-2252.

(36) Berry, J. F.; Bill, E.; Bothe, E.; George, S. D.; Mienert, B.; Neese, F.; Wieghardt, K. *Science* **2006**, *312*, 1937-1941.

(37) Badiei, Y. M.; Krishnaswamy, A.; Melzer, M. M.; Warren, T. H. *J.Am. Chem. Soc.* **2006**, *128*, 15056-15057.

(38) Dey, A.; Hocking, R. K.; Larsen, P.; Borovik, A. S.; Hodgson, K. O.; Hedman, B.; Solomon, E. I. *J . Am. Chem. Soc.* **2006**, *128*, 9825-9833.

(39) Khenkin, A. M.; Kumar, D.; Shaik, S.; Neumann, R. *J. Am Chem. Soc.* **2006**, *128*, 15451-15460.

(40) Thomas, C. M.; Mankad, N. P.; Peters, J. C. *J. Am Chem. Soc.* **2006**, *128*, 4956-4957.

(41) Cowley, R. E.; Bontchev, R. P.; Sorrell, J.; Sarracino, O.; Feng, Y.; Wang, H.; Smith, J. M. *J. Am Chem. Soc.* **2007**, *129*, 2424-2425.

(42) Oliveira, F. T. d.; Chanda, A.; Banerjee, D.; Shan, X.; Mondal, S.; Jr., L. Q.; Bominaar, E. L.; Münck, E.; Collins, T. J. *Science* **2007**, *315*, 835-838.

(43) Ison, E. A.; Cessarich, J. E.; Travia, N. E.; Fanwick, P. E.; Abu-Omar, M. M. *J. Am. Chem. Soc.* **2007**, *129*, 1167-1178.

(44) Shelef, M. *Chem. Rev.* **1995**, *95*, 209-225.

(45) Appleby, A. J.; Foulkes, F. R. *Fuel cell handbook*; Krieger Publising Company, Malabar, Florida, 1993.

(46) Somorjai, G. A. *Introduction to surface chemistry and catalysis*; Wiley: New York, 1994.

(47) Deluga, G. A.; Salge, J. R.; Schmidt, L. D.; Verykios, X. E. *Science* **2004**, *303*, 993-997.

(48) Kim, W. B.; Voitl, T.; Rodriguez-Rivera, G. J.; Dumesic, J. A. *Science* **2004**, *305*, 1280-1283.

(49) Landon, P.; Ferguson, J.; Solsona, B. E.; Garcia, T.; Carley, A. F.; Herzing, A. A.; Kiely, C. J.; Golunskic, S. E.; Hutchings, G. J. *Chem Comm* **2005**, 3385–3387.

(50) Groves, J. T.; Quinn, R. *J. Am. Chem. Soc.* **1985**, *107*, 5790-5792.

(51) Valden, M.; Lai, X.; Goodman, D. W. *Science* **1998**, *281*, 1647-1650.

(52) Neumann, R.; Dahan, M. *J. Am. Chem. Soc.* **1998**, *120*, 11969-11976.

(53) Brink, G.-J.; Arends, I. W. C. E.; Sheldon, R. A. *Science* **2000**, *287*, 1636-1639.

(54) Weinstock, I. A.; Barbuzzi, E. M. G.; Wemple, M. W.; Cowan, J. J.; Reiner, R. S.; Sonnen, D. M.; Heintz, R. A.; Bond, J. S.; Hill, C. L. *Nature* **2001**, *414*, 191-195.

(55) Boring, E.; Geletii, Y. V.; Hill, C. L. *J. Am. Chem. Soc.* **2001**, *123*, 1625-1635.

(56) Rhule, J. T.; Neiwert, W. A.; Hardcastle, K. I.; Do, B. T.; Hill, C. L. *J. Am. Chem. Soc.* **2001**, *123*, 12101-12102.

(57) Boring, E.; Geletii, Y.; Hill, C. L. In *Catalytic Activation of Dioxygen*; Simandi, L. I., Ed.; Kluwer: Dordrecht, 2001.

(58) Dijksman, A.; Marino-González, A.; Payeras, A. M. i.; Arends, I. W. C. E.; Sheldon, R. A. *J. Am. Chem. Soc.* **2001**, *123*, 6826-6833.

(59) Porta, F.; Rossi, M. *J. Mol. Cat A: Chem.* **2003**, *204-205*, 553-559.

(60) Chen, M. S.; Goodman, D. W. *Science* **2004**, *306*, 252-255.

(61) Sanchez-Castillo, M. A.; Couto, C.; Kim, W. B.; Dumesic, J. A. *Angew. Chem. Int. Ed.* **2004**, *43*, 1140 –1142.

(62) Bar-Nahum, I.; Khenkin, A. M.; Neumann, R. *J. Am. Chem. Soc.* **2004**, *126*, 10236-10237.

(63) Neumann, R. In *Transition Metals for Organic Synthesis (2nd Edition)*; Beller, M., Bolm, C., Eds.; Wiley-VCH: Weinheim, 2004; Vol. 2, p 415-426.

(64) Choudhary, T. V.; Goodman, D. W. *Applied Catalysis A: General* **2005**, *291*, 32-36.

(65) *Catalysis by Gold*; Hutchings, G. J.; Haruta, M., Eds.; Elsevier: New York, 2005; Vol. 291.

(66) Hutchings, G. J.; Haruta, M. *Appl. Catal. A: General* **2005**, *291*, 2-5.

(67) Hill, C. L.; Anderson, T. M.; Han, J.; Hillesheim, D. A.; Geletii, Y. V.; Okun, N. M.; Cao, R.; Botar, B.; Musaev, D. G.; Morokuma, K. *J. Mol. Cat., A: Chem.* **2006**, *251*, 234-238.

(68) Haruta, M. *Gold Bulletin* **2004**, *37*, 27-36.

(69) Bond, G. C.; Thompson, D. T. *Gold Bulletin* **2000**, *33*, 41-51.

(70) Anderson, T. M.; Neiwert, W. A.; Kirk, M. L.; Piccoli, P. M. B.; Schultz, A. J.; Koetzle, T., F.; Musaev, D. G.; Morokuma, K.; Cao, R.; Hill, C. L. *Science* **2004**, *306*, 2074-2077.

(71) Anderson, T. M.; Cao, R.; Slonkina, E.; Hedman, B.; Hodgson, K. O.; Hardcastle, K. I.; Neiwert, W. A.; Wu, S.; Kirk, M. L.; Knottenbelt, S.; Depperman, E. C.; Keita, B.;

Nadjo, L.; Musaev, D. G.; Morokuma, K.; Hill, C. L. *J. Am. Chem. Soc.* **2005**, *127*, 11948-11949.

(72) Cao, R.; Anderson, T. M.; Piccoli, P. M. B.; Schultz, A. J.; Koetzle, T. F.; Geletii, Y. V.; Slonkina, E.; Hedman, B.; Hodgson, K. O.; Hardcastle, K. I.; Fang, X.; Kirk, M. L.; Knottenbelt, S.; Kogerler, P.; Musaev, D. G.; Morokuma, K.; Takahashi, M.; Hill, C. L. *J. Am. Chem. Soc.* **2007**, *129*, 11118-11133.

(73) *Gold: Progress in Chemistry, Biochemistry and Technology*; Schmidbaur, H., Ed.; John Wiley & Sons, Ltd.: Chichester, West Sussex, 1999.

(74) Hosokawa, T.; M.Takano; Murahashi, S. I. *J. Am. Chem. Soc.* **1996**, *118*, 3990-3991.

(75) Zhang, Y.; Puddephatt, R. J.; Manojlovic-Muir, L.; Muir, K. W. *J. Chem. Soc., Chem. Comm.* **1996**, 2599-2600.

(76) Singh, A.; Sharp, P. R. *Dalton Trans.* **2005**, 2080-2081.

(77) Li, J. J.; Li, W.; Sharp, P. R. *Inorg. Chem.* **1996**, *35*, 604-613.

(78) Li, J. J.; Li, W.; James, A. J.; Holbert, T.; Sharp, T. P.; Sharp, P. R. *Inorg. Chem.* **1999**, *38*, 1563-1572.

(79) Sharp, P. R. *J. Chem. Soc., Dalton Trans.* **2000**, 2647-2657.

(80) Cinellu, M. A.; Minghetti, G. *Gold Bulletin* **2002**, *35(1)*, 11-20.

(81) Cinellu, M. A.; Minghetti, G.; Cocco, F.; Stoccoro, S.; Zucca, A.; Manassero, M. *Angew. Chem. Int. Ed.* **2005**, *44*, 6892-6895.

(82) Pope, M. T. *Heteropoly and Isopoly Oxometalates*; Springer-Verlag: Berlin, 1983.

(83) Pope, M. T.; Müller, A. *Angew. Chem., Int. Ed.* **1991**, *30*, 34-48.

(84) *Polyoxometalates: From Platonic Solids to Anti-retroviral Activity*; Pope, M. T.; Müller, A., Eds.; Kluwer Academic Publishers: Dordrecht, Netherlands, 1993.

(85) *Polyoxometalate Chemistry From Topology via Self-Assembly to Applications*; Pope, M. T.; Müller, A., Eds.; Kluwer Academic Publishers: Dordrecht, 2001.

(86) *Polyoxometalate Chemistry for Nano-Composite Design*; Yamase, T.; Pope, M. T., Eds.; Kluwer Academic/Plenum Publishers: New York, 2002; Vol. 2.

(87) Borrás-Almenar, J. J.; Coronado, E.; Müller, A.; Pope, M. T. *Polyoxometalate Molecular Science*; Kluwer Academic Publishers: Dordrecht, 2003; Vol. 98.

(88) Müller, A.; Das, S. K.; Krickemeyer, E.; Kuhlmann, C.; Sadakane, M.; Dickman, M. H.; Pope, M. T. *Inorganic Syntheses* **2004**, *34*, 191-200.

(89) Pope, M. T. In *Comprehensive Coordination Chemistry II: From Biology to Nanotechnology*; Wedd, A. G., Ed.; Elsevier Ltd.: Oxford, UK, 2004; Vol. 4, p 635-678.

(90) Hill, C. L. In *Comprehensive Coordination Chemistry-II: From Biology to Nanotechnology*; Wedd, A. G., Ed.; Elsevier Ltd.: Oxford, UK, 2004; Vol. 4, p 679-759.

(91) Baker, L. C. W.; Figgis, J. S. *J. Am. Chem. Soc.* **1970**, *92*, 3794-3797.

(92) Keggin, J. F. *Nature* **1933**, *131*, 908.

(93) Wells, A. F. *Structural Inorganic Chemistry*; Clarendon Press: Oxford, 1945.

(94) Hill, C. L.; Brown, R. B., Jr. *J. Am. Chem. Soc.* **1986**, *108*, 536-538.

(95) Peacock, R. D.; Weakley, T. J. R. *J. Chem. Soc. A* **1971**, 1937-1940.

(96) Kato, C. N.; Shinohara, A.; Hayashi, K.; Nomiya, K. *Inorg. Chem.* **2006**, *45*, 8108-8119.

(97) Knoth, W. H.; Domaille, P. J.; Farlee, R. D. *Organometallics* **1985**, *4*, 62-68.

(98) Okun, N. M.; Anderson, T. M.; Hill, C. L. *J. Am. Chem. Soc.* **2003**, *125*, 3194-3195.

(99) Okun, N. M.; Anderson, T. M.; Hill, C. L. *J. Mol. Catal. A: Chem.* **2003**, *197*, 283-290.

(100) Fang, X.; Anderson, T. M.; Neiwert, W. A.; Hill, C. L. *Inorg. Chem.* **2003**, *42*, 8600-8602.

(101) Finke, R. G.; Droege, M. W.; Domaille, P. J. *Inorg. Chem.* **1987**, *26*, 3886-3896.

(102) Mizuno, N.; Nozaki, C.; Kiyoto, I.; Misono, M. *J. Am. Chem. Soc.* **1998**, *120*, 9267-9272.

(103) Kamata, K.; Yonehara, K.; Sumida, Y.; Yamaguchi, K.; Hikichi, S.; Mizuno, N. *Science* **2003**, *300*, 964-966.

(104) Mizuno, N.; Yamaguchi, K.; Kamata, K. *Coord. Chem. Rev.* **2005**, *249*, 1944-1956.

(105) Botar, B.; Geletii, Y. V.; Kögerler, P.; Musaev, D. G.; Morokuma, K.; Weinstock, I. A.; Hill, C. L. *J. Am. Chem. Soc.* **2006**, *128*, 11268-11277.

(106) Bartis, J.; Kunina, Y.; Blumenstein, M.; Francesconi, L. C. *Inorg. Chem.* **1996**, *35*, 1497-1501.

(107) Luo, Q.; Howell, R. C.; Bartis, J.; Dankova, M.; DeW. Horrocks, J., William; Rheingold, A. L.; Francesconi, L. C. *J. Inorg. Biochem.* **2002**, *41*, 6112-6117.

(108) Zhang, C.; Bensaid, L.; McGregor, D.; Fang, X.; Howell, R. C.; Burton-Pye, B.; Luo, Q.; Todaro, L.; Francesconi, L. C. *J. Cluster Sci.* **2006**, *17*, 389-425.

(109) Sadakane, M.; Dickman, M. H.; Pope, M. T. *Inorg. Chem.* **2001**, *40*, 2715-2719.

(110) Lyon, D. K.; Miller, W. K.; Novet, T.; Domaille, P. J.; Evitt, E.; Johnson, D. C.; Finke, R. G. *J. Am. Chem. Soc.* **1991**, *113*, 7209-7221.

(111) Mansuy, D.; Bartoli, J.-F.; Battioni, P.; Lyon, D. K.; Finke, R. G. *J. Am. Chem. Soc.* **1991**, *113*, 7222-7226.

(112) Randall, W. J.; Lyon, D. K.; Domaille, P. J.; Finke, R. G. In *Inorganic Syntheses*; Darensbourg, M. Y., Ed.; John Wiley & Sons, Inc.: New York, 1998; Vol. 32, p 242-268.

(113) Finke, R. G.; Droege, M. W. *Inorg. Chem.* **1983**, *22*, 1006-1008.

(114) Weakley, T. J. R.; Finke, R. G. *Inorg. Chem.* **1990**, *29*, 1235-1241.

(115) Gómez-García, C. J.; Borrás-Almenar, J. J.; Coronado, E.; Ouahab, L. *Inorg. Chem.* **1994**, *33*, 4016-4022.

(116) Randall, W. J.; Droege, M. W.; Mizuno, N.; Nomiya, K.; Weakley, T. J. R.; Finke, R. G. In *Inorganic Syntheses*; Cowley, A. H., Ed.; John Wiley & Sons, Inc.: New York, 1997; Vol. 31, p 167-185.

(117) Harmalker, S. P.; Leparulo, M. A.; Pope, M. T. *J. Am. Chem. Soc.* **1983**, *105*, 4286-4292.

(118) Finke, R. G.; Rapko, B.; Saxton, R. J.; Domaille, P. J. *J. Am. Chem. Soc.* **1986**, *108*, 2947-2960.

(119) Edlund, D. J.; Saxton, R. J.; Lyon, D. K.; Finke, R. G. *Organometallics* **1988**, *7*, 1692-1704.

(120) Weiner, H.; Aiken III, J. D.; Finke, R. G. *Inorg. Chem.* **1996**, *35*, 7905-7913.

(121) Nomiya, K.; Pohl, M.; Mizuno, N.; Lyon, D. K.; Finke, R. G. *Inorganic Syntheses* **1997**, *31*, 186-201.

(122) Anderson, T. M.; Zhang, X.; Hardcastle, K. I.; Hill, C. L. *Inorg. Chem.* **2002**, *41*, 2477-2488.

(123) Anderson, T. M.; Hardcastle, K. I.; Okun, N.; Hill, C. L. *Inorg. Chem.* **2001**, *40*, 6418-6425.

(124) Mbomekalle, I. M.; Cao, R.; Hardcastle, K. I.; Hill, C. L.; Ammam, M.; Keita, B.; Nadjo, L.; Anderson, T. M. *C. R. Chimie* **2005**, *8*, 1077-1086.

(125) Judd, D. A.; Chen, Q.; Campana, C. F.; Hill, C. L. *J. Am. Chem. Soc.* **1997**, *119*, 5461-5462.

(126) Contant, R.; Tézé, A. *Inorg. Chem.* **1985**, *24*, 4610-4614.

(127) Müller, A.; Peters, F.; Pope, M. T.; Gatteschi, D. *Chem. Rev.* **1998**, *98*, 239-272.

(128) Godin, B.; Chen, Y. G.; Vaissermann, J.; Ruhlmann, L.; Verdaguer, M.; Gouzerh, P. *Angew. Chem. Int. Ed.* **2005**, *44*, 3072-3075.

(129) Rong, C.; Pope, M. T. *J. Am. Chem. Soc.* **1992**, *114*, 2932-2938.

(130) Visser, S. P. d.; Kumar, D.; Neumann, R.; Shaik, S. *Angew. Chem. Int. Ed.* **2004**, *43*, 5661-5665.

Chapter 2 $[MO(OH_2)(PW_9O_{34})_2]$ (M = Pt or Au)

Terminal Platinum and Gold Oxo Complexes with The One Bridging Structure Type: $[MO(OH_2)(PW_9O_{34})_2]^{16-/17-}$ (M = Pt or Au)

Published in part in *Science* **2004**, *306*, 2074-2077
with Travis M. Anderson, Wade A. Neiwert, Martin L. Kirk, Paula M. B. Piccoli, Arthur J. Schultz, Thomas F. Koetzle, Djamaladdin G. Musaev, Keiji Morokuma, and Craig L. Hill

and in *J. Am. Chem. Soc.* **2007**, *129*, 11118-11133
with Travis M. Anderson, Paula M. B. Piccoli, Arthur J. Schultz, Thomas F. Koetzle, Yurii V. Geletii, Elena Slonkina, Britt Hedman, Keith O. Hodgson, Kenneth I. Hardcastle, Xikui Fang, Martin L. Kirk, Sushilla Knottenbelt, Paul Kögerler, Djamaladdin G. Musaev, Keiji Morokuma, Masashi Takahashi, and Craig L. Hill

2.1 Abstract

In contradiction to current bonding paradigms, two isostructural terminal noble metal-oxo (Pt-oxo and Au-oxo) molecular complexes have been synthesized by reaction of K_2PtCl_4 and $AuCl_3$ with metal-oxide-cluster ligands that model redox-active metal oxide surfaces. Use of solid $Na_9[A\text{-}\alpha\text{-}PW_9O_{34}]\bullet 6H_2O$ produces $K_7Na_9[PtO(OH_2)(PW_9O_{34})_2]\bullet 21.5H_2O$ (**1**); use of $K_{10}[\alpha_2\text{-}P_2W_{17}O_{61}]\bullet 20H_2O$ and K_2WO_4 (forming the $[A\text{-}\alpha\text{-}PW_9O_{34}]^{9-}$ ligand *in situ*) produces $K_{15}H_2[AuO(OH_2)(PW_9O_{34})_2]\bullet 25H_2O$ (**2**). Both complexes **1** and **2** crystallize in orthorhombic *Fddd*, with a = 28.596(8) Å, b = 31.788(8) Å, c = 38.347(11) Å, V = 34857(17) Å^3, Z = 16 (final R = 0.0681) for **1**, and with a = 28.594(4) Å, b = 31.866(4) Å, c = 38.241(5) Å, V = 34844(7) Å^3, Z = 16 (final R = 0.0540) for **2**. Very short Pt-oxo (~1.72 Å) and Au-oxo (~1.76 Å) distances are established by both X-ray and 30 K neutron diffraction studies, and the latter confirms oxo and *trans* aqua (H_2O) ligands on Pt/Au. Variable-temperature magnetic susceptibility data for crystalline **1** and **2** establish that both solids are diamagnetic, and ^{31}P and ^{17}O NMR spectroscopy confirm that both remain diamagnetic in solution. Both complexes have been further characterized by FT-IR, thermogravimetric analysis (TGA), differential scanning calorimetry (DSC), and other techniques.

2.2 Introduction

Inorganic, organometallic and catalytic chemists and chemical engineers have speculated whether terminal metal-oxo (O^{2-}) complexes of the late-transition-metal elements may exist as transient intermediates in systems ranging from Cu oxidase enzymes to the surfaces of noble metal oxidation catalysts.[1-10] Despite decades of speculation and attempted synthesis, no terminal metal-oxo complexes of any element to the right of Ru in the periodic table had been reported prior to 2004 with the exception of the d^4 $(mesityl)_3Ir^V$-oxo complex of G. Wilkinson and co-workers,[11] a complex shown subsequently by S. Brown and co-workers to catalyze oxo transfer to phosphines.[12] Terminal metal-oxo complexes of the work-horse catalytic elements in industry, Pd, Au and in particular Pt, have remained elusive. Given the importance of these elements in O_2-based technologies ranging from catalytic converters (Pt, Pd),[13] fuel cell cathodes (Pt, others),[14-18] and catalysts for low-temperature green O_2-based oxidations (Au, Pt, Pd, Ag, others),[19-36] the inability of the investigators to realize any terminal metal-oxo species of these elements is noteworthy. The considerable recent research on metal-oxo systems in biology, chemistry and materials science has been mirrored by noteworthy developments involving mid- and late-transition-metal complexes with terminal multiply bonded ligands in general.[37-66]

The bonds of Pt, Au and other noble-metal elements to oxygen, while weak, were well established from classical diffraction studies of the metal oxides years ago.[67,68] More recently, well characterized compounds with bridging oxygens bound to both Pt or Au, largely the work of Sharp[69,70] and Cinellu,[71-73] respectively, have been reported. Pt/Au-O bonds, including those in the Au_2O_2 unit, which might be viewed as a dimer of

terminal Au-oxo units, have recently been characterized in several molecules.[72] However, all known Pt/Au-O bonds are long (1.90 to 2.10 Å) consistent with a weaker Pt/Au-O interaction. In contrast to bridging or longer and weaker metal-oxygen units, terminal or multiply bonded metal-oxygen units of these elements necessitate significant population of orbitals that are antibonding in the M-O unit rendering these units unstable.

Polytungstates,[74-80] which share structural and reactivity features in common with the metal oxides of broad importance in catalytic technologies (TiO_2, CeO_2, others), are both good σ-donating and π-accepting ligands that may facilitate stabilization and isolation of terminal late transition metal-oxo complex. With the recent findings at hand, we questioned whether terminal Pt/Au-oxo complexes might exist and be isolable. Such species would be of considerable interest in multiple contexts. For example, considerable recent attention has been focused on O_2-based oxidations catalyzed by metal-oxide-supported Au(0) nanoclusters and films[20,28-30,33-35] because these rival the most active catalysts reported to date for such processes. Cationic Au, and in particular, terminal Au-O(H) is thought to be the key intermediate in CO and other oxidations catalyzed by metal-oxide-supported gold.[81-83] Despite this interest, there are no molecular (soluble) models of the Au-metal oxide interface or complexes with Au center(s) in metal oxide like environments. We report here the synthesis of two isostructural terminal Pt/Au-oxo complexes that exhibit multiple bonding between Pt/Au and oxygen, commensurate with shortest such bond distances to date, stabilized by electron-poor d^0 redox-active metal-oxide-like polytungstate ligands.[84,85] The structural, physicochemical and other properties of these complexes are characterized by more than 10 methods.

2.3 Experimental Section

General Methods and Materials

Polytungstate $Na_9[A\text{-}\alpha\text{-}PW_9O_{34}]\bullet 6H_2O$ (**PW_9**),[86] $K_{10}[\alpha_2\text{-}P_2W_{17}O_{61}]\bullet 20H_2O$ (**P_2W_{17}**),[87] and $K_{14}[P_2W_{19}O_{69}(OH_2)]\bullet 24H_2O$ (**P_2W_{19}**),[88] were synthesized using published procedures. Their purities were confirmed by both IR and ^{31}P NMR. Potassium tungsten oxide (K_2WO_4) and gold chloride ($AuCl_3$) were purchased from Alfa Aesar, and were used without further purification. Potassium tetrachloroplatinate (K_2PtCl_4) was purchased from Aldrich, and was used without further purification. Infrared spectra (2% sample in KBr) were recorded on a Thermo Nicolet 6700 instrument. Ambient temperature electronic absorption spectra were acquired using a diode-array Hewlett-Packard 8452A spectrophotometer. ^{31}P NMR measurements were made on a Varian INOVA 400 MHz spectrometer, and peaks were referenced to 85% H_3PO_4. Room-temperature magnetic susceptibilities were measured on a Johnson-Matthey Model MSB-1 magnetic susceptibility balance as neat powders at 24 °C; the balance was calibrated using $Hg[Co(SCN)_4]$ as a standard. Pascal's constants were used to obtain the final diamagnetic corrections. Temperature-dependent magnetic measurements were performed at 0.1 and 1.0 Tesla using a Quantum Design MPMS-5 SQUID magnetometer and employing approximately 80-90 mg of Au-oxo sample in a cylindrical PTFE-sealed sample holder. Differential scanning calorimetric and thermogravimetric data were collected on Instrument Specialists Incorporated DSC 550 and TGA 1000 instruments, respectively. Electrochemical data were obtained using a BAS CV-50W instrument

(Bioanalytical System, Inc., USA). Elemental analyses of K, Na, P, Pt, Au, and W were performed by Desert Analytics (Tucson, Arizona), Kanti Labs (Mississauga, Canada) and Galbraith Laboratories Inc. (Knoxville, Tennessee).

Synthesis of $K_7Na_9[PtO(OH_2)(PW_9O_{34})_2]\bullet 21.5H_2O$ (1)

A 1.0 g (2.4 mmol) sample of potassium tetrachloroplatinate (K_2PtCl_4) is dissolved in 200 mL of deionized water at room temperature (pH = 4) and 3.6 g (1.42 mmol) of freshly prepared $Na_9[A\text{-}\alpha\text{-}PW_9O_{34}]\bullet 6H_2O$ is added quickly with vigorous stirring of the solution. The mixture is stirred until a nearly clear pink solution is obtained (*ca.* 10 sec) (pH = 7), and then a 20 g sample of KCl is added. The solution is stirred for an additional 2 min, and then it is filtered to obtain a white solid. The solid is dried in air under suction for 5 min and then re-dissolved in a minimal amount of water with heating to 55 °C. The clear, colorless solution gradually turns to a deep yellow color over three days. Shortly after the appearance of the deep yellow color, large brown crystals of **1** (1 g, yield 25%) appear along with a small amount of yellow-pink precipitate. The crystals are manually removed from the solution and washed with 5 °C water to remove any precipitate from the surface. IR (2% KBr pellet, 1300 - 400 cm^{-1}): 1072 (s), 1015 (m, sh), 940 (s), 833 (s), 746 (s), 612 (m), and 513 (w). ^{31}P NMR (9 mM solution in D_2O): -8.8 ($\Delta\nu_{1/2}$ = 8 Hz). Electronic spectral data (400 - 800 nm, in H_2O (6.14 mM sample, 1 cm cell path length)) [λ, nm (ε, M^{-1} cm^{-1})]: 428 nm (210), 502 (73) nm and 574 nm (43). Magnetic susceptibility: μ_{eff} = 0 μ_B/mol at 297 K. Anal. Calcd. for $K_7Na_9[PtO(OH_2)(PW_9O_{34})_2]\bullet 21.5H_2O$: K, 4.92; Na, 3.72; P, 1.11; Pt, 3.51; W, 59.47. Found: K, 4.87; Na, 3.66; P, 1.12; Pt, 3.71; W, 60.71. [MW = 5564 g/mol]

Synthesis of $K_{15}H_2[AuO(OH_2)(PW_9O_{34})_2]\bullet 25H_2O$ (2)

A 1.20 g (0.25 mmol) sample of $K_{10}[\alpha_2\text{-}P_2W_{17}O_{61}]\bullet 20H_2O$ was dissolved with stirring in 5 mL of de-ionized water and the solution was brought to a boil. Potassium tungsten oxide, K_2WO_4, 0.16 g (0.5 mmol) was then added. The solution was stirred and refluxed for ~1 d. A 0.38 g (1.25 mmol) sample of gold chloride ($AuCl_3$) was dissolved in 10 mL of water, and the pH of this solution was increased to 6.8 by dropwise addition of 1 M KOH solution. After careful adjustment of the pH value, the Au(III) solution was added to the tungstate solution. The pH of this mixture was then adjusted, again, to 6.8 by dropwise addition of 1 M KOH solution. The mixture was stirred at 60 °C for about 3 h. The clear, orange solution gradually turned dark red over this period. The solution was filtered after it had cooled, and the dark red filtrate afforded, after repeated filtration, deep red, prismatic crystals of **2** (0.50 g, yield 36%, based on P). The crystals were removed from the solution by filtration and dried under suction for 12 h. Analytical data: IR (2% KBr pellet, 1300 - 400 cm^{-1}): 1073 (s), 1019 (m), 963 (sh), 939 (s), 893 (m), 852 (sh), 831 (s), 750 (s), 619 (s), 508 (m). ^{31}P NMR (8 mM solution in D_2O): -8.7 ppm ($\Delta\nu_{1/2}$ = 8 Hz). Electronic spectral data (400 - 800 nm, in H_2O (1.55 mM sample, 1 cm cell pathlength)) [λ, nm (ε, M^{-1} cm^{-1})]: 402 nm (552) and 428 nm (312). Magnetic susceptibility (0.1 and 1.0 Tesla; 2 - 290 K): diamagnetic. Anal. Calcd. for $K_{15}H_2[AuO(OH_2)(PW_9O_{34})_2]\bullet 25H_2O$: K, 10.2; P, 1.1; Au, 3.4; W, 57.8. Found: K, 9.5; P, 1.0; Au, 3.3; W, 57.0. [MW = 5729 g/mol]

An organic soluble form, the tetra-*n*-butylammonium (TBA) salt, of **2a** (the polyanion of **2**), was made by extraction of **2** in 1 M KCl aqueous solution, with a

dichloromethane solution of 10 equivalents of TBACl followed by removal of the dichloromethane solvent. ^{31}P NMR confirmed that there was no decomposition of the polyanion in this ion exchange process (one peak at -15.1 ppm), and thus this hydrophobic salt was used directly in ^{17}O NMR experiments. In addition, TBABr can not be used in place of TBACl in the metathesis extraction because **2a** is reduced by bromide.

X-ray Crystallographic Studies

The complete datasets for **1** and **2** were collected at Emory University. Single crystals of $K_7Na_9[PtO(OH_2)(PW_9O_{34})_2]\bullet 21.5H_2O$ (**1**) and $K_{15}H_2[AuO(OH_2)(PW_9O_{34})_2]\bullet 25H_2O$ (**2**) suitable for X-ray analysis, were each coated with Paratone-N oil, suspended in a small fiber loop, and placed in a cooled gas stream on a Bruker D8 SMART APEX CCD sealed tube diffractometer. Diffraction intensities were measured using graphite monochromated Mo Kα radiation (λ = 0.71073 Å) at 173(2) K and a combination of φ and ω scans with 10 s frames traversing about ω at 0.3° increments. In addition, a second dataset for compound **2** was collected at 96(2) K. Data collection, indexing, and initial cell refinements were carried out using SMART;[89] frame integration and final cell refinements were done using SAINT.[90] The molecular structure of each complex was determined using Direct Methods and Fourier techniques and refined by full-matrix least squares.[91] A multiple absorption correction for each dataset at 173(2) K was applied using the program SADABS,[92] while face indexed absorption correction was applied for the dataset of **2** at 96(2) K. The largest residual electron density for each structure was located close to (less than 1.0 Å from) the W, Pt, Au, and

K atoms and was most likely due to imperfect absorption corrections frequently encountered in heavy-metal atom structures.

Refinement details. The structure of **1** and **2** were solved using Direct Methods and difference Fourier techniques.[91] The K, Na, P, W, Pt and Au atoms in both **1** and **2** were refined anisotropically. The remaining atoms were refined isotropically. Some of the potassium ions and solvent water molecules were refined with partial occupancies; not all the countercations and solvent water molecules could be located in difference Fourier maps because of disorder. Scattering factors and anomalous dispersion corrections are taken from the *International Tables for X-ray Crystallography*. Structure solution, refinement, graphic and generation of publication materials were performed by using SHELXTL, V6.14 software.

Neutron Diffraction Studies

Neutron data collection. Neutron diffraction data were obtained at the Intense Pulsed Neutron Source (IPNS) at Argonne National Laboratory using the time-of-flight Laue single crystal diffractometer (SCD).[93] At the IPNS, pulses of protons are accelerated into a heavy-element target 30 times a second to produce pulses of neutrons by the spallation process. Because of the pulsed nature of the source, neutron wavelengths are determined by time-of-flight based on the de Broglie equation $l = (h/m)\cdot(t/l)$, where h is Planck's constant, m is the neutron mass, and t is the time-of-flight for a flight path l, so that the entire thermal spectrum of neutrons can be used. With position-sensitive area detectors and a range of neutron wavelengths, a solid volume of reciprocal space is sampled with each stationary orientation of the sample and the

detectors. The SCD was recently upgraded with two new ^{6}Li-glass scintillation position-sensitive area detectors, each with active areas of 15 x 15 cm^2 and a spatial resolution of < 1.5 mm. One of the detectors is centered at a scattering angle of 75˚ and a crystal-to-detector distance of 23 cm, and the second detector is at 120˚ and 18 cm. Details of the data collection and analysis procedures have been published previously.[94-96]

Crystals of $K_7Na_9[PtO(OH_2)(PW_9O_{34})_2]\bullet 21.5H_2O$ (**1**) approximately 6 mm^3 in volume and weighing 25 mg and $K_{15}H_2[AuO(OH_2)(PW_9O_{34})_2]\bullet 25H_2O$ (**2**) approximately 15 mm^3 in volume and weighing 60 mg were covered in fluorocarbon grease. The sample was then molded into an aluminum foil "sandwich" and was glued to the end of a standard aluminum pin with epoxy adhesive. The sample was placed on the DISPLEX® cold stage in the SCD, cooled to 260 K under flowing helium, and once frozen was cooled to 30 K under vacuum.

For each setting of the diffractometer angles, data were stored in three-dimensional histogram form with coordinates *x,y,t* corresponding to horizontal and vertical detector positions and the time-of-flight, respectively. An auto-indexing algorithm[97] was used to obtain an initial orientation matrix from the peaks in three preliminary histograms, each collected over five hours. For intensity data collection, runs of between 12 and 24 hours per histogram were initiated, arranged at χ and ϕ values suitable to cover at least one unique octant of reciprocal space. With this counting time, 24 histograms were completed during the 9 days available for the experiment. The recorded histograms were indexed and integrated using individual orientation matrices for each histogram, to allow for any misalignment of the sample. The unit cell approximately matched the X-ray unit cell indicating that the neutron sample was the correct material. Intensities were

integrated about their predicted locations and were corrected for the Lorentz factor, the incident spectrum, and the detector efficiency. A wavelength-dependent spherical absorption correction was applied using cross sections from Sears[98] for the nonhydrogen atoms and from Howard *et al.*[99] for the hydrogen atoms (μ (cm^{-1}) = 0.540+0.405 λ). Symmetry-related reflections were not averaged since different extinction factors are applicable to reflections measured at different wavelengths.

Refinement. Bragg reflections were integrated about their predicted location and were corrected for the Lorentz factor, the incident spectrum and the detector efficiency. The GSAS software package was used for structural analysis.[100] The atomic positions of the potassium cations and the $[MO(OH_2)(PW_9O_{34})_2]$ core of the molecule from the X-ray diffraction structure were used as a initial model to phase the neutron data. Lattice water molecules were located from difference Fourier syntheses. Each of the oxygen atoms attributable to lattice water was associated with strong negative scattering-density peaks, which are indicative of hydrogen atoms. For these peaks that were assigned as hydrogen atoms, subsequent refinement showed significant fractional occupancy and supported their interpretation as "real" atoms. Atom positions from the original X-ray structure that did not appear to have any weight in the neutron structure were omitted from the model. The axial water ligand O1W, bound to Pt/Au *trans* to the O35 oxo ligand, appeared to be disordered. A large area of negative density was located close to this oxygen on the O35-M-O1W axis; other areas of negative density were located off this axis and also close to O1W, indicative that O1W is indeed a water molecule bound to Pt/Au. The hydrogen atoms bound to O1W were not included in the refinement. No such area of negative scattering density was located about the O35 oxo ligand. The refinement was based on

F^2 reflections with a minimum *d*-spacing of 1.0 Å. Weights were assigned as $w(F_o^2) = 1 / [(\sigma^2(F_o^2)]^2$ where $\sigma^2(F_o^2)$ is the variance based on counting statistics. In the final refinement all atoms, including hydrogen atoms, were refined with isotropic displacement parameters. After final refinement the maximum residual peak height in the difference Fourier map was 0.210 fm $Å^{-3}$, which corresponds to approximately 10% of the peak height observed for atom O35 in the Fourier map.

Electrochemistry

Buffer solutions were prepared in Barnstead Nanopure® quality water by mixing desired amounts of chloroacetic acid (Aldrich, 99%) or sulfuric acid (Aldrich, ACS reagent) and sodium hydroxide (Aldrich, 99%). Cyclic voltammograms (CV) were obtained at room temperature with scan rates in the range 2-100 mV/s. All reduction potentials are given versus Ag/AgCl (3 M NaCl) reference electrode ($E_{NHE} = E_{Ag/AgCl}$ + 0.250 V at 25 °C). A coiled Pt-wire was used as an auxiliary electrode. A glassy carbon working electrode was always polished with alumina (Polishing Alumina Fluid, purchased from Bioanalytical Systems, Inc., USA) before use unless otherwise specified.

Bulk electrolysis was performed under argon on a reticulated vitreous carbon working electrode with a coiled Pt-wire as an auxiliary electrode within a fritted glass isolated chamber. Vigorous agitation was provided by a magnetic stirrer and by the passing of argon as a purging gas. Air was rigorously excluded at all times. The total coulombs passed were monitored continuously. The potential for bulk electrolysis was usually set at values 50-300 mV more negative than the redox potential of Au containing species obtained on a freshly polished electrode. However, in most cases these potentials

are much more positive than those required to reduce tungsten. The overall reduction proceeded to Au(0): gold metal deposition was easily seen after electrolysis as a yellow film on the working electrode. The following procedure was applied to minimize a contribution from the background current in bulk electrolysis. This contribution, while usually small, could reach up to 30%, and was dependent on the experimental conditions. After complete reduction of the Au-complex, the working electrode (with deposited metallic gold on its surface) was rinsed with distilled water and then used in bulk electrolysis. This electrolysis was conducted using the same buffer solution but in the absence of the Au complex. The number of coulombs measured, $\mathbf{C_b}$, was subtracted from the charges passed during electrolysis in the presence of Au complex, **C**. The oxidation state of gold, **n**, in the Au-complex was obtained from the total number of electrons required for a complete reduction of Au(III) to Au(0): $\mathbf{n} = (\mathbf{C}–\mathbf{C_b})/FN$, where F is Faraday's constant (9.65×10^4 C/mole) and N is the number of moles of the initially present Au complex. The Au(0) deposited on the working electrode was dissolved by immersing the electrode into a solution of freshly prepared *aqua regia* for 10-15 min.

X-ray Absorption Spectroscopy Studies

All samples were prepared as finely ground solids in boron nitride, pressed into a pellet, and sealed between 38 μm Kapton tape windows in a 1-mm thick aluminum spacer. The X-ray absorption spectra were measured at the Stanford Synchrotron Radiation Laboratory (SSRL) on the unfocused bend magnet beam line 2-3 for Au(III) samples, and the wiggler beam line 9-3 for Au(I) samples, with the ring operating at 3 GeV, 85-100 mA. A water-cooled (beam line 2-3) and liquid-nitrogen cooled (beam line

9-3) Si(220) monochromator was utilized for energy selection at the Au L_2 edge. At beam line 2-3, the monochromator was detuned 50% at 14340 eV to minimize higher harmonic components in the X-ray beam. At beam line 9-3, a collimating pre-monochromator mirror was used for harmonic rejection with the monochromator fully tuned. The data were measured in transmission mode for gold(III) acetate, gold(I) potassium cyanide, and gold(I) sodium thiosulfate, and in fluorescence mode for gold-containing polyoxometalate samples, using a Canberra 13-element solid-state germanium detector. For transmission measurements, the internal energy calibration were performed by simultaneous measurement of the absorption of a reference Au foil placed between two ionization chambers located after the sample. For fluorescence data, the spectrum of the Au foil was collected between the data scans. The first inflection point of the foil was assigned to 13734.0 eV. The sample was maintained at 12 K using an Oxford Instruments CF1208 continuous-flow liquid helium cryostat. A total of 2-6 scans to a k value of 9.5-12.5 $Å^{-1}$ were collected for each sample. The edge features were monitored for photoreduction; no change was observed in any of the samples. The data were normalized using the program XFIT[101] by first subtracting a polynomial background absorbance that was fit to the pre-edge region and extended over the post-edge with control points, followed by fitting a two-region polynomial spline of orders 2 and 3 over the post-edge region. The data were normalized to an edge jump of 1.0 between the background and spline curves at 13750.0 eV.

^{17}O NMR Studies

General methods and materials. ^{17}O NMR spectra were acquired at 81.291 MHz on a Varian UNITY 600 spectrometer. The spectrometer was locked on the ^{2}H resonance of $CDCl_3$, and all chemical shifts were reported relative to D_2O (δ = 0 ppm). Spectral parameters for ^{17}O NMR were the following: pulse width, 10 μs; sweep width, 100,000 Hz; 0.01 s delay; 100,000 transients; 40,000 data points. Spectra were obtained using cylindrical 5-mm o.d. sample tubes (7 in). All samples were dissolved in 50:50 (v:v) CH_3CN-$CDCl_3$ mixture solvent at room temperature. ^{17}O-enriched water (10% $H_2{}^{17}O$) was purchased from Cambridge Isotope Laboratories, and was used without further purification. Tetra-*n*-butylammonium (TBA) chloride was purchased from Aldrich, and were used without further purification.

^{17}O enrichment of $K_{15}H_2[AuO(OH_2)P_2W_{18}O_{68}]\cdot 25H_2O$ (2). The preparation of an organic soluble salt of **2a**, polyanion of **2**, was described above. An exemplary procedure is as follows: a 0.20 g (0.036 mmol) sample of **2** was suspended in 2 mL of 1 M aqueous KCl solution, and then 20 mL solution of $[CH_3(CH_2)_3]_4NCl$ (TBACl, 0.10 g, 0.36 mmol) in CH_2Cl_2 was added quickly with vigorous stirring at room temperature. Upon standing, the mixture separated into a clear yellow organic layer and a cloudy white aqueous layer. The organic layer was separated and filtered using a 0.45-μm nylon membrane filter, and then was concentrated to dryness at room temperature using a rotary evaporator. The resulting solids were dissolved in 1.0 mL of CH_3CN (the purity was checked by ^{31}P NMR; the spectrum had only one peak at -15.1 ppm in $CH_3CN/CDCl_3$ solvent). A 0.10 mL sample of 10% ^{17}O-enriched water was added to this CH_3CN solution and the mixture was kept for 2 d at 50 °C. The mixture was then concentrated

using a rotary evaporator, and the resulting solids were redissolved in 0.5 mL of $CH_3CN/CDCl_3$.

Computational Methods

The calculations of Pt-complex **1** were performed at the hybrid density functional B3LYP level,[102-104] using the Lanl2dz basis set augmented with the polarization d-function on the P atom.[105-107] This basis sets utilizes the relativistic effective core potential for the W and Pt atoms. Geometries of all structures were optimized using the analytical gradient method within the constrained C_{2v}-symmetry. All calculations were performed by the quantum chemical package Gaussian 03.[108]

In the calculations of Au containing complexes, we used SDD basis sets and ECP for Au[109-111] and the aug-cc-pVTZ basis set for the O[112,113] atoms. B3LYP calculations were done using the GAUSSIAN_2003 quantum chemical package.[108] In the Complete Active-State Self Consistent Field (CASSCF) calculations on the small models an active space that included all valence electrons and orbitals from the Au and O atoms was used: for AuO this is a 17 electron / 10 orbital active space, referred to as (17/10); for AuO^+ this is a (16/10) active space; for AuO^{2+} this is a (15/10) active space, and for AuO^{3+} this is a (14/10) active space. All CASSCF and Multi-Reference Single-Double Correlation Interaction (MRSD-CI) calculations were performed by the MOLPRO quantum chemical package.[114]

2.4 Results and Discussion

Synthesis of Terminal Pt-oxo (1) and Au-oxo (2) complexes

In the reaction of Pt(II) (K_2PtCl_4) with $Na_9[A\text{-}\alpha\text{-}PW_9O_{34}]$, a number of processes are occurring simultaneously. Most first-row transition metals react with $[A\text{-}\alpha\text{-}PW_9O_{34}]^{9-}$ much faster than this polytungstate decomposes. However, the reaction of Pt(II) with $[A\text{-}PW_9O_{34}]^{9-}$ is relatively slow, and as a result, significant decomposition of the polytungstate can and does take place as indicated by ^{31}P NMR. Infrared and NMR spectroscopic data (and elemental analyses of Pt, P, and W) suggest, however, that $[Pt^{II}(PW_9O_{34})_2]^{16-}$ is the predominant product that forms if the reaction of Pt(II) and $[A\text{-}PW_9O_{34}]^{9-}$ is quenched after 1.0 minute of reaction (by KCl precipitation). The final product, **1**, is formed by the oxidation of $[Pt^{II}(PW_9O_{34})_2]^{16-}$. However, no crystals form when air is excluded, so dioxygen is almost certainly the terminal oxidant (also, it is the only reasonable oxidant present). Control experiments show that $\alpha\text{-}[PW_{11}O_{39}]^{7-}$ is the only POM-based product formed from the decomposition of $[A\text{-}PW_9O_{34}]^{9-}$ in an aqueous, pH 7 medium.

Successful preparation of the Pt-oxo complex, $K_7Na_9[PtO(OH_2)(PW_9O_{34})_2]$ using $[A\text{-}\alpha\text{-}PW_9O_{34}]^{9-}$ as an inorganic ligand encouraged us to use a similar strategy to synthesize analogous Au-oxo compound. We rationalized that empty electron-withdrawing delocalized metal-based orbitals in the d^0 $[A\text{-}PW_9O_{34}]^{9-}$ might match in energy the d orbitals on the coordinated metal (Au) reasonably well and thus might stabilize a Au-oxo unit by withdrawal of antibonding as well as bonding electron density in this unit. Direct addition of sodium salt of $[A\text{-}PW_9O_{34}]^{9-}$ to different Au(III) solutions, including potassium tetrachloroaurate ($KAuCl_4$), gold chloride ($AuCl_3$) and gold bromide

($AuBr_3$), followed by kinetic precipitation with KCl always gives the all-tungsten complex, $K_{14}[P_2W_{19}(OH_2)O_{69}]\bullet 24H_2O$ (**P_2W_{19}**), which is the decomposition product of $[A\text{-}PW_9O_{34}]^{9-}$ in aqueous solution.[88] Thus, a stable medium for $[A\text{-}PW_9O_{34}]^{9-}$ appears to be important for successful synthesis of the Au-oxo complex. Instead of using the solid sodium salt of $[A\text{-}PW_9O_{34}]^{9-}$ as a reactant, we generate this hydrolytically unstable ligand *in situ* by reaction of $K_{10}[\alpha_2\text{-}P_2W_{17}O_{61}]\bullet 20H_2O$ with K_2WO_4 at pH 6.8.[88] ^{31}P NMR studies indicate, however, that direct addition of highly acidic $AuCl_3$ solution (pH 1.2) still causes the decomposition of $[A\text{-}PW_9O_{34}]^{9-}$ (at this stage $[P_2W_{20}(OH_2)_2O_{69}]^{10-}$ is present; characteristic chemical shift, -12.35 ppm). As a result, the pH of this $AuCl_3$ solution is increased to 6.8 by dropwise addition of 1 M KOH before addition to the solution of $[A\text{-}PW_9O_{34}]^{9-}$ generated *in situ*, and the pH of this mixture is carefully maintained at 6.8 with KOH. The orange solution gradually turns dark red with stirring at 60 °C, and its cooled filtrate affords dark red crystals of $K_{15}H_2[AuO(OH_2)(PW_9O_{34})_2]\bullet 25H_2O$ (**2**) in 36% yield.

Purity of Complexes, 1 and 2

Several techniques established the purity of the bulk samples (versus the analyzed single crystals) of both **1** and **2**. First, elemental analysis conducted on all major elements confirmed the purity of both compounds. Second, ^{31}P NMR showed only one peak for both **1** (-8.80 ppm) and **2** (-8.70 ppm), a result consistent with the C_{2v} symmetry of these polyanions established by the X-ray crystallography (addressed below; **Figure 2.1**). The ^{31}P NMR chemical shifts for all the other phosphotungstates, including $[P_2W_{19}(OH_2)O_{69}]^{14-}$, $[P_2W_{20}(OH_2)_2O_{69}]^{10-}$ and the reactant $[A\text{-}PW_9O_{34}]^{9-}$ are different.

Third, the ^{17}O NMR spectra show the samples are pure. The additional evidence revealed by these spectra is addressed below. Fourth, the very-low temperature optical spectroscopy, cyclic voltammetry, and FT-IR spectra are also consistent with pure complexes (data elaborated below). Fifth, all the above data are in agreement with the formulations of the two complexes based on the diffraction studies of the isolated single crystals. The only sample impurity in any of the experiments in this study was the very large single crystal analyzed by neutron diffraction. As explained in the neutron diffraction section below, some $[P_2W_{19}O_{69}(OH_2)]^{14-}$ formed during the 3 weeks required for growing the crystal of **2** and this co-crystallized with **2**. Importantly, the W impurity at the Au position was not only detected in this very large crystal but also quantified from the crystallographic refinement. A ^{31}P NMR spectrum when this large single crystal was dissolved confirmed this impurity and the co-crystallization: the same quantity of all tungsten compound, $[P_2W_{19}O_{69}(OH_2)]^{14-}$ (33%) and **2** (67%) indicated by the refinement was present.

X-ray crystal structures of 1 and 2

Given the improbability of terminal noble metal-oxo complexes we established both structural types represented by **1** and **2** using single crystal X-ray diffraction. The polyhedral/ball-and-stick representations for both and thermal ellipsoid plots and numbering scheme for **2** are shown in **Figure 2.1**. Datasets and refinement parameters for the X-ray structures of **1** (173 K) and **2** (173 K and 96 K) are summarized in **Table 2.1**.

Crystallographic studies of crystalline **1** and **2** established that they are isostructural. The very short M-O bonds (1.720(18) Å for Pt-oxo, and 1.763(17) Å for Au-oxo) are trans to the longer M-OH_2 bonds (2.29(4) Å). Two symmetrically equivalent

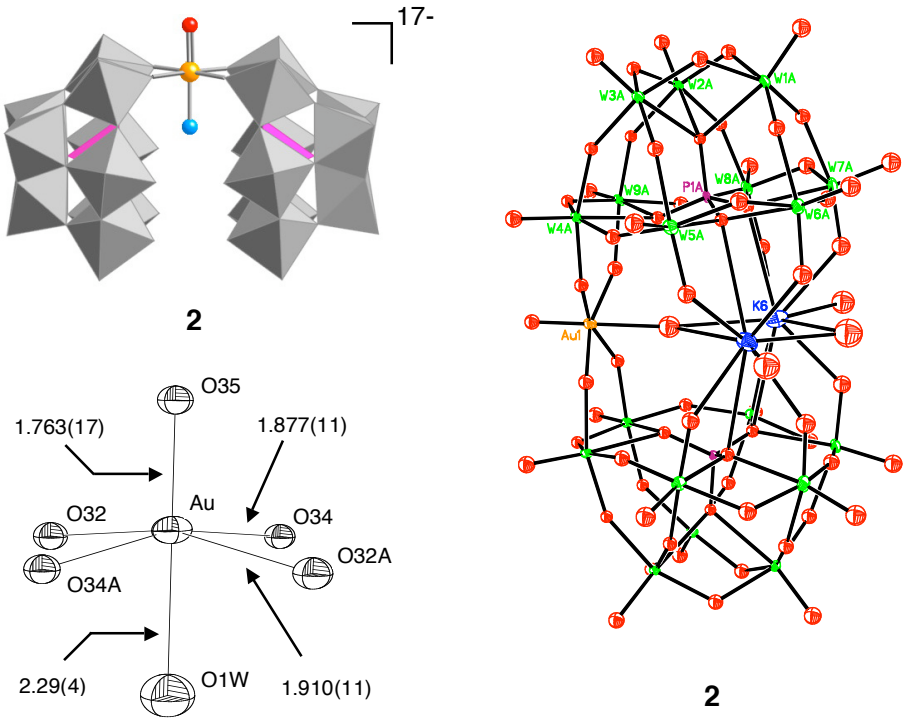

Figure 2.1 Combination polyhedral/ball-and-stick representations of polyanions **1** and **2** (top left) as well as thermal ellipsoid plots and numbering scheme for **2** (right). The WO_6 (or W atom) and PO_4 polyhedra are shown in gray and pink. The Au, O atoms and aqua (H_2O) ligands are shown in yellow, red, and blue, respectively. At the bottom left is X-ray structure around the Au atom in **2**. A short Au-O_{oxo} (1.763(17) Å) bond is *trans* to a longer Au-OH_2 (2.29(4) Å) bond, and the central Au atom is displaced out of the equatorial O_4 plane toward the terminal oxo by 0.31(1) Å.

Table 2.1 Crystal data and refinement parameters for the X-ray structures of $K_7Na_9[PtO(OH_2)(PW_9O_{34})_2]\bullet 21.5H_2O$ (**1**) and $K_{15}H_2[AuO(OH_2)(PW_9O_{34})_2]\bullet 25H_2O$ (**2**) (datasets at both 173(2) K and 96(2) K).

complex	**1**
molecular formula	$H_{45}K_7Na_9O_{91.5}P_2PtW_{18}$
formula wt. (g mol^{-1})	5556.30
temperature (K)	173(2)
radiation (λ, Å)	0.71073
crystal system	orthorhombic
space group	*Fddd* (#70)
a (Å)	28.596(8)
b (Å)	31.788(8)
c (Å)	38.347(11)
Volume ($Å^3$)	34857(17)
Z	16
ρ_{calcd} (g cm^{-3})	4.235
μ (mm^{-1})	25.788
F(000)	39184
crystal size (mm^3)	0.32 × 0.31 × 0.27
reflections collected	61255
independent reflections	10804 [R(int) = 0.0583]
absorption correction	semi-empirical from equivalents
refinement method	full-matrix least-squares on F^2
goodness-of-fit on F^2	1.164
final R indices	$R1^a$ = 0.0681
[R > 2σ (I)]	$wR2^b$ = 0.1656
R indices (all data)	$R1^a$ = 0.0960
	$wR2^b$ = 0.1886
largest diff. peak and hole (e $Å^{-3}$)	13.697 and -4.017

$^aR_1 = \Sigma||F_o| - |F_c|| / |F_o|$

$^bwR_2 = \{\Sigma[w(F_o^2 - F_c^2)^2] / \Sigma[w(F_o^2)^2]\}^{0.5}$

Table 2.1 Continued: Crystal data and refinement parameters for the X-ray structures of $K_7Na_9[PtO(OH_2)(PW_9O_{34})_2]\bullet 21.5H_2O$ (**1**) and $K_{15}H_2[AuO(OH_2)(PW_9O_{34})_2]\bullet 25H_2O$ (**2**) (datasets at both 173(2) K and 96(2) K).

complex	**2** (173(2) K)	**2** (96(2) K)
molecular formula	$H_{54}K_{15}O_{95}P_2AuW_{18}$	$H_{54}K_{15}O_{95}P_2AuW_{18}$
formula wt. (g mol^{-1})	5729.14	5729.14
temperature (K)	173(2)	96(2)
radiation (λ, Å)	0.71073	0.71073
crystal system	orthorhombic	orthorhombic
space group	*Fddd* (#70)	*Fddd* (#70)
a (Å)	28.594(4)	28.605(5)
b (Å)	31.866(4)	31.857(5)
c (Å)	38.241(5)	38.273(6)
Volume ($Å^3$)	34844(7)	34876(10)
Z	16	16
ρ_{calcd} (g cm^{-3})	4.368	4.364
μ (mm^{-1})	26.219	25.902
F(000)	40640	37760
crystal size (mm^3)	0.25 × 0.23 × 0.20	0.45 × 0.44 × 0.28
reflections collected	118464	56787
independent reflections	10902 [R(int) = 0.0823]	10824 [R(int) = 0.1047]
absorption correction	semi-empirical from equivalents	SADABS and face index
refinement method	full-matrix least-squares on F^2	full-matrix least-squares on F^2
goodness-of-fit on F^2	1.048	1.046
final R indices	$R1^a$ = 0.0540	$R1^a$ = 0.0554
[R > 2σ (I)]	$wR2^b$ = 0.2293	$wR2^b$ = 0.1245
R indices (all data)	$R1^a$ = 0.0628	$R1^a$ = 0.0932
	$wR2^b$ = 0.2410	$wR2^b$ = 0.1320
largest diff. peak and hole (e $Å^{-3}$)	5.508 and -8.046	5.644 and -4.069

$^aR_1 = \Sigma||F_o| - |F_c|| / |F_o|$

$^bwR_2 = \{\Sigma[w(F_o^2 - F_c^2)^2] / \Sigma[w(F_o^2)^2]\}^{0.5}$

polytungstate clusters each bind to the central Pt/Au through two oxygens, defining a square equatorial plane in an approximate C_{2v} molecular geometry. The Pt/Au-O_{oxo} bonds are the shortest Pt/Au-O bond in the literature and clearly in the range of terminal multiply bonded transition metal-oxo species.[1,2,6] The distance to the ligand trans to the terminal oxo is 2.29(4) Å strongly suggesting a dative (coordination) Pt/Au-OH_2 bond. Known Pt-OH bond lengths from 50 structures in the Cambridge Structural Database range from 1.943 Å to 2.079 Å and average 1.998 Å. Covalent single Au-O bonds, many of which have been structurally characterized in both gold oxides,[68] and recently reported soluble gold complexes[71,72] with bridging oxo groups are shorter (in the range of 1.90-2.10 Å). Two potassium cations located in the cavity between the two polytungstate units doubtless stabilize the entire sandwich structure by linking the two $[A\text{-}PW_9O_{34}]^{9-}$ frameworks. All X-ray structure determinations are disorder free in the polyanion units, thus we take these values to be definitive. In the structure, the *trans* aqua ligand (oxygen O1W) has large thermal parameters. This results from a slight displacement of this oxygen from the C_2 axis (through the oxo oxygen, Pt/Au and aqua oxygen) by potassium ions and phosphate oxygens O27 that are within van der Waals distance of O1W.

A colorless d^0 analog to compounds **1** and **2** in which tungsten replaces platinum or gold is known: $[WO(OH_2)(PW_9O_{34})_2]^{14-}$.[88] The W≡O bond (1.67 Å) is slightly shorter than the corresponding Pt/Au=O bonds. For a d^2 configuration, the average bond lengths for W(IV)=O, Re(V)=O, and Os(VI)=O are 1.72(6) Å, 1.67(2) Å, and 1.70(3) Å, respectively. For a d^3 configuration, the average bond lengths for W(III)=O and Re(IV)=O are 1.72(3) Å and 1.74(2) Å, respectively. No data for d^3 Os(V)=O were found. The d^6 Re(I) complex reported by Mayer has a Re(I)=O bond distance of 1.756

Å.[4] Given the fact that Pt(IV) and Re(I) are isoelectronic, one would expect the Pt(IV) to have a smaller radius, because it has a higher nuclear proton count and higher effective nuclear charge than Re(I). This would lead to a shorter bond length for Pt(IV)=O than for Re(I)=O. Since both **1** and **2** are isostructural, have similar cations and were crystallized out of unbuffered aqueous solution, and therefore detailed comparison of the two structures is defensible. As expected, the M(Pt or Au)-oxo oxygen distances are quite different (1.720(18) and 1.763(17) Å for Pt and Au, respectively). The increased length by 0.043 Å for the Au-oxo unit is well outside experimental error and is consistent with additional electrons populating d-based orbitals on the Au center. A qualification on this point, however, is that there may be a greater ionic contribution to the Pt(IV)-oxo bond than the effectively isostructural Au(III)-oxo bond.

In both **1** and **2**, the central Pt/Au atom is displaced out of the plane toward the terminal oxo ligand by 0.31(1) Å (it is 0.45 Å displacement of the central W atom in the isostructural all-tungsten complex, $\mathbf{P_2W_{19}}$); this "doming" is a nearly universal feature exhibited by terminal metal-oxo units.[78,79,115] If the pH is lowered from 7 to 2, the reaction conditions used to prepare **1** can lead to formation of the tungsten oxo complex through decomposition of the polytungstate ligands. The X-ray data and elemental analysis showed no evidence for contamination of isolated **1** with this side product.

Neutron Diffraction Studies

Although we felt the distances in the Pt/Au-oxo units in both **1** and **2** were unequivocal based on the disorder-free X-ray structures, we endeavored to use two additional methods to assess this unprecedented structure, Au EXAFS and neutron

diffraction. As expected, interference from the 18 tungsten atoms in **2** made Au EXAFS highly problematical (**Table 2.2**),[116] but neutron diffraction was informative. As an independent structural technique, neutron diffraction can determine not only the absolute structure of molecules but also the location of hydrogens. The latter are effectively never located in even the best X-ray crystallographic structure determinations of polytungstates.

Table 2.2 Electron binding energies for Au and W[116]

	Energy (eV)	
	Au	W
L_1	14353	12100
L_2	13734	11544
L_3	11919	10207

Description of the Fourier maps of 1. Examinations of the Fourier maps around O(35) (**Figure 2.2**A) do not show the significant negative scattering density that is seen around water oxygens in the structure, thus indicating that no hydrogen atom is bound to the oxo ligand. Some negative density, indicated by dashed lines, can be observed in the Fourier maps in the area surrounding O(6w) and may be attributed to the presence of hydrogen atoms, however, given the disorder in this ligand no positive assignments can be made. Small amounts of unassigned negative density are seen in maps throughout the structure, as are small amounts of positive scattering density. Localization of a small amount of this negative density close to Pt(1) and O(35) led us to investigate one such hole. Tentative assignment of this weak Fourier peak (FrPk) as a hydrogen atom gave

distances of 1.25 Å to O(35), 1.91 Å to Pt(1), 1.92 Å to O(29), with a Pt(1)-O(35)-FrPk angle of approximately 76°. A search of the Cambridge Structural Database of metal-O-H angles between 20º and 100° revealed 17 hits for X-ray structures, mostly in the 90-99° range. These hydrogen atoms were located in the difference maps and most were well behaved in subsequent refinements. In the present structure, refinement of fractional occupancy of FrPk as a hydrogen atom gave a very low value for the occupancy (~0.07(9)). Based on the low fractional occupancy and the geometric parameters of this hypothetical Pt-O-H bond FrPk does not appear to represent a "real" atom.

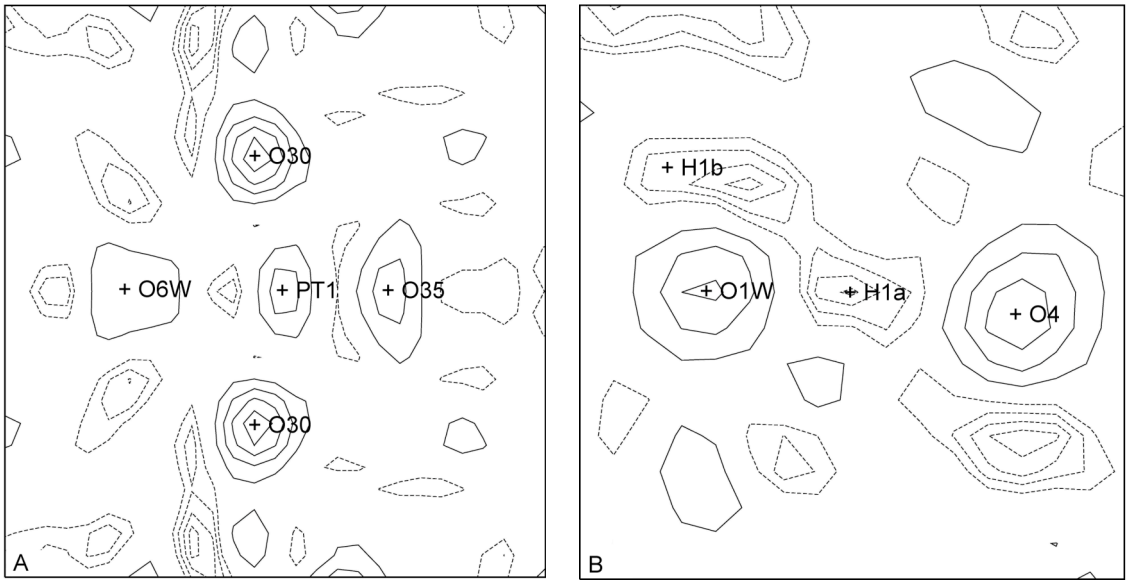

Figure 2.2 F_{obs} Fourier maps derived from single crystal neutron TOF Laue diffraction data taken at 30K on **1**. Data were collected on the Single Crystal Diffractometer at the Intense Pulsed Neutron Source, Argonne National Laboratory. Atom positions in the model are marked with a + and are labeled with their names. In this sample, all non-hydrogen atoms have positive scattering lengths (solid contour lines) and only hydrogen

atoms have negative scattering lengths (dashed lines). (A) Fourier map of the Pt-O35-O6W-O30-O30* plane. Low level negative contours located near O35 were not able to be modeled in a chemically reasonable fashion. This map size is 8 Å on an edge. (B) Fourier map showing the free lattice water O1W-H1a-H1b plane and a nearby O4 (POM) atom. This map is typical of those seen for those water molecules that could be well-modeled. H1a is clearly bound to O1W and appears to be hydrogen-bonded to O4 at a distance of 1.52 Å. An additional unassigned negative scattering region is seen close to O4 and may denote a hydrogen atom associated with neighboring water oxygen atoms. No such feature is seen close to O35 (Pt-oxo) in **Figure 2.2**A. This map size is 5 Å on an edge.

In **Figure 2.2**B, it can be seen that H(1a) and H(1b) are clearly localized and bound to O(1w), and that H(1a) apparently is hydrogen bonded to O(4) at a distance of 1.52 Å. An additional negative scattering region is seen close to O(4) and may denote a hydrogen atom associated with any of a number of neighboring water oxygens; however, a positive assignment was not made here due to the great amount of disorder in this part of the structure. Besides O(1w), there are four water oxygen atoms close to O(4) within a reasonable distance to donate a hydrogen atom and form a hydrogen bond (O(8w), 2.73 Å; O(21w), 2.56 Å; O(10w), 2.85 Å; O(17w), 3.03 Å). This map shows the kind of negative scattering density that would lead to a hydrogen atom assignment, and it is clear that no such feature is seen close to O(35).

Description of the Fourier maps of 2. As shown in **Figure 2.3**A, examinations of the neutron Fourier maps around O35 do not show the significant negative scattering

density that is seen around water oxygen O1W, thus ruling out the possibility that a hydrogen atom is bound to the oxo ligand. In short, the Au-O_{oxo} distance, the doming, and the lack of a hydrogen on the oxo oxygen are three arguments from diffraction studies alone that these complexes are terminal Au-oxo complexes and not Au-hydroxo complexes. Unlike Au-oxo species, Au-hydroxo complexes, while unusual and rare, are nonetheless precedented. The negative density, indicated by dashed contours, observed in the Fourier maps in the area surrounding O1W is attributed to the presence of hydrogen atoms. However, considering the disorder found in this ligand, the hydrogen atoms were not included in the refinement. In **Figure 2.3**B, it can be seen that H4A and H4B are clearly localized and bound to O4W. O4W is in the asymmetric unit, and its nearest neighbors are O15 (also in the asymmetric unit) and O4 (related by the -x+1/2, -y, -z+1/2 symmetry operator). Besides O4W, there are four additional water oxygen atoms with negative density that successfully model as hydrogen atoms. This section of the map shows the kind of negative scattering density that would lead to a hydrogen atom assignment, and it is clear that no such feature is seen close to O35. **Figure 2.3**C presents the Fourier map section from the Au-O35-O1W-O32-O32* plane. The crescent-shaped scattering density at O1W indicates disorder of this aqua ligand about the two-fold axis. This is consistent with the observation in the X-ray structure of **2** that oxygen O1W has large thermal parameters resulting from slight displacement of this oxygen from the C_2 axis by potassium ions and phosphate oxygens O27 that are within van der Waals distance of O1W. The negative scattering density is attributed to hydrogen, but because of the disorder, atom H1A was not included in the refinement.

During initial refinements it was noticed that the isotropic displacement parameter for Au was large in comparison to other heavy atoms in the structure. The all-tungsten compound isostructural to the Au-oxo complex **2**, namely $[P_2W_{19}O_{69}(OH_2)]^{14-}$,

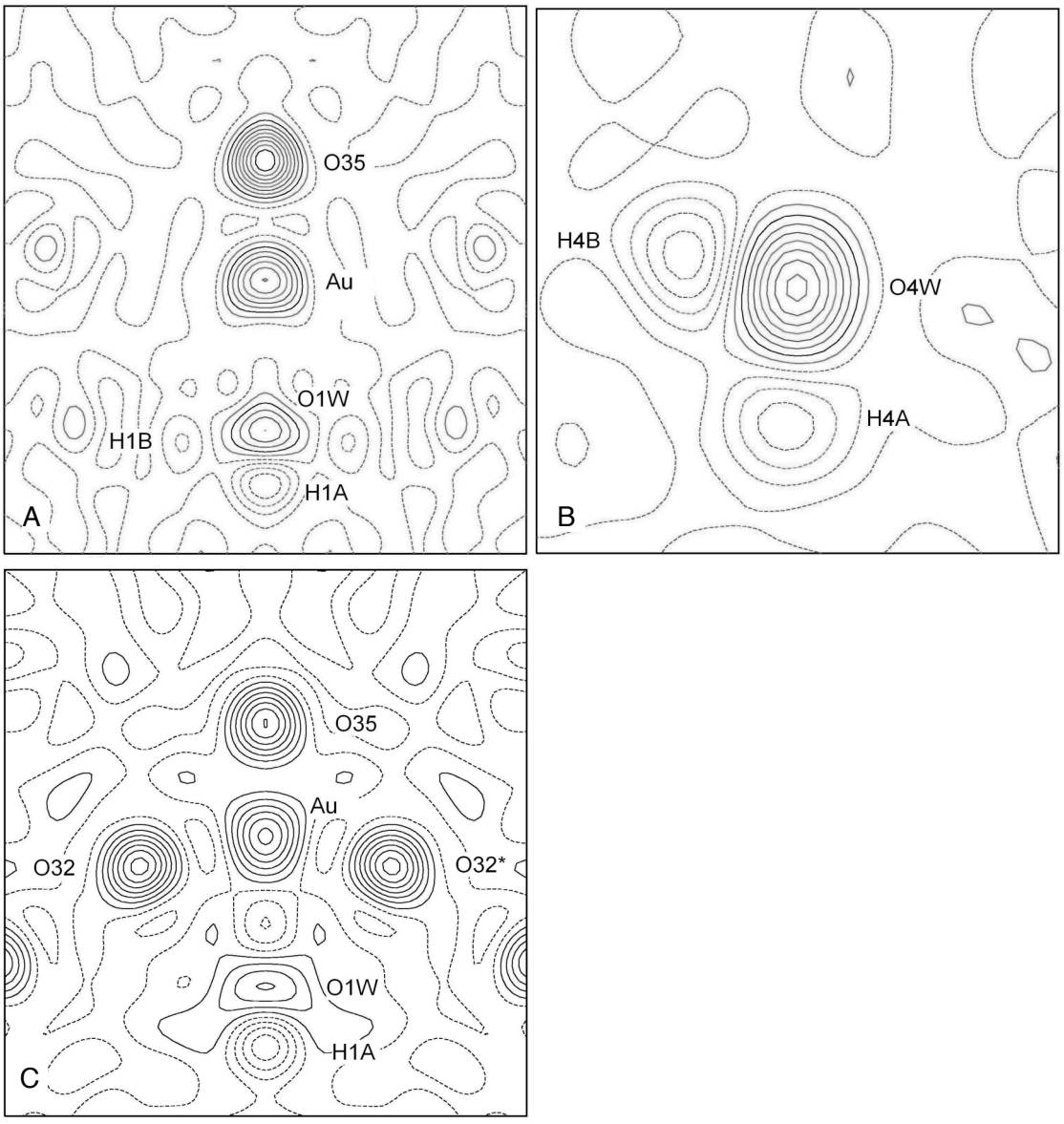

Figure 2.3 F_{obs} Fourier map sections derived from single crystal neutron TOF Laue diffraction data taken at 30 K on **2**. Atom positions are labeled. In these sections, all

non-hydrogen atoms have positive scattering density (solid contour lines), and hydrogen atoms have negative scattering density (dashed lines). (A) Fourier map section (8 Å on an edge) along the Au-O35-O1W two-fold symmetry axis and between the equatorial POM ligands bonded to Au, showing negative scattering density near O1W, indicative of a disordered aqua ligand. Due to the disorder, the protons on O1W were not included in the refinement. Low level negative contours located near O35 could not be refined with any reasonable fractional occupancy. (B) Fourier map section (4 Å on an edge) showing a well-modeled water molecule (O4W-H4A-H4B) in the same asymmetric unit as **Figure 2.3**A. Note that no such feature indicative of a hydrogen atom is seen close to O35 in **Figure 2.3**A. (C) Fourier map section (8 Å on an edge) from the Au-O35-O1W-O32-O32* plane. The crescent-shaped scattering density at O1W indicates disorder of the aqua ligand about the two-fold axis. This situation leads to an unreasonably short Au-O1W distance (1.98(3) Å). The actual distance is longer (2.29(4) Å). The negative scattering density is attributed to hydrogen, but because of the disorder, atom H1A was not included in the refinement.

a hydrolytic decomposition product of **2**, forms during the 3-week process required to grow the giant single crystal required for the neutron diffraction study. Independently we demonstrated using ^{31}P NMR that **2** hydrolyzes to form several tungstates including monomeric tungstate and the polytungstate ligand used in the synthesis initially, [A-$PW_9O_{34}]^{9-}$, and that the latter and tungstate form $[P_2W_{19}O_{69}(OH_2)]^{14-}$ under the crystallization conditions. Once formed, $[P_2W_{19}O_{69}(OH_2)]^{14-}$ co-crystallizes with **2**. This

is not surprising given that these two polyanions are nearly isostructural and have similar charges. Thus in the very large crystal submitted to neutron diffraction studies, some of the molecules have Au at this position and others have W at this position. The fractional occupancy of the Au site was then freely refined to a value of 0.878. Calculations from this value and the scattering lengths of Au and W reveal that the central metal site is populated with 67% Au and 33% W (detailed calculations are at the end of this section).

Despite the co-crystallization, the large crystal was of very high quality and the data analysis confirmed the presence of both the Au-oxo unit (no hydrogen proximal to the oxo oxygen) and the aqua ligand *trans* to the oxo position (both aqua hydrogens, despite positional disorder, were located; **Figure 2.3**). It is worth noting that neutron diffraction is a well-established tool for distinguishing neighboring elements in the periodic table or isotopes of the same element in those cases where the neutron scattering lengths are sufficiently different, including H versus D.[117] In the case of W and Au, with scattering lengths of 4.86 and 7.63 fm, respectively, neutron diffraction data can easily determine the relative occupancies of sites occupied by both elements. Co-crystallization of **2** and $[P_2W_{19}O_{69}(OH_2)]^{14-}$ was confirmed by ^{31}P NMR. Importantly, ^{31}P NMR and other techniques also established that the small crystals of **2** (usually obtained in one day) *submitted for repeated elemental analysis and used in all the other experiments contained no detectable phosphorus impurities including* $[P_2W_{19}O_{69}(OH_2)]^{14-}$.

Table 2.3 Crystal data and structural refinement for the neutron diffraction structures of $K_7Na_9[PtO(OH_2)(PW_9O_{34})_2]\bullet 21.5H_2O$ (**1**) and $K_{15}H_2[AuO(OH_2)(PW_9O_{34})_2]\bullet 25H_2O$ (**2**)

complex	**1**	**2**
formula	$H_{45}K_7Na_9O_{91.5}P_2PtW_{18}$	$H_{54}K_{15}O_{95}P_2AuW_{18}$
formula wt. (g mol^{-1})	5556.30	5728.82
temperature (K)	30(1)	30(1)
crystal system	*orthorhombic*	*orthorhombic*
space group	*Fddd* (#70)	*Fddd* (#70)
a (Å)	28.494(6)	28.72(2)
b (Å)	31.687(9)	31.61(4)
c (Å)	37.988(9)	39.16(1)
V (Å^3)	34298(14)	35555(51)
Z	16	16
d_{calc} (g cm^{-3})	4.187	4.003
size (mm^3)	3 × 2 × 1	4 × 3 × 3
radiation	neutrons	neutrons
data collection technique	time-of-flight Laue	time-of-flight Laue
$\mu(\lambda)$, cm^{-1}	0.464 + 0.314λ	0.540 + 0.405λ
max, min transmission	0.8817, 0.5818	0.8455, 0.4038
extinction parameter	1.2(1) × 10^{-3}	1.2(1) × 10^{-3}
d_{min} (Å)	1.0	1.0
no. of reflections	1864	3435
no. of reflections ($I > 3\sigma(I)$)[a]	1250	2988
no. of parameters refined	195	306
refinement method	Full-matrix least-squares on F^2	Full-matrix least-squares on F^2
R indices $R_w(F^2)$[b], $R(F^2)$[c]	N/A	0.186, 0.192
R indices $R_w(F)$[d], $R(F)$[e]	0.114, 0.122	0.105, 0.132
goodness-of-fit	1.164	2.99

[a]Outliers with $|(F_o^2-F_c^2)| / \sigma F_o^2 > 6$ were rejected

[b]$R_w(F^2) = \{\Sigma[w(F_o^2-F_c^2)^2] / \Sigma[w(F_o^2)^2]\}^{1/2}$

[c]$R(F^2) = \Sigma|F_o^2-F_c^2| / \Sigma|F_o^2|$

[d]$R_w(F) = \{\Sigma[w(|F_o|-|F_c|)^2] / \Sigma[w(|F_o|)^2]\}^{1/2}$

[e]$R(F) = \Sigma||F_o|-|F_c|| / \Sigma|F_o|$

Table 2.4 Bond distances (Å) and angles (°) for the [Pt-O_6] octahedral core as derived from neutron diffraction data

Atoms	Distances or Angles	Atoms	Distances or Angles
Pt1 – O29	1.883(25)	Pt1 – O30*	1.961(28)
Pt1 – O29*	1.883(25)	Pt1 – O35	1.72(6)
Pt1 – O30	1.961(28)	Pt1 – O6W	1.94(9)
O29 – Pt1 – O29*	158.1(29)	O29* – Pt1 – O6W	79.0(14)
O29 – Pt1 – O30	84.9(12)	O30 – Pt1 – O30*	163.6(27)
O29 – Pt1 – O30*	92.0(12)	O30 – Pt1 – O35	98.2(13)
O29 – Pt1 – O35	101.0(14)	O30 – Pt1 – O6W	81.8(13)
O29 – Pt1 – O6W	79.0(14)	O30* – Pt1 – O35	98.2(13)
O29* – Pt1 – O30	92.0(12)	O30* – Pt1 – O6W	81.8(13)
O29* – Pt1 – O30*	84.9(12)	O35 – Pt1 – O6W	180.0
O29* – Pt1 – O35	101.0(14)		

Table 2.5 Bond distances (Å) and angles (°) for the [Au-O_6] octahedral core as derived from neutron diffraction data

Atoms	Distances or Angles	Atoms	Distances or Angles
Au1 – O35	1.771(22)	Au1 – O32*	1.893(12)
Au1 – O1W	1.983(28)	Au1 – O34	1.901(11)
Au1 – O32	1.893(12)	Au1 – O34*	1.901(11)
O32 – Au1 – O32*	163.3(11)	O32* – Au1 – O1W	81.7(6)
O32 – Au1 – O34	89.1(5)	O34 – Au1 – O34*	164.9(11)
O32 – Au1 – O34*	88.7(5)	O34 – Au1 – O35	97.6(6)
O32 – Au1 – O35	98.3(6)	O34 – Au1 – O1W	82.4(6)
O32 – Au1 – O1W	81.7(6)	O34* – Au1 – O35	97.6(6)
O32* – Au1 – O34	88.7(5)	O34* – Au1 – O1W	82.4(6)
O32* – Au1 – O34*	89.1(5)	O35 – Au1 – O1W	180.0
O32* – Au1 – O35	98.3(6)		

Detailed structural refinement information and key bond lengths and angles from neutron diffraction studies on both **1** and **2** are listed in **Table 2.3**, **Table 2.4** (complex **1**) and **Table 2.5** (complex **2**), respectively.

Calculations of the Au:W ratio for the central metal atom site of the neutron diffraction data: (refined Au occupancy)(Au neutron scattering length) = refined fractional occupancy value = x

(0.878)(7.63) = x = 6.701

y(Au scattering length) + (1-y)(W scattering length) = x

y(7.63) + (1-y)(4.86) = 6.701

7.63y + 4.86 – 4.86y = 6.701

2.77y = 1.841

→ y (Au %) = 0.665

1-y (W %) = 0.335

Optical Spectroscopy

The electronic spectrum of **1** has three bands, at 574 nm (band 1), 502 nm (band 2), and 428 nm (band 3), with extinction coefficients of 43, 73, and 210 M^{-1} cm^{-1}, respectively, as well as the intense oxygen-to-tungsten charge transfer bands (absorbance $\lambda < 400$ nm) characteristic of all polytungstates (**Figure 2.4**). Analysis of the electronic absorption spectra of **1** is consistent with tentative assignments for the Pt(IV) ligand field

bands as e → b_1 (bands 1 and 2) and b_2 → b_1 (band 3). Bands 1 and 2 derive from low-symmetry and spin-orbit splitting of the E excited state (A_1 → E transition). Band 3 (A_1 → A_2 transition) is a symmetry forbidden transition in the local C_{4v} symmetry and is likely allowed by a combination of the C_{2v} distortion and mixing of high intensity charge transfer states. Importantly, this assignment results in a d_{xy}-$d_{xz,yz}$ orbital splitting of only ~5000 cm^{-1}, which is highly reduced from the 12,000 to 16,000 cm^{-1} splitting expected for $d^{1,2}$ metal-oxo systems. The reduced splitting can be explained by Pt $d_{xz,yz}$ → W $d_{xz,yz}$ backbonding interactions mediated by the bridging oxo groups. Here, the empty W(VI)

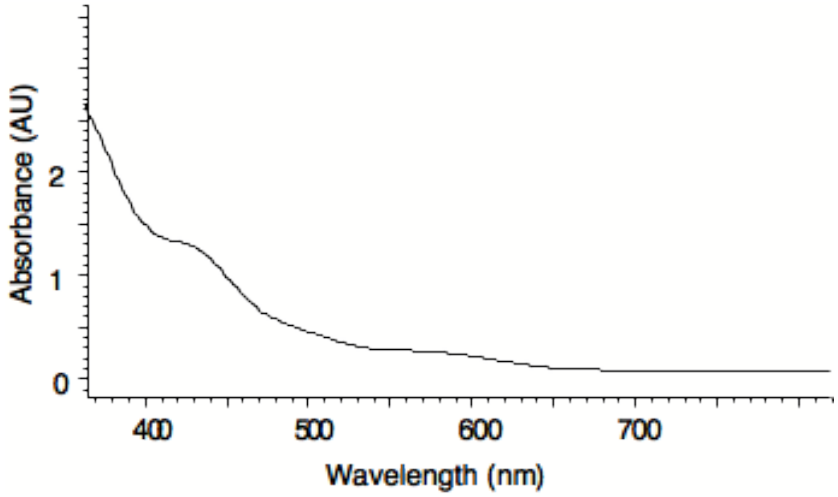

Figure 2.4 Electronic absorption spectrum of **1**. Three absorption bands at 574 nm (band 1), 502 nm (band 2), and 428 nm (band 3) are consistent to the d^6 Pt(IV) oxidation state assignment.

orbitals of e symmetry play a π-acceptor role, lowering the energy of the Pt $d_{xz,yz}$ orbital set and reducing their net antibonding character. This effect has been previously

observed in high-valent iron-oxo systems where the equatorial porphyrin ligand plays a π-acceptor role with respect to the Fe $d_{xz,yz}$ orbitals. As in this previous case, the effect of the backbonding interaction is to strengthen the Pt-O bond by partially delocalizing the Pt(IV) $d_{xz,yz}$ electron density onto the polytungstate portion of the compound. (The detailed discussion of optical spectrum of complex **2** is combined with the other Au-oxo containing polytungstate in Chapter 4.)

Electrochemistry

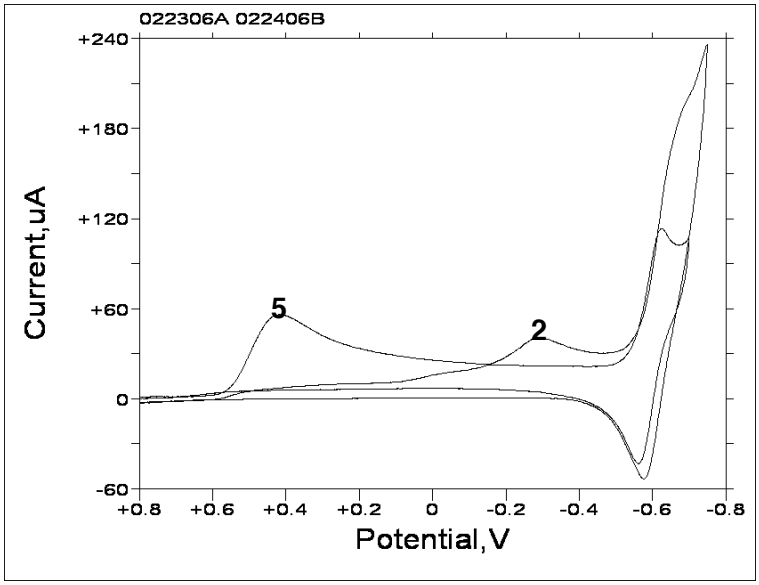

Figure 2.5 Cyclic voltammograms of 2.85 mM **2** and 2.0 mM **5** (the other Au-oxo polytungstate, see Chapter 4) in sodium chloroacetate buffer (0.4 M, pH 3.0) solution. The initial potential was set at +800 mV. Room temperature, scan rate 100 mV/s

The voltammetric behavior of the Au-oxo complex **2** set up the controlled potential coulometry experiments that are of central importance in assigning the Au oxidation state of this unique compound. Since the Au oxidation state is by no means clear from the usual inferences, care was taken to see that all the electrochemical measurements were fully reproducible. A typical cyclic voltammograms (CVs) of 2.85 mM **2** in 0.4 M sodium chloroacetate buffer (pH 3) are shown in **Figure 2.5**. This CV is somewhat similar to that reported for Pd-containing polytungstates. We assign the first reduction wave at *ca.* -290 mV to a reduction of Au(III) to Au(0), which is deposited as a Au(0) film on the working electrode. The second reversible wave at -610 mV ($\Delta E \sim 60$ mV) is a reduction of tungsten (see below). An additional peak is observed at quite high potential (1100 mV; data not shown). The current intensity of this peak dramatically increases with number of CV runs and is attributed to the oxidation of deposited Au(0) on electrode surface followed by reduction of the oxide. The thickness of Au(0) film increases with number of runs, which results in an increase of the current associated with the peak. At the same time the current intensity of peak at -290 mV decreases with number of CV runs. Similar CVs are observed at lower scan rates, 25 and 2 mV/s (data not shown). A CV of the same buffer solution (no **2** present) obtained using the working electrode with deposited Au(0) (after 11 runs with a scan rate 100 mV/s) shows the same peak at 1100 mV. The current intensity of the peak does not increase with number of runs (no more deposition of Au(0) takes place). The reversible peak at -610 mV is assigned to the reduction of tungsten in **2**.

Bulk electrolysis (coulometry at controlled potential) was used to determine the oxidation state of Au in **2**. The number of electrons required for complete reduction of **2**

was determined over a range of applied reduction potential, concentration of **2** and buffer solution (sodium chloroacetate). An increase in the concentration of buffer (0.2 or 0.4 M), a decrease in the concentration of **2** (to 4.2 or 1.0 mM), or application of a more negative potential (350 or 50 mV) results in a formal increase in the number of electrons transferred, **n**, from 3.3 to 4.1 (the latter number may significantly increase with increase of electrolysis time). Under these conditions, the current quickly drops after ~20 min of electrolysis and then reaches a plateau (a "background" current). A contribution of this "background" current to a total charge was estimated from controlled potential electrolysis carried out in a buffer solution without **2** using an electrode with metal gold deposited on its surface (the electrode from a previous electrolysis of **2**). A second controlled potential electrolysis was carried out using working electrode after dissolving metal gold in *aqua regia* solution. Both the control (blank) electrolyses produced similar results, while the charge in a second case was ~20-30% lower. The data were plotted as a dependence of $\mathbf{n} = (\mathbf{C}-\mathbf{C_b})/FN$ *versus* time, where **C** and $\mathbf{C_b}$ are the numbers of coulombs, passed during electrolysis of Au complex and in blank electrolysis using an electrode with metal gold deposited on its surface. Under minimally optimized conditions (applied potential 350 mV, 0.2 M sodium chloroacetate buffer solution, 4.2 mM **2**) the contribution of $\mathbf{C_b}$ to total **C** was less than 15%. A representative curve is given on **Figure 2.6**. After such correction for a "background" current, $\mathbf{n} = 3.15 \pm 0.2$.

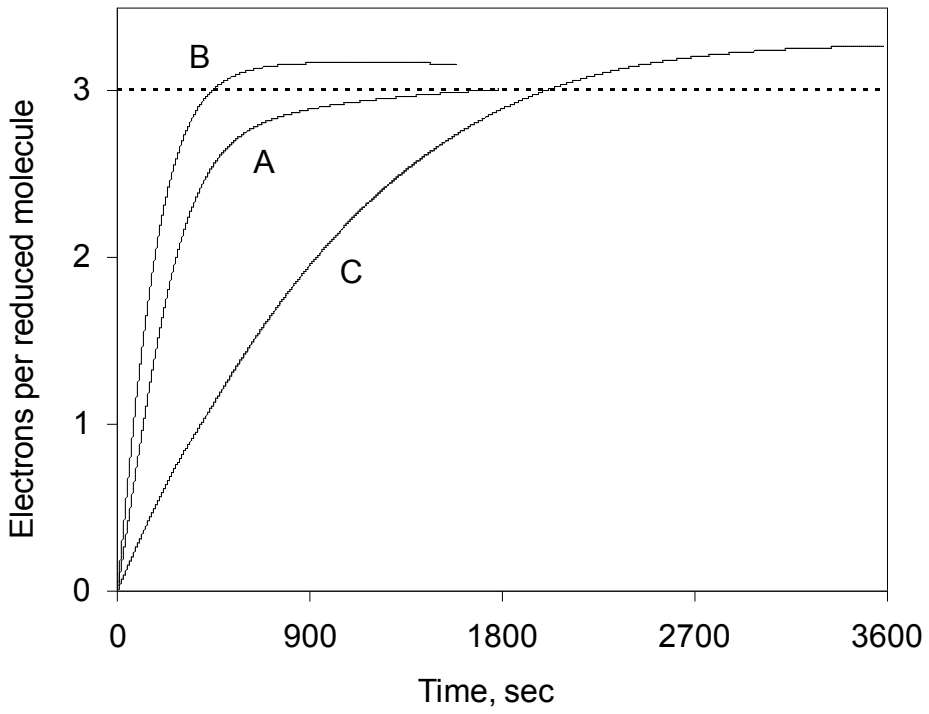

Figure 2.6 Corrected number of electrons, **n** = (**C**-$\mathbf{C_b}$)/FN, passed during bulk electrolysis under controlled potentials as a function of time. (A) 3.37 mM $(NH_4)AuCl_4$, 50 mM sodium sulfate buffer, pH ~2, 0.4 M NaCl, E = 320 mV; (B) 2.0 mM **2**, 50 mM sodium sulfate buffer, pH ~2, 0.4 M NaCl, E = 300 mV; (C) 4.2 mM **5** (see Chapter 4), 0.2 M sodium chloroacetate buffer, pH ~3, E = 350 mV.

Similar data were collected for bulk electrolysis of $AuCl_3$ and $(NH_4)AuCl_4$. Under optimal conditions (with minimal contribution of a "background" current, in chloroacetate buffer) for $AuCl_3$ **n** was 2.7±0.3. While **n** was 3.0±0.2 for $(NH_4)AuCl_4 \bullet 1.3H_2O$ in sulfate buffer in the presence of NaCl (**Figure 2.6**). Here is worth mentioning that $AuCl_3$ is a highly hygroscopic compound resulting in overestimation of molality during weighing. (The molecular weight for $AuCl_3$ was

calculated assuming no water was present in the sample). The amount of coordination water in $(NH_4)AuCl_4 \cdot 1.3H_2O$ was determined experimentally using thermogravimetric analysis (TGA).

X-ray Absorption Spectroscopy Studies

Complex **2** were further studied by X-ray absorption spectroscopy (XAS) to establish the oxidation state of Au. Metal *L*-edge XAS probes the electronic transition from the metal 2*p* orbital into the unoccupied molecular orbitals and continuum states. Spin-orbit coupling splits the 2*p* orbital into the $^2P_{3/2}$ and the $^2P_{1/2}$ states, giving rise to the L_3 and L_2 edges, correspondingly. The L_3 edge possesses the largest edge jump and a smoothly varying background, and thus it is the most widely used *L* edge to probe the local geometric and electronic structure of a metal atom. Unfortunately as noted above, the high content of tungsten in the Au-oxo complex, **2**, despite concerted efforts, precludes the use of the Au L_3 edge for XAS studies of these complexes. Specifically, the Au L_3 edge at 11919 eV occurs just above the W L_2 edge at 11544 eV, and thus the signal from gold would superimpose with a highly oscillating background from the EXAFS of 18 tungsten atoms per one gold atom. We therefore used the Au L_2 edge at 13734 eV to collect the Au XAS data. This edge is situated well above all W *L* edges and the Au L_3 edge (see **Table 2.2** for the list of the energies of *L* edges for W and Au)[116] and is not affected by their EXAFS. The Au L_2-edge features, also, can be expected to be similar to well-established L_3-edge features because L_2 and L_3 absorption edges are dominated, respectively, by the similar $2p_{1/2} \rightarrow 5d_{3/2}$ and $2p_{3/2} \rightarrow 5d_{5/2}$, $5d_{3/2}$ dipole-allowed transitions. That is, at the L_2 edge the $5d_{3/2}$ final-state density contributes to the

transition strength, while at the L_3 edge both $5d_{5/2}$ and $5d_{3/2}$ final-state densities contribute. However, tungsten still absorbs highly at these energies, making the sample non-transparent to X-rays and resulting in a very low signal-to-noise ratio for the Au signal.

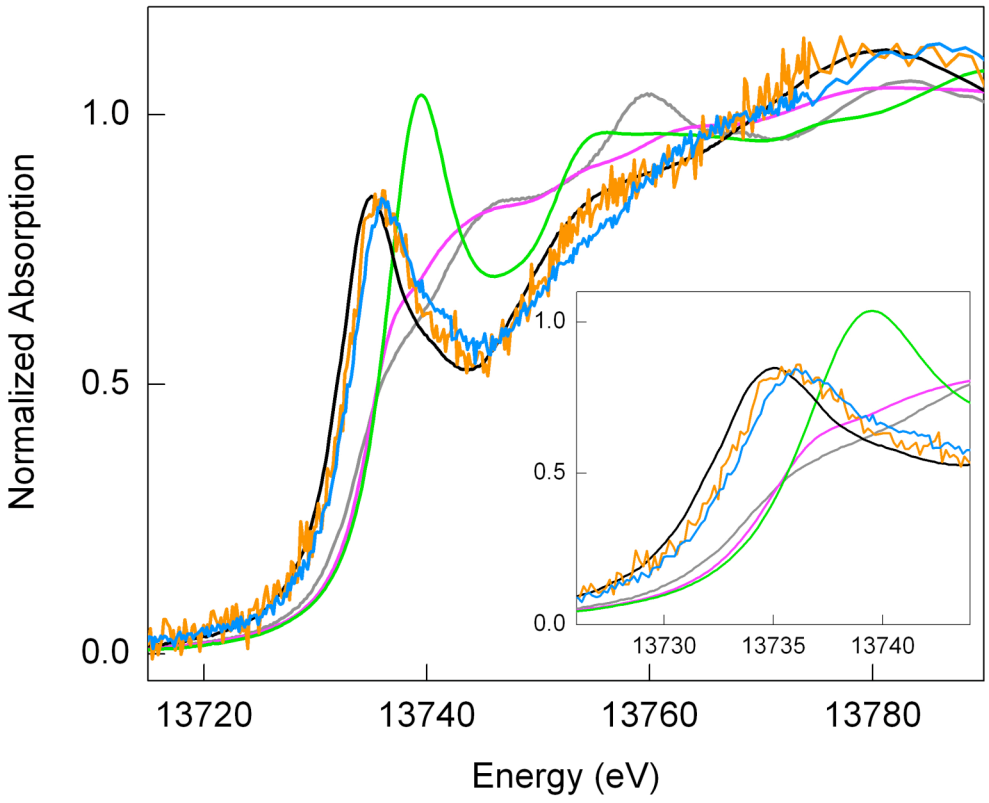

Figure 2.7 Au L_2 near-edge X-ray absorption spectra of $Au^{III}(CH_3COO)_3$ (black), **2** (orange), **5** (blue), $Na_3Au^{I}(S_2O_3)_2$ (magenta), $KAu^{I}(CN)_2$ (green), and Au^0 foil (grey). The edge region is magnified in the inset. Spectra were measured at the Stanford Synchrotron Radiation Laboratory (SSRL) on beam lines 2-3 and 9-3.

The Au L_2-edge XAS spectra of reference compounds $Au^{III}(CH_3COO)_3$, $Na_3Au^{I}(S_2O_3)_2$, $KAu^{I}(CN)_2$, and Au^0 foil are shown in **Figure 2.7**, with the edge region magnified in the inset. The sharp intense peak observed for Au(III) acetate at the absorption threshold, the so-called "white line", can be attributed to the electronic transitions from the $2p_{1/2}$ level to unoccupied molecular orbitals of $5d_{3/2}$ character, by analogy to a similar feature observed at the Au L_3 edge.[118-121] The intensity and the position of the white line should therefore reflect any variations of the density and nature of the unoccupied *d*-states. This effect is observed for Au(I) sodium thiosulfate and Au foil (**Figure 2.7**), for which the white line is nearly absent and it is shifted to higher energy relative to that of Au(III) by 4 eV. Contrary to Au(I) sodium thiosulfate, the spectrum of Au(I) potassium cyanide has an intense white line. This reflects depletion of electron density of the *d*-levels in Au(I) potassium cyanide because of the strong backbonding to the cyanide ligands. The position of the white line in Au(I) potassium cyanide, however, is still indicative of Au(I) as its rising part overlays well with the rising edge of Au(I) sodium thiosulfate. Therefore, the near-edge region at the Au L_2 edge is characteristic of the Au electronic structure and can be used to assign the oxidation state of Au in a sample.

Figure 2.7 also illustrates the Au L_2 near-edge structure for **2**. The position and intensity of the white line are very similar in the spectra of Au(III) acetate and **2** and indicates the same oxidation state for Au in both compounds. The comparison of the spectra of **2** to those of Au(I) compounds provides further evidence of the Au(III) oxidation state in gold-containing polyoxometalates, as the rising part of the edges of **2** is much closer in energy to Au(III) acetate than to any of the Au(I) complexes.

^{17}O NMR studies

In order to obtain ^{17}O NMR spectrum of **2** in nonaqueous solution, organic soluble forms of Au-oxo polytungstate is required. The preparation of the tetrabutylammonium (TBA) salt of **2a** (TBA**2**), its isotopic enrichment with ^{17}O, and ^{31}P NMR confirmation of the purity of the enriched Au-oxo complex are described in the experimental section. The ^{17}O NMR spectra for 2 are shown in **Figure 2.8**. The ^{17}O chemical shifts agree well with the general correlation between downfield chemical shift and oxygen π-bond order, a correlation that has been established from both experimental and theoretical studies.[122-128] In the structure of **2**, there are six types of symmetry-equivalent terminal oxo oxygens each residing in a MO_6 coordination unit of approximate local C_{4v} symmetry: five W-O_{oxo} oxygens with an overall triple bond that appear as five peaks well downfield (690-750 ppm) and an Au-O_{oxo} oxygen appearing at 590 ppm. The chemical shifts for oxygen with single covalent bonds to metal centers in metal oxide ligand environments (metal oxides or polyoxometalates) are usually in the range of 250-450 ppm; those for nearly all bridging oxygens in POMs, including **2**, are in the range of 380 to 450 ppm, and that for water oxygen which has effectively no π bonding is *ca.* 0 ppm. The chemical shift for the terminal Au-oxo oxygen is clearly in the range associated with some π bonding although less than for the d^0 W-O_{oxo} units. Since the variable temperature magnetic and NMR data establish that the Au center in **2** are absolutely diamagnetic (no low-lying paramagnetic states) and the basic electronic structure (the energies and orientations of the bonding orbitals in the metal-oxo unit) are very similar to those in the d^0 W$(O)_5$-O_{oxo} units, it is reasonable that the π bonding arguments and observed chemical shifts for

myriad POMs would apply reasonably well to the terminal oxo oxygen in the $Au(O)_5$-O_{oxo} unit in **2**.

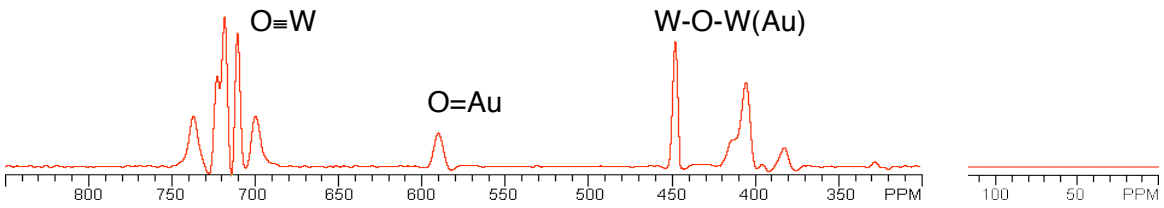

Figure 2.8 ^{17}O NMR spectra of Tetra-*n*-butylammonium (TBA) salt of Au-oxo complex **2** in 50:50 (v:v) CH_3CN:$CDCl_3$.

Computational Studies

Computational studies of model $O=Pt(H_2O)(POM)_2$ systems of varying complexity (from $[PtO]^{2+}$ to $[H_4PtO]^{2-}$ and $[(POM)_2PtO]^{n-}$) indicate that the electronic structure of **1** is strongly affected by the electron accepting capacity of the polytungstates. The application of the various density functional theory and multideterminant-based CASSCF and CASPT2 approaches shows that inclusion of a ligand field (upon going from $[PtO]^{2+}$ to $[H_4PtO]^{2-}$) shifts the d_{x2-y2} orbital to higher energy than the two antibonding d_{xz}(PtO) and d_{yz}(PtO) orbitals. As a result, the diamagnetic state with the $(d_{xy})^2(d_{xz})^2(d_{yz})^2(d_{x2-y2})^0$ orbital configuration becomes the lowest in energy. Inclusion of the POM ligands reduces the antibonding nature of the d_{xz}(PtO) and d_{yz}(PtO) orbitals and also slightly stabilizes them (**Figure 2.9**).

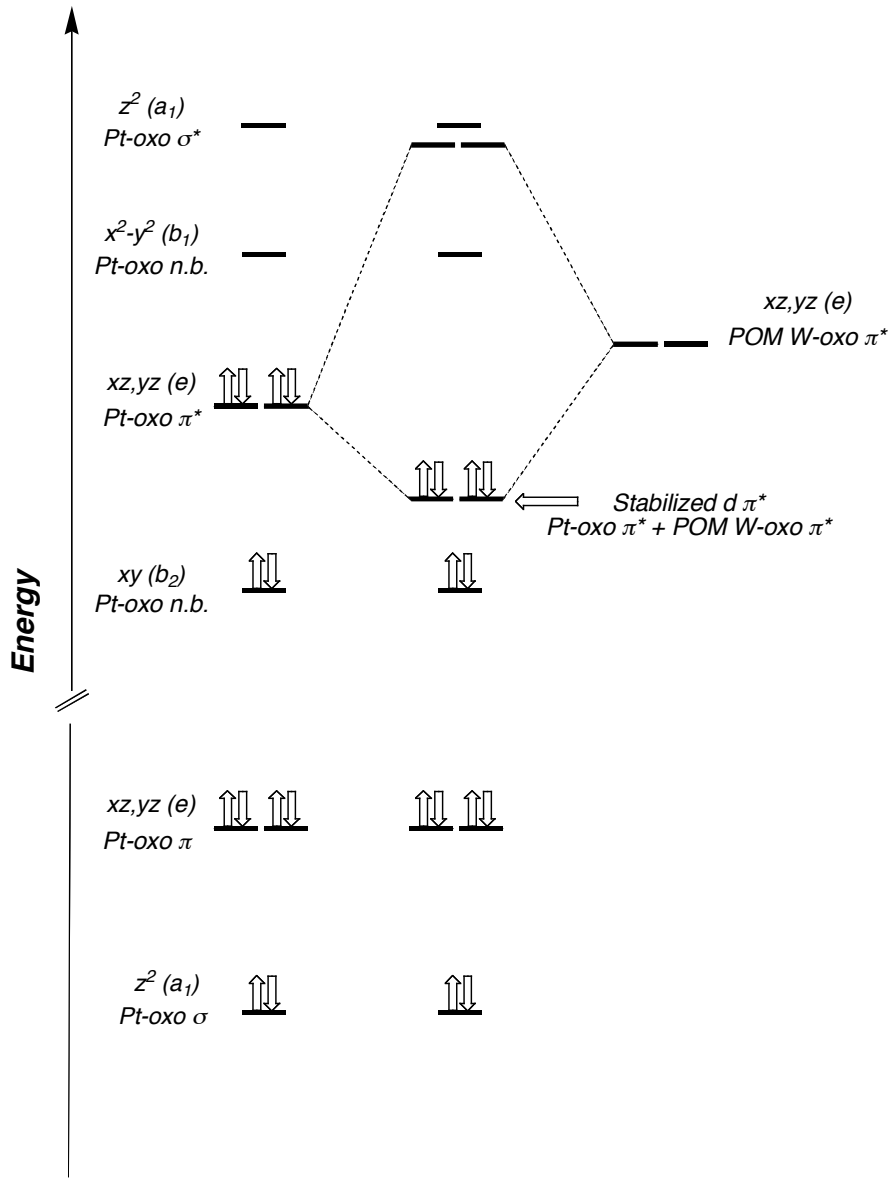

Figure 2.9 Simple molecular orbital diagram for the Pt(IV)-oxo portion of **1** illustrating the stabilization resulting from Pt $d_{xz,yz}$-W $d_{xz,yz}$ interaction and effective donation of electron density from the formal Pt-oxo π* orbitals to delocalized orbitals on the polytungstate ligands. The d orbitals of the metal-oxo unit are shown with their corresponding C_{4v} symmetry labels. Energy ordering for the unperturbed Pt-oxo orbitals (left) are those appropriate for *typical* metal-oxo species and indicate the large

destabilization of the metal $d_{xz,yz}$ *(π*)* and d_{z^2} *(σ*)* orbitals due to antibonding interactions with the terminal oxo. For low d-electron counts (d^{0-2}) the metal-oxo bond order is three, because the d_{xy} orbital is non-bonding with respect to terminal metal-oxo bonding interactions. However, for d^{3-6} electron counts, each additional electron reduces the bond order by 0.5, weakening the metal-oxo bond and potentially activating the oxo ligand.

B3LYP/SDD calculations were also conducted on $O=Au(OH_2)(OH)_4^{n-}$, $O=Au(W_2O_9H_4)_2^{n-}$, and $O=Au(OH_2)(W_2O_9H_4)_2^{n-}$, where n = 1 and 3 (with Au(V) and Au(III) centers, respectively) to model the ligand environment of Au in **2**. However, these calculations were inconclusive because the ligand environment of the Au centers was unstable which indicates that these models are not yet sufficiently close to the actual polytungstate ligands in **2**. From these studies one concludes that use of the full systems, $K_{15}H_2[Au(O)(OH_2)P_2W_{18}O_{68}]$, is necessary to computationally determine the electronic structures and oxidation state of the Au centers. Unfortunately, density functional calculations of such large systems are not technically feasible at present.

We have conducted high level (CASSCF and MRSD-CI) computational studies of the diatomic units, AuO, AuO^+, AuO^{2+}, AuO^{3+}, and of $(NC)AuO^{q+}$ (q = 0, 1 and 2). The findings (electronic structures and oxo dissociation energies) of these studies, summarized below, while certainly of interest, are not highly insightful regarding the properties of **2** because the latter Au-oxo compounds are far more complicated and quite likely distinct electronically in multiple ways from these simple diatomic and tetra-atomic units. Comparisons of these calculated results with the experimental data indicate

that the Au-oxo unit in **2** has multiple bond character similar to $(AuC)^+$ and related species calculated by Pyykkö and co-workers.[129,130]

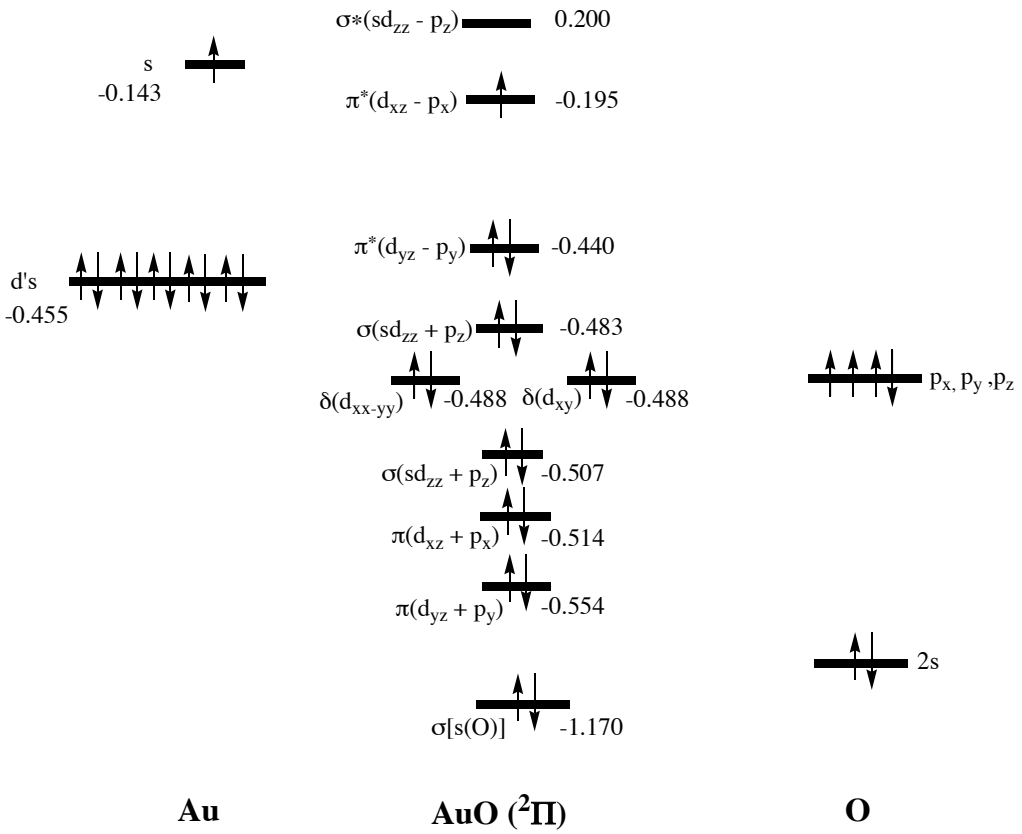

Figure 2.10 Schematic presentation of the MO-correlation diagram for the $^2\prod$ electronic state of the diatomic AuO molecule.

Brief computational analysis of electronic structure and geometry of the AuO, AuO^+, AuO^{2+} and AuO^{3+} systems performed at the DFT (B3LYP), CASSCF (Complete Active-State Self Consistent Field) and MRSD-CI (Multi-Reference Single-Double Correlation Interaction) levels of the theory clearly show that stability of Au-O bond reduces in the order AuO - AuO^+ - AuO^{2+} - AuO^{3+}. This trend is consistent with the

molecular orbital diagram of AuO molecule presented in **Figure 2.10**. As seen from this figure, the ground electronic $^2\prod$ state of AuO with Au(II) has the …$[\pi(d_{yz}+p_y)]^2[\pi(d_{xz}+p_x)]^2[\sigma(sd_{zz}+p_z)]^2[\delta(d_{xy})]^2[\delta(d_{xx-yy})]^2[\sigma(sd_{zz}+p_z)]^2[\pi^*(d_{yz}-p_y)]^2[\pi^*(d_{xz}-p_x)]^1[\sigma^*(sd_{zz}-p_z)]^0$ electronic configuration. The MRSD-CI calculated Au-O bond distance 1.930 Å is in a good agreement with its experimental value of 1.912Å,[131] and previous computational data[132] of AuO. The Au-O bond dissociation energy calculated at the MRSD-CI level is 31.7 kcal/mol, which is also consistent with the previous theoretical studies.

The one electron ionization of AuO corresponds to the removal of an electron from the $\sigma(sd_{zz}+p_z)$ orbital with energy of -0.483 a.u., which is mainly the valence s-orbital of Au atom. This leads to the $Au^{III}O^+$ cation with +1 charge located at the Au-center. Calculations show that $Au^{III}O^+$ has $^3\prod$ ground electronic state with the …$[\sigma(sd_{zz}+p_z)]^2[\pi(d_{yz}+p_y)]^2[\pi(d_{xz}+p_x)]^2[\delta(d_{xy})]^2[\delta(d_{xx-yy})]^2[\pi^*(d_{yz}-p_y)]^2[\sigma(sd_{zz}+p_z)]^1[\pi^*(d_{xz}-p_x)]^1[\sigma^*(sd_{zz}-p_z)]^0$ electronic configuration while its $^3\sum$ state with the …$[\sigma(sd_{zz}+p_z)]^2[\pi^*(d_{yz}-p_y)]^1[\pi^*(d_{xz}-p_x)]^1[\sigma^*(sd_{zz}-p_z)]^0$ is energetically very close. The calculations clearly show that the AuO^+, where Au is in Au(III) oxidation state can exist and is stable relative to the Au^+ + O dissociation limit, while the increase in oxidation state of Au from +2 to +3 slightly reduces the stability of the AuO unit. Indeed, in $Au^{III}O^+$, the Au-O bond distance, 1.981Å, is slightly longer than that for AuO, and the Au^+-O bond energy, 27.8 kcal/mol, is *ca.* 4 kcal/mol smaller than that in $Au^{II}O$.

One should note that the lowest singlet $^1\sum$ state of $Au^{III}O^+$ has multi-determinant character (the largest contributors to the total wavefunction are the …$[\pi^*(d_{yz}-p_y)]^2[\pi^*(d_{xz}-$

$p_x)]^0$ and …$[\pi^*(d_{yz}\text{-}p_y)]^0[\pi^*(d_{xz}\text{-}p_x)]^2$ configurations with 44% weights each) which lie *ca.* 33 kcal/mol higher in energy.

The removal of an electron from the $Au^{III}O^+$ leads to AuO^{2+}, which is stable on potential energy surface at its ground $^4\sum$ electronic state corresponding to the …$[\sigma(sd_{zz}+p_z)]^2[\pi(d_{yz}+p_y)]^2[\pi(d_{xz}+p_x)]^2[\delta(d_{xy})]^2[\delta(d_{xx\text{-}yy})]^2[\sigma^*(sd_{zz}\text{-}p_z)]^1[\pi^*(d_{yz}\text{-}p_y)]^1$ $[\pi^*(d_{xz}\text{-}p_x)]^1$ electron configuration. The Au-O bond distance of AuO^{2+} is calculated to be 2.10 Å. Dissociation of AuO^{2+} to Au^{2+} + O is found to be an endothermic by 58.3 kcal/mol, while the $AuO^{2+} \rightarrow Au^+ + O^+$ is found to be exothermic by 51.7 kcal/mol. Based on these electronic, geometric and energetic data one may conclude that the minimum corresponds to $Au^+(O^+)$. Indeed, all three singly occupied orbitals of the $^4\sum$ ground state of AuO^{2+} are mainly p-AO orbitals of O^+, while all the double occupied σ-, π- and δ-MOs are mainly d-orbitals of Au^+. The $\sigma(sd_{zz}+p_z)$ orbital is the only "real" Au-O bonding orbital. This also is consistent with the calculated (and experimental) ionization potentials of Au^+ and O, which are 19.7 (20.5) and 13.2 (13.614) eV, respectively.

Similarly, we could localize the minima on the potential energy surface of the reaction $Au^{2+} + O^+$ that corresponds to the $^3\sum$ of AuO^{3+}, with the …$[\pi(d_{yz}+p_y)]^2[\pi(d_{xz}+p_x)]^2[\delta(d_{xy})]^2[\delta(d_{xx\text{-}yy})]^2[\sigma(sd_{zz}+p_z)]^2[\pi^*(d_{yz}\text{-}p_y)]^1[\pi^*(d_{xz}\text{-}p_x)]^1$ $[\sigma^*(sd_{zz}\text{-}p_z)]^0$ electron configuration. Although the Au-O bond distance, 1.90Å, is relatively short, the minimum corresponding to AuO^{3+} on the potential energy surface is extremely shallow, and AuO^{3+} dissociates to $Au^{2+} + O^+$ with 264.4 kcal/mol energy. This minimum is 150.4 kcal/mol stable relative to the Au^{3+} + O dissociation limit. Again, these results are consistent with the calculated ionization potentials of Au^{2+} and O, which

are 32.9 eV (758.67 kcal/mol) and 13.2 eV (the experimental value is 13.614 eV) (304.39 kcal/mol), respectively.

Thus, the AuO^{2+} and AuO^{3+} minima on the potential energy surface, with formal Au oxidation states of +4 and +5, are highly unstable with respect to release of reactive O^{+}. However, one can stabilize them under predictable conditions. One of the ways to enhance their stability is by ligation of Au with negatively charged ligands (σ-donating ligands, which will reduce the Coulomb repulsion between the positively charged Au and O centers). The second way is by ligation of Au with strong π-electron withdrawing ligands (which will delocalize the π* electrons in AuO units). Another way is by preventing O^{+} dissociation by $(O^{+})\ldots X$ (non-covalent) interactions in AuO units embedded in the surfaces.

Indeed, calculations of the complexes $(NC)AuO^{q+}$ (q = 0, 1 and 2) support the aforementioned two hypotheses. The (NC)AuO complex where Au is in the +3 oxidation state also has a triplet ground state with Au-O bond distance of 1.956 Å. However, the triplet-singlet energy gap in (NC)AuO, 21.1 kcal/mol, is smaller than 33 kcal/mol in AuO^{+}. In the other words, adding CN^{-} ligand to AuO^{+} reduces both the Au-O bond distance and triplet-singlet energy gap. The calculated trend in the Au-O bond distance correlates with the calculated Au-O bond energy, which increases from 27.8 kcal/mol in AuO^{+} to 31.0 kcal/mol in (NC)AuO.

Similarly, complexes $(NC)Au^{IV}O^{+}$ and $(NC)Au^{V}O^{2+}$ become more stable to both O-atom and O-cation dissociation limits relative to the corresponding AuO^{2+} and AuO^{3+} units. Clearly, having σ-electron donating and π-electron withdrawing ligands tends to stabilize the high oxidation states of Au in AuO fragments.

References

(1) Nugent, W. A.; Mayer, J. M. *Metal-Ligand Multiple Bonds*; John Wiley & Sons, Inc.: New York, 1988.

(2) Holm, R. H. *Chem. Rev.* **1987**, *87*, 1401-1449.

(3) Morris, R. J.; Girolami, G. S. *Polyhedron* **1988**, *7*, 2001-2008.

(4) Spaltenstein, E.; Conry, R. R.; Critchlow, S. C.; Mayer, J. M. *J. Am. Chem. Soc.* **1989**, *111*, 8741-8742.

(5) Holm, R. H.; Donahue, J. P. *Polyhedron* **1993**, *12*, 571-589.

(6) Parkin, G. In *Prog. Inorg. Chem.*; Karlin, K. D., Ed.; Wiley: New York, 1998; Vol. 47, p 1-165.

(7) MacBeth, C. E.; Golombek, A. P.; Jr., V. G. Y.; Yang, C.; Kuczera, K.; Hendrich, M. P.; Borovik, A. S. *Science* **2000**, *289*, 938-941.

(8) Rohde, J.-U.; In, J.-H.; Lim, M. H.; Brennessel, W. W.; Bukowski, M. R.; Stubna, A.; Münck, E.; Nam, W.; Que Jr., L. *Science* **2003**, *299*, 1037-1039.

(9) Green, M. T.; Dawson, J. H.; Gray, H. B. *Science* **2004**, *304*, 1653-1656.

(10) Visser, S. P. d.; Kumar, D.; Neumann, R.; Shaik, S. *Angew. Chem. Int. Ed.* **2004**, *43*, 5661-5665.

(11) Hay-Motherwell, R. S.; Wilkinson, G.; Hussain-Bates, B.; Hursthouse, M. B. *Polyhedron* **1993**, *12*, 2009-2012.

(12) Jacobi, B. G.; Laitar, D. S.; Pu, L.; Wargocki, M. F.; DiPasquale, A. G.; Fortner, K. C.; Schuck, S. M.; Brown, S. N. *Inorg. Chem.* **2002**, *41*, 4815-4823.

(13) Shelef, M. *Chem. Rev.* **1995**, *95*, 209-225.

(14) Appleby, A. J.; Foulkes, F. R. *Fuel cell handbook*; Krieger Publising Company, Malabar, Florida, 1993.

(15) Somorjai, G. A. *Introduction to surface chemistry and catalysis*; Wiley: New York, 1994.

(16) Deluga, G. A.; Salge, J. R.; Schmidt, L. D.; Verykios, X. E. *Science* **2004**, *303*, 993-997.

(17) Kim, W. B.; Voitl, T.; Rodriguez-Rivera, G. J.; Dumesic, J. A. *Science* **2004**, *305*, 1280-1283.

(18) Landon, P.; Ferguson, J.; Solsona, B. E.; Garcia, T.; Carley, A. F.; Herzing, A. A.; Kiely, C. J.; Golunskic, S. E.; Hutchings, G. J. *Chem Comm* **2005**, 3385–3387.

(19) Groves, J. T.; Quinn, R. *J. Am. Chem. Soc.* **1985**, *107*, 5790-5792.

(20) Valden, M.; Lai, X.; Goodman, D. W. *Science* **1998**, *281*, 1647-1650.

(21) Neumann, R.; Dahan, M. *J. Am. Chem. Soc.* **1998**, *120*, 11969-11976.

(22) Brink, G.-J.; Arends, I. W. C. E.; Sheldon, R. A. *Science* **2000**, *287*, 1636-1639.

(23) Weinstock, I. A.; Barbuzzi, E. M. G.; Wemple, M. W.; Cowan, J. J.; Reiner, R. S.; Sonnen, D. M.; Heintz, R. A.; Bond, J. S.; Hill, C. L. *Nature* **2001**, *414*, 191-195.

(24) Boring, E.; Geletii, Y. V.; Hill, C. L. *J. Am. Chem. Soc.* **2001**, *123*, 1625-1635.

(25) Rhule, J. T.; Neiwert, W. A.; Hardcastle, K. I.; Do, B. T.; Hill, C. L. *J. Am. Chem. Soc.* **2001**, *123*, 12101-12102.

(26) Boring, E.; Geletii, Y.; Hill, C. L. In *Catalytic Activation of Dioxygen*; Simandi, L. I., Ed.; Kluwer: Dordrecht, 2001.

(27) Dijksman, A.; Marino-González, A.; Payeras, A. M. i.; Arends, I. W. C. E.; Sheldon, R. A. *J. Am. Chem. Soc.* **2001**, *123*, 6826-6833.

(28) Porta, F.; Rossi, M. *J. Mol. Cat A: Chem.* **2003**, *204-205*, 553-559.

(29) Chen, M. S.; Goodman, D. W. *Science* **2004**, *306*, 252-255.

(30) Sanchez-Castillo, M. A.; Couto, C.; Kim, W. B.; Dumesic, J. A. *Angew. Chem. Int. Ed.* **2004**, *43*, 1140 –1142.

(31) Bar-Nahum, I.; Khenkin, A. M.; Neumann, R. *J. Am. Chem. Soc.* **2004**, *126*, 10236-10237.

(32) Neumann, R. In *Transition Metals for Organic Synthesis (2nd Edition)*; Beller, M., Bolm, C., Eds.; Wiley-VCH: Weinheim, 2004; Vol. 2, p 415-426.

(33) Choudhary, T. V.; Goodman, D. W. *Applied Catalysis A: General* **2005**, *291*, 32-36.

(34) *Catalysis by Gold*; Hutchings, G. J.; Haruta, M., Eds.; Elsevier: New York, 2005; Vol. 291.

(35) Hutchings, G. J.; Haruta, M. *Appl. Catal. A: General* **2005**, *291*, 2-5.

(36) Hill, C. L.; Anderson, T. M.; Han, J.; Hillesheim, D. A.; Geletii, Y. V.; Okun, N. M.; Cao, R.; Botar, B.; Musaev, D. G.; Morokuma, K. *J. Mol. Cat., A: Chem.* **2006**, *251*, 234-238.

(37) Glueck, D. S.; Wu, J.; Hollander, F. J.; Bergman, R. G. *J. Am. Chem. Soc.* **1991**, *113*, 2041-2054.

(38) Andrews, M. A.; Gould, G. L.; Voss, E. J. *Inorg. Chem.* **1996**, *35*, 5740-5742.

(39) Verma, A. K.; Lee, S. C. *J. Am Chem. Soc.* **1999**, *121*, 10838-10839.

(40) Verma, A. K.; Nazif, T. N.; Achim, C.; Lee, S. C. *J. Am Chem. Soc.* **2000**, *122*, 11013-11014.

(41) Mindiola, D. J.; Hillhouse, G. L. *J. Am. Chem. Soc.* **2001**, *123*, 4623-4624.

(42) Melenkivitz, R.; Mindiola, D. J.; Hillhouse, G. L. *J. Am. Chem. Soc.* **2002**, *124*, 3846-3847.

(43) Mindiola, D. J.; Hillhouse, G. L. *J. Am. Chem. Soc.* **2002**, *124*, 9976-9977.

(44) Artero, V.; Proust, A.; Herson, P.; Villain, F.; Moulin, C. C. d.; Gouzerh, P. *J. Amer. Chem. Soc.* **2003**, *125*, 11156-11157.

(45) Thyagarajan, S.; Shay, D. T.; Incarvito, C. D.; Rheingold, A. L.; Theopold, K. H. *J. Am. Chem. Soc.* **2003**, *125*, 4440-4441.

(46) Waterman, R.; Hillhouse, G. L. *J. Am. Chem. Soc.* **2003**, *125*, 13350-13351.

(47) Hu, X.; Meyer, K. *J. Am Chem. Soc.* **2004**, *126*, 16322-16323.

(48) MacBeth, C. E.; Thomas, J. C.; Betley, T. A.; Peters, J. C. *J. Inorg. Chem* **2004**, *43*, 4645-4662.

(49) Seo, M. S.; In, J.-H.; Kim, S. O.; Oh, N. Y.; Hong, J.; Kim, J.; Lawrence Que, J.; Nam, W. *Angew Chem. Int. Ed.* **2004**, *43*, 2417 –2420.

(50) Amisial, L. D.; Dai, X.; Kinney, R. A.; Krishnaswamy, A.; Warren, T. H. *Inorg. Chem.* **2004**, *43*, 6537-6539.

(51) Dai, X.; Warren, T. H. *J. Am Chem. Soc.* **2004**, *126*, 10085-10094.

(52) Kogut, E.; Zeller, A.; Warren, T. H.; Strassner, T. *J. Am. Chem. Soc.* **2004**, *126*, 11984-11994.

(53) Larsen, P. L.; Gupta, R.; Powell, D. R.; Borovik, A. S. *J . Am. Chem. Soc.* **2004**, *126*, 6522-6523.

(54) Klinker, E. J.; Kaizer, J.; Brennessel, W. W.; Woodrum, N. L.; Cramer, C. J.; Lawrence Que, J. *Angew Chem. Int. Ed.* **2005**, *44*, 3690 – 3694.

(55) Rohde, J.-U.; Lawrence Que, J. *Angew Chem. Int. Ed.* **2005**, *44*, 2255 –2258.

(56) Kogut, E.; Wiencko, H. L.; Zhang, L.; Cordeau, D. E.; Warren, T. H. *J. Am Chem. Soc.* **2005**, *127*, 11248-11249.

(57) Abu-Omar, M. M.; Loaiza, A.; Hontzeas, N. *Chem. Rev.* **2005**, *105*, 2227-2252.

(58) Berry, J. F.; Bill, E.; Bothe, E.; George, S. D.; Mienert, B.; Neese, F.; Wieghardt, K. *Science* **2006**, *312*, 1937-1941.

(59) Badiei, Y. M.; Krishnaswamy, A.; Melzer, M. M.; Warren, T. H. *J.Am. Chem. Soc.* **2006**, *128*, 15056-15057.

(60) Dey, A.; Hocking, R. K.; Larsen, P.; Borovik, A. S.; Hodgson, K. O.; Hedman, B.; Solomon, E. I. *J . Am. Chem. Soc.* **2006**, *128*, 9825-9833.

(61) Thomas, C. M.; Mankad, N. P.; Peters, J. C. *J. Am Chem. Soc.* **2006**, *128*, 4956-4957.

(62) Khenkin, A. M.; Kumar, D.; Shaik, S.; Neumann, R. *J. Am Chem. Soc.* **2006**, *128*, 15451-15460.

(63) Klinker, E. J.; Jackson, T. A.; Jensen, M. P.; Stubna, A.; Juhász, G.; Bominaar, E. L.; Münck, E.; Lawrence Que, J. *Angew Chem. Int. Ed.* **2006**, *45*, 7394 –7397.

(64) Cowley, R. E.; Bontchev, R. P.; Sorrell, J.; Sarracino, O.; Feng, Y.; Wang, H.; Smith, J. M. *J. Am Chem. Soc.* **2007**, *129*, 2424-2425.

(65) Oliveira, F. T. d.; Chanda, A.; Banerjee, D.; Shan, X.; Mondal, S.; Jr., L. Q.; Bominaar, E. L.; Münck, E.; Collins, T. J. *Science* **2007**, *315*, 835-838.

(66) Ison, E. A.; Cessarich, J. E.; Travia, N. E.; Fanwick, P. E.; Abu-Omar, M. M. *J. Am. Chem. Soc.* **2007**, *129*, 1167-1178.

(67) Jones, P. G.; Rumpel, H.; Schwarzmann, E.; Sheldrick, G. M.; Paulus, H. *Acta. Cryst.* **1979**, *B35*, 1435-1437.

(68) *Gold: Progress in Chemistry, Biochemistry and Technology*; Schmidbaur, H., Ed.; John Wiley & Sons, Ltd.: Chichester, West Sussex, 1999.

(69) Szuromi, E.; Hui, S.; Sharp, P. R. *J. Am. Chem. Soc.* **2003**, *124*, 10522-10523.

(70) Singh, A.; Sharp, P. R. *Dalton Trans.* **2005**, 2080-2081.

(71) Cinellu, M. A.; Minghetti, G.; Pinna, M. V.; Stoccoro, S.; Zucca, A.; Manassero, M. *Chem. Comm.* **1998**, 2397-2398.

(72) Cinellu, M. A.; Minghetti, G.; Pinna, M. V.; Stoccoro, S.; Zucca, A.; Manassero, M.; Sansoni, M. *J. Chem. Soc., Dalton Trans.* **1998**, 1735-1741.

(73) Cinellu, M. A.; Minghetti, G.; Stoccoro, S.; Zucca, A.; Manassero, M. *Chem. Comm.* **2004**, 1618-1619.

(74) Pope, M. T.; Müller, A. *Angew. Chem., Int. Ed.* **1991**, *30*, 34-48.

(75) *Polyoxometalates: From Platonic Solids to Anti-retroviral Activity*; Pope, M. T.; Müller, A., Eds.; Kluwer Academic Publishers: Dordrecht, Netherlands, 1993.

(76) *Polyoxometalate Chemistry From Topology via Self-Assembly to Applications*; Pope, M. T.; Müller, A., Eds.; Kluwer Academic Publishers: Dordrecht, 2001.

(77) *Polyoxometalate Chemistry for Nano-Composite Design*; Yamase, T.; Pope, M. T., Eds.; Kluwer Academic/Plenum Publishers: New York, 2002; Vol. 2.

(78) Borrás-Almenar, J. J.; Coronado, E.; Müller, A.; Pope, M. T. *Polyoxometalate Molecular Science*; Kluwer Academic Publishers: Dordrecht, 2003; Vol. 98.

(79) Pope, M. T. In *Comprehensive Coordination Chemistry II: From Biology to Nanotechnology*; Wedd, A. G., Ed.; Elsevier Ltd.: Oxford, UK, 2004; Vol. 4, p 635-678.

(80) Hill, C. L. In *Comprehensive Coordination Chemistry-II: From Biology to Nanotechnology*; Wedd, A. G., Ed.; Elsevier Ltd.: Oxford, UK, 2004; Vol. 4, p 679-759.

(81) Bond, G. C.; Thompson, D. T. *Gold Bulletin* **2000**, *33*, 41-51.

(82) Guzman, J.; Gates, B. C. *J. Am. Chem. Soc.* **2004**, *126*, 2672-2673.

(83) Henao, J. D.; Caputo, T.; Yang, J. H.; Kung, M. C.; Kung, H. H. *J. Phys. Chem. B* **2006**, *110*, 8689-8700.

(84) Anderson, T. M.; Neiwert, W. A.; Kirk, M. L.; Piccoli, P. M. B.; Schultz, A. J.; Koetzle, T., F.; Musaev, D. G.; Morokuma, K.; Cao, R.; Hill, C. L. *Science* **2004**, *306*, 2074-2077.

(85) Cao, R.; Anderson, T. M.; Piccoli, P. M. B.; Schultz, A. J.; Koetzle, T. F.; Geletii, Y. V.; Slonkina, E.; Hedman, B.; Hodgson, K. O.; Hardcastle, K. I.; Fang, X.; Kirk, M. L.; Knottenbelt, S.; Kogerler, P.; Musaev, D. G.; Morokuma, K.; Takahashi, M.; Hill, C. L. *J. Am. Chem. Soc.* **2007**, *129*, 11118-11133.

(86) Domaille, P. J. In *Inorganic Syntheses*; Ginsberg, A. P., Ed.; John Wiley and Sons: New York, 1990; Vol. 27, p 96-104.

(87) Contant, R. In *Inorganic Syntheses*; Ginsberg, A. P., Ed.; John Wiley and Sons: New York, 1990; Vol. 27, p 104-111.

(88) Tourné, C. M.; Tourné, G. F. *J. Chem. Soc., Dalton Trans.* **1988**, 2411-2420.

(89) SMART; Bruker AXS, I.; 5.628 ed.; Analytical X-ray Systems: Madison, WI, 2003.

(90) SAINT; Bruker AXS, I.; 6.28 ed.; Analytical X-ray Systems: Madison, WI, 2003.

(91) SHELXTL; 6.14 ed.; Bruker AXS, Inc.: Madison, WI, 2003.

(92) SADABS; Sheldrick, G.; 2.10 ed. 2003.

(93) Schultz, A. J.; Lurgio, P. M. D.; Hammonds, J. P.; Mikkelson, D. J.; Mikkelson, R. L.; Miller, M. E.; Naday, I.; Peterson, P. F.; Porter, R. R.; Worlton, T. G. *Physica B* **2006**, *385-386*, 1059-1061.

(94) Schultz, A. J.; Srinivasan, K.; Teller, R. G.; Williams, J. M.; Lukehart, C. M. *J. Am. Chem. Soc.* **1984**, *106*, 999-1003.

(95) Schultz, A. J. *Trans. Am. Crystallogr. Assoc.* **1987**, *23*, 61-69.

(96) Schultz, A. J.; Derveer, D. G. V.; Parker, D. W.; Baldwin, J. E. *Acta Cryst. C* **1990**, *46*, 276-279.

(97) Jacobson, R. A. *J. Appl. Cryst* **1976**, *19*, 283-286.

(98) Sears, V. F. In *In Methods of Experimental Physics*; Academic Press: Orlando, FL, 1986; Vol. 23, p 521-550.

(99) Howard, J. A. K.; Johnson, O.; Schultz, A. J.; Stringer, A. M. *J. Appl. Cryst.* **1987**, *20*, 120-122.

(100) Larson, A. C.; Dreele, R. B. V. 2000.

(101) Ellis, P. J.; Freeman, H. C. *Journal of Synchrotron Radiation* **1995**, *2*, 190-195.

(102) Becke, A. D. *Phys. Rev. A* **1988**, *38*, 3098-3107.

(103) Becke, A. D. *J.Chem.Phys.* **1993**, *98*, 5648-5652.

(104) Lee, C.; Yang, W.; Parr, R. G. *Phys.Rev. B* **1988**, *37*, 785-789.

(105) Hay, P. J.; Wadt, W. R. *J. Chem. Phys.* **1985**, *82*, 299-310.

(106) Hay, P. J.; Wadt, W. R. *J. Chem. Phys.* **1985**, *82*, 270-283.

(107) Wadt, W. R.; Hay, P. J. *J. Chem. Phys.* **1985**, *82*, 284-298.

(108) Frisch, M. J.; Trucks, G. W.; Schlegel, H. B.; Scuseria, G. E.; Robb, M. A.; Cheeseman, J. R.; Montgomery, J., J. A.; Vreven, T.; Kudin, K. N.; Burant, J. C.; Millam, J. M.; Iyengar, S. S.; Tomasi, J.; Barone, V.; Mennucci, B.; Cossi, M.; Scalmani, G.; Rega, N.; Petersson, G. A.; Nakatsuji, H.; Hada, M.; Ehara, M.; Toyota, K.; Fukuda, R.; Hasegawa, J.; Ishida, M.; Nakajima, T.; Honda, Y.; Kitao, O.; Nakai, H.; Klene, M.; Li, X.; Knox, J. E.; Hratchian, H. P.; Cross, J. B.; Adamo, C.; Jaramillo, J.; Gomperts, R.; Stratmann, R. E.; Yazyev, O.; Austin, A. J.; Cammi, R.; Pomelli, C.; Ochterski, J. W.; Ayala, P. Y.; Morokuma, K.; Voth, G. A.; Salvador, P.; Dannenberg, J. J.; Zakrzewski, V. G.; Dapprich, S.; Daniels, A. D.; Strain, M. C.; Farkas, O.; Malick, D. K.; Rabuck, A. D.; Raghavachari, K.; Foresman, J. B.; Ortiz, J. V.; Cui, Q.; Baboul, A. G.; Clifford, S.; Cioslowski, J.; Stefanov, B. B.; Liu, G.; Liashenko, A.; Piskorz, P.; Komaromi, I.; Martin, R. L.; Fox, D. J.; Keith, T.; Al-Laham, M. A.; Peng, C. Y.; Nanayakkara, A.; Challacombe, M.; Gill, P. M. W.; Johnson, B.; Chen, W.; Wong, M. W.; Gonzalez, C.; Pople, J. A.; 03 Rev. C1 ed.; Gaussian, Inc.: Pittsburgh, 2003.

(109) Haeussermann, U.; Dolg, M.; Stoll, H.; Preuss, H. *Mol. Phys.* **1993**, *78*, 1211-1224.

(110) Dolg, M.; Stoll, H.; Preuss, H.; Pitzer, R. M. *J. Phys. Chem.* **1993**, *97*, 5852-5859.

(111) Dolg, M.; Stoll, H.; Preuss, H. *Theor. Chim. Act.* **1993**, *85*, 441-450.

(112) Kendall, R. A.; Jr., T. H. D.; Harrison, R. J. *J. Chem. Phys.* **1992**, *96*, 6796-6806.

(113) Woon, D. E.; Jr., T. H. D. *J. Chem. Phys.* **1993**, *98*, 1358-1371.

(114) Werner, H. J.; Knowles, P. J. 2003.

(115) Scheidt, W. R. *Systematics of the Stereochemistry of Porphyrins and Metalloporphyrins" Porphyrin Handbook*, 2000; Vol. 3.

(116) Bearden, J. A.; Burr, A. F. *Rev. Mod. Phys.* **1967**, *39*, 125-142.

(117) Kurihara, K.; Tanaka, I.; Chatake, T.; Adams, M. W. W.; Francis E. Jenney, J.; Moiseeva, N.; Bau, R.; Niimura, N. *Proc. Natl. Acad. Sci.* **2004**, *101*, 11215-11220.

(118) Qi, B.; Perez, I.; Ansari, P. H.; Lu, F.; Croft, M. *Phys. Rev. B* **1987**, *36*, 2972-2975.

(119) Benfield, R. E.; Grandjean, D.; Kroll, M.; Pugin, R.; Sawitowski, T.; Schmid, G. *J. Phys. Chem. B* **2001**, *105*, 1961-1970.

(120) Berrodier, I.; Farges, F.; Benedetti, M.; Winterer, M.; Brown, G. E.; Deveughele, M. *Geochimica et Cosmochimica Acta* **2004**, *68*, 3019-3042.

(121) Shaw, C. F.; Schaeffer, N. A.; Elder, R. C.; Eidsness, M. K.; Trooster, J. M.; Calis, G. H. M. *J. Am. Chem. Soc.* **1984**, *106*, 3511-3521.

(122) Filowitz, M.; Klemperer, W. G. *J. Chem. Soc., Chem. Comm.* **1976**, 233-234.

(123) Filowitz, M.; Klemperer, W. G.; Messerle, L.; Shum, W. *J. Am. Chem. Soc.* **1976**, *98*, 2345-2346.

(124) Filowitz, M.; Ho, R. K. C.; Klemperer, W. G.; Shum, W. *Inorg. Chem.* **1979**, *18*, 93-103.

(125) Maksimovskaya, R. I.; Fedotov, M. A. *Zh. Strukt. Khim.* **1981**, *22*, 160-162.

(126) Kintzinger, J. *NMR. Basic Principles & Progress* **1981**, *17*, 1-64.

(127) *^{17}O NMR Spectroscopy in Organic Chemistry*; Boykin, D. W., Ed.; CRC Press, Inc.: Boca Raton, 1991.

(128) Kazansky, L. P.; Chaquin, P.; Fournier, M.; Hervé, G. *Polyhedron* **1998**, *17*, 4353-4364.

(129) Barysz, M.; Pyykkö, P. *Chem. Phys. Lett.* **1998**, *285*, 398-403.

(130) Pyykkö, P.; Riedel, S.; Patzschke, M. *Chem. Eur. J* **2005**, *11*, 3511–3520.

(131) O'Brain, L. C.; Hardimon, S. C.; O'Brain, J. *J. Phys. Chem. A* **2004**, *108*, 11302-11306.

(132) Schwerdtfeger, P.; Dolg, M.; Schwarz, W. H. E.; Bowmaker, G. A.; Boyd, P. D. W. *J. Chem. Phys.* **1989**, *91*, 762-767.

Chapter 3 $[MO(OH)WO(OH_2)(PW_9O_{34})_2]$ (M = Pd)

Terminal Palladium Oxo Complexes Stabilized in an Encapsulating Polytungstate Ligand: $[MO(OH)P_2W_{19}O_{69}(OH_2)]^{13-}$ (M = Pd)

Published in part in *J. Am. Chem. Soc.* **2005**, *127*, 11948-11949

with Travis M. Anderson, Elena Slonkina, Britt Hedman, Keith O. Hodgson, Kenneth I. Hardcastle, Wade A. Neiwert, Shaoxiong Wu, Martin L. Kirk, Sushilla Knottenbelt, Ezra C. Depperman, Bineta Keita, Louis Nadjo, Djamaladdin G. Musaev, Keiji Morokuma, and Craig L. Hill

3.1 Abstract

Use of solid $Na_9[A\text{-}\alpha\text{-}PW_9O_{34}]\bullet 6H_2O$ as a stabilizing inorganic ligand, a terminal Pd-oxo molecular complex, $K_{10}Na_3[PdO(OH)WO(OH_2)(PW_9O_{34})_2]\bullet 16H_2O$ (**3**), has been synthesized by reaction with $Pt(II)SO_4$. Complexes **3** crystallizes in triclinic *P-1* space group, with a = 11.8734(15) Å, b = 17.225(2) Å, c = 22.814(3) Å, α = 90.536(2)°, β = 103.247(2)°, and γ = 108.671(2)°, V = 4285.3(9) Å^3, Z = 2 (final R = 0.0571). Very short Pd-oxo (1.62-1.68 Å) distances are established by both X-ray and extended X-ray absorption fine structure (EXAFS) method. Magnetic susceptibility data for crystalline **3** establish that the solid is diamagnetic, and ^{31}P and ^{17}O NMR spectroscopy confirm that it remains diamagnetic in solution. The complex has been further characterized by FT-IR, thermogravimetric analysis (TGA), differential scanning calorimetry (DSC), and other techniques.

3.2 Introduction

Terminal oxo complexes of the late transition metal elements have been proposed as possible intermediates for oxidations catalyzed by these elements and in technologies where these elements encounter O_2 or other oxidants.[1-19] Despite considerable progress in late-transition-metal-ligand multiple bond chemistry, no high-d-electron count late-transition-metal-oxo complexes were known until the recently reported Pt-oxo complex $K_7Na_9[Pt^{IV}O(OH_2)(PW_9O_{34})_2]$ (**1**),[20] because high-d-electron counts destabilize the metal-

oxo unit.[1-6] Pt-oxo species may well be key intermediates in functioning automobile catalytic converters, fuel cell electrodes and Pt catalysts for O_2-based green organic oxidations.[21-25] A Pd-oxo complex would also be unprecedented and relate to significant Pd-based catalytic chemistry and technology (supported Pd-based catalytic converters and oxidation catalysts).[21-25]

However, attempts to prepare a Pd analogue of **1** in water were unsuccessful because a co-crystalline mixture of an all-tungsten complex $[P_2W_{19}O_{69}(OH_2)]^{14-}$ (**P_2W_{19}**) and $[Pd^{II}(PW_9O_{34})_2]^{16-}$ was obtained.[20] We rationalized that the $PdSO_4$ solution (pH 1.2) is more acidic than K_2PtCl_4 solution (pH 7.0) and the decomposition/isomerization of the polytungstate ligand $[A\text{-}\alpha\text{-}PW_9O_{34}]^{9-}$ to **P_2W_{19}** is faster under this stronger acidity.[26] We now report the first terminal Pd-oxo compound, $K_{10}Na_3[Pd^{IV}O(OH)WO(OH_2)(PW_9O_{34})_2]\bullet 16H_2O$ (**3**). This complex, prepared by an altered route to that for the previously reported Pt-oxo complex, has a structure quite distinct from **1**: an extra $[O=W^{VI}(OH_2)]^{4+}$ unit as the second linkage between the two $[A\text{-}\alpha\text{-}PW_9O_{34}]^{9-}$ ligands significantly increases the stability of the polyanion structure in solution, a medium allowed us to study its chemistry. It is also worthy mentioning here that even bridging Pd-oxo containing complexes are very difficult to obtain and are still very rare with only a few structurally characterized examples, largely contributed by Sharp and co-works.[25,27]

3.3 Experimental Section

General Methods and Materials

Starting material $Na_9[PW_9O_{34}]•7H_2O$ was obtained by the published procedure and its purity was confirmed by infrared spectroscopy and elemental analysis.[28] Elemental analyses of Cl, K, Na, P, Pd, and W were performed by Kanti Labs (Mississauga, Canada) and Desert Analytics (Tucson, Arizona). Infrared spectra (2% sample in KBr) were recorded on a Nicolet 510 instrument. The electronic absorption spectra were taken on a Hewlett-Packard 8452A UV-vis spectrophotometer. The average magnetic susceptibility was measured on a Johnson-Matthey Model MSB-1 magnetic susceptibility balance as neat powders at 24 °C; the balance was calibrated using $Hg[Co(SCN)_4]$ as a standard. Pascal's constants were used to obtain the final diamagnetic corrections. Thermogravimetric data were collected on a TGA 1000 instrument.

Synthesis of $H_{5.6}K_{7.6}Na_{1.4}[Pd_{0.3}\{WO(OH_2)\}_{0.7}(PW_9O_{34})_2]$

A 1.0 g (4.2 mmol) sample of palladium sulfate dihydrate ($PdSO_4•2H_2O$) is dissolved in 150 mL of deionized water at room temperature (pH = 1) and 7.0 g (2.8 mmol) of $Na_9[PW_9O_{34}]•7H_2O$ is added quickly with vigorous stirring of the solution. The mixture is stirred until a nearly clear brown solution is obtained (*ca.* 1 min) and then a 20 g sample of KCl is added to the filtrate and the solution is stirred for an additional 2 min and then filtered to obtain a brown solid. The solid is dried under suction for 10 min and then re-dissolved in a minimal amount of water with heating to 55 °C. After 3 to 7 days, brown-pink crystals (2 g, yield 30%) appear. The crystals are manually removed

from the solution and washed with 5 °C water to remove any precipitate from the surface. IR (2% KBr pellet, 1300 - 400 cm^{-1}): 1070 (s), 1017 (m, sh), 937 (s), 829 (m), 755 (m), 628 (w), and 520 (w). ^{31}P NMR (9 mM solution in D_2O): -8.8 ($\Delta\nu_{1/2}$ = 38 Hz) and -10.2 ppm ($\Delta\nu_{1/2}$ = 10 Hz). Electronic spectral data (400 - 800 nm, in H_2O (1.93 mM sample (in Pd(II)), 1 cm cell path length)) [λ, nm (ε, M^{-1} cm^{-1})]: 438 (246) and 608 (78). Magnetic susceptibility: μ_{eff} = 0 μ_B/mol at 297 K. Anal. Calcd. for $H_{5.6}K_{7.6}Na_{1.4}[Pd^{II}(PW_9O_{34})_2]_{0.3}[WO(H_2O)(PW_9O_{34})_2]_{0.7}$•$20.5H_2O$: K, 5.60; Na, 0.61; P, 1.17; Pd, 0.60; W, 64.80. Found: K, 5.62; Na, 0.65; P, 1.1; Pd, 0.61; W, 63.9. [MW = 5400 g/mol]

Synthesis of $K_{10}Na_3[PdO(OH)WO(OH_2)(PW_9O_{34})_2]$•$16H_2O$ (3)

A 1.0 g (4.2 mmol) sample of palladium sulfate dihydrate ($PdSO_4$•$2H_2O$) is suspended in 50 mL of acetate buffer (0.25 M $NaOOCCH_3$ and 0.25 M $HOOCCH_3$, pH = 4.9) at room temperature and 7.0 g powder (2.8 mmol) of freshly prepared $Na_9[PW_9O_{34}]$•$7H_2O$ is added in *ca.* 1 g portions quickly with vigorous stirring. After 0.5-1 min, 20 g of KCl are added to the nearly clear brown solution (pH = 4.8), and the solution is stirred at 5 °C for 2 additional min. A light brown solid is then separated by filtration, dried under suction for 10 min and re-dissolved in *ca.* 50 mL of water at 55 °C. The solution becomes red-brown in color upon heating. The pH of the solution is lowered from 7.5 to 6.5 by the drop-wise addition of 6 M HCl. After cooling to room temperature, the solution is filtered using a fine filter paper. After an additional 24 to 48 h, small brown plates of **3** appear (5 g, 73% yield based on W). The crystals are filtered and dried in air. Analytical data: IR (2% KBr pellet, 1200 - 400 cm^{-1}): 1089 (m, sh),

1076 (s), 1018 (s), 945 (m), 921 (m), 783 (m), 700 (m), 594 (m), 521 (m), 445 (w), and 413 (w). ^{31}P NMR (5 mM solution in D_2O): -11.7 ppm ($\Delta\nu_{1/2}$ = 7 Hz). Electronic spectral data (400 - 800 nm, in H_2O (3.6 mM sample, 1 cm cell path length)) [λ, nm (ε, M^{-1} cm^{-1})]: 444 nm (272) and 512 nm (sh, 131). Magnetic susceptibility: $\mu_{eff} = 0$ μ_B mol^{-1} at 297 K. Anal. Calcd. for $K_{10}Na_3[PdO(OH)WO(OH_2)(PW_9O_{34})_2]\bullet 16H_2O$: K, 7.03; Na, 1.24; P, 1.11; Pd, 1.91; W, 62.8. Found (Kanti): Cl, <0.01; K, 6.79; Na, 1.25; P, 1.17; Pd, 1.92; W, 63.4. Found (Desert Analytics): Cl, <0.01; K, 7.05; Na, 1.24; P, 1.13; Pd, 1.91; W, 61.8. [MW = 5565 g/mol]

Crystallographic Studies

Single-crystal X-ray crystallographic analysis of $K_{10}Na_3[PdO(OH)WO(OH_2)(PW_9O_{34})_2]\bullet 16H_2O$ **3** and $H_{5.6}K_{7.6}Na_{1.4}[Pd_{0.3}\{WO(H_2O)\}_{0.7}(PW_9O_{34})_2]\bullet 20.5H_2O$ was performed at Emory University at 173 K on a Bruker D8 SMART APEX CCD sealed tube diffractometer with graphite monochromated Mo Kα (0.71073 Å) radiation. Data collection, indexing, and initial cell refinements were carried out using SMART software (version 5.628).[29] Frame integration and final cell refinements were carried out using SAINT (version 6.36A).[30] An absorption correction was applied using SADABS (version 2.10).[31] The structure was determined using direct methods and difference Fourier techniques.[32] The final R1 scattering factors and anomalous dispersion corrections were taken from the International Tables for X-ray Crystallography. Structure solution, refinement, and generation of publication materials were performed using SHELXTL V6.12 software.[32] Ultra-low-temperature data sets of **3** (30 K and 90 K) were collected at Texas A & M University

under the direction of J. Reibenspies and the data was processed as described above. The largest residual electron density for each structure was located close to (less than 1.0 Å) the W, Pd, Na, and K atoms and was most likely due to imperfect absorption corrections often encountered in heavy-metal-atom structures.

The heavy atoms, Na, K, Pd, and W were refined anisotropically. All other atoms were refined isotropically. Some of the atoms were refined with partial occupancies. The central metal site of the complex was modeled as 30% Pd(II) and 70% W(VI), allowing their Uij refinement values to converge independently. Additionally, the atomic coordinates of Pd(1) and W(10) were not constrained, leading to separate positions, where O(35) is a doubly bound oxo on the W and an aqua ligand on the Pd based on their respective bond lengths. The hydrogen atoms were not located. Data collection and refinement parameters are summarized in **Table 3.1**.

Titration Studies

The pH titrations of **3** were performed on 3.6 mM solution (0.2019 g of **3** dissolved in 10 mL of de-ionized water), beginning at pH 6.5 (the natural pH of **3**). The pH was lowered to 2.5 by the dropwise addition of 0.1 M HCl and then increased again to 6.5 by dropwise addition of 0.1 M NaOH. The results show there is a small inflection point at 3.5, which is expected for the protonation of a Pd(IV)-OH unit. In addition, the pH dependent UV-vis experiments and ^{31}P NMR studies of **3** were used to follow this protonation and deprotonation process: both UV-vis and ^{31}P NMR spectra were taken after each change of pH by *ca.* 0.25 unit.

Electronic Absorption Studies

Electronic absorption spectra of **3** were collected on a Hitachi U-3501 UV-Vis-NIR spectrophotometer using a single-beam configuration at 2.0 nm resolution. Ultra-low-temperature spectra were collected at 5 K using a Janis STVP-100 continuous flow cryostat mounted in a custom designed cradle assembly, and the sample temperature was monitored with a Lakeshore silicon-diode (PT-470). The sample was dissolved in a 1:3 water:glycerol mixture in order to obtain a high quality optical glass. The resulting solution was injected through a rubber gasket spacer (approximately 1 mm thick) between two 1 mm thick Infrasil quartz discs in a custom designed sample holder.

^{17}O NMR Studies

^{17}O NMR spectra were recorded at 81.291 MHz on a Varian UNITY 600 spectrometer. The spectrometer was locked on $CDCl_3$, and all chemical shifts are reported relative to D_2O ($\delta = 0$). Spectral parameters for ^{17}O were the following: pulse width, 10 μs; sweep width, 100,000 Hz; 0.01 s delay; 100,000 transients; 40,000 data points. Spectra were obtained using cylindrical 5-mm o.d. sample tubes (7 in). The NMR software package NUTS was used to process the spectra and to correct for "rolling" in the baseline.

The synthesis of an organic soluble form, TBA salt of **3**, as well as its ^{17}O-enriching method are described below: a 0.2 g (0.036 mmol) sample of **3** was dissolved in 2 mL of distilled water at room temperature and the pH value of this solution was lowered to 3.0 by the addition of 0.5 mL of 0.1 M HCl. A solution of 0.151 g $[CH_3(CH_2)_3]_4NBr$ (tetra-*n*-butylammonium bromide, 0.468 mmol) in 20 mL of CH_2Cl_2 was then added quickly

with vigorous stirring for 2 min. Upon standing, the mixture separated into a clean red-brown organic layer and a cloudy white aqueous layer. The organic layer was separated and filtered using a fine filter paper, and then was evaporated to near dryness (on a rotavap) at room temperature. The resulting red-brown solid was dissolved in 5 mL of CH_3CN. The addition of 50 mL of anhydrous diethyl ether to this solution caused an immediate precipitate that was then collected with a fine glass-sintered filter. Re-dissolution of the red-brown solid in CH_3CN followed by re-precipitation with Et_2O five times afforded a pure sample of the tetra-*n*-butylammonium salt of **3**. The purity was checked by ^{31}P NMR; one peak is present at -13.3 ppm in $CH_3CN/CDCl_3$ solvent. ^{17}O-enriched water (0.1 mL) was added to this CH_3CN solution, and the solution was allowed to react for 2 days at 50 ^oC. The solution was again evaporated to near dryness (on a rotavap), and the resulting red-brown solid was dissolved in 0.5 mL of $CH_3CN/CDCl_3$.

For comparison, the sample of its isostructural all-tungsten polytungstate, $K_{10}[P_2W_{20}O_{70}(OH_2)_2]\bullet 22H_2O$ (**P_2W_{20}**) was prepared by the literature procedure[33] (partial translation of *Can. J. Chem.* **1987**, *65*, 568-573: *a mixture of 100 mL of 1 M potassium tungstate and 10 mL of 1 M phosphoric acid was acidified slowly with 51 mL of 3 M HCl. The white precipitate that appeared immediately was redissolved by bringing the solution to a boil. Then, the solution was left at room temperature and the white crystals that began to appear after one day were filtered off and recrystallized in a minimum of water.*), and the organic soluble form of **P_2W_{20}** is obtained by the following procedure: a 0.2 g (0.035 mmol) sample of **P_2W_{20}** was dissolved in 0.1 mL of 10% ^{17}O-enriched water at 50 ^oC and aged for 2 days. This solution was then mixed with 2 mL of water as well as a solution of 0.113 g $[CH_3(CH_2)_3]_4NBr$ (tetra-*n*-butylammonium bromide, 0.352 mmol)

in 20 mL CH_2Cl_2 with vigorous stirring for 2 min. Upon standing, the mixture separated into a clean colorless organic layer and a cloudy white aqueous layer. The organic layer was separated and filtered using a fine filter paper and then was evaporated to near dryness (on a rotavap) at room temperature. The resulting white solid was dissolved in 5 mL of CH_3CN. The addition of 50 mL of anhydrous diethyl ether to this solution produced an immediate precipitate that was collected with a fine glass-sintered filter. Re-dissolution of the red-brown solid in CH_3CN followed by re-precipitation with Et_2O five times afforded a pure sample of the tetra-*n*-butylammonium salt of $\mathbf{P_2W_{20}}$. The purity was checked by ^{31}P NMR; one peak is present at -12.4 ppm.

X-ray Absorption Studies

A 120 mg crystalline sample of **3** was finely ground, and the resultant powder was pressed into a 1 mm thick aluminum spacer with X-ray transparent kapton windows. The Pd *K*-edge X-ray absorption spectra for **3** were measured at the Stanford Synchrotron Radiation Laboratory (SSRL) on focused (Rh-coated toroid) 30-pole wiggler beam line 10-2 with the ring operating at 3 GeV, 85-100 mA. A liquid nitrogen cooled Si(220) monochromator was utilized for energy selection at the Pd *K*-edge. The monochromator was detuned 30% at 25345 eV to minimize higher harmonic components in the X-ray beam. Data were collected in transmission mode, and internal energy calibration was performed by simultaneous measurement of the absorption of a Pd foil placed between two ionization chambers located after the sample. The first inflection point of the foil was assigned to 24349.0 eV. The sample was maintained at 10 K using an Oxford Instruments CF1208 continuous flow liquid helium cryostat. Three scans of the energy

range 24020 – 25345 eV were collected and averaged. The averaged data were processed by fitting a first-order polynomial to the pre-edge region and subtracting this background from the entire spectrum. A three-region spline of orders 2, 3, and 3 was used to model the smooth background above the edge.

Theoretical EXAFS signals were calculated using FEFF (version 7.02),[34] and refinements of the structural model to the data were done by a non-linear least-squares fitting process in *k*-space using EXAFSPAK. Atom coordinates for the initial model were obtained from the crystallographic structure of **3**. The experimental energy threshold E_0 was chosen as 24370 eV and was allowed to vary by a common amount (ΔE_0) for all components within a given fit. The structural parameters that were varied during the refinements included the bond distance (R) and the bond variance (σ^2).

Electrochemistry

Measurements were performed using a glassy carbon electrode in a pH 4.5 buffer. Solutions were de-aerated with Ar for at least 30 min prior to measurements and kept under positive pressure at all times. The source, mounting, and polishing of the glassy carbon electrodes (GC, Tokai, Japan, 3 mm diameter) have been described in previous work. The electrochemical apparatus was an EG & G 273 A under computer control (M270 software). The counter electrode was a platinum gauze of large surface area. All experiments were performed at ambient temperature, and potentials are quoted against a saturated calomel electrode (SCE). The results indicate that **3**, its Pd(II)-precursor ($PdSO_4$), and Pd(II) containing polytungstates have distinct electrochemical behaviours. Due to the limited stability of $[Pd^{II}WO(OH_2)(PW_9O_{34})_2]^{12-}$, further comparisons are

restricted to **3**, a few Pd(II)-substituted polytungstates recently reported in the literature,[35-37] and uncomplexed Pd(II).

Computational Procedures

Complete-Active-Space-Self-Consistent-Field (CASSCF) calculations were performed by the MOLPRO packages[38] using Stuttgart group ECP and corresponding basis sets for transition metal atoms and standard 6-31G** basis sets for main group elements.[39-43] Density Functional B3LYP calculations have been performed at the same basis sets using the Gaussian_2003 software package.[44] CASSCF (20 e / 14 orb) calculations, inclusive of all valence electrons and orbitals, on the $[O=Pd^{IV}(OH)]^{1-}$ model for $K_{10}Na_3[Pd^{IV}O(OH)WO(OH_2)(PW_9O_{34})_2]$, **3**, were conducted.

3.4 Results and Discussion

Synthesis of $K_{10}Na_3[PdO(OH)WO(OH_2)(PW_9O_{34})_2]\bullet 16H_2O$ (3)

The successful synthesis and isolation of a terminal Pt-oxo complex (**1**)[20] by the use of $[A\text{-}\alpha\text{-}PW_9O_{34}]^{9-}$ polytungstate as a stabilizing inorganic ligand has encouraged us to make a Pd analogue (Pd-oxo containing complexes are rare and the terminal Pd=O unit is unprecedented). However, attempts with the same protocol used for synthesis of **1** in water were unsuccessful. A co-crystalline mixture of an all-tungsten complex $[P_2W_{19}O_{69}(OH_2)]^{14-}$ (**P_2W_{19}**) and $[Pd^{II}(PW_9O_{34})_2]^{16-}$ was obtained.[20] As shown in **Figure 3.1**, both Pd(II) and $[O=W^{IV}(OH_2)]^{4+}$ locate at the central linkage site flanking by two [A-

α-$PW_9O_{34}]^{9-}$ ligands. The W10 atom displaces out from the O_4 equatorial plane toward its terminal oxo group by 0.45 Å, while Pd1 atom sits on the center of the same O_4 equatorial plane. This makes the two atoms (Pd1 and W10) distinguishable in crystallographic studies. Free refinement of these two sites gives 30% Pd and 70% W occupancies, implying a co-crystalline mixture of $[P_2W_{19}O_{69}(OH_2)]^{14-}$ (70%) and $[Pd^{II}(PW_9O_{34})_2]^{16-}$ (30%). Importantly, the contents of these two components are further confirmed by repeated elemental analysis and ^{31}P NMR spectroscopy.

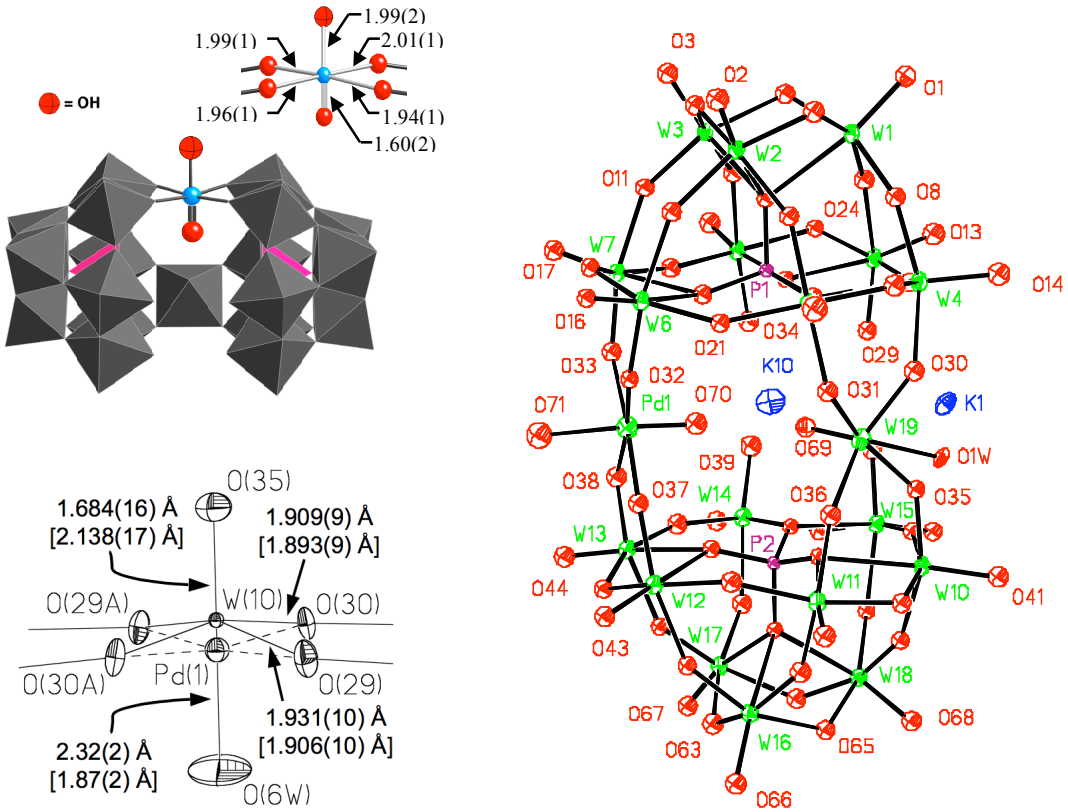

Figure 3.1 Combination polyhedral/ball-and-stick representation of polyanion **3** (top left) as well as thermal ellipsoid plots and numbering scheme for **3** (right). The WO_6 (or W atom) and PO_4 polyhedra are shown in gray and pink. The Pd and O atoms are shown in

blue and red, respectively. A short Pd-O_{oxo} (1.60(2) Å) bond is *trans* to a longer Pd-OH (1.99(2) Å) bond, and the central Pd atom is displaced out of the equatorial O_4 plane toward the terminal oxo by 0.11(1) Å. At the bottom left is the X-ray structure around the linkage position of the co-crystalline mixture of an all-tungsten complex $[P_2W_{19}O_{69}(OH_2)]^{14-}$ (**P_2W_{19}**, 70%) and $[Pd^{II}(PW_9O_{34})_2]^{16-}$ (30%).

Subsequent studies indicate that the starting polytungstate ligand, $[A\text{-}\alpha\text{-}PW_9O_{34}]^{9-}$, is not sable in aqueous solution particularly under acidic environment, where a fast hydrolytic decomposition of this metal-oxide cluster happens to generate several tungstate species including monomeric tungstate. Reaction of two equivalents of $[A\text{-}\alpha\text{-}PW_9O_{34}]^{9-}$ with monomeric tungstate competes with ligation to Pd(II) cation and produces the all-tungsten complex $[P_2W_{19}O_{69}(OH_2)]^{14-}$ in solution,[26] and once it formed, it co-crystallizes with $[Pd^{II}(PW_9O_{34})_2]^{16-}$. Because the $PdSO_4$ solution (pH 1.2) is more acidic than K_2PtCl_4 solution (pH 7.0), the decomposition/reorganization of the polytungstate ligand $[A\text{-}\alpha\text{-}PW_9O_{34}]^{9-}$ to **P_2W_{19}** is faster in the reaction with $PdSO_4$.

In order to slow the decomposition of ligand under the reaction conditions, we rationalized that a higher pH medium is necessary. As a result, we conducted the same reaction in sodium acetate buffer solution. The reaction of Pd(II) (from $PdSO_4$) with $[A\text{-}\alpha\text{-}PW_9O_{34}]^{9-}$ in 0.25 M sodium acetate/0.25 M acetic acid (pH = 4.9) yields the kinetically precipitated (with KCl) product $[Pd^{II}{}_3(PW_9O_{34})_2]^{12-}$. This complex undergoes a rapid, stepwise loss of Pd(II) in acidic media to form $[Pd^{II}WO(OH_2)(PW_9O_{34})_2]^{12-}$, based on ^{31}P and ^{183}W NMR studies performed by Knoth and co-workers on the Zn(II)

Table 3.1 Crystal data and structural refinement for the X-ray structures of $K_{10}Na_3[PdO(OH)P_2W_{19}O_{69}(OH_2)]\bullet 16H_2O$ (**3**) at three different temperatures.

molecular formula	$H_{35}K_{10}Na_3O_{89}P_2PdW_{19}$	$H_{35}K_{10}Na_3O_{89}P_2PdW_{19}$
formula wt.	5580.69	5580.69
temperature (K)	**173(2)**	**90(2)**
radiation (λ, Å)	0.71073	0.71073
crystal system	triclinic	triclinic
space group	*P-1* (#2)	*P-1* (#2)
a (Å)	11.8734(15)	11.9500(8)
b (Å)	17.225(2)	17.3589(12)
c (Å)	22.814(3)	22 .9619(16)
α (°)	90.536(2)	90.478(1)
β (°)	103.247(2)	103.281(1)
γ (°)	108.671(2)	108.628(1)
Volume ($Å^3$)	4285.3(9)	4375.7(5)
Z	2	2
μ (mm^{-1})	26.229	25.703
F(000)	4818	4890
crystal size (mm^3)	0.20 x 0.13 x 0.04	
θ range	1.62 to 28.35º	1.86 to 28.26º
reflections collected	59346	26326
independent reflections	21214 [R(int) = 0.0546]	19071 [R(int) = 0.0398]
absorption correction	semi-empirical from equivalents	semi-empirical from equivalents
max. and min. transmission	0.4201 and 0.0773	1.00 and 0.1974
refinement method	full-matrix least-squares on F^2	full-matrix least-squares on F^2
data/restraints/param.	21214/0/703	19071/0/703
goodness-of-fit on F^2	1.053	1.026
final R indices [R > 2σ (I)]	$R1^a$ = 0.0573 $wR2^b$ = 0.1611	$R1^a$ = 0.0782 $wR2^b$ = 0.2025
R indices (all data)	$R1^a$ = 0.0617 $wR2^b$ = 0.1644	$R1^a$ = 0.0893 $wR2^b$ = 0.2137

$^aR_1 = \Sigma||F_o| - |F_c||/ |F_o|$

$^bwR_2 = \{\Sigma[w(F_o^2 - F_c^2)^2]/\Sigma[w(F_o^2)^2]\}^{0.5}$

Table 3.1 Continued: Crystal data and structural refinement for the X-ray structures of $K_{10}Na_3[PdO(OH)P_2W_{19}O_{69}(OH_2)]\bullet 16H_2O$ (**3**) at three different temperatures.

molecular formula	$H_{35}K_{10}Na_3O_{89}P_2PdW_{19}$
formula wt.	5580.69
temperature (K)	**30(2)**
radiation (λ, Å)	0.71073
crystal system	triclinic
space group	*P-1* (#2)
a (Å)	11.9383(16)
b (Å)	17.332(2)
c (Å)	22.940(3)
α (°)	90.414(3)
β (°)	103.278(2)
γ (°)	108.585(2)
Volume ($Å^3$)	4362.1(10)
Z	2
μ (mm^{-1})	25.772
F(000)	4823
crystal size (mm^3)	
θ range	1.86 to 28.30º
reflections collected	50411
independent reflections	20284 [R(int) = 0.0435]
absorption correction	semi-empirical from equivalents
max. and min. transmission	1.00 and 0.3901
refinement method	full-matrix least-squares on F^2
data/restraints/param.	20284/0/703
goodness-of-fit on F^2	1.031
final R indices [R > 2σ (I)]	$R1^a$ = 0.0558 $wR2^b$ = 0.1365
R indices (all data)	$R1^a$ = 0.0619 $wR2^b$ = 0.1416

$^aR_1 = \Sigma||F_o| - |F_c||/ |F_o|$

$^bwR_2 = \{\Sigma[w(F_o^2 - F_c^2)^2]/\Sigma[w(F_o^2)^2]\}^{0.5}$

analogue.[45] In the final step, Pd(II) is oxidized by O_2 to give the final product $[Pd^{IV}O(OH)WO(OH_2)(PW_9O_{34})_2]^{13-}$ (**3**), and leads to crystalline brown plates of **3**. The purity of bulk sample is confirmed by spectroscopy studies, including FT-IR and ^{31}P NMR; the later shows only one phosphorus peak, a result consistent with the crystallographic studies (two symmetry equivalent phosphorus atoms are present in each molecule, see below).

Crystallographic Studies

Crystallographic studies of **3** establish that the Pd center is coordinated by a tetradentate, clam-shell like polytungstate $[P_2W_{19}(OH_2)O_{69}]^{14-}$ ligand which defines a square equatorial plane (**Figure 3.1**). A very short axial Pd=O bond (1.60-1.63 ± 0.03 Å from three data sets of **3** collected at 30 K, 90 K, and 173 K) is *trans* to a longer Pd-OH bond (1.99(2) Å). The oxo moiety is located in a sterically protected cavity between two $[A\text{-}\alpha\text{-}PW_9O_{34}]^{9-}$ units which are fused together by a single $[O=W(OH_2)]^{4+}$ center. The Pd atom is displaced out of the O_4 equatorial plane (into the central cavity) by 0.10 Å. A total of 13 countercations were located by X-ray crystallography and confirmed by duplicate elemental analyses. Anions other than **3** are clearly absent in the lattice (and the absence of Cl^- was confirmed by elemental analyses), consistent with the +4 oxidation state of Pd and an overall charge of 13- on the molecule. Unlike the Pt-oxo complex, **3** is stable in both solids state and aqueous solution because the extra $[O=W^{VI}(OH_2)]^{4+}$ unit between the two $[A\text{-}PW_9O_{34}]^{9-}$ ligands can stabilize the whole structure by not only increased structural rigidity but also decreased negative charge on the polyanion unit. All crystallographic studies unambiguously rule out cationic Pd counterions to the polyanion

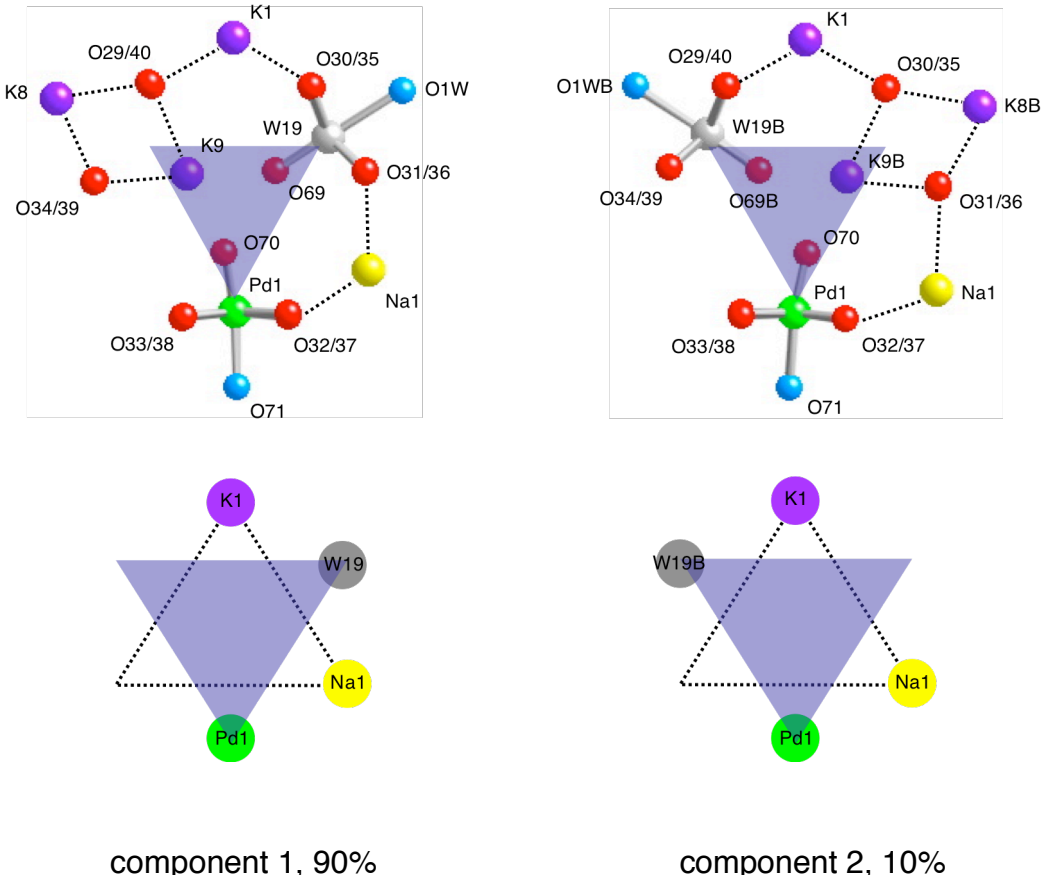

Figure 3.2 Atomic arrangement in the central belt of the polyanion in **3** illustrating the bridging $[O=W^{VI}(OH_2)]^{4+}$ unit, W19, is disordered between two sites, component 1 (left, 90%) and component 2 (right, 10%).

of **3** and suggest that the only one Pd atom established by repeated elemental analyses locates at the bridging site. There are three lines of evidence for OH^- as the ligand *trans* to the oxo unit. First, the 1.99(2) Å bond length is more consistent with a Pd-OH bond than Pd=O or Pd-OH_2 bonds. Second, elemental analyses and X-ray crystallography establish that the overall charge of the molecule is 13-. Third, the protonation and

deprotonation process followed by pH-dependent UV-vis and ^{31}P NMR titration studies strongly suggest the *trans* OH^- ligand.

There is disorder in the plane located between the two $[A\text{-}\alpha\text{-}PW_9O_{34}]^{9-}$ units. This disorder does not affect the positions of any of the atoms in the plane; however, it does cause the positions of the oxo and hydroxo ligands coordinated to Pd to be refined at 100% occupancy with relatively large thermal parameters. A similar phenomenon was observed by Tourné and Weakley in the closely related complex, $[P_2W_{21}O_{71}(OH_2)_3]^{6-}$.[46] In their structure, some atoms in the equatorial plane were refined at partial occupancy. However, ^{183}W NMR studies on this complex suggested that no compositional impurities were present. In the case of **3**, there were no impurities detected by ^{31}P NMR or elemental analyses, and the disorder was a result of interior steric crowding (from neighboring K^+ and O atoms) in the solid state, for example, K10 locates inside of the clam-shell opening and weakly interacting with O70 (bound to Pd) and O69 (bound to W19).

Importantly, two structural issues are worth being discussed here, which are not fully and appropriately addressed in the previous work. First, the linkage W19 as well as its terminal oxo (1.676(12) Å) and trans aqua (2.299(10) Å) ligands are disordered on two of the three vacant sites on the central belt (the third site is occupied by Pd). **Figure 3.2** shows the atomic arrangement and bonding paradigm in the central belt of the polyanion of **3** in the solid state, illustrating the location disorder of W19. In this figure, countercations K1, K8, K9, Na1 as well as Pd1 and W19 (with their axial ligands) define a plane; O29-34 and O35-40 are oxo oxygens from each of the two $[A\text{-}PW_9O_{34}]^{9-}$ ligands and sit above or below the central belt, respectively. In our initial refinement, W19 has a

relatively big thermal parameter compared to other tungsten atoms, indicating possible partial occupancy of tungsten on this site; moreover, a Q (doming out of the square plane defined by O29/40 and O34/39 toward K9) cannot be well modeled because of its short distance/interaction with K8 and K9. It is noticed that although these two sites (W19 and the vacant site in component 1) are symmetry equivalent in the polyanion unit of **3**, they are different in the crystal lattice because two countercations, K1 and Na1, which locate at the central belt and bind to O29/40, O30/35 and O31/36, O32/37, respectively, break down the symmetry (**Figure 3.2**). As a result, W19 can be disordered on these two positions in the solid state as component 1 (90%) and component 2 (10%). Accordingly, its terminal oxo oxygen and trans aqua ligand as well as K8 and K9 are disordered, although their disorder cannot be refined due to the small percentage of component 2.

Second, the thermal parameters of the terminal oxo oxygen on Pd and its *trans* hydroxyl oxygen are unusually big. One would argue for the partial occupancies of these two ligands. In other words, the Pd position is a mixture of octahedral Pd(IV) and square planar Pd(II). However, there are five lines of evidence convincingly suggesting that one and only one kind Pd center, the octahedral $[O=Pd^{IV}(OH)(O\text{-}W)_4]$ unit, is present in each molecule of complex **3**. (1) The negative charge of the polyanion unit is 13- (10 K^+ and 3 Na^+ can be located in all X-ray data sets and be found in repeated elemental analyses), which is in agreement with the formulation, $[Pd^{IV}O(OH)P_2W_{19}O_{69}(OH_2)]^{13-}$. (2) Pd EXAFS result is consistent with an octahedral Pd(IV) center in complex **3** (see below). (3) One peak in ^{31}P NMR (-11.7 ppm) strongly argues that only one Pd center is present. (4) Only one Pd reduction is observed in the electrochemistry. (5) Ultra-low-temperature electronic absorption spectroscopy at 5 K is also consistent with a d^6 Pd(IV) center.

Careful analyses of the three data sets of **3** at 173, 90 and 30 K reveal that the unusual thermal parameters of these two oxygens, O70 and O71, are resulted by the displacement from the ideal C_2 axis of the octahedral [O=Pd^{IV}(OH)(O-W)$_4$] unit due to the repulsion from the crowded environment at the central belt. O70 has a short distance/interaction with K9 (2.435 Å by average) and O69 (2.545 Å by average) within the van der Waals distance of O70; O71 is pushed aside by Na2 and also strongly interacts with O17W, O18W and O23W by hydrogen bonding. The strong repulsion between O70, O69 and K9 has three more results that are worth noticing. (1) O70 is pushed toward Pd1 with a very short Pd-O_{oxo} bond distance (1.62 Å by average). (2) The doming distance of Pd1 from the O_4 equatorial plane (0.1 Å) is small compared to 0.45 Å for terminal W(VI)-oxo based on hundreds of polytungstate structures, suggesting the repulsion of the [O=Pd^{IV}(OH)]$^+$ unit. (3) Displacement of O70/O71 from the ideal C_2 axis is also evidenced by the bended O70-Pd1-O71 angle, 171.2(13) degrees (the angle of O69-W19-O1W is 179.7(5) degrees).

X-ray Absorption Studies

The unprecedented and controversial nature of the title claim, a Pd-oxo unit, combined with the uncertainty from the collective X-ray structures argue strongly that an independent unequivocal structural method to assess the Pd-oxo distance is needed. This is true despite the fact that ^{31}P NMR and elemental analysis data strongly suggest that only **3** is present in the unit cell. In this context, we provide Pd K-edge extended X-ray absorption fine structure (EXAFS) data that address both the crystallographic disorder and the unusually short Pd=O bond distance.

The k^3-weighted EXAFS data for **3** and the corresponding Fourier transform are shown in **Figure 3.3**. Theoretical phase and amplitude parameters for the fit were generated by FEFF (version 7.02),[34] using the crystallographic parameters of **3** for the initial model. The best fit (with reasonable distances and Debye-Waller factors) is obtained with five Pd-O bond distances of 1.96 ± 0.03 Å and one Pd-O bond distance of 1.68 ± 0.03 Å (**Table 3.2**). Therefore, the EXAFS data support the crystallographic conclusions (i.e. a Pd-O bond distance of 1.60-1.63 ± 0.03 Å) within experimental error, despite the disorder (occupancy) problems that adversely affect the precision of the X-ray diffraction results.

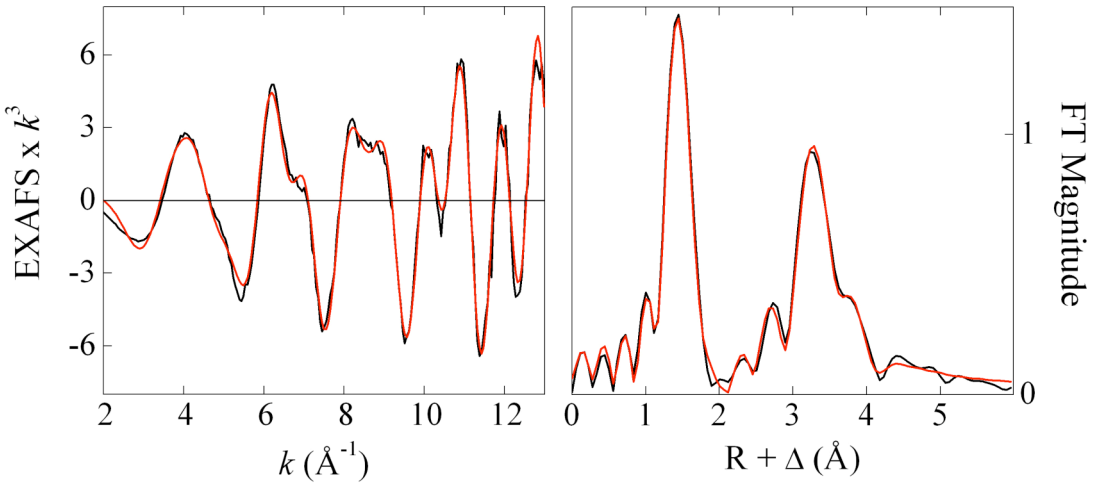

Figure 3.3 Pd *K*-edge EXAFS data (black), fit (red), and the corresponding non-phase shift corrected Fourier transforms for **3**.

Table 3.2 Curve fitting results for the Pd *K*-edge EXAFS of **3**.

Fit #	Coordination model for the first shell	*N*	Scatterer	*R*, Å	σ^2, Å^2	Fit error
1	5 O	5	O	1.97	0.0043	0.217
		4	W	3.60	0.0021	
		4	O-W	3.73	0.0021	
		2	K-O	3.98	0.0023	
		8	O-O	4.67	0.0043	
2	6 O	6	O	1.97	0.0055	0.263
		4	W	3.60	0.0021	
		4	O-W	3.73	0.0020	
		2	K-O	3.98	0.0023	
		8	O-O	4.67	0.0044	
3	1 O	1	O	1.71	0.0154	0.181
	4 O	4	O	1.96	0.0028	
		4	W	3.60	0.0027	
		4	O-W	3.73	0.0023	
		2	K-O	3.96	0.0026	
		8	O-O	4.66	0.0045	
4	1 O	1	O	1.68	0.0067	0.151
	5 O	5	O	1.96	0.0043	
		4	W	3.60	0.0023	
		4	O-W	3.73	0.0023	
		2	K-O	3.97	0.0026	
		8	O-O	4.67	0.0046	
5	1 O	1	O	1.71	0.0146	0.160
	4 O	4	O	1.96	0.0027	
	1 O	1	O	2.41	0.0047	
		4	W	3.59	0.0024	
		4	O-W	3.73	0.0023	
		2	K-O	3.95	0.0027	
		8	O-O	4.62	0.0044	

N is the coordination number, *R* is the mean distance, σ^2 is the bond length variance. The fit error is defined as $[\Sigma(\chi_{exp} - \chi_{calc})^2 k^6 / \Sigma\chi_{exp}{}^2 k^6]^{1/2}$, where χ is the EXAFS data point. The accuracies estimated for bond lengths are approximately ± 0.03 Å; resolution is 0.14 Å.

Titration Studies

The *trans* OH^- ligand on the Pd atom is further confirmed by pH titrations and pH-dependent UV-vis and ^{31}P NMR spectroscopy studies. The natural pH of aqueous solution of **3** at room temperature is 6.5. Addition of HCl shows a small inflection point at 3.5, which is expected for the protonation of a Pd(IV)-OH unit. In addition, this protonation process is followed by electronic absorption spectroscopy: the UV-vis spectrum of 3 starts to change at pH 3.5. As shown in **Figure 3.4**, there are three significant changes in the d-d band at 444 nm upon lowering the pH of the solution below 3.5 (a red shift of 8 nm, loss of a shoulder at 512 nm, and an increase in ε). Importantly, this process is fully reversible upon increasing the pH above 3.5 again by the addition of NaOH. The UV-vis experiments are also corroborated by similar changes in the ^{31}P NMR spectrum of **3** as a function of pH.

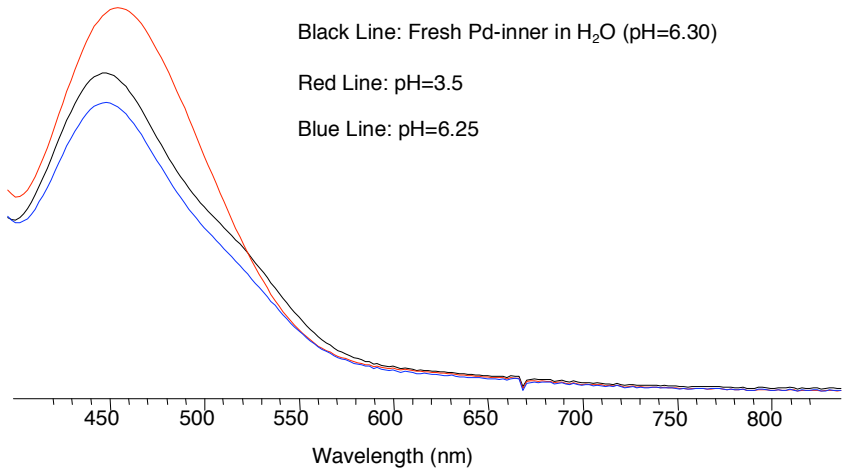

Figure 3.4 pH-dependent UV-vis titration of **3** with HCl and the back titration with NaOH, showing the reversible changes in the d-d bands at 444 nm upon lowering and increasing the pH of the solution.

^{17}O NMR Studies

To observe a ^{17}O nucleus by NMR spectroscopy is difficult for three reasons. First, the isotope ^{17}O has a very low natural abundance (0.037%), which usually necessitates the enrichment of ^{17}O. Second, the ^{17}O nucleus has a rapid nuclear quadrupole relaxation due to its spin 5/2 nucleus with an appreciable electric quadrupole moment, $Q = -2.6 \times 10^{-26}$ cm^2, which in general leads to broad resonances and as a result, a poor spectral resolution and a poor signal to noise ratio, although it allows rapid RF pulsing. Furthermore, the delay times between the end of each RF pulse and the beginning of data collection must be short because of this rapid spin-spin relaxation, which often causes incomplete spectrometer recovery and baseline distortion in transformed spectra. However, the use of ^{17}O NMR spectroscopy as a structural probe is powerful because structurally nonequivalent nuclei usually differentiate well due to their large chemical shift differences, and specific chemical environments usually give characteristic chemical shift values.[47-49] This is especially true for oxygen bonded to transition metals, which is often observed at large chemical shift.[48,49]

The use of a 50:50 (v:v) CH_3CN-$CDCl_3$ mixture solvent instead of a pure $CDCl_3$ affords three benefits: (1) CH_3CN is a much more polar solvent than $CDCl_3$, which increases the solubility of most polyoxometalates. For this kind of giant molecule whose molecular weight is usually around 5500, it is seriously problematic to have a sufficient concentration for NMR studies. (2) CH_3CN has a lower viscosity (0.35 cP at 25 °C) than $CDCl_3$ (0.58 cP at 25 °C). In a homogeneous medium, the relaxation time T_1 for a quadrupolar nucleus, like ^{17}O, is determined by equation 3.1.

$$\frac{1}{T_1} = \frac{1}{T_2} = \frac{3}{125}\left(1+\frac{n^2}{3}\right)\left(\frac{e^2Qq}{\hbar}\right)\tau_c \qquad (3.1)$$

where ($e^2Qq/\hbar$) is the quadrupole coupling constant, **n** is the electronic field gradient asymmetry parameter, and τ_c is the correlation time for molecular rotation ($\tau_c = 4\pi\eta a^3/3kT$, Stokes-Einstein-Debye equation. η, solution viscosity; a, molecular radius; T, temperature). For a given molecule, the molecular radius, the asymmetry parameter and the quadrupole coupling constant are constant, T_1 may be increased only by lowering the viscosity of solution or by elevating the temperature. (3) The presence of adequate protons from CH_3CN in the solvent enables the intermolecular NOE enhancement that increases the sensitivity of ^{17}O NMR since the magnetogyric ratio is -3.63 10^7 rad T^{-1} S^{-1} for ^{17}O.

Previous studies revealed that many polyoxometalates can exchange oxygen with water, and it is advantageous in the ^{17}O enrichment to simply mix regular compounds with ^{17}O-enriched water.[48] However, it is worthy to note that the possibility of selective oxygen exchange (different reactivity at different sites) leads to problems in integrating spectra. The direct use of ^{17}O enriched water as the solvent can result in a rapid oxygen exchange at mild temperature in the case of $K_{10}[P_2W_{20}(OH_2)_2\ O_{70}]$ (**P_2W_{20}**), the all-tungsten complex that is isostructural to **3**. Exchange is less efficient for **3** than **P_2W_{20}** due to its relatively low solubility in water. An alternative approach for enrichment entails carrying out the process in a nonaqueous solvent. The stability of these polyoxometalates in water and in nonaqueous solvents was investigated using ^{31}P NMR.

The ^{17}O NMR spectra for **3** and **P_2W_{20}** are reported in **Figure 3.5**. The ^{17}O chemical shifts agree well with the general correlation between downfield chemical shift

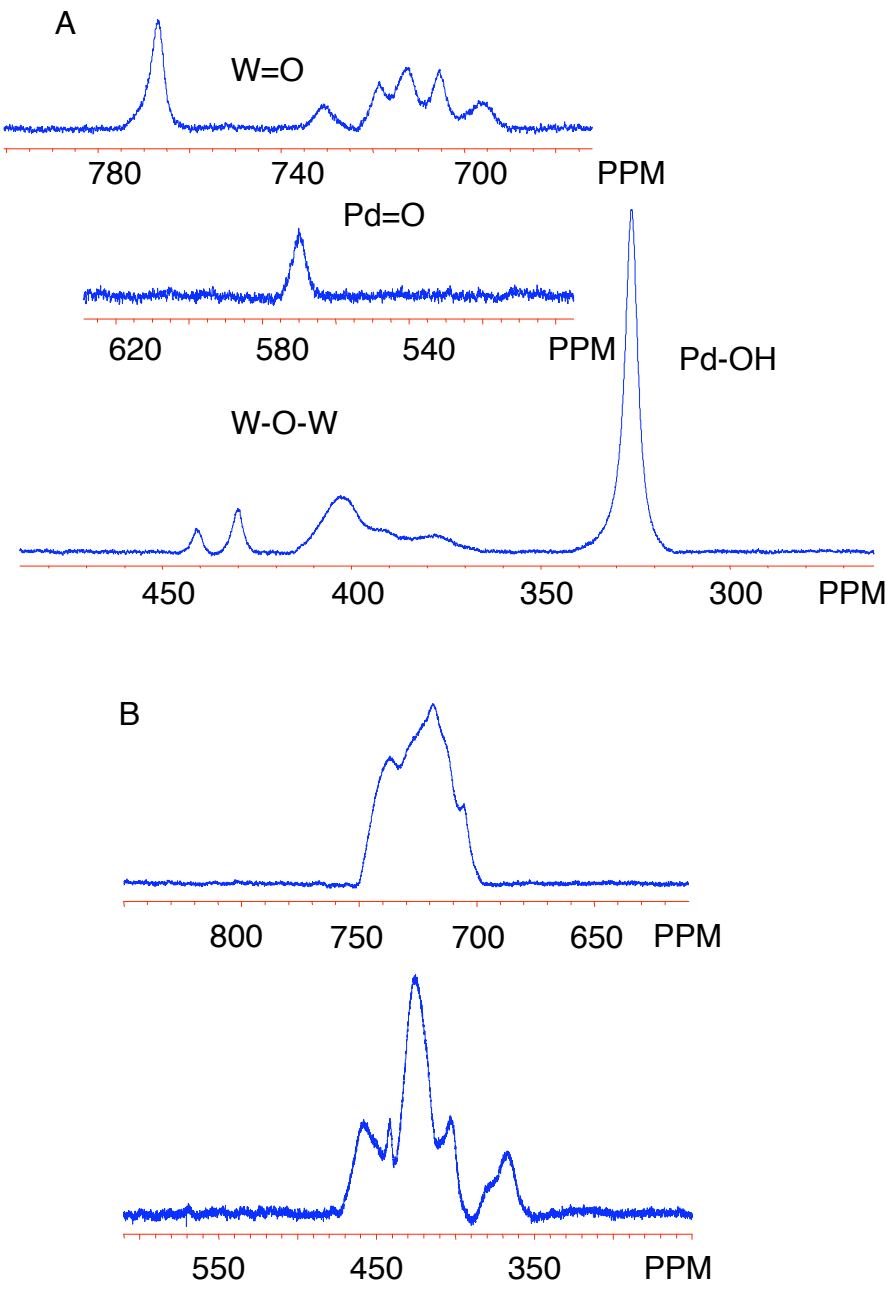

Figure 3.5 ^{17}O NMR spectra of Pd-oxo complex **3** and its isostructural all-tungsten complex, $[P_2W_{20}O_{70}(OH_2)_2]^{10-}$ (**P_2W_{20}**). Two peaks at 330 and 570 ppm (relative to D_2O at 0 ppm) are attributable to the hydroxo and oxo ligands of Pd, respectively. The two peaks are assigned based on the established correlation between downfield chemical shift

and oxygen π-bond order and the fact that they are not observed in the isostructural complex **P_2W_{20}**.

and oxygen π-bond order.[47-52] In the structure of **3**, there are eleven classes of symmetry-equivalent terminal oxo oxygens: ten W=O (triple bond) and a Pd=O (double bond) units. The differences between Pd and W as well as their bond order to oxo oxygens lead to *ca.* 160 ppm upfield shift for the terminal oxo oxygen on Pd. Because of its structural complexity and their relative similar coordination environments, the bridging oxygens of the polyoxoanion framework of **3** are expected to have similar chemical shift values around 370 to 450 ppm. The very strong peak at 326 ppm is assigned to the oxygen of Pd-OH_2 unit (the -OH ligand on Pd has been protonated during extraction from water to CH_2Cl_2, because of the pH to 3.0 is necessary to obtain a completed extraction). The isostructural polytungstate of **3**, $K_{10}[P_2W_{20}(OH_2)_2 O_{70}]$, was also examined by ^{17}O NMR spectroscopy. As expected, the chemical shift ranges of the terminal oxo oxygens on W and the bridging oxygens of the framework are similar to those of **3**. Importantly, there are no peaks around 560 and 320 ppm, which are assigned to the oxygens of Pd=O and Pd-OH_2, respectively. The fact that no peak shows up around 560 ppm in $K_{10}[P_2W_{20}(OH_2)_2O_{70}]$ as well as the correlation between the downfield chemical shift and oxygen π-bond order on Pd both suggest the existence of this unconventional Pd=O unit. The ^{17}O NMR experiments run on an enriched sample of **3** also suggest the solid-state structure is maintained in solution.

Electronic Absorption Studies

In contrast to the related complex **1**, the ultra-low-temperature (5 K) electronic spectrum of **3** has only two weak absorption bands in the visible region of the spectrum, at 19,750 cm^{-1} (506 nm; band 1) and 22,700 cm^{-1} (441 nm; band 2) (**Figure 3.6**). Intense oxygen-to-tungsten charge transfer bands (E > 26,000 cm^{-1}), characteristic of all polytungstates, are found at higher energy.

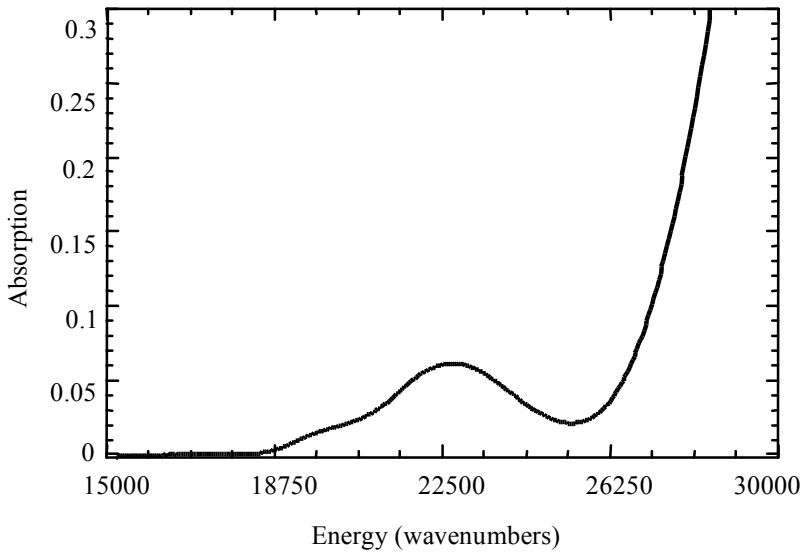

Figure 3.6 Ultra-low-temperature (5 K) electronic absorption spectrum of **3** showing two weak absorption bands in the visible region at 19,750 cm^{-1} (506 nm; band 1) and 22,700 cm^{-1} (441 nm; band 2).

Our analysis of the ultra-low-temperature ligand spectra of **3** is based on that for **1**,[20] with tentative assignments for the Pd(IV) ligand field bands as $e \rightarrow b_1$ (bands 1 and 2) and $b_2 \rightarrow b_1$ (band 2). Spectral fitting indicates that band 2 is likely comprised of two

electronic absorption features due to the larger bandwidth. The e → b_1 one electron promotion results in two components, one under band 1 and one under band 2, due to the effects of low-symmetry and spin-orbit splitting of the E excited state (A_1 → E transition). One-electron promotions to the empty d_{z2} orbital are viewed as unlikely contributors to the low energy ligand field region due to the inherently large ligand field splitting of 4d ions and the very large destabilization of this orbital resulting from strong σ* bonding interactions with the terminal oxo donor.

Electrochemistry

A reduction peak potential for **3** is observed at E_{pc} = -0.47 V (vs SCE), a value substantially more negative than uncomplexed Pd(II) (E_{pc} = -0.28 V vs SCE). At equal concentrations, **3** has both a smaller diffusion coefficient and a larger current intensity than Pd(II) alone. The larger current intensity of **3** is attributed to the larger number of electrons involved in its reduction compared to Pd(II), while the negative potential shift for the reduction of **3** is rationalized by the fact that the terminal oxo ligand is a strong π electron donor (despite the high electronegativity of oxygen). The reduction wave of **3** is observed at a more negative potential than the corresponding process found in the Pd(II)-substituted polytungstate, $[Cs_2K(H_2O)_7Pd_2WO(H_2O)(A\text{-}\alpha\text{-}SiW_9O_{34})_2]^{9-}$ (E_{pc} = -0.32 V vs SCE).[36] Both **3** and this Pd(II) containing polytungstate have the same current intensity for the Pd-reduction waves because there are two Pd(II) centers in each molecule of the later. Finally, the numbers of electrons involved in the exhaustive reductions of the Pd centers within **3** (at -0.45 V vs SCE), $[Cs_2K(H_2O)_7Pd_2WO(H_2O)(A\text{-}\alpha\text{-}SiW_9O_{34})_2]^{9-}$ (at -0.33 V vs SCE), and Pd(II) alone (at -0.32 V vs SCE) were determined by controlled

potential coulometry and found to be 4, 4 and 2 electrons per molecule (or per anion), respectively.

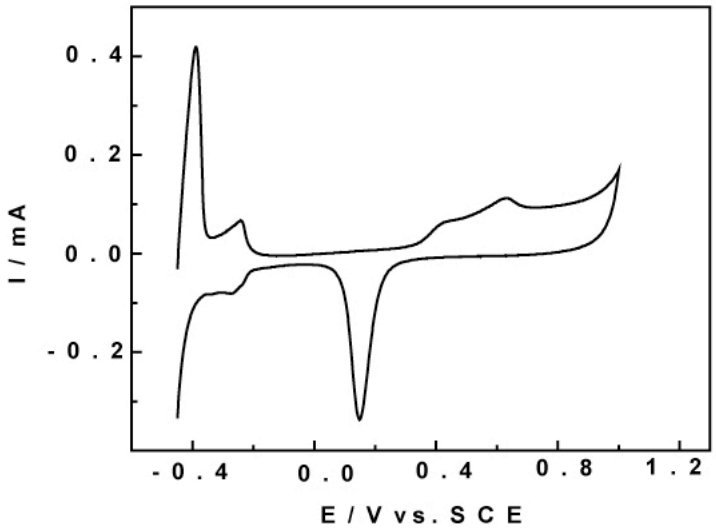

Figure 3.7 Cyclic voltammogram of **3**. The results indicate that **3**, its Pd(II)-precursor ($PdSO_4$), and Pd(II) containing polytungstates have distinct electrochemical behaviours.

Regardless of the compound, the observed first reduction wave features the reductive deposition of Pd(IV)=O or Pd(II) into Pd^0. This was previously observed with other Pd(II)-substituted POMs.[35-37] **Figure 3.7** reveals the main characteristics of a relatively thick film built up from **3**. The scan rate was 2 mV s^{-1}. The deposition of Pd^0 on the electrode surface in the negative potential domain is immediately followed by a sharp cathodic peak (with a sharp and narrow anodic counterpart) that both feature hydrogen sorption/desorption processes. The domain starting from 0.0 V to +1.0 V (vs SCE) in the positive potential direction and back to 0.0 V (vs SCE) unambiguously

represents the oxidation of the deposited Pd surface followed by the reduction of the oxide at +0.148 V (vs SCE). Even the two-step oxidation of the surface at +0.440 V (vs SCE) and + 0.630 V (vs SCE) are characteristic of thick Pd^0 films.[53] In summary, the cyclic voltammogram featured in **Figure 3.7** has essentially the same characteristics as those observed for the deposition of Pd^0 on a glassy carbon electrode surface from Pd(II) solutions.

Pd(IV) oxidation state assignment

Five lines of evidence suggest that the oxidation state of the Pd in **3** is +4. First, 13 countercations (10 K^+ and 3 Na^+) can be located in all X-ray data sets and be found in repeated elemental analyses (no Cl^- is detectable, see Experimental Section). This is consistent with the negative charge of the polyanion of **3**, $[Pd^{IV}O(OH)P_2W_{19}O_{69}(OH_2)]^{13-}$. Second, structural analysis of the Pd atom, including X-ray single crystal diffraction and Pd EXAFS, confirms the multiply bonded terminal oxo ligand and indicates the existence of a d^6 Pd(IV) configuration. Third, four electrons are need to obtain Pd(0) in controlled potential coulometry which is consistent with the reduction of Pd(IV) to metallic Pd(0). Fourth, the diamagnetism of **3** (based on room temperature magnetic susceptibility measurements and ^{31}P NMR) argues for a d^6 Pd(IV) and against a d^8 Pd(II) or d^4 Pd(VI) (for a local C_{4v} metal center). Fifth, the electron absorption spectrum of **3** is also consistent with a six-coordinated local C_{4v} Pd(IV) with d^6 electronic configuration.

Computational Results

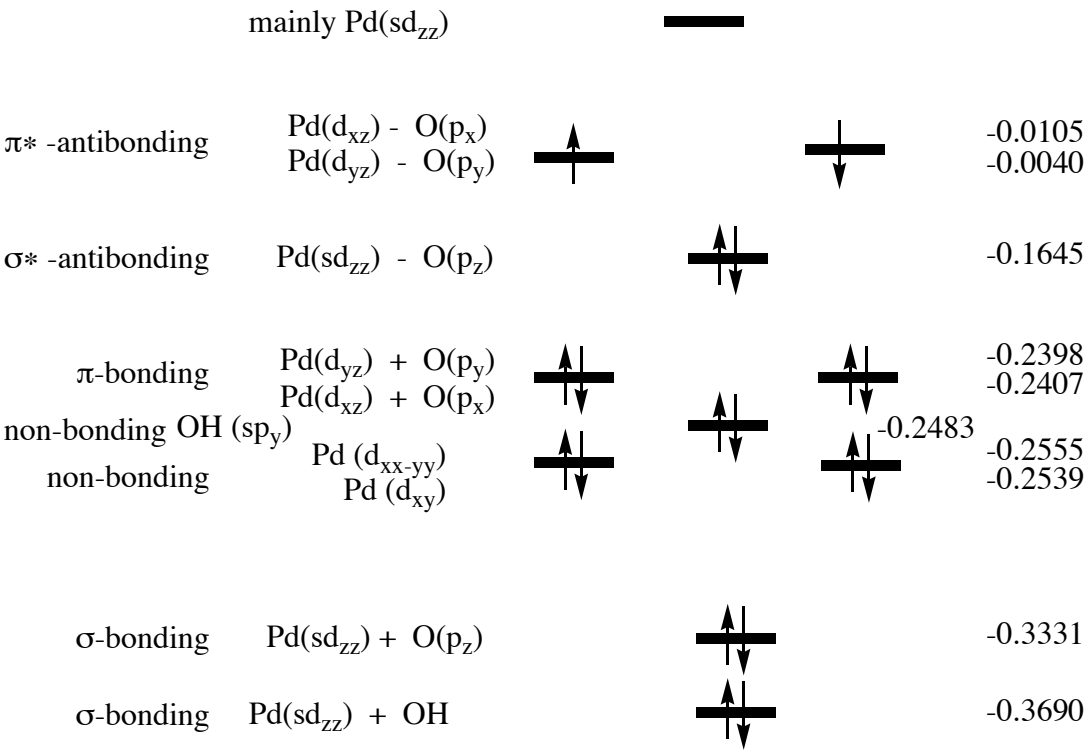

Figure 3.8 Molecular orbital diagram of the model $[O=Pd^{IV}(OH)]^{1-}$. Only the important orbitals of this model are presented. All energetics are in a.u.

The calculations indicate that the ground electronic state of this model is an open-shell singlet state with the following valence-electron configuration $[\sigma(Pd\text{-}OH)]^2[\sigma(Pd=O)]^2[\delta(Pd)]^4[\pi(OH)]^2[\pi(Pd=O)]^4[\sigma^*(Pd=O)]^2[\pi^*(Pd=O)]^2[\sigma(Pd)]^0$ (**Figure 3.8**). The lowest triplet state with the same orbital occupancy lies only 3.3 kcal/mol higher in energy. Significantly, the DFT method (e.g. B3LYP) incorrectly describes the lower-lying states of this $[OPd^{IV}(OH)]^{1-}$ model. At the B3LYP level, the triplet state is

the ground state, while the lowest singlet state with the following valence-electron configuration, $[\sigma(\text{Pd-OH})]^2[\sigma(\text{Pd=O})]^2[\delta(\text{Pd})]^4[\pi(\text{OH})]^2[\pi(\text{Pd=O})]^4[\sigma^*(\text{Pd=O})]^2[\sigma(\text{Pd})]^2[\pi^*(\text{Pd=O})]^0$, lies about 19.1 kcal/mol higher in energy.

References

(1) Holm, R. H. *Chem. Rev.* **1987**, *87*, 1401-1449.

(2) Holm, R. H.; Donahue, J. P. *Polyhedron* **1993**, *12*, 571-589.

(3) Parkin, G. In *Prog. Inorg. Chem.*; Karlin, K. D., Ed.; Wiley: New York, 1998; Vol. 47, p 1-165.

(4) Nugent, W. A.; Mayer, J. M. *Metal-Ligand Multiple Bonds*; John Wiley & Sons, Inc.: New York, 1988.

(5) Borovik, A. S. *Acc. Chem. Res.* **2005**, *38*, 54-61.

(6) Bakac, A. In *Advances in Inorganic Chemistry* 2004; Vol. 55, p 1-59.

(7) Miskowski, V. M.; Gray, H. B.; Hopkins, M. D. *Advances in Transition Metal Coordination Chemistry* **1996**, *1*, 159-186.

(8) Morris, R. J.; Girolami, G. S. *Polyhedron* **1988**, *7*, 2001-2008.

(9) Spaltenstein, E.; Conry, R. R.; Critchlow, S. C.; Mayer, J. M. *J. Am. Chem. Soc.* **1989**, *111*, 8741-8742.

(10) Rohde, J.-U.; In, J.-H.; Lim, M. H.; Brennessel, W. W.; Bukowski, M. R.; Stubna, A.; Münck, E.; Nam, W.; Que Jr., L. *Science* **2003**, *299*, 1037-1039.

(11) MacBeth, C. E.; Golombek, A. P.; Jr., V. G. Y.; Yang, C.; Kuczera, K.; Hendrich, M. P.; Borovik, A. S. *Science* **2000**, *289*, 938-941.

(12) Green, M. T.; Dawson, J. H.; Gray, H. B. *Science* **2004**, *304*, 1653-1656.

(13) Holland, P. L.; Andersen, R. A.; Bergman, R. G. *Comments on Inorganic Chemisry* **1999**, *21(1-3)*, 115-129.

(14) Sharp, P. R. *Dalton Trans.* **2000**, *16*, 2647-2657.

(15) Schroder, D.; Schwarz, H.; Shaik, S. In *Structure and Bonding*; Springer-Verlag GmbH: Berlin, 2000; Vol. 97 (Metal-Oxo and Metal-Peroxo Species in Catalytic Oxidations), p 91-123.

(16) Siegbahn, P. E. M.; Crabtree, R. H. In *Structure and Bonding*; Publisher: Springer-Verlag GmbH: Berlin, 2000; Vol. 97, p 125-144.

(17) Hay-Motherwell, R. S.; Wilkinson, G.; Hussain-Bates, B.; Hursthouse, M. B. *Polyhedron* **1993**, *12*, 2009-2012.

(18) Jacobi, B. G.; Laitar, D. S.; Pu, L.; Wargocki, M. F.; DiPasquale, A. G.; Fortner, K. C.; Schuck, S. M.; Brown, S. N. *Inorg. Chem.* **2002**, *41*, 4815-4823.

(19) Eckert, N. A.; Stoian, S.; Smith, J. M.; Bominaar, E. L.; Münck, E.; Holland, P. L. *J. Amer. Chem. Soc.* **2005**, *127*, 9344-9345.

(20) Anderson, T. M.; Neiwert, W. A.; Kirk, M. L.; Piccoli, P. M. B.; Schultz, A. J.; Koetzle, T., F.; Musaev, D. G.; Morokuma, K.; Cao, R.; Hill, C. L. *Science* **2004**, *306*, 2074-2077.

(21) Appleby, A. J.; Foulkes, F. R. *Fuel cell handbook*; Krieger Publising Company, Malabar, Florida, 1993.

(22) Somorjai, G. A. *Introduction to surface chemistry and catalysis*; Wiley: New York, 1994.

(23) Shelef, M. *Chem. Rev.* **1995**, *95*, 209-225.

(24) Malleron, J.-L.; Fiaud, J.-C.; Legros, J.-Y. *Handbook of Palladium-Catalyzed Organic Reactions: Synthetic Aspects and Catalytic Cycles*; Academic Press: San Diego, CA., 1997.

(25) Singh, A.; Sharp, P. R. *Dalton Trans.* **2005**, 2080-2081.

(26) Tourné, C. M.; Tourné, G. F. *J. Chem. Soc., Dalton Trans.* **1988**, 2411-2420.

(27) Sharp, P. R. *J. Chem. Soc., Dalton Trans.* **2000**, 2647-2657.

(28) Domaille, P. J. In *Inorganic Syntheses*; Ginsberg, A. P., Ed.; John Wiley and Sons: New York, 1990; Vol. 27, p 96-104.

(29) SMART; Bruker AXS, I.; 5.628 ed.; Analytical X-ray Systems: Madison, WI, 2003.

(30) SAINT; Bruker AXS, I.; 6.28 ed.; Analytical X-ray Systems: Madison, WI, 2003.

(31) SADABS; Sheldrick, G.; 2.10 ed. 2003.

(32) SHELXTL; 6.14 ed.; Bruker AXS, Inc.: Madison, WI, 2003.

(33) Contant, R. *Can. J. Chem.* **1987**, *65*, 568-573.

(34) Ankudinov, A. L.; Rehr, J. J. *Phys. Rev. B* **1997**, *56*, R1712-R1715.

(35) Bi, L.-H.; Reicke, M.; Kortz, U.; Keita, B.; Nadjo, L.; Clark, R. J. *Inorg. Chem.* **2004**, *43*, 3915-3920.

(36) Bi, L.-H.; Kortz, U.; Keita, B.; Nadjo, L.; Borrmann, H. *Inorg. Chem.* **2004**, *43*, 8367-8372.

(37) Bi, L.-H.; Kortz, U.; Keita, B.; Nadjo, L.; Daniels, L. *Eur. J. Inorg. Chem.* **2005**, 3034-3041.

(38) Werner, H. J.; Knowles, P. J. 2003.

(39) Schwerdtfeger, P.; Dolg, M.; Schwarz, W. H. E.; Bowmaker, G. A.; Boyd, P. D. W. *J. Chem. Phys.* **1989**, *91*, 762-767.

(40) Andrae, D.; Haubermann, U.; Dolg, M.; Stoll, H.; Preub, H. *Theor. Chim. Acta* **1990**, *77*, 123-141.

(41) Bergner, A.; M., D.; Küchle, W.; Stoll, H.; Preuss, H. *Mol. Phys.* **1993**, *80*, 1431-1441.

(42) Dolg, M.; Stoll, H.; Preuss, H.; Pitzer, R. M. *J. Phys. Chem.* **1993**, *97*, 5852-5859.

(43) Dolg, M.; Stoll, H.; Preuss, H. *Theor. Chim. Act.* **1993**, *85*, 441-450.

(44) Frisch, M. J.; Trucks, G. W.; Schlegel, H. B.; Scuseria, G. E.; Robb, M. A.; Cheeseman, J. R.; Montgomery, J., J. A.; Vreven, T.; Kudin, K. N.; Burant, J. C.; Millam, J. M.; Iyengar, S. S.; Tomasi, J.; Barone, V.; Mennucci, B.; Cossi, M.; Scalmani, G.; Rega, N.; Petersson, G. A.; Nakatsuji, H.; Hada, M.; Ehara, M.; Toyota, K.; Fukuda, R.; Hasegawa, J.; Ishida, M.; Nakajima, T.; Honda, Y.; Kitao, O.; Nakai, H.; Klene, M.; Li, X.; Knox, J. E.; Hratchian, H. P.; Cross, J. B.; Adamo, C.; Jaramillo, J.; Gomperts, R.; Stratmann, R. E.; Yazyev, O.; Austin, A. J.; Cammi, R.; Pomelli, C.; Ochterski, J. W.; Ayala, P. Y.; Morokuma, K.; Voth, G. A.; Salvador, P.; Dannenberg, J. J.; Zakrzewski, V. G.; Dapprich, S.; Daniels, A. D.; Strain, M. C.; Farkas, O.; Malick, D. K.; Rabuck, A. D.; Raghavachari, K.; Foresman, J. B.; Ortiz, J. V.; Cui, Q.; Baboul, A. G.; Clifford, S.; Cioslowski, J.; Stefanov, B. B.; Liu, G.; Liashenko, A.; Piskorz, P.; Komaromi, I.; Martin, R. L.; Fox, D. J.; Keith, T.; Al-Laham, M. A.; Peng, C. Y.; Nanayakkara, A.; Challacombe, M.; Gill, P. M. W.; Johnson, B.; Chen, W.; Wong, M. W.; Gonzalez, C.; Pople, J. A.; 03 Rev. C1 ed.; Gaussian, Inc.: Pittsburgh, 2003.

(45) Knoth, W. H.; Domaille, P. J.; Harlow, R. L. *Inorg. Chem.* **1986**, *25*, 1577-1584.

(46) Tourné, C. M.; Tourné, G. F.; Weakley, T. J. R. *J. Chem. Soc. Dalton Trans.* **1986**, 2237-2242.

(47) *^{17}O NMR Spectroscopy in Organic Chemistry*; Boykin, D. W., Ed.; CRC Press, Inc.: Boca Raton, 1991.

(48) Filowitz, M.; Ho, R. K. C.; Klemperer, W. G.; Shum, W. *Inorg. Chem.* **1979**, *18*, 93-103.

(49) Klemperer, W. G. *Angew. Chem., Int. Ed.* **1978**, *17*, 246-254.

(50) Besecker, C. J.; Klemperer, W. G.; Maltbie, D. J.; Wright, D. A. *Inorg. Chem.* **1985**, *24*, 1027-1032.

(51) Filowitz, M.; Klemperer, W. G.; Messerle, L.; Shum, W. *J. Am. Chem. Soc.* **1976**, *98*, 2345-2346.

(52) Maksimovskaya, R. I.; Burtseva, K. G. *Polyhedron* **1985**, *4*, 1559-1562.

(53) Lubert, K. H.; Guttmann, M.; Beyer, L.; Kalcher, K. *Electrochem. Commun.* **2001**, *3*, 102-106.

Chapter 4 $[MO(OH_2)(WO(OH_2))_2(PW_9O_{34})_2]$ (M = Pd or Au)

Terminal Palladium and Gold Oxo Units Coordinated in The Monovacant Clam Shell Like Polytungstate Ligand: $[MO(OH_2)P_2W_{20}O_{70}(OH_2)_2]^{8-/9-}$ (M = Pd or Au)

Published in part in *J. Am. Chem. Soc.* **2007**, *129*, 11118-11133

with Travis M. Anderson, Paula M. B. Piccoli, Arthur J. Schultz, Thomas F. Koetzle, Yurii V. Geletii, Elena Slonkina, Britt Hedman, Keith O. Hodgson, Kenneth I. Hardcastle, Xikui Fang, Martin L. Kirk, Sushilla Knottenbelt, Paul Kögerler, Djamaladdin G. Musaev, Keiji Morokuma, Masashi Takahashi, and Craig L. Hill

4.1 Abstract

Two terminal noble metal-oxo molecular complexes have been synthesized by using the stabilizing monovacant polytungstate ligand $K_{10}[P_2W_{20}O_{70}(OH_2)_2]\bullet 22H_2O$ (**P_2W_{20}**). Reaction of $PdSO_4$ produces $K_8[PdO(OH_2)P_2W_{20}O_{70}(OH_2)_2]\bullet 22H_2O$ (**4**); reaction of $AuCl_3$ produces $K_7H_2[AuO(OH_2)P_2W_{20}O_{70}(OH_2)_2]\bullet 27H_2O$ (**5**). Both complex **4** and **5** crystallizes in hexagonal system, and the crystallographic structure of **5** can be solved in *P6(3)/mmc* space group, with a = 16.1730(9) Å, b = 16.1730(9) Å, c = 19.7659(15) Å, V = 4477.4(5) Å^3, Z = 2 (final R = 0.0634). Very short Au-oxo (~1.76 Å) and Pd-oxo (~1.70 Å) distances are established by X-ray and extended X-ray absorption fine structure method, respectively. Seven findings clarify that Pd/Au and not W is present in the noble metal-oxo position in **4** and **5**. Five lines of evidence are consistent with the presence of d^8 Au(III) centers that are stabilized by the flanking polytungstate ligands in both **5**: redox titrations, electrochemical measurements, 17 K optical spectra, Au L_2 edge X-ray absorption spectroscopy, and Au-oxo bond distances. Variable-temperature magnetic susceptibility data for crystalline **4** and **5** establish that both solids are diamagnetic, and ^{31}P and ^{17}O NMR spectroscopy confirm that both remain diamagnetic in solution. Both complexes have been further characterized by FT-IR, thermogravimetric analysis (TGA), differential scanning calorimetry (DSC), and many other techniques.

4.2 Introduction

Terminal metal-oxo complexes of the late-transition-metal elements have long been proposed and sought experimentally but only realized recently,[1-9] although several reviews of mid-transition-metal oxo and related compounds and their chemistry from a range of perspectives address fundamental issues of these units in chemical bonding, challenges in synthetic coordination chemistry, core reactivities of the highly oxidized forms of these elements, including oxo transfer, and the roles of such species in both homogeneous and heterogeneous catalytic oxidation processes.[1-6,10-22] Recent reports of terminal sulfido (S^{2-}),[23] imido (NR^{2-}),[24-26] phosphinidene (PR^{2-}),[27] carbene (CR_2^{2-})[28,29] and nitrido (N^{3-})[30] complexes of the late-transition-metal elements have advanced our understanding of the stability and reactivity of these multiply bonded ligands and complexes. Terminal metal-oxo (O^{2-}) complexes of these elements are particularly problematical to prepare and investigate because the mismatch of metal and ligand atom (oxygen) electronegativities and orbital energies are maximal and consequent orbital overlaps and thus metal-ligand bond energies are minimal. Furthermore, high d-electron configurations are particularly antibonding in terminal metal-oxo species, and the number of d electrons necessarily increases as one moves from left to right across the periodic table.[1,3,4]

Major interest in the terminal metal-oxo species of the noble and coinage metal elements including Pd, Pt, Ag, and Au derives from that fact that these elements, particularly as supported on redox-active metal oxides such as titania and ceria, constitute some of the most technologically and economically significant O_2 (or air)-based catalytic processes at present. Supported Pt and Pd are the operating core of nearly all automobile

catalytic converters, the lead materials for fuel cell cathodes, and the key catalysts for O_2 (or air)-based oxidations central to much green oxidation chemistry.[31-34] Supported Pd-Au materials (nanoclusters and others) are the principal catalysts for current industrial processes including vinyl acetate monomer (VAM) synthesis.[34-36] Supported Au materials have been under intense investigation as low-temperature catalysts for oxidation of CO and other reactants,[37-41] and supported Ag materials are the catalysts for industrial O_2-based ethylene oxidation (ethylene oxide technology).[42-44]

Polyoxometalates (POMs)[45-49] including polytungstate, polymolybdate and polyvanadate units share many of the characteristics of ceria and titania including facile and reversible redox chemistry and in some cases metal-based (metal-oxide unit based) orbitals that are not unlike those on ceria or titania surfaces. Using appropriate polytungstate ligands we were above to prepare and characterize a Pt^{IV}-oxo complex, $K_7Na_9[Pt^{IV}O(OH_2)(PW_9O_{34})_2]$ (**1**),[7] the first terminal metal-oxo complex of an element in columns 10-12 of the periodic table. Subsequently, using a more stable and sterically protecting polytungstate ligand system, we were able to prepare and characterize a Pd(IV)-oxo complex, $K_{10}Na_3[Pd^{IV}O(OH)WO(OH_2)(PW_9O_{34})_2]$ (**3**).[8] Formation of both these complexes requires O_2; the syntheses conducted under inert atmospheres (N_2 or Ar) produce only conventional (square planar, d^8) Pt or Pd complexes with polytungstate ligands.[7] The unprecedented nature of these high-d-electron-count late-transition-metal oxo complexes (d^6), compelled us to go to unusual lengths to verify our physical and electronic structural assignments including the use of multiple single crystal X-ray structure data sets down to liquid He temperatures, neutron diffraction data and EXAFS, ultra-low-temperature optical spectra, ^{17}O NMR spectra and several other methods.

Importantly, our recent work indicate that extra $[O=W^{VI}(OH_2)]^{4+}$ linkages between the two $[A\text{-}\alpha\text{-}PW_9O_{34}]^{9-}$ ligands can increase the stability of the whole structure by not only increased structural rigidity but also decreased negative charge on the polyanion unit.[8] We now report here the preparation of a third class of late-transition-metal oxo complexes using a new type of polytungstate ligand, $[P_2W_{20}O_{70}(OH_2)_2]^{10-}$.[9] Both complexes, $K_8[Pd^{IV}O(OH_2)P_2W_{20}O_{70}(OH_2)_2]$ (**4**) and $K_7H_2[Au^{III}O(OH_2)P_2W_{20}O_{70}(OH_2)_2]$ (**5**), are more stable in solution than previously documented Pt-oxo **1** and Au-oxo **2** and more amenable to solution reactivity studies than the first Pd-oxo **3**. The electronic and physical properties of **4** and **5** have been investigated experimentally, and oxo transfer from the noble metal center to organic molecules, the first reactivity reported for a late-transition-metal oxo compound, is addressed in the following reactivity section.

4.3 Experimental Section

General Methods and Materials

$K_{14}[P_2W_{19}O_{69}(OH_2)]\bullet 24H_2O$ (**P_2W_{19}**),[50] $K_{10}[P_2W_{20}O_{70}(OH_2)_2]\bullet 22H_2O$ (**P_2W_{20}**)[51] and $K_4H_2[P_2W_{21}O_{71}(OH_2)_3]\bullet 28H_2O$ (**P_2W_{21}**)[52] were synthesized using published procedures. Their purities were confirmed by both IR and ^{31}P NMR. Palladium sulfate dihydrate ($PdSO_4\bullet 2H_2O$) and gold chloride ($AuCl_3$) were purchased from Alfa Aesar, and were used without further purification. Infrared spectra (2% sample in KBr) were recorded on a Thermo Nicolet 6700 instrument. Ambient temperature electronic absorption spectra were acquired using a diode-array Hewlett-Packard 8452A

spectrophotometer (aqueous solution) equipped with a magnetic stirrer and temperature controller (HP 89090A) and a Hitachi U-3501 UV-Vis-NIR spectrophotometer using a double-beam configuration at 2.0 nm resolution (butyronitrile solution). ^{31}P NMR measurements were made on a Varian INOVA 400 MHz spectrometer, and peaks were referenced to 85% H_3PO_4. Room-temperature magnetic susceptibilities were measured on a Johnson-Matthey Model MSB-1 magnetic susceptibility balance as neat powders at 24 °C; the balance was calibrated using $Hg[Co(SCN)_4]$ as a standard. Pascal's constants were used to obtain the final diamagnetic corrections. Temperature-dependent magnetic measurements were performed at 0.1 and 1.0 Tesla using a Quantum Design MPMS-5 SQUID magnetometer and employing approximately 80-90 mg of each sample in a cylindrical PTFE-sealed sample holder. Differential scanning calorimetric and thermogravimetric data were collected on Instrument Specialists Incorporated DSC 550 and TGA 1000 instruments, respectively. Electrochemical data were obtained using a BAS CV-50W instrument (Bioanalytical System, Inc., USA). Elemental analyses of K, P, Pd, Au, and W were performed by Desert Analytics (Tucson, Arizona), Kanti Labs (Mississauga, Canada) and Galbraith Laboratories Inc. (Knoxville, Tennessee). The ^{197}Au Mössbauer spectroscopy (200 mg sample) measured at 12 K for a week was unsuccessful (showed no signal) because of interference from the tungsten atoms present. The same problem has been documented in attempting to acquire ^{57}Fe Mössbauer spectra of iron-containing polytungstates.[53,54]

Synthesis of $K_8[Pd^{IV}O(OH_2)P_2W_{20}O_{70}(OH_2)_2]\bullet 22H_2O$ (4)

A 1.00 g (0.176 mmol) sample of $K_{10}[P_2W_{20}(OH_2)_2O_{70}]\bullet 22H_2O$ is dissolved in 5 mL of de-ionized water at room temperature, and 0.046 g (0.194 mmol) of palladium sulfate dihydrate ($PdSO_4\bullet 2H_2O$) is added to the clear, colorless solution with stirring. The dark brown mixture is heated at 55 °C for 1 h, cooled to room temperature, and filtered with VWR 410 qualitative filter paper (diameter 9.0 cm) within 24 h. The large, dark brown crystals of **4** normally appear in 2 days if the solution is allowed to stand in air at room temperature (0.80 g, 79% yield based on W). The crystals are filtered and dried in air. Analytical data: IR (2% KBr pellet, 1200 - 400 cm^{-1}): 1096 (s), 1086 (s, sh), 1031 (m), 961 (s), 937 (m), 768 (m), 715 (m), 629 (m), 525 (m), and 447 (m). ^{31}P NMR (5 mM solution in D_2O): -12.8 ppm ($\Delta\nu_{1/2}$ = 5 Hz). Electronic spectral data (400 - 800 nm, in H_2O (3.6 mM sample, 1 cm cell path length)) [λ, nm (ε, M^{-1} cm^{-1})]: 452 nm (114) and 514 nm (sh, 48). Anal. Calcd. for $K_8[PdO(OH_2)P_2W_{20}O_{70}(OH_2)_2]\bullet 22H_2O$: K, 5.44; ($OH_2$), 6.89; P, 1.08; Pd, 1.85; W, 64.0. Found: K, 5.3; (OH_2), 6.85; P, 0.97; Pd, 1.7; W, 64.1. [MW = 5744 g/mol] An organic soluble form, the tetra-*n*-butylammonium (TBA) salt, of **4a** (the polyanion of **4**), was made as follows: a 0.2 g (0.035 mmol) sample of **4** was dissolved in 2 mL of water as well as a solution of 0.086 g $[CH_3(CH_2)_3]_4NBr$ (Tetra-*n*-butylammonium bromide, 0.267 mmol) in 20 mL CH_2Cl_2 with vigorous stirring for 2 min. Upon standing, the mixture separated into a clean red-brown organic layer and a clean colorless aqueous layer. The organic layer was separated and filtered using a fine filter paper, and then was rotovapped to dryness at room temperature. The resulting red-brown solid was a pure sample of tetra-*n*-butylammonium salt of **4** (the purity was

checked by ^{31}P NMR which has one peak at -13.5 ppm in 0.5 mL $CH_3CN/CDCl_3$ solvent).

Synthesis of $K_7H_2[Au^{III}O(OH_2)P_2W_{20}O_{70}(OH_2)_2]\bullet 27H_2O$ (5)

A 1.00 g (0.176 mmol) sample of $K_{10}[P_2W_{20}(OH_2)_2O_{70}]\bullet 22H_2O$ was dissolved in 5 mL of de-ionized water at room temperature, and 0.27 g (0.890 mmol) of gold chloride ($AuCl_3$) was added to the clear, colorless solution with stirring. The red-orange mixture was stirred at 55 °C for about 2 h and gradually turned dark red over this period. The hot solution was cooled to room temperature, and then filtered through VWR 410 qualitative filter paper (porosity 0.45 μm). The large, red crystals of **5** normally appear in 2 d if the solution is allowed to stand in air at room temperature (0.80 g, yield 78%, based on P). The crystals were removed from the solution by filtration and dried under suction for 12 h. Analytical data: IR (2% KBr pellet, 1300 - 400 cm^{-1}): 1089 (s), 1032 (s), 963 (s), 942 (m), 855 (sh), 755 (s), 698 (m), 660 (sh), 602 (sh), 525 (m). ^{31}P NMR (10 mM solution in D_2O): -13.15 ppm ($\Delta\nu_{1/2}$ = 8 Hz). Electronic spectral data (400 - 800 nm, in H_2O (1.65 mM sample, 1 cm cell pathlength)) [λ, nm (ε, M^{-1} cm^{-1})]: 402 nm (485) and 428 nm (295). Magnetic susceptibility (0.1 and 1.0 Tesla; 2 - 290 K): diamagnetic. Anal. Calcd. for $K_7H_2[Au(O)(OH_2)P_2W_{20}O_{70}(OH_2)_2]\bullet 27H_2O$: K, 4.6; P, 1.0; Au, 3.3; W, 62.5. Found: K, 4.5; P, 1.0; Au, 3.2; W, 61.9. [MW = 5888 g/mol] An organic soluble form, the K⊂*cis*-dicyclohexano-18-crown-6 salt, of **5a** (the polyanion of **5**) was made by adding 5 equivalents of *cis*-dicyclohexano-18-crown-6 to an acetonitrile solution of **5**. ^{31}P NMR confirmed that treatment with *cis*-dicyclohexano-18-crown-6 produced no detectable

decomposition of the polyanion (-15.5 ppm), and thus this hydrophobic salt was used directly in ^{17}O NMR experiments including oxo transfer reactivity.

X-ray Crystallographic Studies

The complete datasets for **4**, **5** and **P_2W_{20}** were collected at Emory University. Single crystals of $K_8[PdO(OH_2)P_2W_{20}O_{70}(OH_2)_2]\bullet 22H_2O$ (**4**), $K_7H_2[AuO(OH_2)P_2W_{20}O_{70}(OH_2)_2]\bullet 27H_2O$ (**5**) and $K_{10}[P_2W_{20}O_{70}(OH_2)_2]\bullet 22H_2O$ (**P_2W_{20}**) suitable for X-ray analysis, were each coated with Paratone-N oil, suspended in a small fiber loop, and placed in a cooled gas stream on a Bruker D8 SMART APEX CCD sealed tube diffractometer. Diffraction intensities were measured using graphite monochromated Mo Kα radiation (λ = 0.71073 Å) at 173(2) K and a combination of φ and ω scans with 10 s frames traversing about ω at 0.3° increments. Data collection, indexing, and initial cell refinements were carried out using SMART;[55] frame integration and final cell refinements were done using SAINT.[56] The molecular structure of each complex was determined using Direct Methods and Fourier techniques and refined by full-matrix least squares.[57] A multiple absorption correction for each dataset at 173(2) K was applied using the program SADABS.[58] The largest residual electron density for structures **5** and **P_2W_{20}** was located close to (less than 1.0 Å from) the W, Au, and K atoms and was most likely due to imperfect absorption corrections frequently encountered in heavy-metal atom structures.

Refinement details. The structure of **5** and **P_2W_{20}** were solved using Direct Methods and difference Fourier techniques.[57] The K, P, W, Au atoms were refined anisotropically. Some of the potassium ions and solvent water molecules were refined

with partial occupancies; not all the countercations and solvent water molecules could be located in difference Fourier maps because of disorder. Scattering factors and anomalous dispersion corrections are taken from the *International Tables for X-ray Crystallography*. Structure solution, refinement, graphic and generation of publication materials were performed by using SHELXTL, V6.14 software.

X-ray Absorption Spectroscopy Studies

EXAFS Studies of 4. A 150 mg crystalline sample of **4** was finely ground, and the resultant powder was pressed into a 1 mm thick aluminum spacer with X-ray transparent kapton windows. The Pd *K*-edge X-ray absorption spectra for **4** were measured at the Stanford Synchrotron Radiation Laboratory (SSRL) on focused (Rh-coated toroid) 30-pole wiggler beam line 10-2 with the ring operating at 3 GeV, 85-100 mA. A liquid nitrogen cooled Si(220) monochromator was utilized for energy selection at the Pd *K*-edge. The monochromator was detuned 30% at 25345 eV to minimize higher harmonic components in the X-ray beam. Data were collected in transmission mode, and internal energy calibration was performed by simultaneous measurement of the absorption of a Pd foil placed between two ionization chambers located after the sample. The first inflection point of the foil was assigned to 24349.0 eV. The sample was maintained at 10 K using an Oxford Instruments CF1208 continuous flow liquid helium cryostat. Three scans of the energy range 24020 – 25345 eV were collected and averaged. The averaged data were processed by fitting a first-order polynomial to the pre-edge region and subtracting this background from the entire spectrum. A three-region spline of orders 2, 3, and 3 was used to model the smooth background above the edge.

Theoretical EXAFS signals were calculated using FEFF (version 7.02),[59] and refinements of the structural model to the data were done by a non-linear least-squares fitting process in *k*-space using EXAFSPAK. Atom coordinates for the initial model were obtained from the crystallographic structure of **3**. The experimental energy threshold E_0 was chosen as 24370 eV and was allowed to vary by a common amount (ΔE_0) for all components within a given fit. The structural parameters that were varied during the refinements included the bond distance (R) and the bond variance (σ^2).

XAS Studies of 5. Sample was prepared as finely ground solids in boron nitride, pressed into a pellet, and sealed between 38 μm Kapton tape windows in a 1-mm thick aluminum spacer. The X-ray absorption spectra were measured at the Stanford Synchrotron Radiation Laboratory (SSRL) on the unfocused bend magnet beam line 2-3 for Au(III) samples, and the wiggler beam line 9-3 for Au(I) samples, with the ring operating at 3 GeV, 85-100 mA. A water-cooled (beam line 2-3) and liquid-nitrogen cooled (beam line 9-3) Si(220) monochromator was utilized for energy selection at the Au L_2 edge. At beam line 2-3, the monochromator was detuned 50% at 14340 eV to minimize higher harmonic components in the X-ray beam. At beam line 9-3, a collimating pre-monochromator mirror was used for harmonic rejection with the monochromator fully tuned. The data were measured in transmission mode for gold(III) acetate, gold(I) potassium cyanide, and gold(I) sodium thiosulfate, and in fluorescence mode for gold-containing polyoxometalate samples, using a Canberra 13-element solid-state germanium detector. For transmission measurements, the internal energy calibration were performed by simultaneous measurement of the absorption of a reference Au foil placed between two ionization chambers located after the sample. For

fluorescence data, the spectrum of the Au foil was collected between the data scans. The first inflection point of the foil was assigned to 13734.0 eV. The sample was maintained at 12 K using an Oxford Instruments CF1208 continuous-flow liquid helium cryostat. A total of 2-6 scans to a *k* value of 9.5-12.5 $Å^{-1}$ were collected for each sample. The edge features were monitored for photoreduction; no change was observed in any of the samples. The data were normalized using the program XFIT[60] by first subtracting a polynomial background absorbance that was fit to the pre-edge region and extended over the post-edge with control points, followed by fitting a two-region polynomial spline of orders 2 and 3 over the post-edge region. The data were normalized to an edge jump of 1.0 between the background and spline curves at 13750.0 eV.

Ultra-Low-Temperature Electronic Absorption Spectroscopy

These spectra were collected using a Janis STVP-100 continuous flow cryostat mounted in a custom designed cradle assembly, and the sample temperature was monitored with a Lakeshore silicon-diode (PT-470). The sample was dissolved in a 1:3 water:glycerol mixture in order to obtain a good optical glass. The resulting solution was injected through a rubber gasket spacer (approximately 1 mm thick) between two 1-mm thick Infrasil quartz discs in a custom designed sample holder. Gaussian resolution of spectral bands was accomplished using GRAMS AI software.

pH Dependent UV-vis and ^{31}P NMR Titrations

The pH titrations of **4** were performed on 3.6 mM solution (0.2079 g sample of **4** dissolved in 10 mL of deuterium water). The initial pH is 4.3 (the natural pH of **4**). The pH was lowered to 1.0 by the dropwise addition of 0.1 M HCl and then increased again to the initial values by dropwise addition of 0.1 M NaOH. UV-vis and ^{31}P NMR spectra were taken at each *ca.* 0.5 pH change.

The pH titrations of **5** were performed in two opposite directions. (1) A 0.2082 g sample of **5** was dissolved in 10 mL of de-ionized water (3.54 mM, the initial pH was 2.95). The pH was lowered to 0.38 by dropwise addition of 0.1 M HCl and then increased again to the initial value by dropwise addition of 0.1 M NaOH. (2) A 0.1059 g sample of **5** was dissolved in 10 mL of de-ionized water (1.80 mM, the initial pH was 3.21). The pH was increased to 7.53 by dropwise addition of 0.1 M NaOH and then lowered again to the initial value by dropwise addition of 0.1 M HCl. UV-vis spectra were taken after each change of pH by *ca.* 0.25 unit.

Electrochemistry

Cyclic voltammograms (CV) were obtained at room temperature with scan rates in the range 2-100 mV/s. All reduction potentials are given versus Ag/AgCl (3 M NaCl) reference electrode ($E_{NHE} = E_{Ag/AgCl} + 0.250$ V at 25 °C). A coiled Pt-wire was used as an auxiliary electrode. A glassy carbon working electrode was always polished with alumina (Polishing Alumina Fluid, purchased from Bioanalytical Systems, Inc., USA) before use unless otherwise specified. Bulk electrolysis was performed under argon on a reticulated vitreous carbon working electrode with a coiled Pt-wire as an auxiliary

electrode within a fritted glass isolated chamber. Vigorous agitation was provided by a magnetic stirrer and by the passing of argon as a purging gas. Air was rigorously excluded at all times. The total coulombs passed were monitored continuously. All details are described in the previous sections.

Chemical Titrations

Syntheses of α-$K_4[SiW_{12}O_{40}]$[61] and α-$Na_5[AlW_{12}O_{40}]$[62-64] were described in the literature. Solutions of their 1-electron reduced forms, $[SiW_{12}O_{40}]^{5-}$ and $[AlW_{12}O_{40}]^{6-}$, (henceforth POM_{red}) were obtained by electrochemical reduction of $[SiW_{12}O_{40}]^{4-}$ and $[AlW_{12}O_{40}]^{5-}$ at controlled potentials.[65] The concentrations of the reduced forms of $[SiW_{12}O_{40}]^{5-}$ and $[AlW_{12}O_{40}]^{6-}$ were determined from the absorbance at 500 nm ($\varepsilon = 8.9 \times 10^2$ and 9.7×10^2 $M^{-1}cm^{-1}$, respectively). The solutions of the reduced complexes were stable under argon. The potentiometric titration was carried out under argon using a platinum VWR® sympHony combination redox electrode. The readings of this electrode are versus SCE. In a typical experimental procedure the redox potential of $[SiW_{12}O_{40}]^{4-}$ (or $[AlW_{12}O_{40}]^{5-}$) solution was measured as a function of the total amount of Au species added in small increments. All manipulations were carried out under argon in thoroughly deaerated solutions. The data were plotted as dependence of redox potential versus $(Au)/(POM_{red})_o$, where (Au) is the total amount of Au-complex added in mmol, and $(POM_{red})_o$ is the initial amount of POM_{red} in mmol.

The stoichiometry of the reaction of **5** with 2,2'-azino-bis(3-ethyl benzothiazoline-6-sulfonic acid) ($ABTS^{2-}$) (ammonium salt, Aldrich, 98%) or $[Fe^{II}(CN)_6]^{4-}$ (potassium salt, Aldrich, 99%) were determined as follows: 0.05 mL of 1 mM **5** was added to 2.45

mL of 2 mM $ABTS^{2-}$ in 50 mM sodium chloroacetate buffer. The yields of reaction products, [$ABTS^{\bullet-}$], were quantified 2-3 min after mixing from the absorbances at 645 and 660 nm ($\varepsilon_{645} = 1.35 \times 10^4$ and $\varepsilon_{660} = 1.2 \times 10^4$ $M^{-1}cm^{-1}$);[66,67] an average value of the two numbers was used. A similar procedure was applied to determine the yield of $[Fe^{III}(CN)_6]^{3-}$: compound **5** (final concentrations 0.2 mM) was added to 4.5 mM $[Fe^{II}(CN)_6]^{4-}$ in 50 mM sodium chloroacetate buffer (pH 3) or in 50 mM sodium phosphate buffer (pH 7.2). The $[Fe^{III}(CN)_6]^{3-}$ product was quantified in 2-3 min after mixing from the absorbance at 420 nm ($\varepsilon_{420} = 1.02 \times 10^3$ $M^{-1}cm^{-1}$).

A similar technique was used in an attempt to determine the reaction stoichiometry of **5** reduction by $[SiW_{12}O_{40}]^{5-}$ using electronic absorption spectroscopy: **5** was mixed with a slight excess of $[SiW_{12}O_{40}]^{5-}$ and the amount of $[SiW_{12}O_{40}]^{5-}$ consumed was determined from the decrease in absorbance at 740 nm ($\varepsilon_{740} = 1.53 \times 10^3$ $M^{-1}cm^{-1}$). However, this technique resulted in irreproducible data due to a formation of unstable Au(0) particles with a relatively high absorbance at 740 nm (which also changed in time). All manipulations described above were carried out under argon with meticulous exclusion of air.

^{17}O NMR Studies

General methods and materials. ^{17}O NMR spectra were acquired at 81.291 MHz on a Varian UNITY 600 spectrometer. The spectrometer was locked on the ^2H resonance of $CDCl_3$, and all chemical shifts were reported relative to D_2O ($\delta = 0$ ppm). Spectral parameters for ^{17}O NMR were the following: pulse width, 10 μs; sweep width, 100,000 Hz; 0.01 s delay; 100,000 transients; 40,000 data points. Spectra were obtained using

cylindrical 5-mm o.d. sample tubes (7 in). All samples were dissolved in 50:50 (v:v) CH_3CN-$CDCl_3$ mixture solvent at room temperature. ^{17}O-enriched water (10% $H_2{}^{17}O$) was purchased from Cambridge Isotope Laboratories, and was used without further purification. Tetra-*n*-butylammonium (TBA) chloride and *cis*-dicyclohexano-18-crown-6 were purchased from Aldrich, and were used without further purification.

^{17}O enrichment of $K_8[PdO(OH_2)P_2W_{20}O_{70}(OH_2)_2]\cdot 22H_2O$ (4). The preparation of an organic soluble salt of **4a**, polyanion of **4**, was described above. An exemplary procedure is as follows: a 0.2 g (0.035 mmol) sample of **4** was dissolved in 0.2 mL of 10% ^{17}O-enriched water at 50 ^oC and aged for 2 days. This solution was then mixed with 2 mL of water as well as a solution of 0.086 g $[CH_3(CH_2)_3]_4NBr$ (Tetra-*n*-butylammonium bromide, 0.267 mmol) in 20 mL CH_2Cl_2 with vigorous stirring for 2 min. Upon standing, the mixture separated into a clean red-brown organic layer and a clean colorless aqueous layer. The organic layer was separated and filtered using a fine filter paper, and then was rotovapped to dryness at room temperature. The resulting red-brown solid was a pure sample of tetra-*n*-butylammonium salt of **4** (the purity was checked by ^{31}P NMR which has one peak at -13.5 ppm in 0.5 mL $CH_3CN/CDCl_3$ solvent).

^{17}O enrichment of $K_7H_2[AuO(OH_2)P_2W_{20}O_{70}(OH_2)_2]\cdot 27H_2O$ (5). Two methods were used to obtain ^{17}O-enriched **5** in an organic solvent. Method (1): a 0.20 g (0.036 mmol) sample of **5** was dissolved in 0.30 mL of 10% ^{17}O-enriched water and incubated at 50 °C for 2 d. This solution was then concentrated to dryness at room temperature using a rotary evaporator. A 0.067 g (0.18 mmol) sample of *cis*-dicyclohexano-18-crown-6 was added to the dried solids of **5**, and the mixture was redissolved in 0.5 mL

$CH_3CN/CDCl_3$ at room temperature. The purity was checked by ^{31}P NMR; the spectrum had only one peak at -15.5 ppm. Method (2): a 0.20 g (0.036 mmol) sample of **5** was dissolved at room temperature in 2.0 mL of CH_3CN containing 0.067 g (0.18 mmol) of *cis*-dicyclohexano-18-crown-6, and then 0.20 mL of 10% ^{17}O-enriched water was added. The mixture was incubated at room temperature for 2 d. This solution was then concentrated to dryness at room temperature, affording the K⊂*cis*-dicyclohexano-18-crown-6 salt of **5**. The dried solid was redissolved in 0.5 mL of $CH_3CN/CDCl_3$, and its purity was checked by ^{31}P NMR; the spectrum had only one peak at -15.5 ppm.

4.4 Results and Discussion

Synthesis

Previously we reported that Pd(II) reacts with $Na_9[A\text{-}\alpha\text{-}PW_9O_{34}]$ in pure water to yield a co-crystalline mixture of $[Pd^{II}(PW_9O_{34})_2]^{16-}$ and $[P_2W_{19}O_{69}(OH_2)]^{14-}$.[7] However, if this synthesis is performed in 0.25 M sodium acetate/0.25 M acetic acid buffer to control the pH and ionic strength, then $[Pd^{IV}O(OH)WO(OH_2)(PW_9O_{34})_2]^{13-}$ forms in solution and the $K_{10}Na_3$ salt of this complex forms diffraction quality crystals of **3**.[8] Studies of this unconventional late-transition-metal oxo (LTMO) complex in solution by ^{31}P NMR, ^{17}O NMR, UV-vis, and cyclic voltammetry are all consistent and all suggest that the presence of the nineteenth W atom, which fuses two $[A\text{-}\alpha\text{-}PW_9O_{34}]^{9-}$ ligands together, adds considerable stability to the complex. In other words the LTMO complexes with one bridge between the two $[A\text{-}PW_9O_{34}]^{9-}$ units, as exemplified by the

initial platinum and gold LTMO complexes, $K_7Na_9[Pt^{IV}O(OH_2)(PW_9O_{34})_2]$ (**1**) and $K_{15}H_2[Au^{III}O(OH_2)(PW_9O_{34})_2]$ (**2**), are less stable than those with two bridges between the two $[A\text{-}PW_9O_{34}]^{9-}$ units, as exemplified by the subsequently reported palladium LTMO complex, $K_{10}Na_3[Pd^{IV}O(OH)WO(OH_2)(PW_9O_{34})_2]$ (**3**). By obvious extension, we reasoned that the monovacant phosphotungstate ligand, $[P_2W_{20}O_{70}(OH_2)_2]^{10-}$, might also prove to be a good ligand system that would insure a similar geometrical and electronic structural environment for noble metals to that experienced in **1-3** (high-d-electron count M=O centers are stabilized by π-accepting ligands) yet simultaneously provide much greater hydrolytic stability than that afforded by the $[A\text{-}PW_9O_{34}]^{9-}$ ligands alone in **1** and **2**. This monovacant, clam-shell-like polyanion, $\mathbf{P_2W_{20}}$, has two $[(H_2O)W{=}O]^{4+}$ units bridging the two $[A\text{-}PW_9O_{34}]^{9-}$ moieties and provides the most hydrolytically stable late-transition metal oxo complexes to date. Reaction of Pd(II) with $[P_2W_{20}O_{70}(OH_2)_2]^{10-}$ in a 1.1:1 ratio (respectively), followed by air oxidation, leads to the formation of $K_8[PdO(OH_2)P_2W_{20}O_{70}(OH_2)_2]\bullet 22H_2O$ (**4**). The reaction was closely monitored by ^{31}P NMR and **4** was the only product detected in the synthesis. Similarly, reaction of $AuCl_3$ with $\mathbf{P_2W_{20}}$ (molar ratio, 5:1) in water at 55 °C results in a dark red solution, which on cooling, affords red crystals of $K_7H_2[Au(O)(OH_2)P_2W_{20}O_{70}(OH_2)_2]\bullet 27H_2O$ (**5**) in 78% yield, a Au-oxo complex that is stable in aqueous solution at autogenous pH and in the absence of reducing agents.

Magnetism of Au LTMO complexes, 2 and 5

Variable-temperature measurements of the magnetic susceptibility at 0.1 and 1.0 Tesla between 2 and 290 K indicated temperature-independent diamagnetism, i.e. flat χ

vs. T curves, for both **2** ($\chi_{dia/TIP}$(**2**) = -10.2 × 10^{-4} emu mol^{-1}) and **5** ($\chi_{dia/TIP}$(**5**) = -9.8 × 10^{-4} emu mol^{-1}). These numbers compare well to the corresponding non-functionalized isopolytungstate cluster compounds $\mathbf{P_2W_{19}}$ ($\chi_{dia/TIP}$($\mathbf{P_2W_{19}}$) = -10.0 × 10^{-4} emu mol^{-1}) and $\mathbf{P_2W_{21}}$ ($\chi_{dia/TIP}$($\mathbf{P_2W_{21}}$) = -9.5 × 10^{-4} emu mol^{-1}) if differences in the numbers of potassium cations and crystal water molecules are taken into account. Molar diamagnetic susceptibilities for $\mathbf{P_2W_{19}}$ and $\mathbf{P_2W_{21}}$ have been established for the same conditions. The substitution of a $W^{VI}(O)(OH_2)$ group in $\mathbf{P_2W_{19}}$ and $\mathbf{P_2W_{21}}$ by a $Au^{III}(O)(OH_2)$ group in **2** and **5** causes a slight increase in the absolute values, part of which is attributable to an increase in the number of counter cations. Note that temperature-independent paramagnetic (TIP) contributions are significant for all polyoxotungstates; corresponding diamagnetic values for compounds **2**, **5**, $\mathbf{P_2W_{19}}$ and $\mathbf{P_2W_{21}}$ calculated from tabulated Pascal constants would greatly overestimate the actual experimental susceptibilities.

X-ray Crystallographic Studies

X-ray single crystal diffraction method is applied on the crystals of both **4** and **5**. Unfortunately, the polyanion units of both, $[PdO(OH_2)P_2W_{20}O_{70}(OH_2)_2]^{8-}$ (**4a**) and $[AuO(OH_2)P_2W_{20}O_{70}(OH_2)_2]^{9-}$ (**5a**) are disordered. However this type of disorder (about the C_3 axis resulting in crystallographically imposed D_{3h} symmetry on the C_{2v} molecule), has been noted in the isostructural all-tungsten complex $[P_2W_{21}O_{71}(OH_2)_3]^{6-}$ in which the $O=M(OH_2)$ (M = Pd or Au) is replaced by $O=W(OH_2)$,[52] and it can be well modeled. Polyanion **5a** has C_{2v} symmetry and crystallizes in the hexagonal space group $P6_3/mmc$. The site symmetry of the P atoms is $3m$ (C_{3v}), imposing the principle 3-fold axis (vertical) on the crystal structure. In addition, all atoms on the equatorial plane

(including W, Au and their terminal oxo and aqua groups) sit on the *mm* symmetry sites; therefore, the anion exhibits a crystallographically imposed D_{3h} symmetry overall. The consequence of this imposed symmetry is an overall apparent disorder in the equatorial plane of the anion. The two W atoms on the equatorial plane, as well as their outward-oriented aqua ligands and inward-oriented oxo groups, are evenly split on the three interior *mm* sites (ideal site-occupancy factor 2/3). On the other hand, the Au atom, along with its external (outward directed) oxo and inward directed aqua group, is disordered over the three exterior *mm* sites (ideal site-occupancy factor 1/3). The refined site-occupancy factor is approximately 65:35 for W and Au, respectively, rather than 67:33. This result suggests that a few of the tungsten sites are vacant in the crystal resulting in a slightly higher weight for Au occupancy. This disorder model (on the initial polytungstate, $[P_2W_{21}O_{71}(OH_2)_3]^{6-}$) was revealed in part by careful ^{183}W NMR work by Tourné and co-workers.[52] One test of the validity of the disorder model is that all the key distances in **5a** including Au-O_{oxo}, Au-OH_2 (aqua ligand *trans* to oxo ligand), Au-OW (Au-O bonds in the equatorial plane), and Au-C_t (displacement of Au out of the mean equatorial O_4 plane toward the terminal oxo group) are almost identical within experimental error to those in triply determined disorder-free structure of **2** (Au-O distances for both compounds are given in the **Figure 4.1** caption), indicating nearly identical Au(O)(OH_2)(O-W)$_4$ coordination spheres in both structures. Crystal data and refinement parameters for the X-ray structures of **5** and **P_2W_{20}** are summarized in **Table 4.1**.

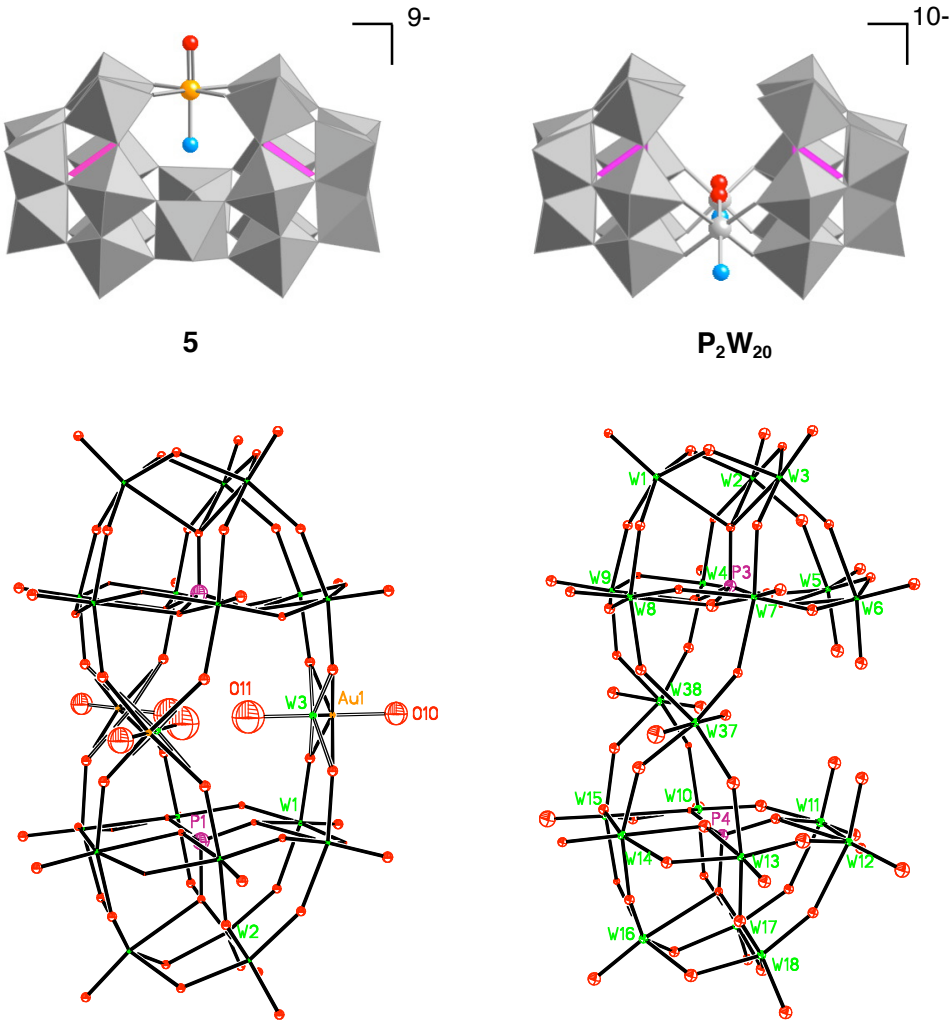

Figure 4.1 Combination polyhedral/ball-and-stick representations of polyanions **5** (top left) and $[P_2W_{20}O_{70}(H_2O)_2]^{10-}$ (**P_2W_{20}**, top right), the stabilizing ligand of **5**. Thermal ellipsoid plots and numbering scheme for polyanions **5** (bottom left) and **P_2W_{20}** (bottom right). The WO_6 (or W atom) and PO_4 polyhedra are shown in gray and pink. The Au, O atoms and aqua (H_2O) ligands are shown in yellow, red, and blue, respectively. The coordination sphere around the Au atom in **5** (Au-O_{oxo}, 1.77(4) Å; Au-OH_2, 2.32(6) Å; doming distance of the Au atom, 0.32(1) Å) is almost identical to that triply determined, disorder free structures of Au-oxo complex **2** (a short Au-O_{oxo} (1.763(17) Å) bond is

trans to a longer Au-OH_2 (2.29(4) Å) bond, and the central Au atom is displaced out of the equatorial O_4 plane toward the terminal oxo by 0.31(1) Å). The two tungsten units linking the two [A-α-PW_9O_{34}]$^{9-}$ units in **P_2W_{20}** are shown in ball-and-stick notation. The short, inward-oriented W-O_{oxo} (1.696(13), 1.701(14) Å) bonds in **P_2W_{20}** are *trans* to the longer, outward-oriented W-OH_2 (2.265(15), 2.306(14) Å) bonds.

^{31}P NMR confirmed the purity of the samples from which the single crystals of **4** and **5** for diffraction were obtained: no phosphotungstates of any kind, including [$P_2W_{21}O_{71}(OH_2)_3$]$^{6-}$, were present in either sample. Importantly, addition of authentic samples of **P_2W_{20}** (the starting monovacant polytungstate ligand) or/and **P_2W_{21}** (the isostructural all-tungsten polytungstate) to the aqueous solution of **4** and **5** show no changes to the LTMO complex peaks and give the new characteristic chemical shifts of **P_2W_{20}** or/and **P_2W_{21}** at -12.30 or/and -13.25 ppm (**Figure 4.2**). This finding, in turn, shows that (1) the noble metals, Pd and Au, are not countercations to the polyanions of **4a** and **5a**, respectively, but incorporated in the polytungstate frameworks and (2) the polyanions do not undergo metal exchange or any other kind of isomerization in solution.

X-ray Absorption Spectroscopy Studies

EXAFS Studies of 4. As shown in **Figure 4.3**, the new Pd-oxo polytungstate compound **4** has very similar edge and EXAFS spectra to the previous reported Pd-oxo complex **3**: addition of the short Pd-O improves the fit quality.[8] The short Pd-O distance is certainly needed for a good fit, and it is about 1.70 Å with uncertainty ~0.03-0.05 Å.

All these results indicate a multiply bonded terminal oxo ligand on the six-coordinated local C_{4v} Pd center, and suggest a very similar Pd coordination sphere in both **3** and **4**.

The EXAFS data of Pd-oxo complexes **3** and **4** are best described using slightly different coordination spheres above 3.7 Å. The main results, however, are independent of these differences. For both sets of data, an additional atom in the first shell improves the fit in a similar manner. Also, scattering from equatorial oxygen atoms and tungsten atoms is always refined to physically reasonable values. The differences in the outer shell description can be due to the differences in the structures of **3** and **4** (as can be seen from the comparison of the corresponding Fourier transforms), and also because of a worse quality of **4** data, which makes it difficult to refine small scattering contributions.

XAS Studies of 5. As shown in previous section (**Figure 2.7**), the sharp intense peak at the absorption threshold, the so-called "white line", can be attributed to the electronic transitions from the $2p_{1/2}$ level to unoccupied molecular orbitals of $5d_{3/2}$ character, by analogy to a similar feature observed at the Au L_3 edge.[68-71] The intensity and the position of the white line should therefore reflect any variations of the density and nature of the unoccupied *d*-states. Therefore, the near-edge region at the Au L_2 edge is characteristic of the Au electronic structure and can be used to assign the oxidation state of Au in a sample. **Figure 2.7** also illustrates the Au L_2 near-edge structure of **2** and **5**. The position and intensity of the white line is very similar in the spectra of **2** and **5** and indicates the same oxidation state for Au in both compounds of interest. The similarity of this feature to the white line of Au(III) acetate suggests, in turn, that Au is present as Au(III) in the polyoxometalate complexes. The comparison of the spectra of **2** and **5** to those of Au(I) compounds provides further evidence of the Au(III) oxidation state in

Table 4.1 Crystal data and refinement parameters for the X-ray structures of $K_7H_2[AuO(OH_2)P_2W_{20}O_{70}(OH_2)_2]\bullet 27H_2O$ (**5**) and $K_{10}[P_2W_{20}O_{70}(OH_2)_2]\bullet 22H_2O$ (**P_2W_{20}**).

complex	**5**	**P_2W_{20}**
molecular formula	$H_{62}K_7O_{101}P_2AuW_{20}$	$H_{48}K_{10}O_{94}P_2W_{20}$
formula wt. (g mol^{-1})	5887.80	5682.02
temperature (K)	173(2)	173(2)
radiation (λ, Å)	0.71073	0.71073
crystal system	hexagonal	orthorhombic
space group	*P6(3)/mmc* (#194)	*Pca2(1)* (#29)
a (Å)	16.1730(9)	25.956(2)
b (Å)	16.1730(9)	19.0818(15)
c (Å)	19.7659(15)	33.801(3)
Volume ($Å^3$)	4477.4(5)	16741(2)
Z	2	4
ρ_{calcd} (g cm^{-3})	4.198	4.377
μ (mm^{-1})	27.713	27.972
F(000)	4956	19276
crystal size (mm^3)	0.33 × 0.28 × 0.17	0.39 × 0.34 × 0.29
reflections collected	59942	229187
independent reflections	2107 [R(int) = 0.0697]	41719 [R(int) = 0.0769]
absorption correction	semi-empirical from equivalents	semi-empirical from equivalents
refinement method	full-matrix least-squares on F^2	full-matrix least-squares on F^2
goodness-of-fit on F^2	1.248	1.022
final R indices	$R1^a$ = 0.0634	$R1^a$ = 0.0483
[R > 2σ (I)]	$wR2^b$ = 0.2677	$wR2^b$ = 0.1172
R indices (all data)	$R1^a$ = 0.0639	$R1^a$ = 0.0542
	$wR2^b$ = 0.2683	$wR2^b$ = 0.1209
largest diff. peak and hole (e $Å^{-3}$)	11.568 and -6.549	7.969 and -9.547

$^a R_1 = \Sigma||F_o| - |F_c|| / |F_o|$

$^b wR_2 = \{\Sigma[w(F_o^2 - F_c^2)^2] / \Sigma[w(F_o^2)^2]\}^{0.5}$

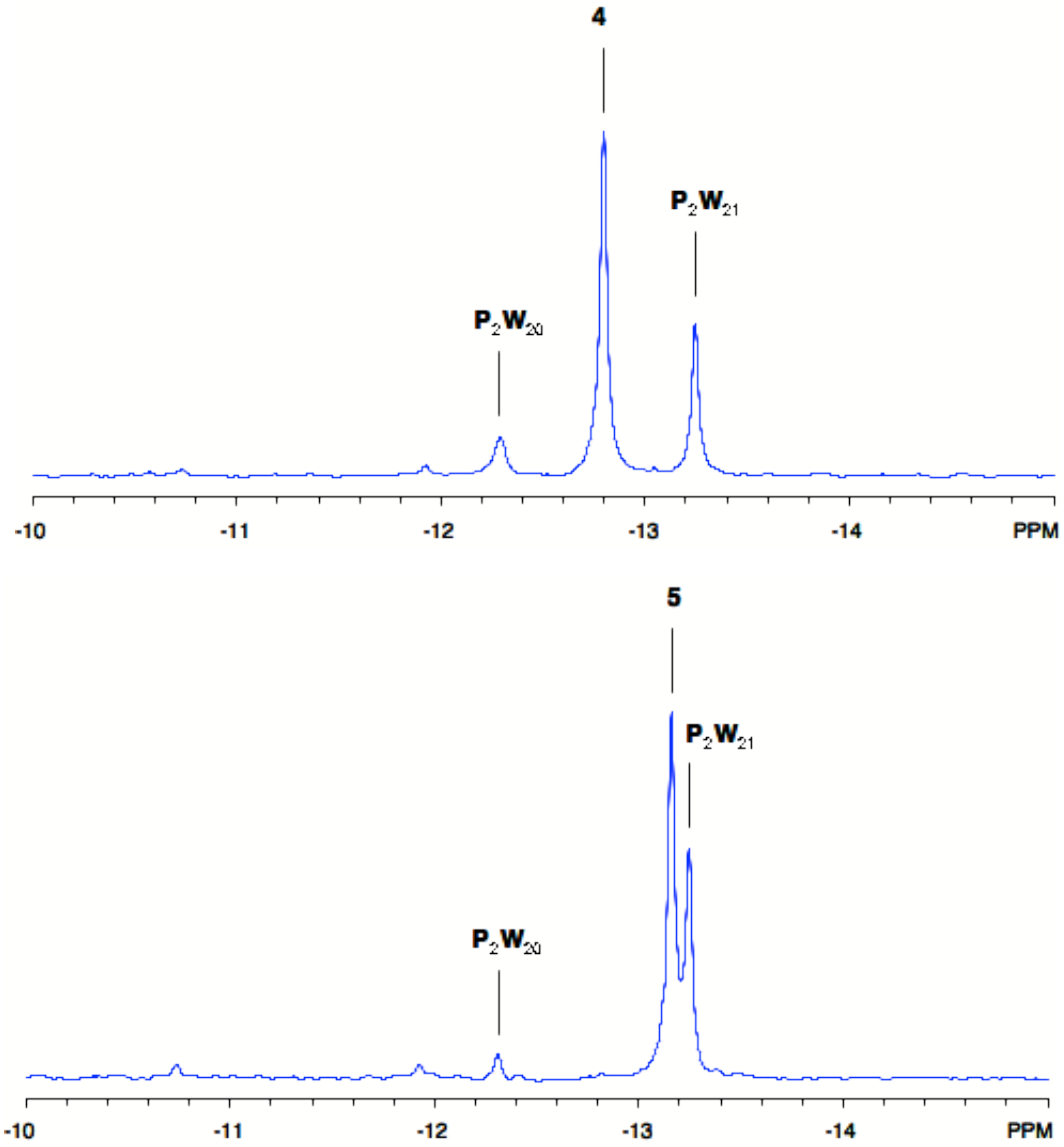

Figure 4.2 ^{31}P NMR spectra of Pd-oxo complex **4** (top) and Au-oxo complex **5** (bottom) with the addition of authentic samples of the starting polytungstate ligand $[P_2W_{20}O_{70}(H_2O)_2]^{10-}$ (**P_2W_{20}**) as well as the isostructural all-tungsten complex $[P_2W_{21}O_{71}(H_2O)_3]^{6-}$ (**P_2W_{21}**).

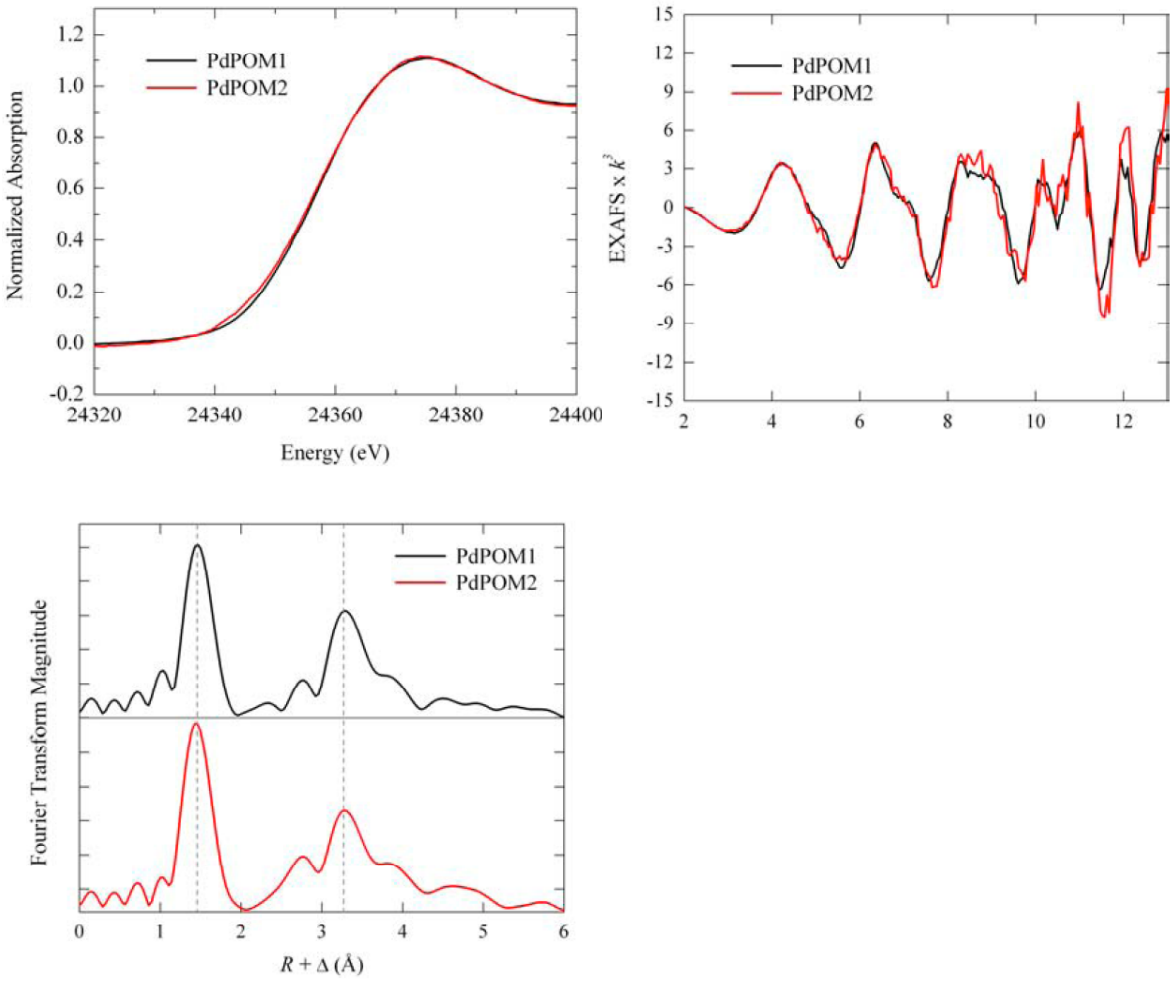

Figure 4.3 Pd *K*-edge EXAFS data and the corresponding non-phase shift corrected Fourier transforms for Pd-oxo complexes **3** (black) and **4** (red).

gold-containing polyoxometalates, as the rising part of the edges of **2** and **5** is much closer in energy to Au(III) acetate than to any of the Au(I) complexes. The similarity of the spectra of **2** and **5** suggests a high degree of similarity in the electronic and geometric environment of Au in the two complexes.

Ultra-Low-Temperature Electronic Absorption Spectroscopy

Very-low temperature (17 K) electronic absorption spectroscopy was collected for the Au-oxo complex **5**. The sample was dissolved in a 1:3 water:glycerol mixture in order to obtain a good optical glass; the spectrum (**Figure 4.4**) possesses two weak

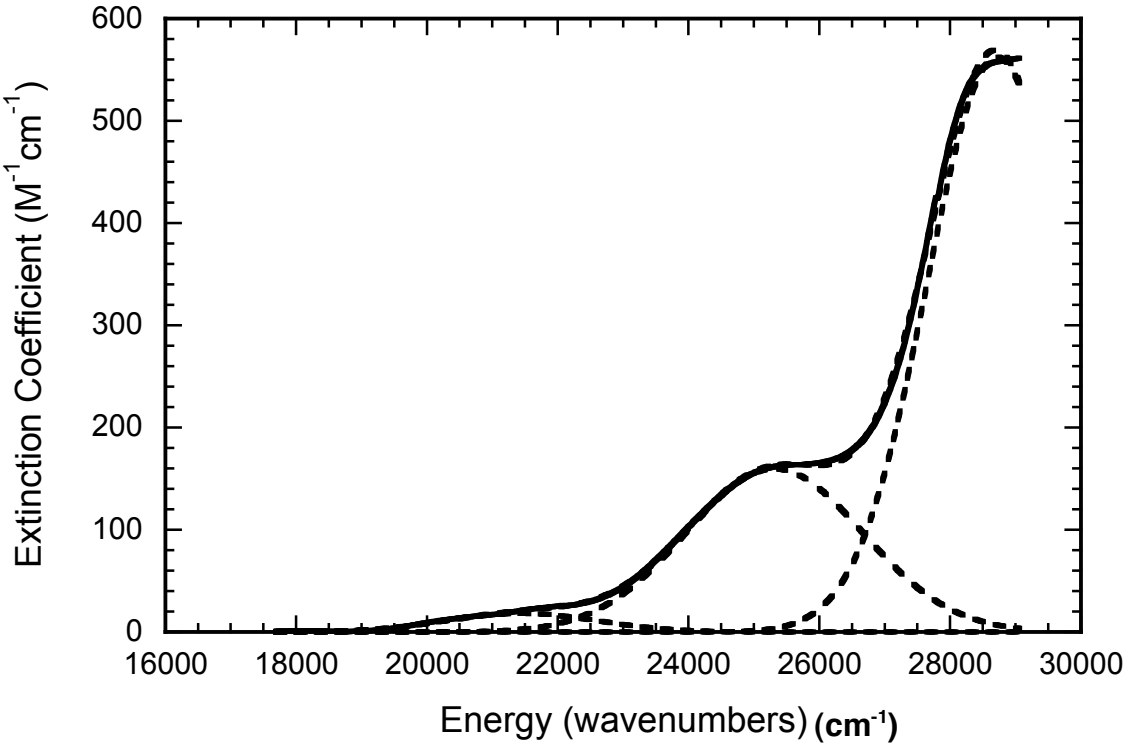

Figure 4.4 Low temperature (17 K) electronic absorption spectrum of **5** in a 1:3 water:glycerol glass with band deconvolution.

absorption bands, at 21,440 cm^{-1} (466 nm, band 1) and 25,310 cm^{-1} (372 nm, band 2), with extinction coefficients of 18 and 160 $M^{-1}cm^{-1}$, respectively. The Au(III)-to-W(VI) and more intense oxygen-to-W(VI) charge transfer bands are found at higher energy (E >

26,000 cm^{-1}). Our analysis of the ligand field spectrum of **5** is based on our previous assignments of the unprecedented Pt(IV)-oxo[7] **1** and Pd(IV)-oxo[8] **3** sites bound by POM ligands and assumes a strong ligand field imparted on the metal center by the bridging and terminal oxo ligands. Based on our previous studies of high-valent transition metal complexes with a single terminal oxo ligand, we anticipate a similar d orbital splitting pattern with the metal d_{z^2} orbital highest in energy due to strong antibonding interactions between the terminal oxo p_z orbital and the Au d_{z^2} orbital. Similarly, strong π antibonding interactions between the terminal oxo $p_{x,y}$ orbitals and the Au $d_{xz,yz}$ destabilize the latter orbitals. The d_{xy} orbital is higher in energy than the π antibonding $d_{xz,yz}$ orbitals because it is sigma antibonding with respect to the four equatorial oxygens (W-O- ligands). For a d^8 system, this yields a diamagnetic ground state with a $(d_{x^2-y^2})^2(d_{xz})^2(d_{yz})^2(d_{xy})^2(d_{z^2})^0$ orbital configuration in C_{2v} symmetry. Using this ground state electronic configuration and ligand field splitting pattern, ligand field transitions occur from the doubly occupied Au based d orbitals to the empty Au d_{z^2} orbital, and we can now make tentative assignments for the observed Au(III) ligand field bands. The lowest energy ligand field one-electron promotion will therefore be $xy \rightarrow z^2$. Since there are no additional transitions found at energies down to 5,000 cm^{-1} in the room temperature solution electronic absorption spectrum we can make tentative assignments for the 21,440 cm^{-1} and 25,310 cm^{-1} ligand field bands as $xy \rightarrow z^2$ ($^1A_1 \rightarrow {}^3A_2$) for band 1 and $xy \rightarrow z^2$ ($^1A_1 \rightarrow {}^1A_2$) for band 2. The $^1A_1 \rightarrow {}^1A_2$ transition is symmetry forbidden in the local C_{2v} symmetry and its intensity likely derives from a combination of vibronic coupling and small static distortions that lower the symmetry from idealized C_{2v}. The weak spin-forbidden $^1A_1 \rightarrow {}^3A_2$ transition gains intensity by spin-orbit coupling with its spin-

allowed $^1A_1 \rightarrow {}^1A_2$ partner. This assignment leads to a d_{xy}-d_{z^2} orbital splitting (e_g splitting) of ~25,000 cm^{-1} due to the strong terminal oxo ligand field. The equatorial oxo ligand field is likely markedly weaker than the axial field due to the fact that the O_{eq} ligands are bridging to high valent W(VI) centers while the axial oxo is terminal. Finally, the experimentally determined $^1A_2 \rightarrow {}^3A_2$ splitting of ~4,000 cm^{-1} may be compared with an ~4,000 cm^{-1} $^1E \rightarrow {}^3E$ splitting observed in the ligand field spectrum of d^2 $[MoOL_4Cl]^{1+}$ complexes,[72] lending further support for our assignment of the lowest ligand field states for **5** as being comprised of exchange split singlet and triplet $xy \rightarrow z^2$ excitations. Despite marked efforts, these orbital and electronic transition assignments could not be confirmed by DFT calculations because the complexes and models thereof are unstable.

pH Dependent UV-vis and ^{31}P NMR Titrations

Previous pH dependent UV-vis and ^{31}P NMR titration studies on **3** indicates that the *trans* Pd-OH bond (1.99(2) Å) starts to be protonated at pH 3.5,[8] where there are three changes in the UV-vis spectra, the d-d band at 444 nm red shifts 8 nm as well as an increase in excitation coefficient, and the lost of the should at 512 nm. In addition, the UV-vis experiments are corroborated by similar changes in the ^{31}P NMR spectrum of **3** as a function of pH (0.25 ppm shift to downfield). Importantly, all changes in UV-vis and ^{31}P NMR are reversible upon increasing the pH back to 6.5 again (the natural pH of **3** in aqueous solution).

The same experiments are utilized to investigate the *trans* ligand to the Pd-oxo unit in **4**. Interestingly, there is no inflection point even the pH value of the solution of **4** has

been lowered to below 1.0, which suggests protonation does not likely happen on **4**. The pH titration result is confirmed by its related UV-vis and ^{31}P NMR studies, which show no changes in both spectra as a function of pH. One argument to explain this difference

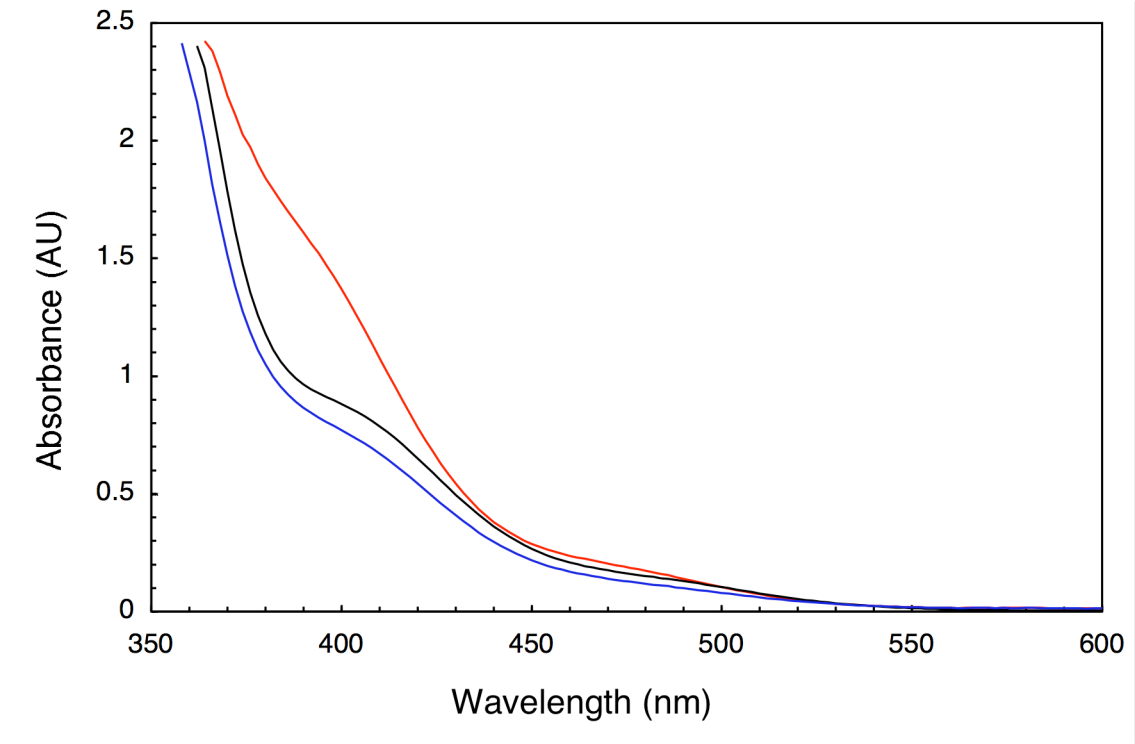

Figure 4.5 pH-dependent UV-vis titration of **5** with NaOH and the back titration with HCl, showing the reversible changes in the d-d bands at 410 nm upon increasing and lowering the pH of the solution.

is that the *trans* ligand of the Pd-oxo unit in **4** is buried in the central cavity of a polytungstate framework, and is protected from protonation. However, previous hydrogen-deuterium exchange studies (β-effect) by ^{183}W NMR on an isostructural complex, $[P_2W_{21}O_{71}(OH_2)_3]^{6-}$,[52] has verified that the interior H_2O ligand in the central

equatorial plane can undergo slow exchange. As a result, the pH titration studies of **4** suggest that the *trans* ligand to the terminal Pd=O is a not a hydroxyl group but an aqua ligand.

Similarly, the *trans* ligand to the terminal Au-oxo unit in the polyanion of **5** is further confirmed by pH-dependent UV-vis titrations. The ambient temperature UV-visible spectrum of **5** in aqueous solution does not change when the pH is dropped to as low as 0.38, suggesting a *trans* aqua ligand on the Au center. Also consistent with the presence of a *trans* aqua ligand in 5 is that the UV-vis spectrum in water changes when titrated with base: changes are clearly apparent at *ca.* pH 5.8 (a red shift and an increase in ε, **Figure 4.5**) and this change continues until a pH value of *ca.* 7.5 is reached. Moreover, this process is fully reversed by subsequently decreasing the pH by addition of HCl – the *trans* hydroxo ligand is re-protonated to the aqua ligand. Thus acid-based titrations monitored by electronic absorption spectroscopy confirm the finding of the X-ray and neutron diffraction studies that an aqua ligand is *trans* to the Au-oxo unit in **5**.

Electrochemistry

Figure 4.6 shows the cyclic voltammogram of **4** in a pH 4.5 medium. The results indicate that **4** has distinct electrochemical behaviors from conventional Pd(II)-substituted polytungstates and free Pd(II) ($PdSO_4$).[73-75] In short, two redox systems are observed in the negative potential domain: the first reduction wave is attributed to the Pd(IV) into Pd(0) and the second redox couple features the hydrogen sorption/desorption process on the deposited Pd(0) film.

The Pd(IV) into Pd(0) reduction wave of **4** appears at -0.320 V vs SCE, a slightly more negative potential than observed for the transformation of Pd(II) into Pd(0) in the case of $PdSO_4$ (-0.280 V vs SCE). In contrast, this Pd(IV) reduction wave is by roughly 0.150 V less negative than obtained, in the same experimental conditions, for the same process, in the case of **3**. These differences highlight the important influence exerted on the redox properties of Pd centers by their environments within these compounds. In short, the result, hardly predictable qualitatively, is obtained that a Pd(IV) center within a POM is more difficult to reduce than Pd(II) in solution. Furthermore, the Pd(IV) centers within the two different POMs considered here are reduced at distinctly different potentials.

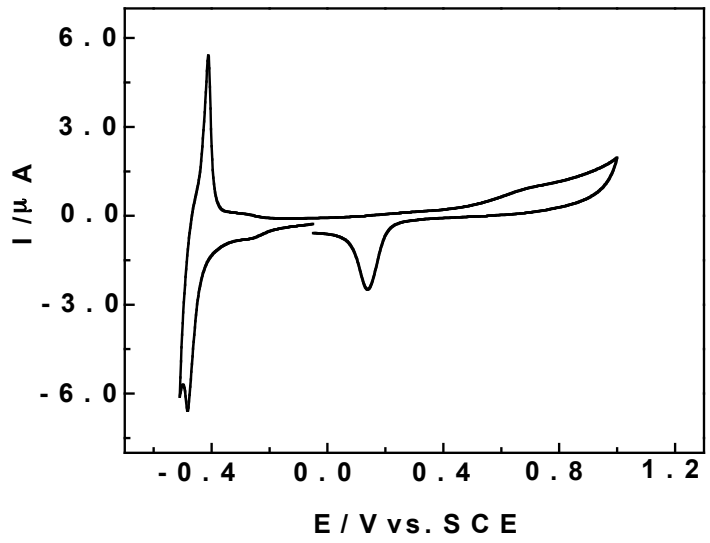

Figure 4.6 Cyclic voltammogram of **4** in a pH 4.5 medium, showing distinct electrochemical behaviors from conventional Pd(II)-substituted polytungstates and free Pd(II) ($PdSO_4$).

The characteristics of the voltammetric pattern attributed to the hydrogen sorption/desorption process depend on the number of cycles. For example, the current intensities associated with the cathodic and anodic parts of this process increase as the thickness of the deposited Pd(0) film increases. Immediately following this redox couple, the proton/water reduction process begins and is supposed to preclude from any clear observation of the W waves. This conclusion relies upon the assumption that the potential locations for both processes should be close to the corresponding ones observed for the precursor lacunary POM $\mathbf{P_2W_{20}}$ (-0.760 V and -0.896 V respectively). In the domain starting from -0.05 V to +1.0 V in the positive potential direction and back to -0.05 V is observed the oxidation of the deposited Pd(0) surface followed by reduction of the oxide. The characteristics of this deposited film parallel those obtained previously with other Pd-containing POMs. As expected, the film thickness increases with the number of cycles or the duration potentiostatic electrolysis. Here, as in all the previous examples, the better symmetry of the hydrogen sorption/desorption wave following the Pd(0) deposition wave from the complexes stands in contrast with the relative asymmetry of the same process in the case of uncomplexed Pd^{2+} cation. More generally, this observation underscores the better quality of the films deposited from Pd-containing POMs over that from uncomplexed Pd(II).

Finally, the number of electrons involved in the exhaustive reduction of the Pd-center within **4** was determined by controlled potential coulometry at a fixed potential of -0.350 V vs SCE. The measured value of 4.0 ± 0.1 electrons per POM molecule support the conclusion that a Pd(IV) complex is studied actually. During the electrolysis, the characteristic blue colour of reduced W centers was not observed. The cyclic

voltammogram shown in **Figure 4.7** was run with the large surface area glassy carbon plate used for controlled potential electrolysis and on which a thick Pd(0) film was deposited. This cyclic voltammogram is interesting because it shows the characteristic "two step oxidation" of the surface of thick Pd(0) films.[76]

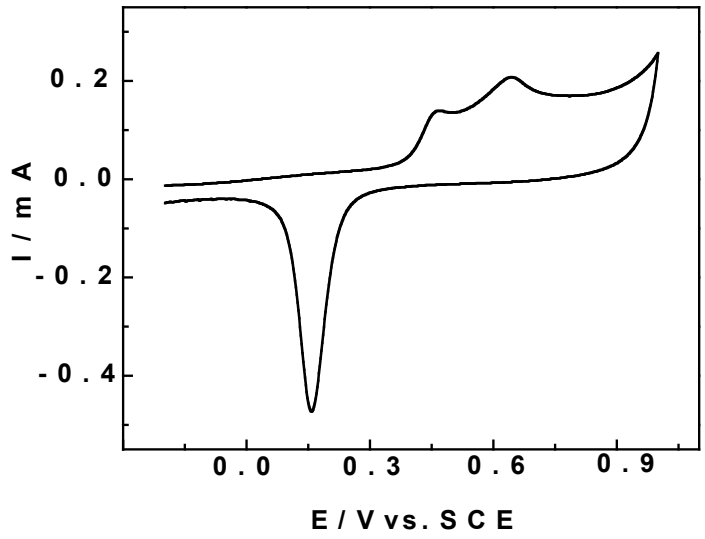

Figure 4.7 Cyclic voltammetry (CV) characterization of a thick film of **4** in its preparation medium (2 x 10^{-4} M of **4** + (0.4 M CH_3COONa + CH_3COOH) pH = 4.5 buffer). Working electrode: glassy carbon; reference electrode: SCE; scan rate: 2 mV s^{-1}. It shows the characteristic "two step oxidation" of the surface of thick Pd(0) films.

CVs of Au-oxo containing complexes, 2.85 mM **2** and 2.0 mM **5** in 0.4 M sodium chloroacetate buffer (pH 3), are shown for comparison in **Figure 2.5**. We assign the first reduction wave at *ca.* 420 mV to a reduction of Au(III) to Au(0), which is deposited as a Au(0) film on the working electrode. The reduction of Au(III) to Au(0) in **2** solution

proceeds at much more negative potential, -290 mV, the approximate value expected given the much higher charge on polyanion **2a** (17-) versus **5a** (9-). The second reversible wave at -590 mV ($\Delta E \sim 60$ mV) is a reduction of tungsten (see below). An additional peak is observed at quite high potential (1100 mV; data not shown). The current intensity of this peak dramatically increases with number of CV runs and is attributed to the oxidation of deposited Au(0) on electrode surface followed by reduction of the oxide. The thickness of Au(0) film increases with number of runs, which results in an increase of the current associated with the peak. At the same time the current intensity of peak at 420 mV decreases with number of CV runs. Similar CVs are observed at lower scan rates, 25 and 2 mV/s (data not shown). A CV of the same buffer solution (no **5** present) obtained using the working electrode with deposited Au(0) (after 11 runs with a scan rate 100 mV/s) shows the same peak at 1100 mV. The current intensity of the peak does not increase with number of runs (no more deposition of Au(0) takes place). The reversible peak at -590 mV is assigned to the reduction of tungsten in **5** (or in $\mathbf{P_2W_{20}}$, the demetalated POM). Indeed, a CV of 0.5 mM $K_{10}[P_2W_{20}(OH_2)_2O_{70}]\bullet 22H_2O$ in 0.4 M sodium chloroacetate buffer (pH 3) shows the peak at the same potential, -590 mV, with the same current intensity. Bulk electrolysis (coulometry at controlled potential) confirm the Au(III) oxidation state assignment in **5**: three electrons (**n** was found to be *ca.* 3.2) are need for the complete conversion of gold to Au(0) (**Figure 2.6**, bright Au mirrors are produced in the bulk electrolysis experiments).

Chemical Titrations

Reactions of **5** with $ABTS^{2-}$ or $[Fe^{II}(CN)_6]^{4-}$ are fast and produce the intensively green colored $ABTS^{\bullet-}$ or the yellow $[Fe^{III}(CN)_6]^{3-}$ during mixing. Both reaction products, $ABTS^{\bullet-}$ and $[Fe^{III}(CN)_6]^{3-}$, are stable under argon. Their yields were quantified by their characteristic UV-vis spectra. The intensively colored $ABTS^{\bullet-}$ has maxima at 417, 645 and 728 nm, and the $[Fe^{III}(CN)_6]^{3-}$ has a maximum at 420 nm.

Under typical experimental conditions, addition of 0.02 mM **5** (final concentration) to 2 mM $ABTS^{2-}$ produced 0.04 mM $ABTS^{\bullet-}$. The yield was independent of $[ABTS^{2-}]$ and linearly proportional to the amount of **5** added. On average 2.05 ± 0.15 $ABTS^{\bullet-}$ were formed per equivalent of **5** present. This stoichiometry is consistent with a reduction of Au(III) to a Au(I) species. However, a demetallation of $Au^{I}P_2W_{20}$ complex to form other stable Au(I) species can not be ruled out since similar results were obtained in the reaction of $ABTS^{2-}$ with $(NH_4)AuCl_4$. The reduction potential of $ABTS^{\bullet-}/ABTS^{2-}$ is relatively high, 440 mV (SCE) and close to the potential (415 mV) required for electrochemical reduction of **5**. A large excess of $ABTS^{2-}$ over **5** results in complete reduction of Au(III) to Au(I); further reduction of Au(I) to Au(0) is probably unfavorable.

A stoichiometric amount of a stronger reducing agent should completely reduce Au(III) to Au(0). We attempted to use $[Fe^{II}(CN)_6]^{4-}$ as a reducing agent (E = 235 mV vs. SCE, determined from CV in 50 mM sodium chloroacetate buffer, pH 3.0, in the presence of 0.3 M KCl). However, the reduction of **5** proceeds to completion only in presence of excess of $[Fe^{II}(CN)_6]^{4-}$. For example, a mixture of 0.2 mM **5** (final concentration) and an excess of $[Fe^{II}(CN)_6]^{4-}$ (4.5 mM) produces 2.3-2.6 equivalent of $[Fe^{III}(CN)_6]^{3-}$, consistent with a partial reduction of Au(I) to Au(0). Interestingly, a

similar stoichiometry is obtained in the reduction of $(NH_4)AuCl_4$ by $[Fe^{II}(CN)_6]^{4-}$. Furthermore, if the reaction is carried out in the presence of NaCN (> 1 mM), then 2.0 ± 0.1 of $[Fe^{III}(CN)_6]^{3-}$ are formed per equivalent of **5**. Such a behavior is in agreement with a reduction of Au(III) to Au(I), with the latter stabilized by cyanide anions.

When the stronger one-electron reducing agent, $[SiW_{12}O_{40}]^{5-}$ (E = -195 mV SCE), is used to titrate **5**, Au(0) particles are quickly produced which preclude quantification of the reaction stoichiometry using UV-visible spectroscopy. Therefore, we monitored the titration of $[SiW_{12}O_{40}]^{5-}$ by **5** using solution reduction potentials. The potential of the

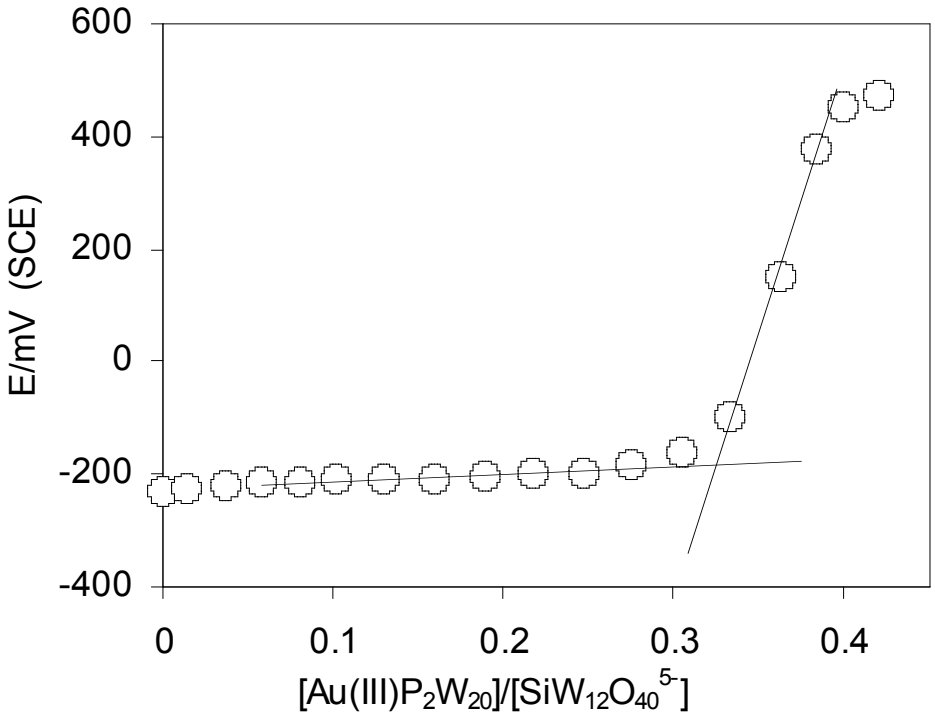

Figure 4.8 Changes in the reduction potential of the $SiW_{12}O_{40}^{5-}/SiW_{12}O_{40}^{4-}$ solution (initial concentration 0.87 mM $SiW_{12}O_{40}^{5-}$) upon addition of **5** (1 mM in stock solution).

Conditions: 25 mM sodium chloroacetate buffer (pH 3.0), room temperature, argon atmosphere.

$[SiW_{12}O_{40}]^{5-}/[SiW_{12}O_{40}]^{4-}$ solution is controlled by the ratio of reduced and oxidized forms (-230 mV when the ratio is 7). Oxidation of $[SiW_{12}O_{40}]^{5-}$ by **5** decreases this ratio resulting in a slow increase in reduction potential from -230 mV to -150 mV (corresponding to $[SiW_{12}O_{40}^{5-}]/[SiW_{12}O_{40}^{4-}] = 0.07$). If all $[SiW_{12}O_{40}]^{5-}$ is oxidized, then the solution reduction potential is controlled by Au(III)/Au(0) couple. This results in a sharp increase in solution reduction potential (> 400 mV, **Figure 4.8**). A titration end-point determined from intersection of two straight lines shown on **Figure 4.8** proves that 3.05 ± 0.15 equivalents (average of two independent experiments) of $[SiW_{12}O_{40}]^{5-}$ are required to reduce 1 equivalent of **5**, consistent with the reduction of Au(III) to Au(0). The formation of Au(0) particles is clearly seen. A control titration of $[SiW_{12}O_{40}]^{5-}$ by $(NH_4)AuCl_4$ gave 3.1 ± 0.15 as the stoichiometric coefficient.

We also attempted to reductively titrate freshly dissolved **2** with three other well-defined and well documented one-electron reductants, $[SiW_{12}O_{40}]^{5-}$, $[AlW_{12}O_{40}]^{6-}$ and thiosulfate. Mixing of the blue colored solutions of the 1-electron-reduced POMs, $[SiW_{12}O_{40}]^{5-}$ or $[AlW_{12}O_{40}]^{6-}$ with a solution of **2** results in an immediate decoloration of solutions; Au(0) particles are formed much more slowly. Addition of **2** to solutions of $[SiW_{12}O_{40}]^{5-}$ or $[AlW_{12}O_{40}]^{6-}$ results in a quick increase of solution reduction potential, which then decreases with time. In general, redox titrations with the reagents to well-

defined end-points was not highly reproducible. Freshly dissolved **2** does not react with $ABTS^{2-}$ or with $[Fe^{II}(CN)_6]^{4-}$.

^{17}O NMR Studies

The ^{17}O NMR spectra for **4** and **5** are shown in **Figure 4.9**. The ^{17}O chemical shifts agree well with the general correlation between downfield chemical shift and oxygen π-bond order, a correlation that has been established from both experimental and theoretical studies.[77-81] There are two peaks at 545 ppm and 325 ppm (**Figure 4.9**A), which are assigned to the oxygens of Pd=O and Pd-OH_2, respectively, and are in good agreement with those in previously reported **3**. Two differences are worthy noting here: (1) The ^{17}O NMR peak of the terminal oxo oxygen on Pd in **4** upfield shifts about 25 ppm comparing to **3**. The reason for this difference may be that the Pd=O unit in **3** has a more crowding environment from a terminal oxo of the central W (located 2.57 Å away) and a potassium countercation in the central vacant site (located 2.35 Å away). It is true that **3** has an unexpected short Pd=O bond distance (1.60-1.63 ± 0.03 Å) and small out-of-plane displacement of Pd (0.08-0.103 ± 0.004 Å). (2) The ^{17}O NMR peak at 325 ppm in the spectra of **4** is much less intense than that of **3**. This may attribute to the difficulty in exchanging the interior H_2O in **4** and consequent lower ^{17}O enrichment.

The two ^{17}O NMR spectra of **5** obtained by both aqueous and organic-medium enriching methods are similar except that the second spectrum (**Figure 4.9**C) for enrichment conducted in an organic solvent, has a better signal-to-noise ratio than the first one (**Figure 4.9**B). In the structure of **5**, there are seven classes of symmetry-equivalent terminal oxo positions: six W-O_{oxo} oxygens that appear as five peaks from

730-790 ppm and the Au-O_{oxo} oxygen that appears at 605 ppm, an ensemble of chemical shifts that are in good agreement with those in **2**. Similarly, the chemical shifts of the bridging oxygens in **5** are in the range of 400 to 450 ppm.

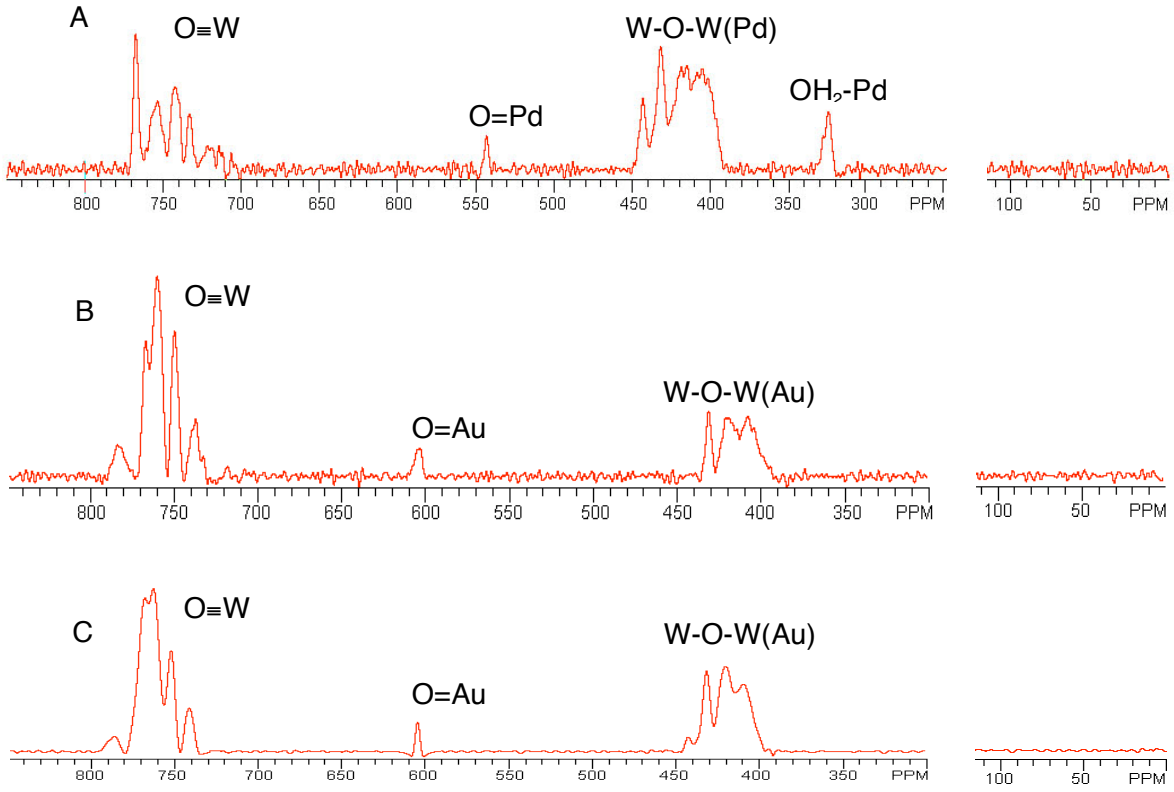

Figure 4.9 ^{17}O NMR spectra of Pd-oxo **4** and Au-oxo **5** complexes in 50:50 (v:v) CH_3CN:$CDCl_3$. (A) Tetra-*n*-butylammonium (TBA) salt of **4**. (B) K⊂*cis*-dicyclohexano-18-crown-6 salt of **5** enriched in aqueous solution. (C) K⊂*cis*-dicyclohexano-18-crown-6 salt of **5** enriched in acetonitrile.

Atomic Occupancy at the Au Position

The skeptical reader might require specific evidence that Au and Au only resides at this position in the structures and not W or a mixture of W and Au (and that the one Au atom established from the multiple full elemental analyses is not distributed over the polyanion units, **2a** and **5a**).[9] All the diffraction work unequivocally rules out cationic Au counterions to polyanions **2a** and **5a**. There are at least seven arguments that we feel collectively provide compelling evidence for the Au atom residing only at the one central bridging position indicated in X-ray structures of **2a** and **5a**. First, the ^{31}P NMR spectra would show multiple peaks if the Au atom resided at a second (or additional) position(s), but only one singlet is seen for both complexes (chemical shift values in H_2O and organic solvents are given above). In addition, the ^{31}P NMR spectrum indicates that **5** is stable in aqueous solution in the presence of other polytungstates, including $\mathbf{P_2W_{21}}$ which is isostructural to **5** (if the Au were to be replaced by W). This finding, in turn, shows that the polyanions do not undergo metal exchange or any other kind of isomerization in solution. Second, the ^{17}O NMR spectra show a single peak for the Au-oxo oxygen with the expected chemical shift. In addition, the other peaks in the spectra are correct for the polyanion structures indicated by the X-ray structures. Third, the displacement of the Au and W atoms in the metal-oxo units out of the equatorial plane (the doming distance) are 0.31 Å and 0.45 Å, respectively, a difference that is well outside the experimental error in the X-ray structures. All the W-oxo units in both **2a** and **5a** average near 0.45 Å. Fourth, the terminal Au-oxo distances in **2a** and **5a** (both 1.77 Å) are both longer than all the terminal W-oxo distances (1.67 Å) in each structure and the difference in these distances is outside experimental error. Fifth, the redox titrations, and sixth the coulometry are

consistent with a single type of Au center in both complexes. Seventh, the one and only sample that does have some W at the Au position, namely the very large single crystal used in the neutron diffraction, does contain both W and Au at this position (a co-crystallization of **2** and the isostructural all-tungsten compound, $\mathbf{P_2W_{19}}$). This Au/W mixture can not only be quantified (67% Au and 33% W) from the final refined neutron diffraction data but this same ratio is confirmed when this crystal is dissolved and the ^{31}P NMR spectrum obtained. On consideration of all these points, the only possibility is that the single Au atom per polyanion resides at the bridging central position indicated by the X-ray structures.

Au Oxidation State

Five independent techniques are consistent with Au(III) d^8 electronic configurations in both **2** and **5**:[9] (a) chemical titrations on both complexes indicate that 3 electrons per polyanion are required to produce Au(0); (b) coulometric measurements also indicate that 3 electrons convert the Au-oxo complexes to Au(0) (indeed, bright Au mirrors are produced in the bulk electrolysis experiments); (c) the optical spectrum of **5** in water-glycerol glasses at 17 K is distinct from the optical spectrum of the d^6 Pd(IV)-oxo complex and consistent with a d^8 electronic configuration in a six-coordinate C_{2v} structure that is clearly present in **2** and **5** from all the diffraction studies (both **2a** and **5a** exhibit approximate local C_{4v} symmetry around the Au atom in the $Au(O)(OH_2)(O\text{-}W)_4$ primary coordination sphere); (d) the Au L_2 near-edge X-ray absorption spectra of both **2** and **5** are consistent with Au(III) centers in both complexes; and (e) a careful comparison of the X-ray crystal structures of the isostructural Pt(IV)-oxo complex **1** and **2**. This

comparison reveals a fifth strong argument for the d^8 Au(III) electronic configuration in the latter.[7,9] Both the Pt-oxo complex **1** and **2** are isostructural, have similar cations and were crystallized out of unbuffered aqueous solution, and therefore detailed comparison of the two structures is defensible. As expected, the M(Pt or Au)-oxo oxygen distances are quite different (1.720(18) and 1.763(17) Å for Pt and Au, respectively). The increased length by 0.043 Å for the Au-oxo unit is well outside experimental error and is consistent with additional electrons populating d-based orbitals on the Au center. A qualification on this point, however, is that there may be a greater ionic contribution to the Pt(IV)-oxo bond than the effectively isostructural Au(III)-oxo bond. Electron paramagnetic resonance and magnetic circular dichroism spectroscopies are not applicable because both **2** and **5** are diamagnetic.

While these five lines of evidence, collectively, would seemingly provide fairly compelling evidence that **2** and **5** contain Au(III) d^8 centers, we are not yet prepared to absolutely rule out Au(V) d^6 centers. Perhaps the most definitive technique to probe the Au oxidation state would be ^{197}Au Mössbauer spectroscopy because the isomer shift correlates very well with oxidation date (at least in the case of ^{57}Fe Mössbauer spectroscopy and quite likely in the case of ^{197}Au Mössbauer spectroscopy),[82] but strong nonresonance absorption by the many tungsten atoms present rendered the Au signal unobservable for both complexes.

4.5 Conclusions

(1) Two terminal Au-oxo compounds, **2** and **5**, have been prepared and characterized by more than 10 physicochemical methods. Appropriate polytungstate ligands stabilize these elusive species sufficiently that they can be isolated and studied. The collective experimental data provide seven arguments given in the Discussion section that the single Au atom in both **2** and **5** resides only at the central position indicated by the X-ray structures and not in other positions.

(2) The purity of both **2** and **5** were established by multiple elemental analyses on all elements, ^{17}O NMR, ^{31}P NMR, and indirectly by several additional techniques including cyclic voltammetry, chemical titrations, thermogravimetric analysis, differential scanning calorimetry and other methods.

(3) Both structural types of terminal Au-oxo compounds represented by **2** and **5** have been established using single crystal X-ray diffraction down to 30 K and exhibit nearly identical $Au(O)(OH_2)(O\text{-}W)_4$ coordination spheres with very short $Au\text{-}O_{oxo}$ bond distances (1.763(17) for **2** and 1.77(4) Å for **5**). The disorder-free structure of **2** was further corroborated by neutron diffraction studies, which also confirmed both the Au-oxo unit (no hydrogen proximal to the oxygen) and the aqua ligand *trans* to the oxo position (both aqua hydrogens, despite positional disorder, were located). The ^{17}O NMR chemical shifts of the terminal oxo groups on Au in both **2** and **5** were also consistent with multiple bonding (and π bonding) between the Au and terminal oxo oxygen.

(4) The results from five independent techniques addressed in the Discussion section are consistent with Au(III) d^8 electronic configurations in **2** and **5**. While all these results collectively provide a strong argument for this electronic assignment, we are not

prepared to absolutely rule out Au(V) d^6 electronic configurations for these complexes at this time.

(5) Complexes **2** and **5** are well-defined compounds that model the metal oxide-Au interface, exhibit high valent Au centers in metal oxide molecular environments, and reveal more of the fundamental chemistry of gold and oxygen. The structural, reactivity and other properties of these complexes will be addressed in subsequent studies.

References

(1) Holm, R. H. *Chem. Rev.* **1987**, *87*, 1401-1449.

(2) Holm, R. H.; Donahue, J. P. *Polyhedron* **1993**, *12*, 571-589.

(3) Parkin, G. In *Prog. Inorg. Chem.*; Karlin, K. D., Ed.; Wiley: New York, 1998; Vol. 47, p 1-165.

(4) Nugent, W. A.; Mayer, J. M. *Metal-Ligand Multiple Bonds*; John Wiley & Sons, Inc.: New York, 1988.

(5) Borovik, A. S. *Acc. Chem. Res.* **2005**, *38*, 54-61.

(6) Bakac, A. In *Advances in Inorganic Chemistry* 2004; Vol. 55, p 1-59.

(7) Anderson, T. M.; Neiwert, W. A.; Kirk, M. L.; Piccoli, P. M. B.; Schultz, A. J.; Koetzle, T., F.; Musaev, D. G.; Morokuma, K.; Cao, R.; Hill, C. L. *Science* **2004**, *306*, 2074-2077.

(8) Anderson, T. M.; Cao, R.; Slonkina, E.; Hedman, B.; Hodgson, K. O.; Hardcastle, K. I.; Neiwert, W. A.; Wu, S.; Kirk, M. L.; Knottenbelt, S.; Depperman, E. C.; Keita, B.;

Nadjo, L.; Musaev, D. G.; Morokuma, K.; Hill, C. L. *J. Am. Chem. Soc.* **2005**, *127*, 11948-11949.

(9) Cao, R.; Anderson, T. M.; Piccoli, P. M. B.; Schultz, A. J.; Koetzle, T. F.; Geletii, Y. V.; Slonkina, E.; Hedman, B.; Hodgson, K. O.; Hardcastle, K. I.; Fang, X.; Kirk, M. L.; Knottenbelt, S.; Kogerler, P.; Musaev, D. G.; Morokuma, K.; Takahashi, M.; Hill, C. L. *J. Am. Chem. Soc.* **2007**, *129*, 11118-11133.

(10) Miskowski, V. M.; Gray, H. B.; Hopkins, M. D. *Advances in Transition Metal Coordination Chemistry* **1996**, *1*, 159-186.

(11) Morris, R. J.; Girolami, G. S. *Polyhedron* **1988**, *7*, 2001-2008.

(12) Spaltenstein, E.; Conry, R. R.; Critchlow, S. C.; Mayer, J. M. *J. Am. Chem. Soc.* **1989**, *111*, 8741-8742.

(13) Rohde, J.-U.; In, J.-H.; Lim, M. H.; Brennessel, W. W.; Bukowski, M. R.; Stubna, A.; Münck, E.; Nam, W.; Que Jr., L. *Science* **2003**, *299*, 1037-1039.

(14) MacBeth, C. E.; Golombek, A. P.; Jr., V. G. Y.; Yang, C.; Kuczera, K.; Hendrich, M. P.; Borovik, A. S. *Science* **2000**, *289*, 938-941.

(15) Green, M. T.; Dawson, J. H.; Gray, H. B. *Science* **2004**, *304*, 1653-1656.

(16) Holland, P. L.; Andersen, R. A.; Bergman, R. G. *Comments on Inorganic Chemisry* **1999**, *21(1-3)*, 115-129.

(17) Sharp, P. R. *Dalton Trans.* **2000**, *16*, 2647-2657.

(18) Schroder, D.; Schwarz, H.; Shaik, S. In *Structure and Bonding*; Springer-Verlag GmbH: Berlin, 2000; Vol. 97 (Metal-Oxo and Metal-Peroxo Species in Catalytic Oxidations), p 91-123.

(19) Siegbahn, P. E. M.; Crabtree, R. H. In *Structure and Bonding*; Publisher: Springer-Verlag GmbH: Berlin, 2000; Vol. 97, p 125-144.

(20) Hay-Motherwell, R. S.; Wilkinson, G.; Hussain-Bates, B.; Hursthouse, M. B. *Polyhedron* **1993**, *12*, 2009-2012.

(21) Jacobi, B. G.; Laitar, D. S.; Pu, L.; Wargocki, M. F.; DiPasquale, A. G.; Fortner, K. C.; Schuck, S. M.; Brown, S. N. *Inorg. Chem.* **2002**, *41*, 4815-4823.

(22) Eckert, N. A.; Stoian, S.; Smith, J. M.; Bominaar, E. L.; Münck, E.; Holland, P. L. *J. Amer. Chem. Soc.* **2005**, *127*, 9344-9345.

(23) Vicic, D. A.; Jones, W. D. *J. Am. Chem. Soc.* **1999**, *21*, 4070-4071.

(24) Mindiola, D. J.; Hillhouse, G. L. *J. Am. Chem. Soc.* **2001**, *123*, 4623-4624.

(25) Thyagarajan, S.; Shay, D. T.; Incarvito, C. D.; Rheingold, A. L.; Theopold, K. H. *J. Am. Chem. Soc.* **2003**, *125*, 4440-4441.

(26) Lucas, R. L.; Powell, D. R.; Borovik, A. S. *J. Amer. Chem. Soc.* **2005**, *127*, 11596-11597.

(27) Melenkivitz, R.; Mindiola, D. J.; Hillhouse, G. L. *J. Am. Chem. Soc.* **2002**, *124*, 3846-3847.

(28) Mindiola, D. J.; Hillhouse, G. L. *J. Am. Chem. Soc.* **2002**, *124*, 9976-9977.

(29) Kogut, E.; Zeller, A.; Warren, T. H.; Strassner, T. *J. Am. Chem. Soc.* **2004**, *126*, 11984-11994.

(30) MacBeth, C. E.; Thomas, J. C.; Betley, T. A.; Peters, J. C. *J. Inorg. Chem* **2004**, *43*, 4645-4662.

(31) Appleby, A. J.; Foulkes, F. R. *Fuel cell handbook*; Krieger Publising Company, Malabar, Florida, 1993.

(32) Somorjai, G. A. *Introduction to surface chemistry and catalysis*; Wiley: New York, 1994.

(33) Malleron, J.-L.; Fiaud, J.-C.; Legros, J.-Y. *Handbook of Palladium-Catalyzed Organic Reactions: Synthetic Aspects and Catalytic Cycles*; Academic Press: San Diego, CA., 1997.

(34) Singh, A.; Sharp, P. R. *Dalton Trans.* **2005**, 2080-2081.

(35) Luyben, M. L.; Tyreus, B. D. *Computers & Chem. Eng.* **1998**, *22(7-8)*, 867-877.

(36) Macleod, N.; Keel, J. M.; Lambert, R. M. *Appl. Catal. A,* **2004**, *261*, 37-46.

(37) Valden, M.; Lai, X.; Goodman, D. W. *Science* **1998**, *281*, 1647-1650.

(38) Chen, M. S.; Goodman, D. W. *Science* **2004**, *306*, 252-255.

(39) Arrii, S.; Morfin, F.; Renouprez, A. J.; Rousset, J. L. *J. Am. Chem. Soc.* **2004**, *126*, 1199-1205.

(40) Kim, W. B.; Voitl, T.; Rodriguez-Rivera, G. J.; Dumesic, J. A. *Science* **2004**, *305*, 1280-1283.

(41) *Catalysis by Gold*; Hutchings, G. J.; Haruta, M., Eds.; Elsevier: New York, 2005; Vol. 291.

(42) Barteau, M. A. *Topics in Catalysis* **2003**, *22*.

(43) Linic, S.; Piao, H.; Adib, K.; Barteau, M. A. *Angew. Chem. Int. Ed.* **2004**, *43*, 2918-2921.

(44) Linic, S.; Barteau, M. A. *J. Am. Chem. Soc.* **2004**, *126*, 8086-8087.

(45) *Polyoxometalate Chemistry From Topology via Self-Assembly to Applications*; Pope, M. T.; Müller, A., Eds.; Kluwer Academic Publishers: Dordrecht, 2001.

(46) *Polyoxometalate Chemistry for Nano-Composite Design*; Yamase, T.; Pope, M. T., Eds.; Kluwer Academic/Plenum Publishers: New York, 2002; Vol. 2.

(47) Pope, M. T. In *Comprehensive Coordination Chemistry II: From Biology to Nanotechnology*; Wedd, A. G., Ed.; Elsevier Ltd.: Oxford, UK, 2004; Vol. 4, p 635-678.

(48) Hill, C. L. In *Comprehensive Coordination Chemistry-II: From Biology to Nanotechnology*; Wedd, A. G., Ed.; Elsevier Ltd.: Oxford, UK, 2004; Vol. 4, p 679-759.

(49) Kozhevnikov, I. V. *Catalysis by Polyoxometalates*; Wiley: Chichester, England, 2002; Vol. 2.

(50) Tourné, C. M.; Tourné, G. F. *J. Chem. Soc., Dalton Trans.* **1988**, 2411-2420.

(51) Contant, R. *Can. J. Chem.* **1987**, *65*, 568-573.

(52) Tourné, C. M.; Tourné, G. F.; Weakley, T. J. R. *J. Chem. Soc. Dalton Trans.* **1986**, 2237-2242.

(53) Zhang, X.; Chen, Q.; Duncan, D. C.; Campana, C.; Hill, C. L. *Inorg. Chem.* **1997**, *36*, 4208-4215.

(54) Zhang, X.; Chen, Q.; Duncan, D. C.; Lachicotte, R. J.; Hill, C. L. *Inorganic Chemistry* **1997**, *36*, 4381-4386.

(55) SMART; Bruker AXS, I.; 5.628 ed.; Analytical X-ray Systems: Madison, WI, 2003.

(56) SAINT; Bruker AXS, I.; 6.28 ed.; Analytical X-ray Systems: Madison, WI, 2003.

(57) SHELXTL; 6.14 ed.; Bruker AXS, Inc.: Madison, WI, 2003.

(58) SADABS; Sheldrick, G.; 2.10 ed. 2003.

(59) Ankudinov, A. L.; Rehr, J. J. *Phys. Rev. B* **1997**, *56*, R1712-R1715.

(60) Ellis, P. J.; Freeman, H. C. *Journal of Synchrotron Radiation* **1995**, *2*, 190-195.

(61) Tézé, A.; Hervé, G. In *Inorganic Syntheses*; Ginsberg, A. P., Ed.; John Wiley and Sons: New York, 1990; Vol. 27, p 85-96.

(62) Weinstock, I. A.; Cowan, J. J.; Barbuzzi, E. M. G.; Zeng, H.; Hill, C. L. *J. Am. Chem. Soc.* **1999**, *121*, 4608-4617.

(63) Cowan, J. J.; Bailey, A. J.; Heintz, R. A.; Do, B. T.; Hardcastle, K. I.; Hill, C. L.; Weinstock, I. A. *Inorg. Chem.* **2001**, *40*, 6666-6675.

(64) Cowan, J. J.; Hill, C. L.; Reiner, R. S.; Weinstock, I. A. In *Inorganic Syntheses*; Coucouvanis, D., Ed.; John Wiley& Sons, Inc.: New York, 2002; Vol. 33, p 18-26.

(65) Geletii, Y. V.; Hill, C. L.; Bailey, A. J.; Hardcastle, K. I.; Atalla, R. H.; Weinstock, I. A. *Inorg. Chem.* **2005**, *44*, 8955-8966.

(66) Scott, S. L.; Chen, W.-J.; Bakac, A.; Espanson, J. H. *J. Phys. Chem.* **1993**, *97*, 6710-6714.

(67) Forni, L. G.; Mora-Arellano, V. O.; Packer, J. E.; Willson, R. L. *J. Chem. Soc. Perkin Trans. 2* **1986**, *1*, 1-6.

(68) Qi, B.; Perez, I.; Ansari, P. H.; Lu, F.; Croft, M. *Phys. Rev. B* **1987**, *36*, 2972-2975.

(69) Benfield, R. E.; Grandjean, D.; Kroll, M.; Pugin, R.; Sawitowski, T.; Schmid, G. *J. Phys. Chem. B* **2001**, *105*, 1961-1970.

(70) Berrodier, I.; Farges, F.; Benedetti, M.; Winterer, M.; Brown, G. E.; Deveughele, M. *Geochimica et Cosmochimica Acta* **2004**, *68*, 3019-3042.

(71) Shaw, C. F.; Schaeffer, N. A.; Elder, R. C.; Eidsness, M. K.; Trooster, J. M.; Calis, G. H. M. *J. Am. Chem. Soc.* **1984**, *106*, 3511-3521.

(72) Re, R. E. D.; Hopkins, M. D. *Inorg. Chem.* **2002**, *41*, 6973-6985.

(73) Bi, L.-H.; Reicke, M.; Kortz, U.; Keita, B.; Nadjo, L.; Clark, R. J. *Inorg. Chem.* **2004**, *43*, 3915-3920.

(74) Bi, L.-H.; Kortz, U.; Keita, B.; Nadjo, L.; Borrmann, H. *Inorg. Chem.* **2004**, *43*, 8367-8372.

(75) Bi, L.-H.; Kortz, U.; Keita, B.; Nadjo, L.; Daniels, L. *Eur. J. Inorg. Chem.* **2005**, 3034-3041.

(76) Lubert, K. H.; Guttmann, M.; Beyer, L.; Kalcher, K. *Electrochem. Commun.* **2001**, *3*, 102-106.

(77) Filowitz, M.; Ho, R. K. C.; Klemperer, W. G.; Shum, W. *Inorg. Chem.* **1979**, *18*, 93-103.

(78) *^{17}O NMR Spectroscopy in Organic Chemistry*; Boykin, D. W., Ed.; CRC Press, Inc.: Boca Raton, 1991.

(79) Besecker, C. J.; Klemperer, W. G.; Maltbie, D. J.; Wright, D. A. *Inorg. Chem.* **1985**, *24*, 1027-1032.

(80) Klemperer, W. G. *Angew. Chem., Int. Ed.* **1978**, *17*, 246-254.

(81) Filowitz, M.; Klemperer, W. G.; Messerle, L.; Shum, W. *J. Am. Chem. Soc.* **1976**, *98*, 2345-2346.

(82) Berry, J. F.; Bill, E.; Bothe, E.; George, S. D.; Mienert, B.; Neese, F.; Wieghardt, K. *Science* **2006**, *312*, 1937-1941.

Chapter 5 $[(MO(OH_2))_2WO(OH_2)(PW_9O_{34})_2]$ (M = Pd)

A Dinuclear Terminal Palladium Oxo Complex: $[(MO(OH_2))_2P_2W_{19}O_{69}(OH_2)]^{10-}$ (M = Pd)

Prepared for submission to *J. Am. Chem. Soc.*

with Elena Slonkina, Britt Hedman, Keith O. Hodgson, Kenneth I. Hardcastle, Travis M. Anderson, Djamaladdin G. Musaev, Keiji Morokuma, and Craig L. Hill

5.1 Abstract

For the first time, a molecular complex with two terminal palladium-oxo units is successfully synthesized and isolated as crystalline needles. The di-Pd-oxo complex $Cs_{3.5}K_3Na_{3.5}[(O=Pd^{IV}(OH_2))_2P_2W_{19}O_{68}(OH)_2]\bullet 20H_2O$ (**6**) crystallizes in monoclinic *C2/m* space group, with a = 32.2750(7) Å, b = 16.4638(4) Å, c = 16.2229(4) Å, β = 94.161(2)°, V = 8597.6(4) Å^3, and Z = 4 (final R = 0.0639). Very short Pd-oxo distance (1.66 angstrom) is established by both X-ray single crystal diffraction and extended X-ray absorption fine structure methods, indicating a multiply bound terminal oxo ligand on a d^6 Pd(IV) center. Crystallography studies show that the two terminal Pd-oxo units are neighboring and the oxo ligands are sterically protected by a non-oxidizable metal-oxide-cluster (polytungstate) ligand. The terminal oxygen on the Pd(IV)-oxo unit can selectively transfer to other substrates, resulting in a Pd(II) polytungstate, $Cs_5K_3Na_2[Pd^{II}{}_2P_2W_{19}O_{69}(OH_2)]\bullet 18H_2O$ (**7**), isolated and characterized by X-ray crystallography. Complex **7** crystallizes in monoclinic *P2(1)/n* space group, with a = 16.7117(6) Å, b = 19.5981(7) Å, c = 26.0240(9) Å, β = 95.454(2)°, V = 8484.7(5) Å^3, and Z = 4 (final R = 0.0496). The di-Pd-oxo complex has been further characterized by FT-IR, ^{31}P NMR spectroscopy, thermogravimetric analysis (TGA), differential scanning calorimetry (DSC), and other techniques.

5.2 Introduction

Palladium complexes and redox metal oxides (such as titania and ceria) supported Pd(0) are widely used as homogenous and heterogenous catalysts in O_2-based green organic oxidations, catalytic converters, fuel cell cathodes and many others, and attract major interests in some of the most technologically and economically significant processes at present.[1-15] Palladium-oxo, especially, terminal Pd-oxo (O^{2-}) species are well thought to be involved in these Pd-based catalytic chemistry and technology and have long been sought experimentally.[1-4,16] However, due to the maximal mismatch of metal and ligand atom (oxygen) electronegativities and orbital energies, and furthermore, the population of antibonding orbitals in the high d-electron counts metal-oxo unit, the preparation and investigation of the terminal metal-oxo complexes of the late transition metal elements (e.g. Pd-oxo) is highly problematic. Although numerous studies have been carried out, the structural and chemical features of the supported noble metals especially supported palladium are still not well understood.

Recently, we were above to prepare and characterize several late transition-metal oxo (LTMO) complexes[17-19] using appropriate polytungstate ligands,[20-24] which are metal oxide clusters that share many features in common with the redox metal-oxide supports and can act as π acceptors to delocalize the d electron counts on the metals. These complexes can play as the molecular models for the investigation of the interface between noble metals and metal-oxide surfaces and for the reactivity studies. However, all these isolated LTMO complexes to date contain only one terminal noble metal-oxo unit in each molecule. Considering the distinctive electronic and chemical properties involved in the multinuclear nanostructured metals on the support[25-27] (a good example is

shown by Goodman and co-workers that the gold bilayer structure is significantly more active than the monolayer in the catalytic oxidation of carbon monoxide[28]), we now report the synthesis and characterization of the first dinuclear terminal Pd-oxo complex, $Cs_{3.5}K_3Na_{3.5}[(O=Pd(OH_2))_2P_2W_{19}O_{68}(OH)_2]$ (**6**). The two neighboring Pd-oxo units are incorporated in a polytungstate ligand, which resembles the anchored dinuclear noble metal active sites on metal oxide surfaces (**Figure 5.1**). Interestingly, the deoxygenated form of **6** can be obtained by reaction with oxo accepting reagents, and the structure of its isolated crystalline form is confirmed by X-ray single crystal diffraction. To the best of our knowledge, this is the first time to report a well-documented, clean oxo transfer reaction of the transition metal elements in group 10-12 on the periodic table.

5.3 Experimental Section

General Methods and Materials

Complex $Na_9[A\text{-}\alpha\text{-}PW_9O_{34}]\bullet 7H_2O$ was obtained by published procedures.[29] Its purity was confirmed by both FT-IR and ^{31}P NMR. Palladium sulfate dihydrate ($PdSO_4\bullet 2H_2O$) was purchased from Alfa Aesar, and was used without further purification. Elemental analyses of Cs, K, Na, P, Pd and W were performed by Desert Analytics (Tucson, Arizona) and Galbraith Laboratories (Knoxville, Tennessee). Infrared spectra (2% sample in KBr) were recorded on a Thermo Nicolet 6700 instrument. ^{31}P NMR measurements were made on a Varian INOVA 400 MHz spectrometer, and peaks were referenced to 85% H_3PO_4. Electronic absorption spectra of **6** were collected on a

Hitachi U-3501 UV-Vis-NIR spectrophotometer using a single-beam configuration at 2.0 nm resolution. Average magnetic susceptibilities were measured on a Johnson-Matthey Model MSB-1 magnetic susceptibility balance as neat powders at 24 °C; the balance was calibrated using $Hg[Co(SCN)_4]$ as a standard. Pascal's constants were used to obtain the final diamagnetic corrections. Thermogravimetric data were collected on Instrument Specialists Incorporated TGA 1000 instruments.

Synthesis of $Cs_{3.5}K_3Na_{3.5}[(O=Pd^{IV}(OH_2))_2P_2W_{19}O_{68}(OH)_2]\bullet 20H_2O$ (6)

A 1.0 g (4.2 mmol) sample of palladium sulfate dihydrate ($PdSO_4\bullet 2H_2O$) is suspended in 50 mL of acetate buffer (0.25 M $NaOOCCH_3$ and 0.25 M $HOOCCH_3$, pH = 4.9) at room temperature and 7 g (2.8 mmol) of $Na_9[A\text{-}PW_9O_{34}]\bullet 7H_2O$ is added in *ca.* 1 g portions quickly with vigorous stirring. After 0.5-1 min, 10 g of CsCl are added to the nearly clear brown solution (pH = 3), and the solution is stirred for 2 additional min. A light brown solid is then separated by filtration, dried in air for 10 min and re-dissolved in *ca.* 150 mL of water at 55 °C. The solution becomes red-brown in color upon heating. Then, 3.82 g sample of LiCl and 6.70 g sample of KCl are added to this solution, and the pH of the solution is lowered from 7.5 to 6.5 by the drop-wise addition of 6 M HCl. After cooling to room temperature, the solution is filtered using a fine filter paper. After an additional 24 to 48 h, small brown needles of **6** appear (0.5 g, 6% yield). The crystals are filtered and dried in air. Analytical data: IR (2% KBr pellet, 1200 - 400 cm^{-1}): 1077 (s), 1018 (s), 946 (s), 921 (s), 849 (sh), 800 (sh), 748 (s), 717 (s), 669 (m), 652 (sh), 591 (s), and 516 (w). ^{31}P NMR (2 mM solution in D_2O): -12.0 ppm ($\Delta\nu_{1/2}$ = 8 Hz). Electronic spectral data (400 - 800 nm, in H_2O (3.6 mM sample, 1 cm cell path length))

[λ, nm (ε, M^{-1} cm^{-1})]: 447 nm (299) and 520 nm (sh, 122). Magnetic susceptibility: μ_{eff} = 0 μ_B mol^{-1}. Anal. Calcd. for $Cs_{3.5}K_3Na_{3.5}[(O=Pd^{IV}(OH_2))_2P_2W_{19}O_{68}(OH)_2]\bullet 20H_2O$: Cs, 7.78; K, 1.96; Na, 1.35; P, 1.04; Pd, 3.56; W, 58.4. Found: Cs, 8.02; K, 2.10; Na, 1.25; P, 0.90; Pd, 3.62; W, 57.8. [MW = 5981 g/mol]

Crystallography Studies

The complete datasets for **6**, **7** and **8** were collected at Emory University. Single crystals of $Cs_{3.5}K_3Na_{3.5}[(O=Pd^{IV}(OH_2))_2P_2W_{19}O_{68}(OH)_2]\bullet 20H_2O$ (**6**), $Cs_5K_3Na_2[Pd^{II}{}_2P_2W_{19}O_{69}(OH_2)]\bullet 18H_2O$ (**7**) and $Cs_5K_3Na_3[Pd^{II}{}_{2.5}P_2W_{18.5}O_{68.5}(OH_2)_{0.5}]\bullet 18H_2O$ (**8**) suitable for X-ray analysis, were each coated with Paratone-N oil, suspended in a small fiber loop, and placed in a cooled gas stream on a Bruker D8 SMART APEX CCD sealed tube diffractometer. Diffraction intensities were measured using graphite monochromated Mo Kα radiation (λ = 0.71073 Å) at 173(2) K and a combination of φ and ω scans with 10 s frames traversing about ω at 0.3° increments. Data collection, indexing, and initial cell refinements were carried out using SMART;[30] frame integration and final cell refinements were done using SAINT.[31] The molecular structure of each complex was determined using Direct Methods and Fourier techniques and refined by full-matrix least squares.[32] A multiple absorption correction, including face indexed absorption correction, was applied using the program SADABS.[33] The largest residual electron density for each structure was located close to (less than 1.0 Å from) countercation atom and was most likely due to imperfect absorption corrections frequently encountered in heavy-metal atom structures. Crystal data and structural refinement for the X-ray structures of

$Cs_{3.5}K_3Na_{3.5}[(O=Pd^{IV}(OH_2))_2P_2W_{19}O_{68}(OH)_2]$ (**6**), $Cs_5K_3Na_3[Pd^{II}_{2.5}P_2W_{18.5}O_{68.5}(OH_2)_{0.5}]$ (**8**) and $Cs_5K_3Na_2[Pd^{II}_2P_2W_{19}O_{69}(OH_2)]$ (**7**) are summarized in **Table 5.1**. All the atoms were refined anisotropically except solvent water molecules. Scattering factors and anomalous dispersion corrections are taken from the *International Tables for X-ray Crystallography*. Structure solution, refinement, graphic and generation of publication materials were performed by using SHELXTL, V6.14 software.[32]

X-ray Absorption Spectroscopy

A 150 mg crystalline sample of **6** was finely ground, and the resultant powder was pressed into a 1 mm thick aluminum spacer with X-ray transparent kapton windows. The Pd *K*-edge X-ray absorption spectra for **6** were measured at the Stanford Synchrotron Radiation Laboratory (SSRL) on focused (Rh-coated toroid) 30-pole wiggler beam line 10-2 with the ring operating at 3 GeV, 85-100 mA. A liquid nitrogen cooled Si(220) monochromator was utilized for energy selection at the Pd *K*-edge. The monochromator was detuned 30% at 25345 eV to minimize higher harmonic components in the X-ray beam. Data were collected in transmission mode, and internal energy calibration was performed by simultaneous measurement of the absorption of a Pd foil placed between two ionization chambers located after the sample. The first inflection point of the foil was assigned to 24349.0 eV. The sample was maintained at 10 K using an Oxford Instruments CF1208 continuous flow liquid helium cryostat. Three scans of the energy range 24020 – 25345 eV were collected and averaged. The averaged data were processed by fitting a first-order polynomial to the pre-edge region and subtracting this background

from the entire spectrum. A three-region spline of orders 2, 3, and 3 was used to model the smooth background above the edge.

Theoretical EXAFS signals were calculated using FEFF (version 7.02),[34] and refinements of the structural model to the data were done by a non-linear least-squares fitting process in *k*-space using EXAFSPAK. Atom coordinates for the initial model were obtained from the crystallographic structure of **6**. The experimental energy threshold E_0 was chosen as 24370 eV and was allowed to vary by a common amount (ΔE_0) for all components within a given fit. The structural parameters that were varied during the refinements included the bond distance (R) and the bond variance (σ^2).

Reduction of 6 with Na_2SO_3 and $(CH_3)_2S$

Reductions of **6** by oxo accepting reagents, such as sodium sulfite (Na_2SO_3), dimethyl sulfide (DMS) and triphenylphosphine (Ph_3P), are conducted in aqueous solution. An exemplary procedure is described as below: a 20 mg solid sample of **6** is dissolved in 5 mL of deionized water at room temperature with vigorous stirring. After complete dissolution of **6**, the electronic absorption spectrum of the fresh brown solution is collected. One equivalent of reducing agent (e.g. Na_2SO_3) is then added to the solution, and the reaction is followed by electronic absorption spectroscopy. More reducing agent is applied if the reaction does not go to completion. Addition of a small amount of CsCl solid causes a precipitation, and the structure of crystalline precipitates is determined by X-ray single crystal diffraction.

Computational Studies

All calculations were performed using the Gaussian 03[35] program at the B3LYP/Lanl2dz level of theory. An overall charge and spin multiplicity of the studied structures chosen to be "4-" and "1", respectively.

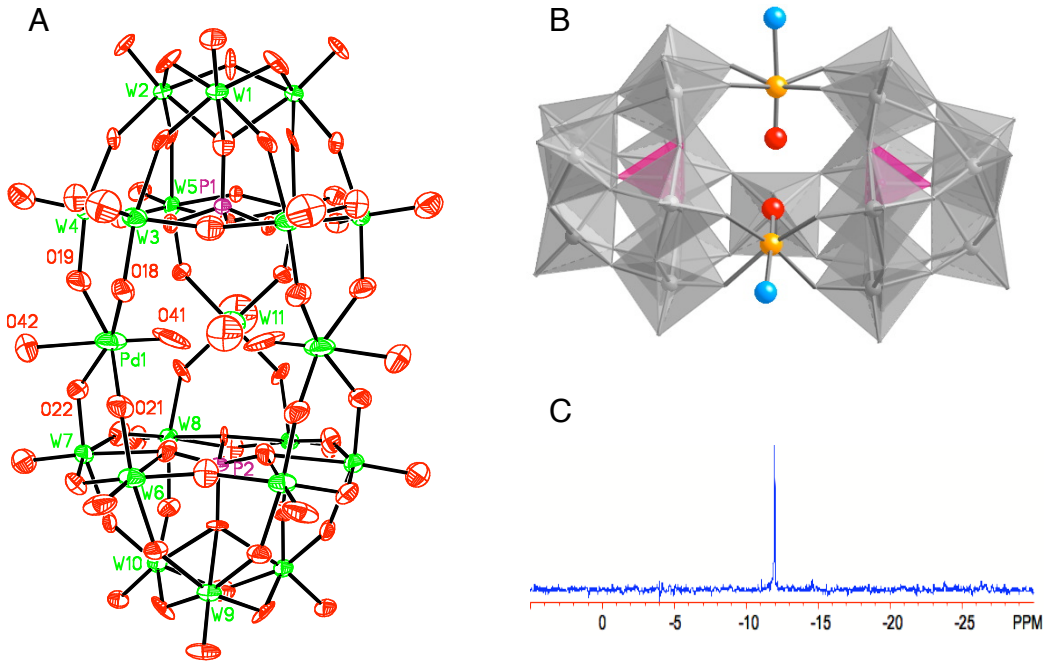

Figure 5.1 Combination polyhedral/ball-and-stick representation of polyanion **6** (top right) and its thermal ellipsoid plots and numbering scheme (left). The WO_6 (or W atom) and PO_4 polyhedra are shown in gray and pink. The Pd, O atoms and aqua (H_2O) ligands are shown in yellow, red, and blue, respectively. The very short Pd-O bond on the axial position is 1.66(3) Å, and is trans to a longer Pd-OH_2 bond (2.199(18) Å). The central Pd atom is displaced out of the equatorial O_4 plane toward the terminal oxo by 0.30(2) Å. ^{31}P NMR spectrum of 6 in aqueous solution (bottom right), showing one single peak at -12.00 ppm, a result consistent to the crystallographic studies.

Table 5.1 Crystal data and structural refinement for the X-ray structures of $Cs_{3.5}K_3Na_{3.5}[(O=Pd^{IV}(OH_2))_2P_2W_{19}O_{68}(OH)_2]$ (**6**), $Cs_5K_3Na_3[Pd^{II}_{2.5}P_2W_{18.5}O_{68.5}(OH_2)_{0.5}]$ (**8**) and $Cs_5K_3Na_2[Pd^{II}_2P_2W_{19}O_{69}(OH_2)]$ (**7**)

complex	**6**
molecular formula	$H_{46}Cs_{3.5}K_3Na_{3.5}O_{94}P_2Pd_2W_{19}$
formula wt. (g mol^{-1})	5981.18
temperature (K)	173(2)
radiation (λ, Å)	0.71073
crystal system	Monoclinic
space group	*C2/m* (#12)
a (Å)	32.2750(7)
b (Å)	16.4638(4)
c (Å)	16.2229(4)
β (º)	94.161(2)
Volume ($Å^3$)	8597.6(4)
Z	4
ρ_{calcd} (g cm^{-3})	4.474
μ (mm^{-1})	27.481
F(000)	9984
crystal size (mm^3)	0.22 × 0.10 × 0.03
reflections collected	33998
independent reflections	8929 [R(int) = 0.0750]
absorption correction	SADABS and face index
refinement method	full-matrix least-squares on F^2
goodness-of-fit on F^2	1.011
final R indices [R > 2σ (I)]	$R1^a$ = 0.0639 $wR2^b$ = 0.2088
R indices (all data)	$R1^a$ = 0.0942 $wR2^b$ = 0.2400
largest diff. peak and hole (e $Å^{-3}$)	6.001 and -9.586

$^aR_1 = \Sigma||F_o| - |F_c|| / |F_o|$

$^bwR_2 = \{\Sigma[w(F_o^2 - F_c^2)^2] / \Sigma[w(F_o^2)^2]\}^{0.5}$

Table 5.1 Continued: Crystal data and structural refinement for the X-ray structures of $Cs_{3.5}K_3Na_{3.5}[(O=Pd^{IV}(OH_2))_2P_2W_{19}O_{68}(OH)_2]$ (**6**), $Cs_5K_3Na_3[Pd^{II}_{2.5}P_2W_{18.5}O_{68.5}(OH_2)_{0.5}]$ (**8**) and $Cs_5K_3Na_2[Pd^{II}_2P_2W_{19}O_{69}(OH_2)]$ (**7**)

complex	**8**	**7**
molecular formula	$H_{37}Cs_5K_3Na_3O_{87}P_2Pd_{2.5}W_{18.5}$	$H_{38}Cs_5K_3Na_2O_{88}P_2Pd_2W_{19}$
formula wt. (g mol^{-1})	6009.26	6041.99
temperature (K)	173(2)	173(2)
radiation (λ, Å)	0.71073	0.71073
crystal system	Monoclinic	Monoclinic
space group	*C2/m* (#12)	*P2(1)/n* (#14)
a (Å)	32.0196(6)	16.7117(6)
b (Å)	16.3455(3)	19.5981(7)
c (Å)	20.4233(4)	26.0240(9)
β (º)	119.7830(10)	95.454(2)
Volume ($Å^3$)	9277.2(3)	8484.7(5)
Z	4	4
ρ_{calcd} (g cm^{-3})	4.274	4.619
μ (mm^{-1})	25.899	28.469
F(000)	10252	10136
crystal size (mm^3)	0.23 × 0.16 × 0.05	0.25 × 0.18 × 0.16
reflections collected	82211	128168
independent refls.	9824 [R(int) = 0.0787]	17452 [R(int) = 0.0962]
absorption correction	SADABS and face index	SADABS and face index
refinement method	full-matrix least-squares on F^2	full-matrix least-squares on F^2
goodness-of-fit on F^2	1.015	1.015
final R indices	$R1^a$ = 0.0433	$R1^a$ = 0.0496
[R > 2σ (I)]	$wR2^b$ = 0.1672	$wR2^b$ = 0.1610
R indices (all data)	$R1^a$ = 0.0496	$R1^a$ = 0.0615
	$wR2^b$ = 0.1752	$wR2^b$ = 0.1725
largest diff. peak and hole (e $Å^{-3}$)	4.961 and -2.866	4.762 and -4.686

$^aR_1 = \Sigma||F_o| - |F_c|| / |F_o|$

$^bwR_2 = \{\Sigma[w(F_o^2 - F_c^2)^2] / \Sigma[w(F_o^2)^2]\}^{0.5}$

5.4 Results and Discussion

Synthesis

In our recent studies on the first isolated and fully characterized terminal Pd-oxo complex, $K_{10}Na_3[Pd^{IV}O(OH)WO(OH_2)(PW_9O_{34})_2]$,[18] we suggest that the reaction of Pd(II) (from $PdSO_4$) with $[A\text{-}\alpha\text{-}PW_9O_{34}]^{9-}$ in 0.25 M sodium acetate/0.25 M acetic acid buffer (pH = 4.9) yields the kinetically precipitated (with KCl) product $[Pd^{II}_3(PW_9O_{34})_2]^{12-}$, which undergoes a rapid, stepwise loss of Pd(II) in acidic media and oxidation by air to form $[Pd^{IV}O(OH)WO(OH_2)(PW_9O_{34})_2]^{13-}$ (**3**). In order to confirm the above suggested reaction mechanism, attempts are made to grow crystals of the kinetic precipitates and determine its structure by X-ray diffraction. It is noticed (see the next section) that use of Cs countercation can stabilize the polyanion structure from hydrolytic decomposition in solution and the speciation can be controlled by the nature of countercations and ionic strength. With these findings on hand, we carry out the same reaction of Pd(II) and $[A\text{-}PW_9O_{34}]^{9-}$ using CsCl as the precipitation reagent.

Addition of the solid sample of polytungstate cluster $Na_9[A\text{-}\alpha\text{-}PW_9O_{34}]$ to the suspension of Pd(II) (from $PdSO_4$) in acetate buffer (pH = 4.9) results in a clear, dark brown solution in *ca.* 10 seconds. Kinetic precipitation by CsCl affords a large amount of brown solids, which are collected by frit filtration and redissolved in 1 M LiCl/1 M KCl solution at 55 ºC under air. Small, brown crystalline needles of **6** form in 2 days if the solution is allowed to an exposure to air. Complex **6** is stable in both solid state and liquid solution. Thermogravimetric analysis shows no loss of dioxygen for the crystalline sample until 750 ºC (**Figure 5.2**). In the liquid solution, one single peak (-12.0 ppm, peak width at half height $\Delta\nu_{1/2}$ = 8 Hz) is observed in the ^{31}P NMR spectroscopy, a result

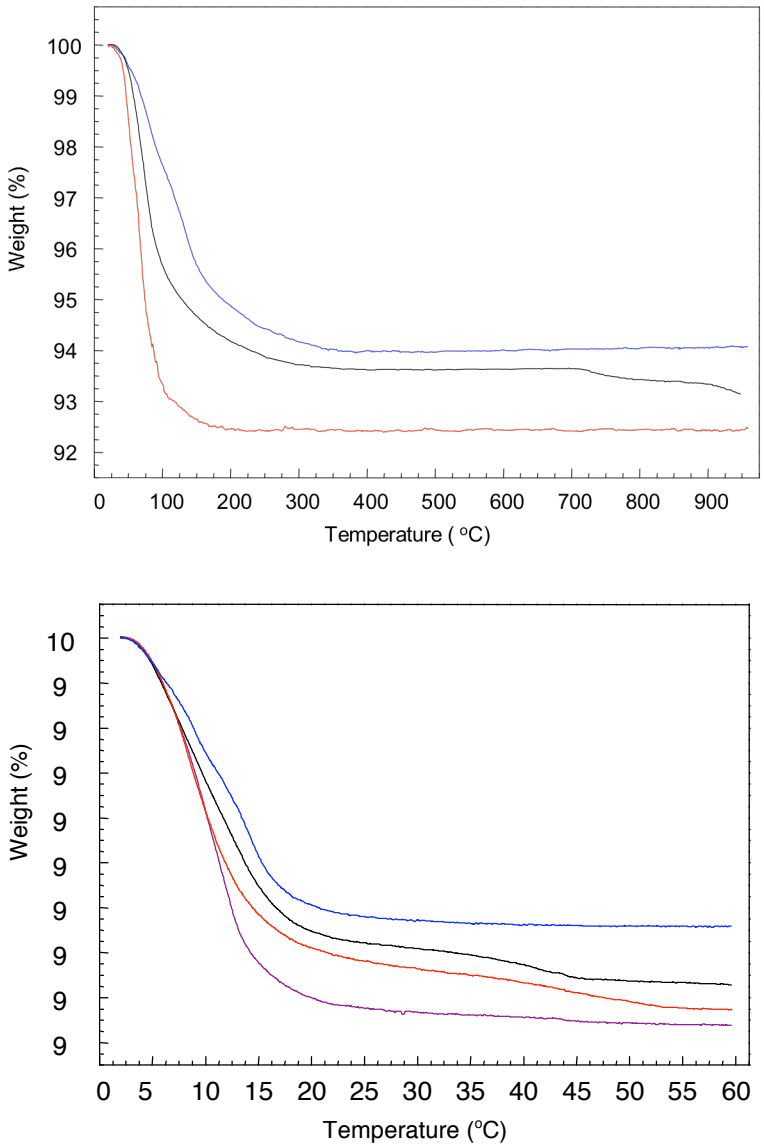

Figure 5.2 Top: thermogravimetric analysis (TGA) of Pd-oxo complex **6** (black) and all-tungsten complexes, $\mathbf{P_2W_{19}}$ (blue) and $\mathbf{P_2W_{20}}$ (red). Bottom: thermogravimetric analysis (TGA) of Au-oxo complexes **2** (black) and **5** (red) compared to their isostructural all-tungsten complexes, $\mathbf{P_2W_{19}}$ (blue) and $\mathbf{P_2W_{21}}$ (purple), respectively.

consistent to the crystallography studies showing that the two phosphor atoms in each molecule are symmetry equivalent (**Figure 5.1**, see below). This result suggests not only the purity of the bulk sample but also the stability of **6** in solution: no other detectable polytungstate species are found in ^{31}P NMR studies. Both magnetic susceptibility result and the chemical shift and peak width in NMR spectrum indicate diamagnetism of **6**.

Thermogravimetric Analysis (TGA)

An interesting result is noticed when the crystalline solid of **6** is applied to thermogravimetric analysis (TGA). As shown in **Figure 5.2**, complex **6** starts to lose additional weight at 720 °C, while the weights of the all-tungsten analogies, $K_{14}[P_2W_{19}O_{69}(OH_2)]$ and $K_{10}[P_2W_{20}O_{70}(OH_2)_2]$, remain constant. This difference as well as the weight percent lost (0.53%) indicates the loss of two oxygen atoms on the two Pd atoms. The similar phenomena are also observed in the previous Au-oxo containing complexes **2** and **5** (**Figure 5.2**).[19] Both terminal Au-oxo complexes starts to lose additional weight at a much lower temperature (450 °C), a result consistent to the common knowledge that gold oxide is thermodynamically less stable than palladium oxide. The thermal evolution of O_2 is under investigation.

Structural Studies

The unprecedented structure type represented by **6** is determined by X-ray single crystal diffraction. Complex **6** crystallize in monoclinic *C2/m* space group, and the two phosphor atoms and W1, W9 and W11 are locating on the symmetry plane (**Figure 5.1**).

Two symmetrically equivalent Pd atoms are six-coordinated: each is bound to two [A-$PW_9O_{34}]^{9-}$ ligands through four oxygens which define a square equatorial plane around the Pd center. The Pd-O_{eq} bond lengths vary from 2.028(18) to 2.086(18) Å, values in the range of singly bonded Pd-O distances (1.95 to 2.10 Å). The very short Pd-O bond on the axial position is 1.66(3) Å, which is consistent with a multiply bonded terminal oxo oxygen on a Pd atom.[36-41] A longer Pd-OH_2 bond (2.199(18) Å) is trans to this terminal Pd=O bond. As commonly seen in the terminal metal-oxo units, the Pd atom is displaced out from the equatorial plane toward the oxo ligand by 0.30(2) Å. Importantly, the Pd=O bond points into the central cavity surrounded by the non-oxidizable polytungstate ligand environment. This structural feature makes the terminal oxo ligand on the Pd atom sterically protected and renders the possibility for selective oxo transfer to small substrates.

The coordination sphere around Pd is further confirmed by an independent structural technique, extended X-ray absorption fine structure (EXAFS). The data for $Cs_{3.5}K_3Na_{3.5}[(O=Pd^{IV}(OH_2))_2P_2W_{19}O_{68}(OH)_2]\bullet 20H_2O$ (**6**) have been fit with models including 4, 5, or 6 oxygen atoms in the first shell at various distances and 4 tungsten atoms at 3.57 Å. EXAFS results indicate that a ~1.7 Å Pd-O component is needed for the data set, as in previous studies with $K_{10}Na_3[Pd^{IV}O(OH)WO(OH_2)(PW_9O_{34})_2]\bullet 16H_2O$ (**3**) and $K_8[Pd^{IV}O(OH_2)P_2W_{20}O_{70}(OH_2)_2]\bullet 22H_2O$ (**4**), a result consistent to the X-ray diffraction studies that six-coordinated Pd(IV) centers with short terminal Pd-oxo bonds are presented in **6**.

Pd(IV) Oxidation State Assignment

The oxidation state of Pd in **6**, after the establishment of the composition and physical structure, is then studied by several methods, and all suggest a d^6 Pd(IV) electronic configuration. First, the six coordination sphere around Pd as well as the Pd-O bond lengths are consistent with the 4+ oxidation state, and bond valence calculation suggests Pd(IV) assignment. Second, electronic absorption spectroscopy shows two absorption bands in the visible region, at 19,230 cm^{-1} (band 1) and 22,370 cm^{-1} (band 2). The electronic absorption spectrum of **6** is similar to those well-documented Pd-oxo polytungstate complexes **3** (19,530 and 22,520 cm^{-1})[18] and **4** (19,450 and 22,120 cm^{-1}), and these two bands are assigned to the Pd(IV) ligand field bands as $e \rightarrow b_1$ (band 1) and $b_2 \rightarrow b_1$ (band 2) based on our previous experiences. Third, all the countercations can be located in X-ray crystallography and found by elemental analysis, and the resulted charge balance calculation supports the 4+ oxidation state at Pd. Finally, the diamagnetism of **6** confirmed by magnetic susceptibility studies and NMR chemical shift and peak width is consistent with a d^6 Pd(IV) electronic structure.

Reduction of 6

In order to study its reactivity, complex **6** is treated with several reducing/oxo-accepting regents. Addition of sodium sulfite (Na_2SO_3) to the water solution of **6** causes a change in the electronic absorption spectrum (**Figure 5.3**). The bump like maxima around 450 nm disappears; and synchronously, the absorption between 380 and 420 nm increases. This change is indicative of a reduction of Pd(IV) in solution. However, the reduction of **6** by Na_2SO_3 is not stoichiometric: extra reducing agent Na_2SO_3 is needed

for the complete reaction (no more changes in the UV-vis spectra). Importantly, addition of a small amount of solid CsCl salt to the above resulted solution affords an intensely brown colored, X-ray quality plate crystals **8**. Crystallography studies reveal its structure and composition. Similar to the starting Pd(IV)-oxo complex **6**, the plate crystal is in the monoclinic *C2/m* space group, although the unit cell is different. Two square-planar coordinated Pd centers are symmetry equivalent through a mirror plane (**Figure 5.4**). The four Pd-O_{eq} bond distances (from 1.960(10) to 1.990(9) Å) are in good agreement to the Pd-O single bond, suggesting a conventional Pd(II) center incorporated in a polytungstate ligand environment. This result also confirms that the Pd(IV)-oxo unit is reduced by addition of sulfite.

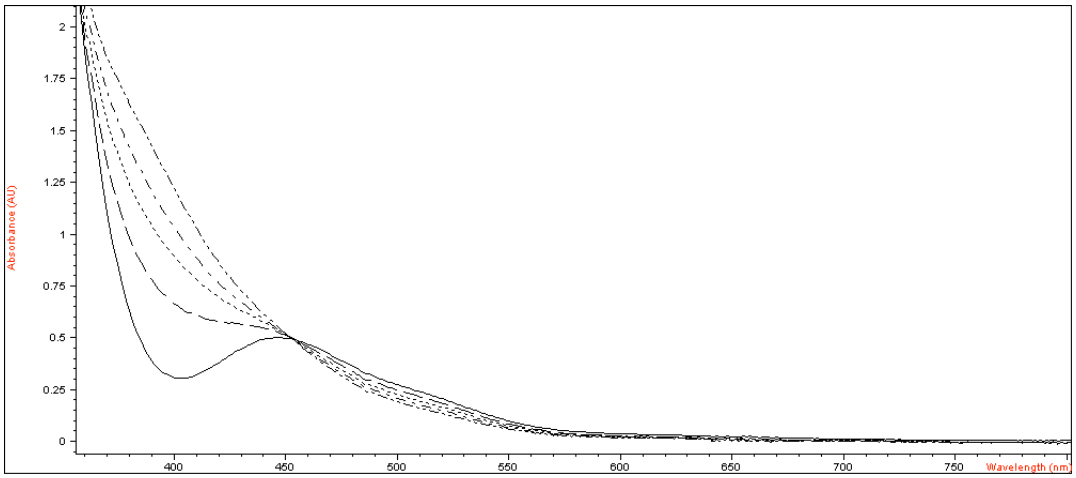

Figure 5.3 Reductive titration of Pd(IV) center in **6** followed by electronic absorption spectroscopy, showing the increased absorption bands at the ranges of 350-450 nm when the Pd(IV) center is reduced.

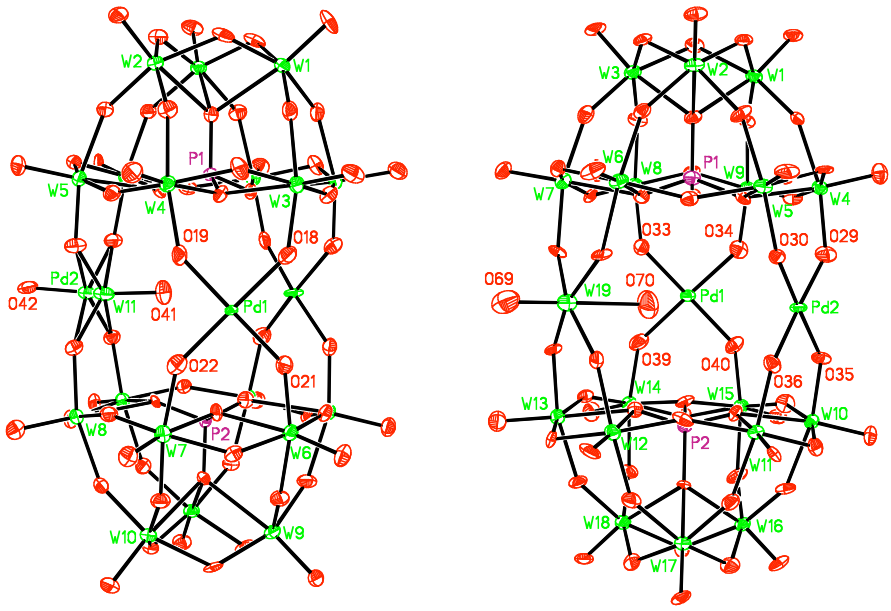

Figure 5.4 Thermal ellipsoid plots and numbering scheme for the two reduced products **8** (left) and **7** (right).

During our initial refinement, we found that the original W11 site in the polyanion of **8** splits to two positions. Free refinement as two positional disordered tungsten atoms led to no reasonable occupancies. In consideration of the very large thermal parameters of the two oxygens bound to this site, O41 and O42, we then modeled the two splits as 50% regular square-planar Pd(II) and 50% $[O=W^{VI}(OH_2)]^{4+}$ (the fractional occupancies are freely determinated). Importantly, the existence of the cocrystalline mixture, $[Pd_{2.5}P_2W_{18.5}O_{68.5}(OH_2)_{0.5}]^{11-}$ (**8**), is also evidenced by ^{31}P NMR spectroscopy: two peaks at -13.68 and -14.20 ppm with similar intensity are observed. In the reaction of **6** with sulfite, it is noticed above that the complete reduction is reached only with excess of SO_3^{2-}. The resulted deoxygenated form, $[Pd_2P_2W_{19}O_{69}(OH_2)]^{10-}$, may partially

decompose under this basic environment and generate the tri-Pd sandwich structure *in situ*. Once it forms in solution, the tri-Pd sandwich complex, $[Pd_3P_2W_{18}O_{68}]^{12-}$, crystallize together with the deoxygenated form of **6** to give the cocrystalline mixture **8**.

A cleaner oxo transfer of **6** is achieved by reacting with dimethyl sulfide. Similar changes in the electronic absorption spectroscopy are observed, indicating the reduction of the Pd(IV)-oxo unit. The formation of dimethyl sulfoxide, the oxidized product, is convinced by ^1H NMR spectroscopy, whose chemical shift is at 1.60 ppm in D_2O. The reaction solution affords deep brown, crystalline prisms **7** at room temperature. Crystallography studies confirm that the prism crystallizes in monoclinic *P2(1)/n* space group. Two independent square-planar Pd(II) centers present in an asymmetric unit cell, each flanked by two $[A\text{-}PW_9O_{34}]^{9-}$ polytungstate ligands through four oxygens (**Figure 5.4**). The $Pd\text{-}O_{eq}$ bond distances of both Pd1 (average 1.976(12) Å) and Pd2 (average 1.962(11) Å) are normal for the Pd-O single bond. Unlike the reaction of **6** with sodium sulfite, no decomposition of the deoxygenated form happens. The W11 atom as well as its terminal oxo and *trans* aqua ligands are well refined with full occupancies, and this leads to the unambiguous determination of the polyanion as $[Pd^{II}_2P_2W_{19}O_{69}(OH_2)]^{10-}$ (**7**).

Interestingly, no reaction takes place between **6** and the more bulky oxo-accepting reagent, triphenylphosphine. Although it is well-understood that the formation of a $Ph_3P{=}O$ bond (-73.8 kcal mol^{-1}) is thermodynamically more favorable than a $Me_2S{=}O$ bond (-27.1 kcal mol^{-1}),[37] the very bulky phenyl groups on the phosphorus atom make the oxo transfer reaction challenging if not impossible with the terminal Pd=O group, which is sterically protected by the non-oxidizable inorganic polytungstate ligand environment. The experiment results are confirmed by the following computational studies.

Computational Studies

Previous experimental results show that no reaction takes place between **6** and the more bulky oxo-accepting reagent triphenylphosphine (PPh_3), in spite of the fact that the bond energy of the formed $O{=}PPh_3$ bond is (~ 45 kJ/mol) larger than that for $O{=}SMe_2$. It is expected that one of reasons of the observed difference in reactivity of **6** with DMS and PPh_3 is a steric repulsion between the reagent and **6,** which is expected to be larger for more bulky reagent PPh_3 than SMe_2.

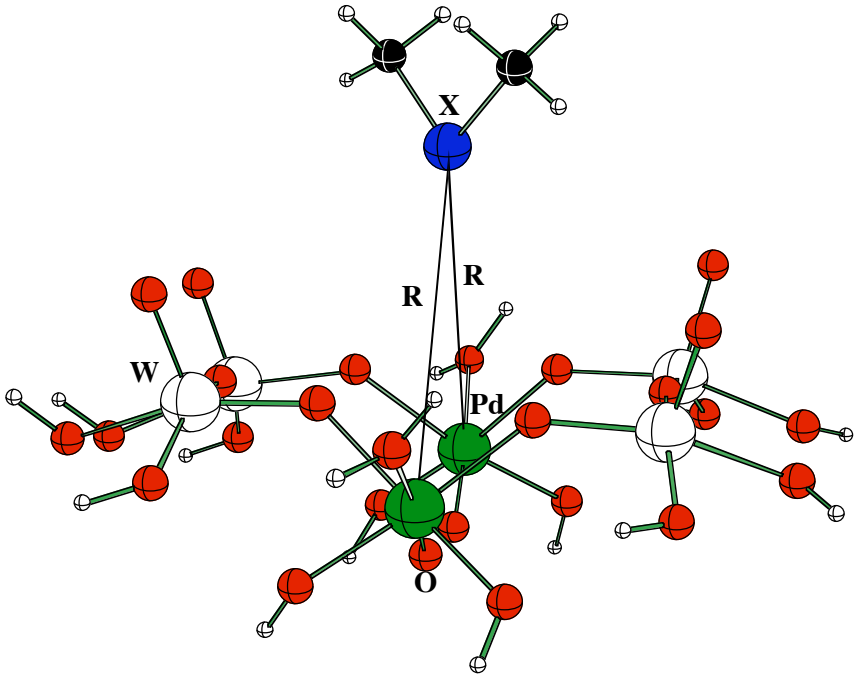

Figure 5.5 The **6m-XL$_n$** model used in the calculations. For simplicity, we have presented only case with **XL$_n$** = SMe_2.

The performed DFT calculations on the model system **6m-XL$_n$** support this assumption (where, **6m,** $[(O=Pd^{IV}(OH_2))_2W_4O_{22}H_{12}]^{4-}$, is chosen to be a model of **6**, which was cut from **6** and terminating of the resulted dangling -O bonds with H-ligands; **XL$_n$** is DMS and PPh_3 (see **Figure 5.5**). In these calculations, the positions of all atoms of **6m** and **XL$_n$** were fixed at their experimental and DFT optimized values, respectively. Total energy of **6m-XL$_n$** was calculated at the given Pd-X (X = S and P) distance, R, which varied from 5.5 Å to 3.5 Å with a step of 0.2 Å. Calculated changes (ΔE_{tot}) to total energy of these systems as a function of Pd-X distance are schematically presented in **Figure 5.6**. As seen from this scheme a steric repulsion between the **6m** and **XL$_n$** fragments is much larger for **XL$_n$** = PPh_3 than SMe_2, a result consistent to the experimental observations.

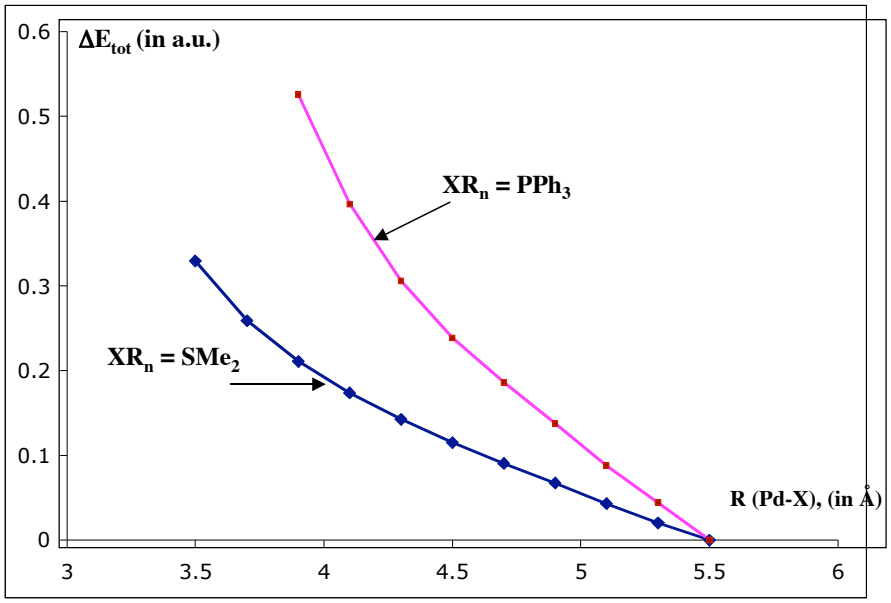

Figure 5.6 Schematic presentation of the changes to the total energies of **6m-XL$_n$** as a function of Pd-X distance (blue line is for **XL$_n$** = DMS, and red line is for **XL$_n$** = PPh_3).

References

(1) Appleby, A. J.; Foulkes, F. R. *Fuel cell handbook*; Krieger Publising Company, Malabar, Florida, 1993.

(2) Somorjai, G. A. *Introduction to surface chemistry and catalysis*; Wiley: New York, 1994.

(3) Malleron, J.-L.; Fiaud, J.-C.; Legros, J.-Y. *Handbook of Palladium-Catalyzed Organic Reactions: Synthetic Aspects and Catalytic Cycles*; Academic Press: San Diego, CA., 1997.

(4) Singh, A.; Sharp, P. R. *Dalton Trans.* **2005**, 2080-2081.

(5) Luyben, M. L.; Tyreus, B. D. *Computers & Chem. Eng.* **1998**, *22(7-8)*, 867-877.

(6) Macleod, N.; Keel, J. M.; Lambert, R. M. *Appl. Catal. A,* **2004**, *261*, 37-46.

(7) Grate, J. R.; Hamm, D. R.; Mahajan, S. In *Polyoxometalates: From Platonic Solids to Anti-retroviral Activity*; Pope, M. T., Müller, A., Eds.; Kluwer Academic Publishers: Dordrecht, 1994, p 281-305.

(8) Davison, S. F.; Mann, B. E.; Maitlis, P. M. *Journal of the Chemical Society, Dalton Transactions: Inorg. Chem.* **1984**, 1223-1228.

(9) Lee, C. W.; Lee, J. S.; Cho, N. S.; Kim, K. D.; Lee, S. M.; Oh, J. S. *J. Mol. Catal.* **1993**, *80*, 31-41.

(10) Kuznetsova, L. I.; Matveev, K. I. *Kinetics and Catalysis* **1984**, *25*, 1274-1275.

(11) Kuznetsova, N. I.; Detusheva, L. G.; Kuznetsova, L. I.; Fedotov, M. A.; Likholobov, V. A. *J. Mol. Cat A: Chem.* **1996**, *114*, 131-139.

(12) Nishimura, T.; Maeda, Y.; Kakiuchi, N.; Uemura, S. *J. Chem. Soc., Perkin Trans. 1* **2000**, *24*, 4301-4305.

(13) Steinhoff, B. A.; Stahl, S. S. *Organic Letters* **2002**, *4*, 4179-4181.

(14) Stahl, S. S. *Angew. Chem. Int. Ed.* **2004**, *43*, 3400-3420.

(15) Hu, A.; Ogasawara, M.; Sakamoto, T.; Okada, A.; Nakajima, K.; Takahashi, T.; Lin, W. *Adv. Synth. Catal.* **2006**, *348*, 2051-2056.

(16) Shelef, M. *Chem. Rev.* **1995**, *95*, 209-225.

(17) Anderson, T. M.; Neiwert, W. A.; Kirk, M. L.; Piccoli, P. M. B.; Schultz, A. J.; Koetzle, T., F.; Musaev, D. G.; Morokuma, K.; Cao, R.; Hill, C. L. *Science* **2004**, *306*, 2074-2077.

(18) Anderson, T. M.; Cao, R.; Slonkina, E.; Hedman, B.; Hodgson, K. O.; Hardcastle, K. I.; Neiwert, W. A.; Wu, S.; Kirk, M. L.; Knottenbelt, S.; Depperman, E. C.; Keita, B.; Nadjo, L.; Musaev, D. G.; Morokuma, K.; Hill, C. L. *J. Am. Chem. Soc.* **2005**, *127*, 11948-11949.

(19) Cao, R.; Anderson, T. M.; Piccoli, P. M. B.; Schultz, A. J.; Koetzle, T. F.; Geletii, Y. V.; Slonkina, E.; Hedman, B.; Hodgson, K. O.; Hardcastle, K. I.; Fang, X.; Kirk, M. L.; Knottenbelt, S.; Kogerler, P.; Musaev, D. G.; Morokuma, K.; Takahashi, M.; Hill, C. L. *J. Am. Chem. Soc.* **2007**, *129*, 11118-11133.

(20) *Polyoxometalate Chemistry From Topology via Self-Assembly to Applications*; Pope, M. T.; Müller, A., Eds.; Kluwer Academic Publishers: Dordrecht, 2001.

(21) *Polyoxometalate Chemistry for Nano-Composite Design*; Yamase, T.; Pope, M. T., Eds.; Kluwer Academic/Plenum Publishers: New York, 2002; Vol. 2.

(22) Pope, M. T. In *Comprehensive Coordination Chemistry II: From Biology to Nanotechnology*; Wedd, A. G., Ed.; Elsevier Ltd.: Oxford, UK, 2004; Vol. 4, p 635-678.

(23) Hill, C. L. In *Comprehensive Coordination Chemistry-II: From Biology to Nanotechnology*; Wedd, A. G., Ed.; Elsevier Ltd.: Oxford, UK, 2004; Vol. 4, p 679-759.

(24) Kozhevnikov, I. V. *Catalysis by Polyoxometalates*; Wiley: Chichester, England, 2002; Vol. 2.

(25) Brown, G. E.; Henrich, V. E.; Casey, W. H.; Clark, D. L.; Eggleston, C.; Felmy, A.; Goodman, D. W.; Grätzel, M.; Maciel, G.; McCarthy, M. I.; Nealson, K. H.; Sverjensky, D. A.; Toney, M. F.; Zachara, J. M. *Chem. Rev.* **1999**, *99*, 77-174.

(26) Valden, M.; Lai, X.; Goodman, D. W. *Science* **1998**, *281*, 1647-1650.

(27) Choudhary, T. V.; Goodman, D. W. *Appl. Catal. A: General* **2005**, *291*, 32-36.

(28) Chen, M. S.; Goodman, D. W. *Science* **2004**, *306*, 252-255.

(29) Domaille, P. J. In *Inorganic Syntheses*; Ginsberg, A. P., Ed.; John Wiley and Sons: New York, 1990; Vol. 27, p 96-104.

(30) SMART; Bruker AXS, I.; 5.628 ed.; Analytical X-ray Systems: Madison, WI, 2003.

(31) SAINT; Bruker AXS, I.; 6.28 ed.; Analytical X-ray Systems: Madison, WI, 2003.

(32) SHELXTL; 6.14 ed.; Bruker AXS, Inc.: Madison, WI, 2003.

(33) SADABS; Sheldrick, G.; 2.10 ed. 2003.

(34) Ankudinov, A. L.; Rehr, J. J. *Phys. Rev. B* **1997**, *56*, R1712-R1715.

(35) Frisch, M. J.; Trucks, G. W.; Schlegel, H. B.; Scuseria, G. E.; Robb, M. A.; Cheeseman, J. R.; Montgomery, J., J. A.; Vreven, T.; Kudin, K. N.; Burant, J. C.; Millam, J. M.; Iyengar, S. S.; Tomasi, J.; Barone, V.; Mennucci, B.; Cossi, M.; Scalmani, G.;

Rega, N.; Petersson, G. A.; Nakatsuji, H.; Hada, M.; Ehara, M.; Toyota, K.; Fukuda, R.; Hasegawa, J.; Ishida, M.; Nakajima, T.; Honda, Y.; Kitao, O.; Nakai, H.; Klene, M.; Li, X.; Knox, J. E.; Hratchian, H. P.; Cross, J. B.; Adamo, C.; Jaramillo, J.; Gomperts, R.; Stratmann, R. E.; Yazyev, O.; Austin, A. J.; Cammi, R.; Pomelli, C.; Ochterski, J. W.; Ayala, P. Y.; Morokuma, K.; Voth, G. A.; Salvador, P.; Dannenberg, J. J.; Zakrzewski, V. G.; Dapprich, S.; Daniels, A. D.; Strain, M. C.; Farkas, O.; Malick, D. K.; Rabuck, A. D.; Raghavachari, K.; Foresman, J. B.; Ortiz, J. V.; Cui, Q.; Baboul, A. G.; Clifford, S.; Cioslowski, J.; Stefanov, B. B.; Liu, G.; Liashenko, A.; Piskorz, P.; Komaromi, I.; Martin, R. L.; Fox, D. J.; Keith, T.; Al-Laham, M. A.; Peng, C. Y.; Nanayakkara, A.; Challacombe, M.; Gill, P. M. W.; Johnson, B.; Chen, W.; Wong, M. W.; Gonzalez, C.; Pople, J. A.; 03 Rev. C1 ed.; Gaussian, Inc.: Pittsburgh, 2003.

(36) Holm, R. H. *Chem. Rev.* **1987**, *87*, 1401-1449.

(37) Holm, R. H.; Donahue, J. P. *Polyhedron* **1993**, *12*, 571-589.

(38) Parkin, G. In *Prog. Inorg. Chem.*; Karlin, K. D., Ed.; Wiley: New York, 1998; Vol. 47, p 1-165.

(39) Nugent, W. A.; Mayer, J. M. *Metal-Ligand Multiple Bonds*; John Wiley & Sons, Inc.: New York, 1988.

(40) Borovik, A. S. *Acc. Chem. Res.* **2005**, *38*, 54-61.

(41) Bakac, A. In *Advances in Inorganic Chemistry* 2004; Vol. 55, p 1-59.

Chapter 6 Countercation Effect

Cesium Countercation Effect: Controlled Speciation of Polytungstates by Cs^+

Prepared for submission to *J. Am. Chem. Soc.*

with Cindee Yates, Kevin O'Halloran, Kenneth I. Hardcastle, Elena Slonkina, Britt Hedman, Keith O. Hodgson, Travis M. Anderson, and Craig L. Hill

6.1 Abstract

In recently published Pd-oxo work, $K_{10}Na_3[Pd^{IV}O(OH)P_2W_{19}O_{69}(OH_2)]\bullet 16H_2O$ (**3**), we suggest that the kinetically precipitated intermediate has a tri-palladium sandwich structure, $[Pd^{II}_3(PW_9O_{34})_2]^{12-}$ (**9**). However, the X-ray single crystal diffraction studies of this intermediate is not available at that time. We now report the X-ray structures of the K and CsNa salts of **9**. Complex K**9** crystallizes in triclinic *P-1* space group, with a = 12.4963(10) Å, b = 15.7787(13) Å, c = 23.6600(19) Å, α = 81.443(2)°, β = 86.9260(10)°, γ = 70.900(2)°, V = 4359.2(6) Å^3, and Z = 2 (final R = 0.0658). Complex CsNa**9** crystallizes in triclinic *P-1* space group, with a = 13.1124(13) Å, b = 17.9240(18) Å, c = 19.687(2) Å, α = 96.873(2)°, β = 91.089(2)°, γ = 105.602(2)°, V = 4418.1(8) Å^3, and Z = 2 (final R = 0.1433). The stronger countercation effect of Cs^+ than that of K^+ or Na^+ stabilizes the tri-palladium sandwich structure in solution, and this effect was confirmed by similar reaction using $[A\text{-}\alpha\text{-}SiW_9O_{34}]^{10-}$, a silicon polytungstates analogue: reaction of Pd(II) and $[A\text{-}\alpha\text{-}SiW_9O_{34}]^{10-}$ under higher concentration of Cs^+ leads to the isostructural tri-palladium sandwich compound, $Cs_9Na_5[Pd^{II}_3(SiW_9O_{34})_2]\bullet 16H_2O$ (**10**), crystallizing in monoclinic *P2(1)/n* space group, with a = 16.8223(4) Å, b = 19.7847(4) Å, c = 26.9337(6) Å, β = 99.0300(10)°, V = 8853.1(3) Å^3, and Z = 4 (final R = 0.0574). However, the same reaction under lower concentration of Cs^+ (the same ionic strength with supplementary K^+) give the decomposed product, $Cs_5K_3Na_4[Pd^{II}_2WO(OH_2)(SiW_9O_{34})_2]\bullet 16H_2O$ (**11**), crystallizing in monoclinic *P2(1)/n* space group, with a = 16.6422(5) Å, b = 19.6154(7) Å, c = 25.9525(8) Å, β = 95.342(2)°, V = 8435.2(5) Å^3, and Z = 4 (final R = 0.0781). These findings together strongly suggest

that the speciation of Pd substituted polytungstates can be controlled by countercations. All complexes were further characterized by FT-IR and thermogravimetric analysis (TGA).

6.2 Introduction

Supported palladium nanoparticles on the redox metal-oxide surface are principal catalysts in many O_2-based green catalytic oxidation reactions and technologies, including CO oxidation, alkene epoxidation, methane combustion and so on.[1-6] Terminal or bridging palladium-oxo species are normally thought to be the active intermediates in these very important processes, and thus, many efforts have been made for decades by synthetic chemists to make Pd-oxo containing molecular complexes as a model for the mechanism studies.[4,7] However, largely because of the big mismatch of the orbital energies and electronegativities of palladium and oxygen, only a few isolated and structurally characterized Pd-oxo compounds have been reported.

The use of lacunary polyoxometalates (POM)[8-12] as inorganic ligands to synthesize and isolate palladium substituted POM is particularly interesting for several reasons. First, polyoxometalates, including polyoxotungstates and polyoxomolybdates, are transition metal-oxo clusters that share many geometrical and electronic features in common with the redox metal-oxide surfaces used in supported noble metal catalytic oxidations. Second, incorporation of Pd atom into the POM frameworks can lead to the Pd-oxo molecular complexes, which can be then isolated and characterized by many structural methods and physiochemical spectroscopies, such as X-ray single crystal

diffraction, extended X-ray absorption fine structure method, electronic absorption spectroscopy, and so on. Third, both aqueous and organic solution soluble forms of the Pd-substituted POM are available. This greatly benefits the reactivity studies of the molecular Pd-oxo species. Forth, the ability to extensively and easily alter their molecular properties (structure, solubility, potential, charge, size, etc.) as well as their structural and chemical stability make POM highly interesting and promising in this field for not only synthetic reasons but also reactivity studies. Last but not least, both strong σ-donating and π-accepting properties of lacunary POM as inorganic ligands render the possibility for them to coordinate and stabilize high-valent terminal Pd(IV)=O units which are typically labile in conventional organic ligand environments.

In 2005, we reported the first isolated and fully characterized terminal Pd=O complex, $K_{10}Na_3[Pd^{IV}O(OH)P_2W_{19}O_{69}(OH_2)]\bullet 16H_2O$ (**3**),[13] where the $[O=Pd^{IV}\text{-}OH]^+$ unit is flanked by the clamshell like polytungstate ligand, $[P_2W_{19}O_{69}(OH_2)]^{14-}$, through four oxygens which define a equatorial plane around the central Pd atom. The very short Pd=O bond (1.62 ± 3 Å from 3 data sets at 173, 90, and 30K) is trans to a longer Pd-OH bond (1.99(2) Å). Based on FT-IR spectroscopy and previous studies by Knoth and co-workers on the Zn(II) analogue,[14] the kinetically precipitated (by KCl) intermediate is proposed to be a tri-Pd sandwich polytungstate, $[Pd^{II}_3(PW_9O_{34})_2]^{12-}$, which undergoes a rapid, stepwise loss of Pd(II) in acidic media and an oxidation by air to form $[Pd^{IV}O(OH)WO(OH_2)(PW_9O_{34})_2]^{13-}$. However, the X-ray diffraction studies for this intermediate are not available at that time.

Interestingly, Kortz and co-workers reported several Pd-substituted polytungstates recently.[15-17] Two common structural features of these complexes are worthy noting

here. First, all these compounds only contain the conventional four-coordinated square-planar Pd(II) centers (no terminal Pd(IV)=O is represented as **3** does). Second, all these compounds invariably have the $[M_3(XW_9O_{34})_2]^{n-}$ structure type (M = Pd atom or $[O=W^{VI}\text{-}OH_2]^{4+}$ unit; X is p block elements, like Si, P, Ge, As, and so on). By carefully analyzing the structures of these Pd-substituted polytungstates and synthetic conditions, we realized that high concentration of Cs countercation used by Kortz *et al.* stabilizes the tri-metal sandwich structure in solution by stronger interaction of Cs^+ with the polyanion unit. Particularly, Cs^+ favors the occupancy of the central belt position (**Figure 6.1**), playing as extra linkages between the two $[A\text{-}\alpha\text{-}XW_9O_{34}]^{n-}$ units and stabilizing the whole structure from hydrolytic decomposition.

With these findings on hand, we questioned whether the use of Cs countercation can facilitate the isolation of crystalline solids of the proposed intermediate from kinetic precipitation, $[Pd^{II}_3(PW_9O_{34})_2]^{12-}$. We now reported the first structural analysis of this tri-Pd sandwich phosphorus polytungstate complex **9**. Importantly, the similar reactions conducted between Pd(II) (from $PdSO_4{\bullet}2H_2O$) and its silicon polytungstate analogue, $[A\text{-}\alpha\text{-}SiW_9O_{34}]^{10-}$ collaborate the countercation effect in controlled speciation: reaction of Pd(II) and $[A\text{-}\alpha\text{-}SiW_9O_{34}]^{10-}$ under higher concentration of Cs^+ leads to the isostructural tri-Pd sandwich compound, $Cs_9Na_5[Pd^{II}_3(SiW_9O_{34})_2]{\bullet}16H_2O$ (**10**); while the same reaction under lower concentration of Cs^+ (ionic strength keeps the same by the addition of supplementary K^+) gives the decomposed/degenerated product, $Cs_5K_3Na_4[Pd^{II}_2WO(OH_2)(SiW_9O_{34})_2]{\bullet}16H_2O$ (**11**). These results are consistent with the successful synthesis and isolation of the first terminal Pd=O complex by Hill and co-

workers, while only conventional Pd(II)-substituted polytungstates are obtained by Kortz *et al.* who always use high concentration of Cs countercation in their synthesis.

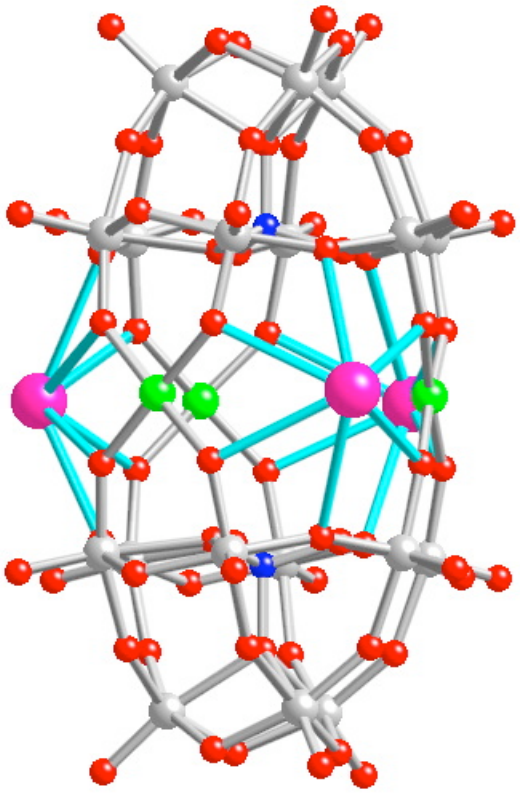

Figure 6.1 Ball-and-stick representation of polyanion $[Pd_3Si_2W_{18}O_{68}]^{14-}$, showing the three Cs^+ cations locating at the central belt of the sandwich structure. Pd, W, Si, O and Cs atoms are shown in green, gray, blue, red and pink, respectively. The interaction between Cs^+ cations and oxo oxygens on the polyanion is illustrated as light blue bonds. These extra linkages between the two $[A\text{-}\alpha\text{-}SiW_9O_{34}]^{10-}$ ligands increase the solution stability of the whole sandwich structure.

6.3 Experimental Section

General Methods and Materials

$Na_9[A\text{-}\alpha\text{-}PW_9O_{34}]\bullet 7H_2O$[18] and $Na_{10}[A\text{-}\alpha\text{-}SiW_9O_{34}]\bullet 24H_2O$[19] were obtained by the published procedure and their purities were confirmed by infrared spectroscopy and elemental analysis. Elemental analyses of Cs, K, Na, P, Si, Pd and W were performed by Kanti Labs (Mississauga, Canada), Desert Analytics (Tucson, Arizona) and Galbraith (Knoxville, Tennessee). Infrared spectra (2% sample in KBr) were recorded on a Nicolet 510 instrument. The electronic absorption spectra were taken on a Hewlett-Packard 8452A UV-vis spectrophotometer. The average magnetic susceptibility was measured on a Johnson-Matthey Model MSB-1 magnetic susceptibility balance as neat powders at 24 °C; the balance was calibrated using $Hg[Co(SCN)_4]$ as a standard. Pascal's constants were used to obtain the final diamagnetic corrections. Thermogravimetric data were collected on a TGA 1000 instrument.

Synthesis of $K_{12}[Pd^{II}_3(PW_9O_{34})_2]\bullet 18H_2O$ (K9)

A 1.0 g (4.2 mmol) sample of palladium sulfate dihydrate ($PdSO_4\bullet 2H_2O$) is suspended in 50 mL of acetate buffer (0.25 M $NaOOCCH_3$ and 0.25 M $HOOCCH_3$, pH = 4.9) at room temperature and 7 g (2.8 mmol) of $Na_9[A\text{-}PW_9O_{34}]$ is added in *ca.* 1 g portions quickly with vigorous stirring. After 0.5-1 min, 20 g of KCl are added to the nearly clear brown solution, and the solution is stirred at 5 °C for 2 additional min. A light brown solid is then separated by filtration, dried in air for 10 min and re-dissolved in *ca.* 50 mL of water at 55 °C. The solution becomes red-brown in color upon heating.

The pH of the solution is lowered from 7.5 to 6.5 by the drop-wise addition of 6 M HCl. After cooling to room temperature, the solution is filtered using a fine filter paper. After 24 h, brown plates of crystalline $K_{10}Na_3[Pd^{IV}O(OH)P_2W_{19}O_{69}(OH_2)]$ (**3**) first appear (5 g, 73% yield based on W). These crystals of **3** are filtered and dried in air. The filtrate is collected and evaporates under air at room temperature. After an additional 48 h, more crystals (brown plates) of **3** grow up with a small amount of crystalline brown prisms of K**9**. Due to the difficulty for the separation of K**9**, only X-ray single crystal diffraction and FT-IR are applied for characterization. Analytical data for K**9**: IR (2% KBr pellet, 1200 - 400 cm^{-1}): 1086 (s), 1015 (s), 944 (s), 916 (s), 782 (s), 696 (m), 590 (m), 514 (m), and 450 (w).

Synthesis of $Cs_8Na_4[Pd^{II}_3(PW_9O_{34})_2]\bullet 18H_2O$ (CsNa9)

A 1.0 g (4.2 mmol) sample of palladium sulfate dihydrate ($PdSO_4\bullet 2H_2O$) is suspended in 50 mL of acetate buffer (0.25 M $NaOOCCH_3$ and 0.25 M $HOOCCH_3$, pH = 4.9) at room temperature and 7 g (2.8 mmol) of $Na_9[A\text{-}PW_9O_{34}]$ is added in *ca.* 1 g portions quickly with vigorous stirring. After 0.5-1 min, 10 g of CsCl are added to the nearly clear brown solution, and the solution is stirred at 5 °C for 2 additional min. A light brown solid is then separated by filtration, dried in air for 10 min and re-dissolved in *ca.* 150 mL of water at 55 °C. The solution becomes red-brown in color upon heating. The pH of the solution is lowered from 7.5 to 6.5 by the drop-wise addition of 6 M HCl. After cooling to room temperature, the solution is filtered using a fine filter paper. After 24 h, brown plates of CsNa**9** appear (2 g, 30% yield based on W). The crystals are filtered and dried in air. Analytical data: IR (2% KBr pellet, 1200 - 400 cm^{-1}): 1088 (s),

1018 (s), 945 (s), 915 (s), 780 (s), 695 (m), 592 (m), 515 (m), and 451 (w). Magnetic susceptibility: μ_{eff} = 0 μ_B mol^{-1} at 297 K. Anal. Calcd. For $Cs_8Na_4[Pd^{II}_3(PW_9O_{34})_2]\bullet 18H_2O$: Cs, 17.0; Na, 1.47; P, 0.99; Pd, 5.1; W, 52.9. Found: Cs, 16.3; Na, 1.35; P, 0.90; Pd, 4.92; W, 51.8. [MW = 6258 g/mol]

Synthesis of $Cs_9Na_5[Pd^{II}_3(SiW_9O_{34})_2]\bullet 16H_2O$ (10)

A 0.25 g (1.05 mmol) sample of palladium sulfate dihydrate ($PdSO_4\bullet 2H_2O$) is suspended in 15 mL of acetate buffer (0.25 M $NaOOCCH_3$ and 0.25 M $HOOCCH_3$, pH = 4.9) at room temperature and 1.75 g (0.6 mmol) of $Na_{10}[A\text{-}SiW_9O_{34}]$ is added quickly with vigorous stirring. After 0.5-1 min, 2.2 mL of 1.0 M CsCl was added dropwise. The cloudy solution is heated to 60 °C until the solution clears and then cooled to room temperature. Upon cooling, the solution is filtered using a fine filter paper. After 12 h, big brown prisms of **10** appear (1.10 g, 55%). The crystals are collected and dried in air. Analytical data: IR (2% KBr pellet, 1200 - 400 cm^{-1}): 996 (s), 936 (s), 881 (s), 777 (s), 678 (m), 550 (w), 531 (m), and 442 (m). Magnetic susceptibility: μ_{eff} = 0 μ_B mol^{-1} at 297 K. Anal. Calcd. for $Cs_9Na_5[Pd^{II}_3(SiW_9O_{34})_2]\bullet 16H_2O$: Cs, 18.8; Na, 1.80; Si, 0.88; Pd, 5.0; W, 51.9. Found: Cs, 18.6; Na, 1.61; Si, 0.80; Pd, 4.52; W, 50.1. [MW = 6372 g/mol]

Synthesis of $Cs_5K_3Na_4[Pd^{II}_2WO(OH_2)(SiW_9O_{34})_2]\bullet 16H_2O$ (11)

A 0.25 g (1.05 mmol) sample of palladium sulfate dihydrate ($PdSO_4\bullet 2H_2O$) is suspended in 15 mL of acetate buffer (0.25 M $NaOOCCH_3$ and 0.25 M $HOOCCH_3$, pH =

4.9) at room temperature and 1.75 g (0.6 mmol) of $Na_{10}[A\text{-}SiW_9O_{34}]$ is added quickly with vigorous stirring. After 0.5-1 min, 1.1 mL of 1.0 M KCl was added dropwise followed by 1.1 mL of 1.0 M CsCl. The solution is heated to 60 °C and cooled to room temperature. Upon cooling, the solution is filtered using a fine filter paper. After 1 week, brown blocks of **11** appear (0.9 g, 45%). The crystals are collected and dried in air. Analytical data: IR (2% KBr pellet, 1200 - 400 cm^{-1}): 1002 (s), 940 (s), 888 (s), 776 (s), 697(w), 590 (w), 532 (m), and 443 (m). Magnetic susceptibility: $\mu_{eff} = 0\ \mu_B\ mol^{-1}$ at 297 K. No elemental analysis is conducted on this complex because it is the same as a literature compound published by Kortz based on (1) X-ray single crystal diffraction (the same unit cell and structure) and (2) infrared spectroscopy. [MW = 6046 g/mol]

Crystallographic Studies

Single-crystal X-ray crystallographic analyses of $K_{12}[Pd^{II}_3(PW_9O_{34})_2]\bullet 18H_2O$ (K**9**), $Cs_8Na_4[Pd^{II}_3(PW_9O_{34})_2]\bullet 18H_2O$ (CsNa**9**), $Cs_9Na_5[Pd^{II}_3(SiW_9O_{34})_2]\bullet 16H_2O$ (**10**) and $Cs_5K_3Na_4[Pd^{II}_2WO(OH_2)(SiW_9O_{34})_2]\bullet 16H_2O$ (**11**) were performed at Emory University at 173 K on a Brüker D8 SMART APEX CCD sealed tube diffractometer with graphite monochromated Mo Kα (0.71073 Å) radiation. Data collection, indexing, and initial cell refinements were carried out using SMART software (version 5.628).[20] Frame integration and final cell refinements were carried out using SAINT (version 6.36A).[21] Absorption correction was applied using SADABS (version 2.10).[22] The structure was determined using direct methods and difference Fourier techniques.[23] The final R1 scattering factors and anomalous dispersion corrections were taken from the International Tables for X-ray Crystallography. Structure solution, refinement, and generation of

publication materials were performed using SHELXTL V6.12 software.[23] Crystal data and structural refinement for the X-ray structures of K**9**, CsNa**9**, **10** and **11** are summarized in **Table 6.1**, and their thermal ellipsoid plots are shown in **Figure 6.2**.

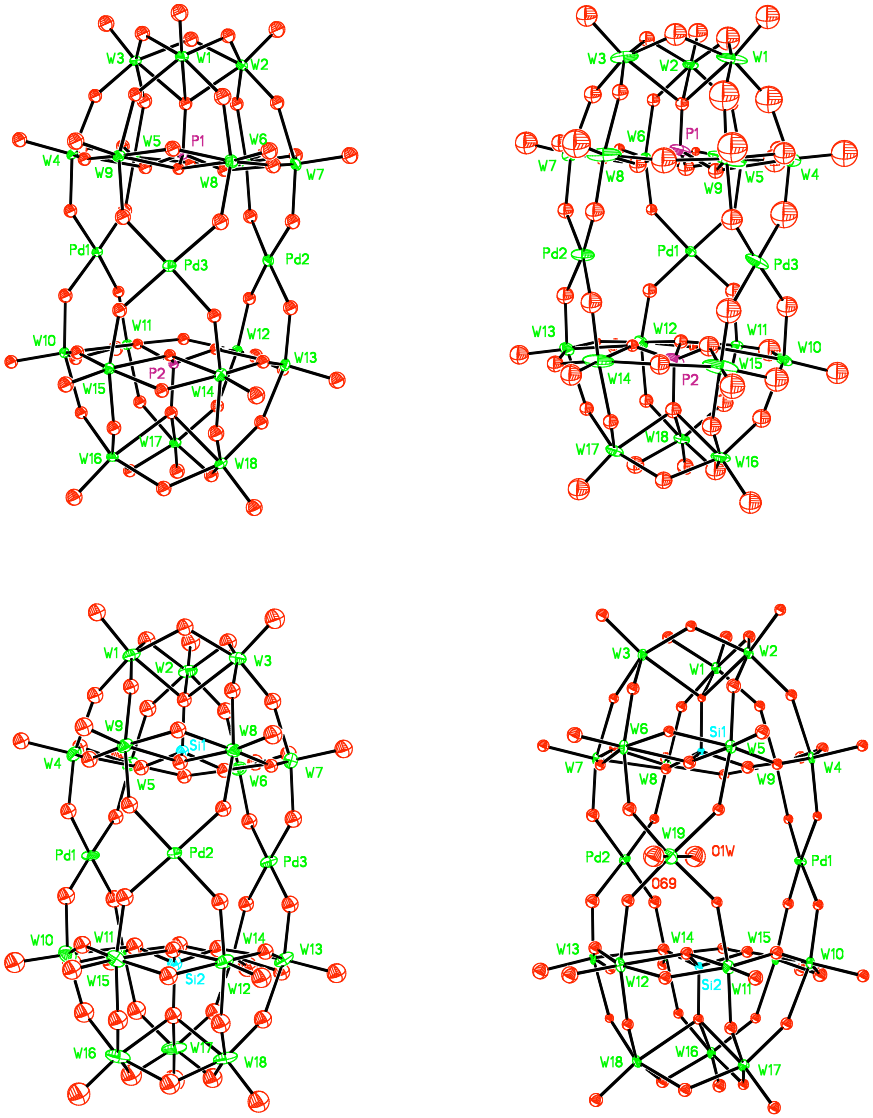

Figure 6.2 Thermal ellipsoid plots and numbering scheme for K**9** (top left), CsNa**9** (top right), **10** (bottom left) and **11** (bottom right).

Table 6.1 Crystal data and structural refinement for the X-ray structures of K**9**, CsNa**9**, **10** and **11**

complex	K**9**	CsNa**9**
molecular formula	$H_{36}K_{12}O_{86}P_2Pd_3W_{18}$	$H_{36}Cs_8Na_4O_{86}P_2Pd_3W_{18}$
formula wt.	5571.92	6257.94
temperature (K)	173(2)	173(2)
radiation (λ, Å)	0.71073	0.71073
crystal system	triclinic	triclinic
space group	*P-1* (#2)	*P-1* (#2)
a (Å)	12.4963(10)	13.1124(13)
b (Å)	15.7787(13)	17.9240(18)
c (Å)	23.6600(19)	19.687(2)
α (°)	81.443(2)	96.873(2)
β (°)	86.9260(10)	91.089(2)
γ (°)	70.900(2)	105.602(2)
Volume ($Å^3$)	4359.2(6)	4418.1(8)
Z	2	2
μ (mm^{-1})	24.964	27.321
F(000)	4840	5216
crystal size (mm^3)	0.34 x 0.14 x 0.06	0.10 x 0.07 x 0.02
θ range	1.38 to 28.35º	1.48 to 23.26º
reflections	60653	43171
independent reflections	21650 [R(int) = 0.0691]	12696 [R(int) = 0.0995]
absorption correction	semi-empirical from equivalents	semi-empirical from equivalents
refinement method	full-matrix least-squares on F^2	full-matrix least-squares on F^2
data/restraints/param.	21650/0/725	12696/0/632
goodness-of-fit on F^2	1.077	1.057
final R indices [R > 2σ (I)]	$R1^a$ = 0.0658 $wR2^b$ = 0.1677	$R1^a$ = 0.1433 $wR2^b$ = 0.3331
R indices (all data)	$R1^a$ = 0.0795 $wR2^b$ = 0.1777	$R1^a$ = 0.1635 $wR2^b$ = 0.3483

$^a R_1 = \Sigma||F_o| - |F_c||/ |F_o|$

$^b wR_2 = \{\Sigma[w(F_o^2 - F_c^2)^2]/\Sigma[w(F_o^2)^2]\}^{0.5}$

Table 6.1 Continued: Crystal data and structural refinement for the X-ray structures of K**9**, CsNa**9**, **10** and **11**

complex	**10**	**11**
molecular formula	$H_{32}Cs_9Na_5O_{84}Si_2Pd_3W_{18}$	$H_{34}Cs_5K_3Na_4O_{86}Si_2Pd_2W_{19}$
formula wt.	6372.03	6046.16
temperature (K)	173(2)	173(2)
radiation (λ, Å)	0.71073	0.71073
crystal system	monoclinic	monoclinic
space group	*P2(1)/n* (#14)	*P2(1)/n* (#14)
a (Å)	16.8223(4)	16.6422(5)
b (Å)	19.7847(4)	19.6154(7)
c (Å)	26.9337(6)	25.9525(8)
β (°)	99.0300(10)	95.342(2)
Volume (Å^3)	8853.1(3)	8435.2(5)
Z	4	4
μ (mm^{-1})	27.348	28.637
F(000)	10327	10216
crystal size (mm^3)	0.13 x 0.12 x 0.07	0.32 x 0.18 x 0.05
θ range	1.53 to 26.40º	1.30 to 26.45º
reflections	73552	54739
independent reflections	18102 [R(int) = 0.0662]	17250 [R(int) = 0.0817]
absorption correction	semi-empirical from equivalents	semi-empirical from equivalents
max. and min. transmission	0.2505 and 0.1252	0.3285 and 0.0394
refinement method	full-matrix least-squares on F^2	full-matrix least-squares on F^2
data/restraints/param.	18102/0/641	17250/0/655
goodness-of-fit on F^2	1.033	1.036
final R indices [R > 2σ (I)]	R1[a] = 0.0574 wR2[b] = 0.1507	R1[a] = 0.0781 wR2[b] = 0.1952
R indices (all data)	R1[a] = 0.0792 wR2[b] = 0.1641	R1[a] = 0.1071 wR2[b] = 0.2204

[a] $R_1 = \Sigma||F_o| - |F_c||/ |F_o|$

[b] $wR_2 = \{\Sigma[w(F_o^2 - F_c^2)^2]/\Sigma[w(F_o^2)^2]\}^{0.5}$

6.4 Results and Discussion

Synthesis of K9 and CsNa9

Recently, we reported the successful synthesis and isolation of the first terminal Pd-oxo complex $K_{10}Na_3[Pd^{IV}O(OH)P_2W_{19}O_{69}(OH_2)]$ (**3**).[13] After harvesting **3** using frit, we noticed that the filtrate gives a little more crystalline product in 48 h at room temperature. Most of the crystals (> 90%) are brown plates of **3**, confirmed by infrared spectroscopy and unit cell checking. However, a very small amount of brown prisms (K**9**) also appear, which have a different FT-IR spectrum. X-ray diffraction studies on the prism confirm its different structure, a tri-palladium sandwich with two $[A\text{-}PW_9O_{34}]^{9-}$ units fused together by three d^8 Pd(II) atoms (**Figure 6.3**). Interestingly, the FT-IR spectra of K**9** and the kinetically precipitated intermediate (by KCl) are very similar, suggesting that the kinetic precipitates have the same tri-Pd sandwich structure which undergo a stepwise loss of Pd(II) in the acidic crystallization media (based on ^{31}P and ^{183}W NMR studies performed by Knoth and co-workers on the Zn(II) analogue[14]), and finally convert to the terminal Pd-oxo complex **3** in air. Unfortunately, due to the bad yield of K**9** and dominant crystals of **3** under this condition (K**9** and **3** are in equilibrium in solution, and **3** is the favorite species), the bulk sample of K**9** is only characterized by infrared spectroscopy (elemental analysis, ^{31}P NMR and TGA all need a relatively large amount of sample).

In order to get more structural and chemical information about the kinetic precipitates, crystallization of them without decomposition is essential. Our previous

studies on palladium-substituted polytungstates suggest that Cs countercation could stabilize the tri-Pd sandwich structure by stronger countercation effect of Cs^+ than that of K^+ or Na^+: the interaction between Cs^+ and the polyanion unit, especially those Cs^+ atoms locating around the central tri-Pd plane, is stronger than that of K^+ or Na^+ (see the crystallographic studies below), and acts as extra linkages between the two [A-α-$PW_9O_{34}]^{9-}$ units to stabilize the whole structure from hydrolytic decomposition. Then, we decided to precipitate the kinetic intermediate, the tri-Pd sandwich complex, using CsCl. Recrystallization of the Cs salt of precipitates in water affords crystalline brown plates of CsNa**9**, whose infrared spectrum is similar to that of K**9** and the kinetically precipitated solids. X-ray single crystal diffraction on CsNa**9** confirms the tri-Pd sandwich structure (see below, **Figure 6.3**), the same polyanion structure represented also by K**9**. These results together strongly indicate that the kinetically precipitated intermediate (both by KCl or CsCl) is a tri-Pd sandwich complex, $[Pd^{II}_3(PW_9O_{34})_2]^{12-}$, which is possible to undergo a stepwise loss of Pd(II) in acidic crystallization media and convert to complex **3** under air.

The successful stabilization and isolation of the tri-Pd sandwich structure from aqueous solution with Cs countercation suggest that the speciation of Pd-substituted polytungstates can be controlled by the addition of Cs^+. Importantly, it is worthy noting here that $Cs_{3.5}K_3Na_{3.5}[(O{=}Pd^{IV}(OH_2))_2P_2W_{19}O_{68}(OH)_2]{\bullet}20H_2O$ (**6**), the di-Pd-oxo complex documented before (Chapter 5), is synthesized using very similar procedure and condition as CsNa**9**. The only difference between them is addressed below: complex **6** is obtained by recrystallization of the kinetic precipitations (by CsCl) in KCl/LiCl aqueous solution, while complex CsNa**9** is recrystallized from water. The replacement of Cs^+

countercation by K^+ and Li^+ in solution, which have weaker interaction with polyanion units, destabilizes the whole $[Pd^{II}_3(PW_9O_{34})_2]^{12-}$ sandwich structure. Hydrolytic decomposition of this polyanion will gradually lose Pd(II) atom(s) and generate several polytungstate species including monotungstate (WO_4^{2-}) in solution, which can then react with the degraded form $[Pd^{II}_2(PW_9O_{34})_2]^{14-}$ to afford $[Pd^{II}_2WO(OH_2)(PW_9O_{34})_2]^{10-}$ (it is can be seen that one Pd(II) is replaced by a $[O=W^{IV}(OH_2)$ unit). In the final step, Pd(II) is oxidized by air to give the final product $Cs_{3.5}K_3Na_{3.5}[(O=Pd^{IV}(OH_2))_2P_2W_{19}O_{68}(OH)_2]$ (**6**).

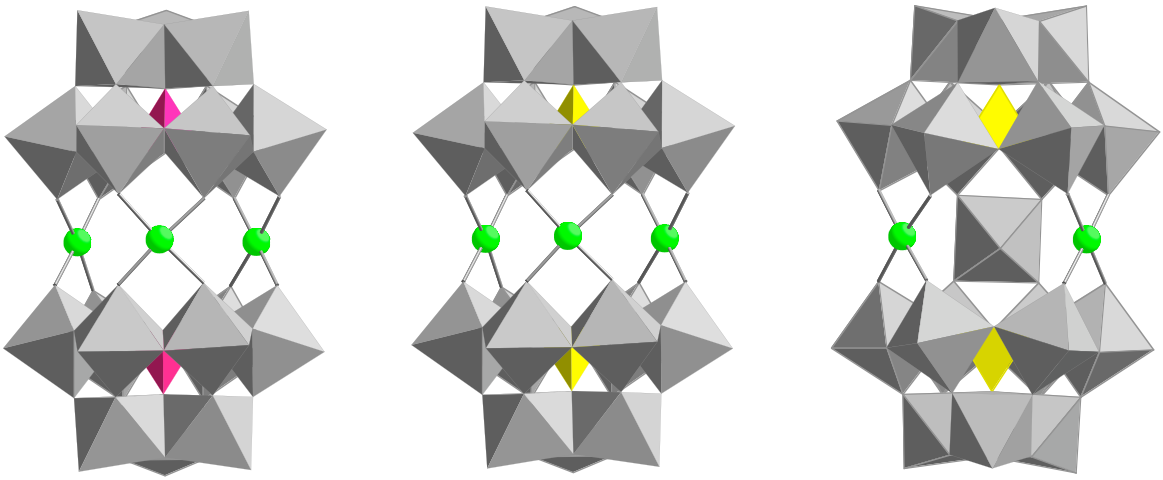

Figure 6.3 Combination polyhedral/ball-and-stick representations of polyanions **9** (left) **10** (middle) and **11** (right). The WO_6 (or W atom), PO_4 and SiO_4 polyhedra are shown in gray, pink and yellow, respectively. The Pd atom is shown in green.

Effect of Cs Countercation in the Synthesis, Controlled Speciation of 10 and 11

The finding that Cs countercations can stabilize the M_3 (here is tri-Pd) sandwich structure is confirmed by reactions between $PdSO_4$ and $[A\text{-}\alpha\text{-}SiW_9O_{34}]^{10-}$, a silicon analogue of $[A\text{-}\alpha\text{-}PW_9O_{34}]^{9-}$. Addition of $[A\text{-}SiW_9O_{34}]^{10-}$ to the suspended $PdSO_4$ (molar ratio, 2:3) in sodium acetate buffer results in a clear brown solution. To this solution, 1.0 M CsCl is added dropwisely until the solution becomes cloudy (*ca.* 2.2 mL), and then it is heated to 60 °C until the solution clears again. The cooled solution is filtered using fine filter papers, and the filtrate gives big crystalline brown prisms of **10** in 12 h. X-ray diffraction studies confirm that the tri-Pd sandwich structure, $[Pd^{II}_3(SiW_9O_{34})_2]^{14-}$, is represented by the polyanion of **10** (**Figure 6.3**). The purity of the bulk sample of **10** is checked by FT-IR and elemental analysis (9 Cs and 5 Na are found by both crystallographic studies and elemental analysis), and its stability in the solid state is screened by TGA, showing no decomposition under 200 °C.

Interestingly, the same reaction of $PdSO_4$ and $[A\text{-}SiW_9O_{34}]^{10-}$ with less addition of Cs^+ (1.1 mL of 1.0 M CsCl and 1.1 mL of 1.0 M KCl, the ionic strength is the same as in the synthesis of **10**) results in a different product, brown blocks of **11**. The structure type represented by the polyanion of **11** is solved by X-ray single crystal diffraction, showing one of the three Pd(II) atoms in the polyanion of **10** is replaced by a $[O{=}W^{IV}(OH_2)]^{4+}$ unit (**Figure 6.3**). The polyanion formula of **11**, $[Pd^{II}_2Si_2W_{19}O_{69}(OH_2)]^{12-}$, can then be ambiguously determined, showing it is a published structure by Kortz and co-workers in 2004.[16] Careful comparison of **11** with this literature compound affords further evidences that they are the same. First, both crystallize in the same space group with identical unit cell (monoclinic *P2(1)/n*, a = 16.6422(5) Å, b = 19.6154(7) Å, c = 25.9525(8) Å, β =

95.342(2)°, V = 8435.2(5) $Å^3$, Z = 4). Second, the same countercations (5 Cs^+, 3 K^+ and 4 Na^+) are found in both structures. Third, the identical infrared spectra and cyclic voltammetry behaviors indicate they are the same compounds. Since **10** and **11** are synthesized using the same starting materials and are crystallized from the same buffer solution with identical ionic strength except that higher concentration of Cs is used in the synthesis of **10**, one can conclude that Cs countercation does control the speciation of Pd-substituted polytungstate by stabilizing the tri-Pd sandwich structure. The stepwise loss of Pd(II) in **10**, followed by hydrolytic decomposition of the polytungstate unit, results in the formation of **11** in solution.

We also tried to conduct the same reaction ($PdSO_4$ + $[A\text{-}SiW_9O_{34}]^{10-}$) in the absence of Cs cation. However, efforts to grow X-ray quality crystals with the addition of 2.2 mL of 1.0 M KCl to the same reaction solution are unsuccessful. Very thin hexagonal brown plates are always obtained, which poorly diffract on the X-ray diffractometer. Importantly, these crystals do show a different infrared spectrum compared to both **10** and **11**.

Crystallographic Studies of K9, CsNa9, 10 and 11

The three structures of conventional d^8 Pd(II) polytungstates, **9** (in both K and CsNa salts), **10** and **11**, are carefully studied by X-ray single crystal diffraction. In the structure of **9**, two $[A\text{-}\alpha\text{-}PW_9O_{34}]^{9-}$ units are linked together by three square planar Pd(II) centers to form a tri-Pd sandwich structure, $[Pd^{II}_3(PW_9O_{34})_2]^{12-}$, (**Figure 6.3**). In our knowledge, the polyanion of **9** represents the first structurally characterized tri-Pd sandwich structure without lone electron pair on the central tetrahedral heteroatom. Kortz *et al.* synthesized

two tri-Pd sandwich structures before, but both have the $[B\text{-}X^{III}W_9O_{33}]^{9-}$ polytungstate ligands (X = As or Sb), in which the central tetrahedral heteroatom has a lone electron pair pointing into the cavity surrounded by the three Pd(II) atoms. The big electron densities of the two lone pairs, each from one $[B\text{-}X^{III}W_9O_{33}]^{9-}$ unit, prevent the ligation of oxygen-based ligands to the axial position of Pd(II) and the formation of a terminal Pd-oxo complex. On the other hand, $[A\text{-}\alpha\text{-}PW_9O_{34}]^{9-}$ ligand has no lone electron pair (phosphor is tetrahedrally bound to one μ_4-oxo and three μ_3-oxo), rendering the possibility to flank/support the $[O{=}Pd^{IV}(OH)]^+$ unit. The Pd-O bond distances (1.959-1.992(12) Å) and the O-Pd-O bond angles (87.1-94.3(5), 174.6-176.2(5) degree) of the PdO_4 groups in K**9** are regular for a square planar coordination of d^8 Pd(II). The average Pd•••Pd distance and P•••P separation in K**9** are 5.595 and 6.638 Å, respectively; both are extensively longer than the Pd•••Pd (4.39 Å) and Sb•••Sb (4.97 Å) distances in $[Pd^{II}_3(SbW_9O_{33})_2]^{12-}$ reported by Kortz and co-wrkers.[15] The increased space for each Pd should also take the advantage to be coordinated with extra ligands when it is oxidized. In addition to the three Pd(II) atoms, the central belt of the polyanion of K**9** contains three K^+ ions, each bind to four flanking μ_2-oxo oxygens (Pd-O-W) from two $Pd(O\text{-}W)_4$ groups (similarly, three Cs^+ ions locate at the central belt of CsNa**9**).

The polyanion of **10** is isostructural to **9** with the central phosphorus atoms replaced by silicon atoms. The Pd-O bond distances (1.943-1.991(14) Å) and the O-Pd-O bond angles (88.3-91.5(6), 175.7-179.2(6) degree) of the PdO_4 groups as well as the average Pd•••Pd distance (5.876 Å) and Si•••Si separation (6.755 Å) in **10** are very similar to those established in **9**. Three Cs^+ countercations sit on the central belt of the polyanion like those K^+ (or Cs^+) atoms do in K**9** (or Cs**9**). Interestingly, there is a Cs^+ atom locating

at the center of the cavity surrounded by the three Pd(II) atoms and the two [A-$SiW_9O_{34}]^{9-}$ polytungstate ligands. The distances of this Cs^+ from Pd1-3 are 3.478(4), 3.314(4) and 3.386(4) Å, respectively. Since the hydrated alkali ions are too big to access the center of the cavity once the tri-Pd sandwich structure is formed, it is believed that this Cs^+ kindly acts as a template to bring two [A-$SiW_9O_{34}]^{10-}$ units together and coordinate three Pd(II) atoms to form **10**. Crystallographic studies of **11** suggest it is a literature compound, $[Pd^{II}_2W(O)(OH_2)(SiW_9O_{34})_2]^{12-}$, which is confirmed by three lines of evidence mentioned above.

6.5 Conclusion

In conclusion, three conventional d^8 Pd(II)-substituted polytungstates, $[Pd^{II}_3(PW_9O_{34})_2]^{12-}$ (**9**), $[Pd^{II}_3(SiW_9O_{34})_2]^{14-}$ (**10**), and $[Pd^{II}_2WO(OH_2)(SiW_9O_{34})_2]^{12-}$ (**11**) have been successfully synthesized and isolated, and their structures have been ambiguously determined by X-ray diffraction method. Complex **9** and **10** represent the first structurally characterized tri-Pd sandwich structures without lone electron pair on the central tetrahedral heteroatom of the polytungstate ligands. This important structural feature makes these complexes to be possible precursors for the terminal Pd=O species. Furthermore, we demonstrated experimentally that Cs countercation does play a crucial role in these syntheses: the interaction between Cs^+ and polyanion units is strong and controls the speciation of Pd-substituted polytungstates in solution. These factors together are essential for the formation of terminal Pd=O polytungstates.

References

(1) Appleby, A. J.; Foulkes, F. R. *Fuel cell handbook*; Krieger Publising Company, Malabar, Florida, 1993.

(2) Somorjai, G. A. *Introduction to surface chemistry and catalysis*; Wiley: New York, 1994.

(3) Malleron, J.-L.; Fiaud, J.-C.; Legros, J.-Y. *Handbook of Palladium-Catalyzed Organic Reactions: Synthetic Aspects and Catalytic Cycles*; Academic Press: San Diego, CA., 1997.

(4) Singh, A.; Sharp, P. R. *Dalton Trans.* **2005**, 2080-2081.

(5) Luyben, M. L.; Tyreus, B. D. *Computers & Chem. Eng.* **1998**, *22(7-8)*, 867-877.

(6) Macleod, N.; Keel, J. M.; Lambert, R. M. *Applied Catalysis, A: General* **2004**, *261(1)*, 37-46.

(7) Shelef, M. *Chem. Rev.* **1995**, *95*, 209-225.

(8) *Polyoxometalate Chemistry From Topology via Self-Assembly to Applications*; Pope, M. T.; Müller, A., Eds.; Kluwer Academic Publishers: Dordrecht, 2001.

(9) *Polyoxometalate Chemistry for Nano-Composite Design*; Yamase, T.; Pope, M. T., Eds.; Kluwer Academic/Plenum Publishers: New York, 2002; Vol. 2.

(10) Pope, M. T. In *Comprehensive Coordination Chemistry II: From Biology to Nanotechnology*; Wedd, A. G., Ed.; Elsevier Ltd.: Oxford, UK, 2004; Vol. 4, p 635-678.

(11) Hill, C. L. In *Comprehensive Coordination Chemistry-II: From Biology to Nanotechnology*; Wedd, A. G., Ed.; Elsevier Ltd.: Oxford, UK, 2004; Vol. 4, p 679-759.

(12) Kozhevnikov, I. V. *Catalysis by Polyoxometalates*; Wiley: Chichester, England, 2002; Vol. 2.

(13) Anderson, T. M.; Cao, R.; Slonkina, E.; Hedman, B.; Hodgson, K. O.; Hardcastle, K. I.; Neiwert, W. A.; Wu, S.; Kirk, M. L.; Knottenbelt, S.; Depperman, E. C.; Keita, B.; Nadjo, L.; Musaev, D. G.; Morokuma, K.; Hill, C. L. *J. Am. Chem. Soc.* **2005**, *127*, 11948-11949.

(14) Knoth, W. H.; Domaille, P. J.; Harlow, R. L. *Inorg. Chem.* **1986**, *25*, 1577-1584.

(15) Bi, L.-H.; Reicke, M.; Kortz, U.; Keita, B.; Nadjo, L.; Clark, R. J. *Inorg. Chem.* **2004**, *43*, 3915-3920.

(16) Bi, L.-H.; Kortz, U.; Keita, B.; Nadjo, L.; Borrmann, H. *Inorg. Chem.* **2004**, *43*, 8367-8372.

(17) Bi, L.-H.; Kortz, U.; Keita, B.; Nadjo, L.; Daniels, L. *Eur. J. Inorg. Chem.* **2005**, 3034-3041.

(18) Domaille, P. J. In *Inorganic Syntheses*; Ginsberg, A. P., Ed.; John Wiley and Sons: New York, 1990; Vol. 27, p 96-104.

(19) Laronze, N.; Marrot, J.; Herve, G. *Inorg. Chem.* **2003**, *42*, 5857-5862.

(20) SMART; Bruker AXS, I.; 5.628 ed.; Analytical X-ray Systems: Madison, WI, 2003.

(21) SAINT; Bruker AXS, I.; 6.28 ed.; Analytical X-ray Systems: Madison, WI, 2003.

(22) SADABS; Sheldrick, G.; 2.10 ed. 2003.

(23) SHELXTL; 6.14 ed.; Bruker AXS, Inc.: Madison, WI, 2003.

Chapter 7 Reactivity Studies

Oxo Transfer and Reoxidation: Reactivity Studies of $[MO(OH_2)P_2W_{20}O_{70}(OH_2)_2]^{8-/9-}$ (M = Pd or Au)

Prepared for submission to *J. Am. Chem. Soc.*

with Travis M. Anderson, Elena Slonkina, Britt Hedman, Keith O. Hodgson, Kenneth I. Hardcastle, Yurii V. Geletii, Martin L. Kirk, Sushilla Knottenbelt, Shaoxiong Wu, Louis Nadjo, and Craig L. Hill

7.1 Abstract

Terminal Au-oxo complex $K_7H_2[AuO(OH_2)P_2W_{20}O_{70}(OH_2)_2]\bullet 27H_2O$ (**5**) and Pd-oxo complex $K_8[PdO(OH_2)P_2W_{20}O_{70}(OH_2)_2]\bullet 22H_2O$ (**4**), which are considerably stable in both aqueous and organic solution, are applied for reactivity studies. The terminal oxo oxygen on the Au(III)=O center of **5** can transfer to other oxo accepting substrates, like triphenylphosphine, dimethyl sulfide and tetrahydrothiophene. The reduced Au(I) center is not stable in the polytungstate environment, leading to a demetalation product $[P_2W_{20}O_{70}(OH_2)_2]^{10-}$ (**P_2W_{20}**). Similarly, the terminal oxo oxygen on the Pd(IV)=O center of **4** can transfer, but more importantly, the deoxygenated form, $[Pd(II)P_2W_{20}O_{70}(OH_2)_2]^{8-}$ (**12**), is stable in solution. Isolation of **12** as crystalline plates is facilitated by the addition of dimethylammonium hydrochloride. The dimethylammonium (DMA) salt of **12** crystallizes in monoclinic *P2(1)/c*, with a = 11.7359(4) Å, b = 32.7975(14) Å, c = 22.1673(8) Å, β = 98.168(2)°, V = 8445.8(6) Å^3, Z = 4 (final R = 0.0672). Crystallographic studies confirm the oxo transfer: a new square-planar d^8 Pd(II) center is coordinated in the polytungstate ligand. Interestingly, Pd(II) polytungstate **12** can be reoxidized to form the terminal Pd(IV)=O complex **4** with dioxygen. The reoxygenation process is followed by ^{31}P NMR and electronic absorption spectroscopy, and the O_2 activation on the Pd center is further confirmed by ^{17}O labeling experiments. Catalytic oxidation (O_2-based) of trimethylphosphite to trimethylphosphate with **4** also highlights this unique Pd center for O_2 activation under mild condition.

7.2 Introduction

Noble metal complexes (e.g. Pt, Pd and Au) and redox metal-oxides (such as titania and ceria) supported noble metals have attracted major attention as the homogenous and heterogenous catalysts in O_2-based green organic oxidation in some of the most technologically and economically significant processes at present.[1-14] Noble metal-oxo, especially, terminal metal-oxo (O^{2-}) species are well thought to be involved in these catalytic processes and have long been sought experimentally.[1-4,15-18] Recently, by the use of polyoxometalate (POM) as the stabilizing ligands, we have first successfully synthesized and fully characterized several terminal metal-oxo complexes with the group 10 and 11 elements (one Pt-oxo, three Pd-oxo and two Au-oxo species).[19-21] Polyoxometalate[22-26] are metal oxide clusters that share many chemical and electronic features in common with the redox metal-oxide supports, and the lacunary POM derivatives act as inorganic ligands with both good σ-donating and π-accepting properties.

As the molecular model for the redox metal-oxides supported noble metal catalysts, the reactivity/O_2 activation properties of these molecular late transition metal-oxo (LTMO) complexes are essentially interesting. However, no reactivity studies are documented for the molecular LTMO complexes except a terminal d^4 $(mesityl)_3Ir^V$-oxo compound synthesized by G. Wilkinson and co-workers[27] and subsequently shown by S. Brown and co-workers[28] to catalyze oxo transfer to phosphines. Here we report the detailed reactivity studies, including stoichiometric oxo transfer and catalytic oxidation, of a terminal Au(III)-oxo complex $K_7H_2[AuO(OH_2)P_2W_{20}O_{70}(OH_2)_2]\bullet 27H_2O$ (**5**) and a terminal Pd(IV)-oxo complex $K_8[PdO(OH_2)P_2W_{20}O_{70}(OH_2)_2]\bullet 22H_2O$ (**4**). There are two

reasons for the selection of **4** and **5** for reactivity studies from all six synthesized LTMO complexes. First, the one-bridged structure, $[Pt^{IV}O(OH_2)(PW_9O_{34})_2]^{16-}$ (**1**) and $[Au^{III}O(OH_2)(PW_9O_{34})_2]^{17-}$ (**2**), is not stable in aqueous solution. Second, the terminal oxo on the Pd(IV)=O center of complex $[PdO(OH)P_2W_{19}O_{69}(OH_2)]^{13-}$ (**3**) and $[(PdO(OH_2))_2P_2W_{19}O_{68}(OH)_2]^{10-}$ (**6**) orients into the sterically protected polytungstate cavity, which makes the oxo transfer reaction and subsequent reoxygenation with dioxygen difficult. On the other hand, however, both **4** and **5** have the terminal M=O (M = Pd and Au) units point out from the cavity surrounded by polytungstate ligand environments, and utilize two extra $[O=W^{VI}(OH_2)]^{4+}$ linkages between the two $[A\text{-}\alpha\text{-}PW_9O_{34}]^{9-}$ ligands to increase the stability of the whole polyanion structures in both aqueous and organic solution.

7.3 Experimental Section

General Methods and Materials

Terminal Au-oxo complex $K_7H_2[AuO(OH_2)P_2W_{20}O_{70}(OH_2)_2]\bullet 27H_2O$ (**5**) and Pd-oxo complex $K_8[PdO(OH_2)P_2W_{20}O_{70}(OH_2)_2]\bullet 22H_2O$ (**4**) were synthesized using published procedures.[21] The organic soluble forms of both complexes, the K⊂*cis*-dicyclohexano-18-crown-6 salt of **5** and the tetra-*n*-butylammonium (TBA) salt of **4** were obtained by the methods described before (Chapter 4). Their purities were confirmed by both IR and ^{31}P NMR spectroscopy. Importantly, TBABr can not be used in the metathesis extraction of **5** because its Au(III)=O center is reduced by bromide. Palladium

chloride ($PdCl_2$) and potassium tetrachloropalladate (K_2PdCl_4) were purchased from Alfa Aesar, and were used without further purification. Tetraphenylphosphonium bromide (Ph_4PBr), dimethylammonium hydrochloride (DMACl), triphenylphosphine (Ph_3P) and trimethylphosphite (MeO_3P) were purchased from Aldrich, and were used without further purification.

Infrared spectra (2% sample in KBr) were recorded on a Thermo Nicolet 6700 instrument. Ambient temperature electronic absorption spectra were acquired using a diode-array Hewlett-Packard 8452A spectrophotometer equipped with a magnetic stirrer and temperature controller (HP 89090A). ^{31}P NMR measurements were made on a Varian INOVA 400 MHz spectrometer, and peaks were referenced to 85% H_3PO_4. The GC analysis was performed using a Hewlett-Packard 6890 GC equipped with a HP-5 capillary column (poly(5% diphenyl/95% dimethylsiloxane, 30 m) and an FID detector. Trimethylphosphate product was identified using an authentic commercial sample (Aldrich).

^{17}O NMR spectra were acquired at 81.291 MHz on a Varian UNITY 600 spectrometer. The spectrometer was locked on the ^2H resonance of $CDCl_3$, and all chemical shifts were reported relative to D_2O (δ = 0 ppm). Spectral parameters for ^{17}O NMR were the following: pulse width, 10 μs; sweep width, 100,000 Hz; 0.01 s delay; 100,000 transients; 40,000 data points. Spectra were obtained using cylindrical 5-mm o.d. sample tubes (7 in). All samples were dissolved in 50:50 (v:v) CH_3CN-$CDCl_3$ mixture solvent at room temperature. ^{17}O-enriched water (10% $H_2{}^{17}O$) was purchased from Cambridge Isotope Laboratories, and was used without further purification. Tetra-

n-butylammonium (TBA) bromide and *cis*-dicyclohexano-18-crown-6 were purchased from Aldrich, and were used without further purification.

Stoichiometric Oxo Transfer of Au-oxo Complex 5

The ^{17}O-enriched organic soluble form of **5** was prepared by the published procedure: a 0.20 g (0.036 mmol) sample of **5** was dissolved at room temperature in 2.0 mL of CH_3CN containing 0.067 g (0.18 mmol) of *cis*-dicyclohexano-18-crown-6, and then 0.20 mL of 10% ^{17}O-enriched water was added. The mixture was incubated at room temperature for 2 d. This solution was then concentrated to dryness at room temperature, affording the K⊂*cis*-dicyclohexano-18-crown-6 salt of **5**. The dried solid was redissolved in 0.5 mL of $CH_3CN/CDCl_3$, and its purity was checked by ^{31}P NMR; the spectrum had only one peak at -15.5 ppm.

Argon was bubbled for 15 minutes through *ca.* 1 mL of $CH_3CN/CDCl_3$ containing 0.20 g (0.034 mmol) of a ^{17}O-enriched sample of **5** in a cylindrical 5-mm o.d. sample tube (7 in), and then a 9.2 mg (0.035 mmol) sample of triphenylphosphine was added quickly. After addition of triphenylphosphine, the NMR tube was immediately sealed, and a ^{31}P NMR spectrum was taken in *ca.* 2 min. The mixture was allowed to react at least 1 h at room temperature for complete conversion. The mixture was subsequently analyzed by both ^{31}P and ^{17}O NMR spectroscopy. The reaction was also carried out with 3 (27.6 mg, 0.105 mmol) or 5 (46.0 mg, 0.175 mmol) equivalents of triphenylphosphine over **5**.

Stoichiometric Oxo Transfer of Pd-oxo Complex 4

The ^{17}O-enriched organic soluble form of **4** was prepared by the published procedure: a 0.2 g (0.035 mmol) sample of **4** was dissolved in 0.2 mL of 10% ^{17}O-enriched water at 50 $^{\circ}C$ and aged for 2 days. This solution was then mixed with 2 mL of water as well as a solution of 0.086 g $[CH_3(CH_2)_3]_4NBr$ (Tetra-*n*-butylammonium bromide, 0.267 mmol) in 20 mL CH_2Cl_2 with vigorous stirring for 2 min. Upon standing, the mixture separated into a clean red-brown organic layer and a clean colorless aqueous layer. The organic layer was separated and filtered using a fine filter paper, and then was rotovapped to dryness at room temperature. The resulting red-brown solid was a pure sample of tetra-*n*-butylammonium salt of **4** (the purity was checked by ^{31}P NMR which has one peak at -13.5 ppm in 0.5 mL $CH_3CN/CDCl_3$ solvent).

Bubble the ^{17}O-enriched sample of **4** (0.2 g, 0.035 mmol) in *ca.* 1 mL of $CH_3CN/CDCl_3$ solvent in a cylindrical 5-mm o.d. sample tube (7 in) with argon for at least 15 minutes, and then a 7 mg (0.027 mmol) of triphenylphosphine was added quickly. After the addition of triphenylphosphine, this NMR tube was sealed immediately, and allowing the oxo transfer reaction to go to completion (at least 1 hour at room temperature). The solution was subsequently analyzed by both ^{31}P and ^{17}O NMR spectroscopy. The reaction was also carried out with 3 (27.6 mg, 0.105 mmol) equivalents of triphenylphosphine over **4**, and the solution was also analyzed by ^{31}P and ^{17}O NMR.

The deoxygenated product, $[Pd^{II}P_2W_{20}O_{70}(OH_2)_2]^{8-}$ (**12**), is treated with the aqueous solution of dimethylammonium hydrochloride (DMA^+Cl^-) to give a yellow aqueous layer, which is separated and filtered using a fine filter paper. Crystalline yellow-brown

plates of **12** were obtained by precipitation with addition of appropriate amount of solid KCl. Analytical data: IR (2% KBr pellet, 1300 - 400 cm^{-1}): 1090 (s), 1028 (s), 959 (s), 935 (m), 769 (s), 719 (sh), 629 (s), 518 (s), 449 (s). ^{31}P NMR (8 mM solution in D_2O): -13.0 ppm ($\Delta\nu_{1/2}$ = 8 Hz). Anal. Calcd. for $(Me_2NH_2)_7K[PdP_2W_{20}O_{70}(OH_2)_2]\bullet 18H_2O$: C, 2.96; N, 1.72; K, 0.68; P, 1.0; Pd, 1.87; W, 64.6. Found: C, 3.15; N, 1.78; K, 0.62; P, 0.8; Pd, 1.86; W, 65.2. [MW = 5687 g/mol]

Figure 7.1 shows the ^{31}P NMR chemical shifts of complexes **5**, **4**, Ph_3P and $Ph_3P{=}O$ in 50:50 (v:v) CH_3CN:$CDCl_3$ solution.

Crystallography Studies of the Deoxygenated Product 12

The complete dataset for **12** was collected at Emory University. Single crystal of $(Me_2NH_2)_7K[PdP_2W_{20}O_{70}(OH_2)_2]$ (**12**) suitable for X-ray analysis, was coated with Paratone-N oil, suspended in a small fiber loop, and placed in a cooled gas stream on a Bruker D8 SMART APEX CCD sealed tube diffractometer. Diffraction intensities were measured using graphite monochromated Mo Kα radiation (λ = 0.71073 Å) at 173(2) K and a combination of φ and ω scans with 10 s frames traversing about ω at 0.3° increments. Data collection, indexing, and initial cell refinements were carried out using SMART;[29] frame integration and final cell refinements were done using SAINT.[30] The molecular structure was determined using Direct Methods and Fourier techniques and refined by full-matrix least squares.[31] A multiple absorption correction was applied using the program SADABS.[32] The largest residual electron density was located close to (less than 1.0 Å from) the W and Pd atoms and was most likely due to imperfect absorption corrections frequently encountered in heavy-metal atom structures.

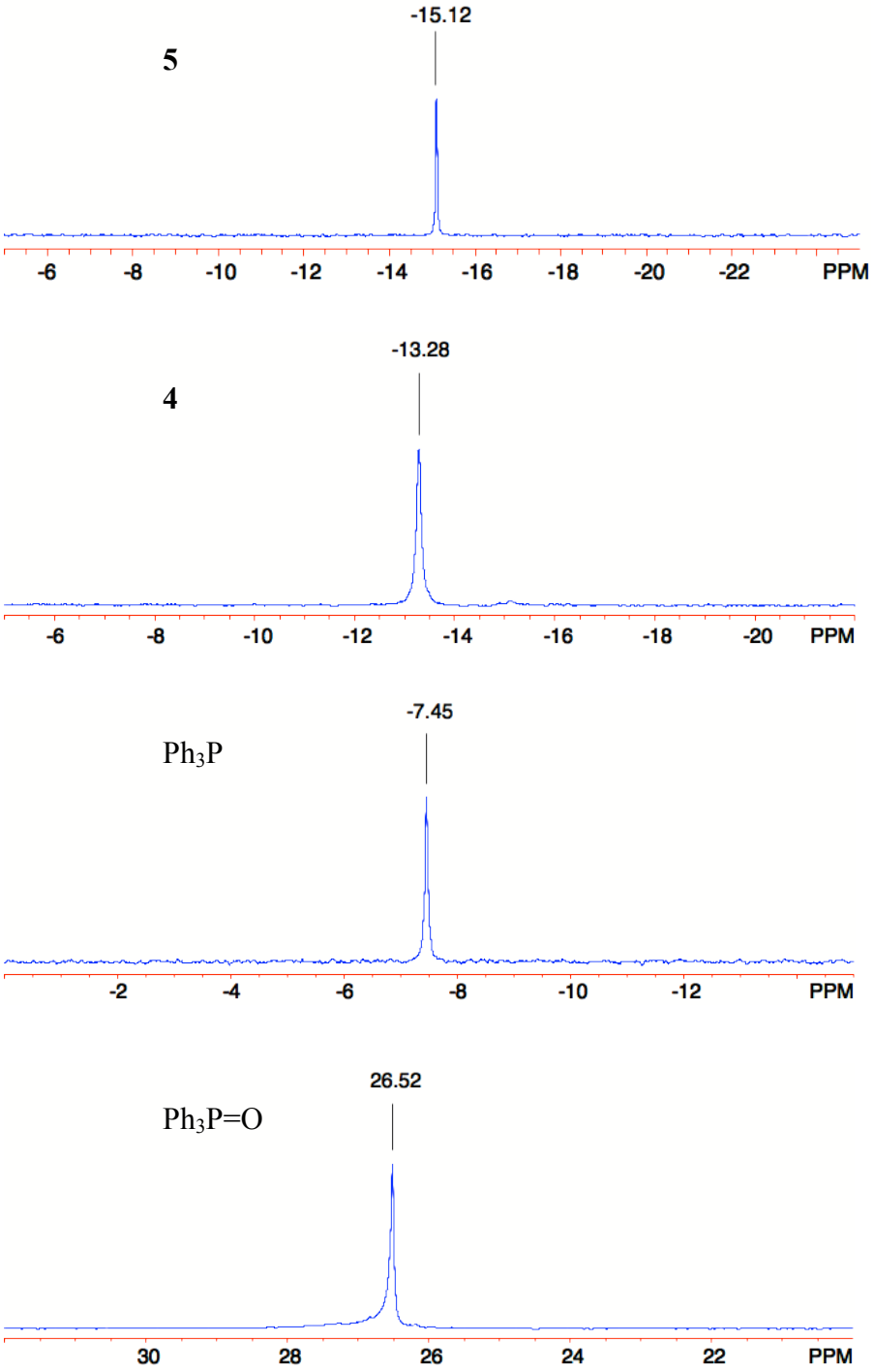

Figure 7.1 ^{31}P NMR spectra of Au-oxo complex **5** (K⊂*cis*-dicyclohexano-18-crown-6 salt), Pd-oxo complex **4** (tetra-*n*-butylammonium (TBA) salt), Ph_3P and Ph_3P=O in 50:50 (v:v) CH_3CN:$CDCl_3$ solution.

Refinement details. The structure of **12** was solved using Direct Methods and difference Fourier techniques.[31] The K, Pd, and W atoms in **12** were refined anisotropically. The remaining atoms were refined isotropically. Some of the solvent water molecules were refined with partial occupancies. Scattering factors and anomalous dispersion corrections are taken from the *International Tables for X-ray Crystallography*. Structure solution, refinement, graphic and generation of publication materials were performed by using SHELXTL, V6.14 software.

Reoxygenation of Pd(II) Complex 12

After the complete oxo transfer reaction between terminal Pd-oxo complex **4** and one equivalent of triphenylphosphine at room temperature (indicated by ^{31}P NMR spectroscopy, all Ph_3P (-7.45 ppm) is converted to the oxidized product $Ph_3P{=}O$ (26.52 ppm) in minutes), the resulted solution is exposed to air. The reoxygenation process is followed by electronic absorption spectroscopy and ^{31}P NMR, showing that the deoxygenated Pd(II) polytungstate $[Pd^{II}P_2W_{20}O_{70}(OH_2)_2]^{8-}$ (**12**) is reoxidized to form Pd-oxo complex **4** by air. In a separate experiment, the *in situ* generated **12** is treated with ^{17}O-enriched dioxygen $^{17}O_2$, and the resulted solution is analyzed by ^{17}O NMR.

Catalytic Properties of Pd-oxo Complex 4

The reaction was carried out in 20 mL pressure vessels with internal threads for use with a PTFE bushing as a pressure seal. The vessel was purged with O_2, and then 2.15

mL of acetonitrile, 0.15 mL of trimethylphosphite (~ 530 mM), tetra-*n*-butylammonium salt of **4** (1.5 mM), and 0.1 mL 1,3-dichlorobenzene (an internal standard for GC-analysis) were added. The vessel was sealed and placed into a thermostated oil-bath (80±1 °C). At a certain time interval, the reaction vessel was cooled dawn in the ice, opened and a small aliquot was withdrawn for GC-analysis. Then the cooled reaction vessel was purged with O_2, sealed and placed again into oil-bath. The GC analysis was performed using a Hewlett-Packard 6890 GC equipped with a HP-5 capillary column (poly(5% diphenyl/95% dimethylsiloxane, 30 m) and an FID detector. The product, trimethylphosphate, was identified using an authentic commercial sample.

Comparative Reaction: $[Pd^{II}Br_4]^{2-}$ + Ph_3P

As a control experiment, the organic soluble form of a regular square-planar Pd(II) complex $(Ph_4P)_2PdBr_4$ is synthesized: to a stirred suspension of $PdCl_2$ (2mmol) in methylene chloride (20 mL) was added a solution of tetraphenylphosphonium bromide (Ph_4PBr, 4 mmol) in CH_2Cl_2 (10 mL). The heterogeneous mixture slowly turned to red homogeneous solution. After 12 h at room temperature, the solution was evaporated under vacuum to give red oil, which is then recrystallized from a CH_2Cl_2-CH_3CN mixture solvent to afford dark-brown crystalline prisms of $(Ph_4P)_2PdBr_4$. If ethanol-acetone (EtOH-CH_3COCH_3) mixture is used for crystal growth, brown crystalline plates of $(Ph_4P)_2Pd_2Br_6$ are obtained. The crystals were collected by filtration and thoroughly dried under suction.

The reaction of $(Ph_4P)_2PdBr_4$ (or $(Ph_4P)_2Pd_2Br_6$) with triphenylphosphine (Ph_3P) is conducted under the same conditions as used for terminal Pd-oxo complex **4**. ^{31}P NMR

spectra indicate that no oxidation happens: there is no $Ph_3P{=}O$ peak at 26.50 ppm shown up, and only ligand exchange happens: two bromides on the Pd(II) atom are replaced by two Ph_3P molecules, leading to a *trans*-$Pd^{II}(Ph_3P)_2Br_2$.

The structures of all these regular Pd(II) complexes, $(Ph_4P)_2PdBr_4$, $(Ph_4P)_2Pd_2Br_6$ and *trans*-$Pd^{II}(Ph_3P)_2Br_2$, were determined by X-ray single crystal diffraction. The complete datasets were collected at Emory University. Single crystals of $(Ph_4P)_2PdBr_4$, $(Ph_4P)_2Pd_2Br_6$ and *trans*-$Pd^{II}(Ph_3P)_2Br_2$ suitable for X-ray analysis, were each coated with Paratone-N oil, suspended in a small fiber loop, and placed in a cooled gas stream on a Bruker D8 SMART APEX CCD sealed tube diffractometer. Diffraction intensities were measured using graphite monochromated Mo Kα radiation (λ = 0.71073 Å) at 173(2) K and a combination of φ and ω scans with 10 s frames traversing about ω at 0.3° increments. Data collection, indexing, and initial cell refinements were carried out using SMART;[29] frame integration and final cell refinements were done using SAINT.[30] The molecular structure of each was determined using Direct Methods and Fourier techniques and refined by full-matrix least squares.[31] A multiple absorption correction was applied using the program SADABS.[32]

7.4 Results and Discussion

Stoichiometric Oxo Transfer of Au-oxo Complex 5

Addition of triphenylphosphine (Ph_3P) to the K⊂*cis*-dicyclohexano-18-crown-6 salt of **5** in $CH_3CN/CDCl_3$ under argon immediately yields a clear, colorless solution, and

triphenylphosphine oxide ($Ph_3P=O$, confirmed by ^{31}P NMR spectroscopy). The transformation of the solution from yellow to colorless upon addition of Ph_3P, indicates that the terminal oxo on Au is transferred, and the Au(III) is reduced to Au(I). This oxo transfer reaction was carefully investigated by both ^{31}P and ^{17}O NMR spectroscopy (**Figure 7.2** and **Figure 7.3**, respectively). In the ^{17}O NMR spectra, the Au=O peak at 605 ppm disappears with the addition of 3 equivalents of Ph_3P, and a new peak at 45 ppm, assigned to the oxygen of $Ph_3P=O$, appears synchronously. Addition of 5 equivalents of Ph_3P does not cause a distinct change in the ^{17}O NMR spectra except that the $Ph_3P=O$ peak at 45 ppm increases in size. Production of $Ph_3P=O$ is also confirmed by ^{31}P NMR spectroscopy: a single peak at 26.52 ppm. In addition to the oxo transfer process, ^{31}P NMR spectroscopy establishes that the resulting Au(I) is subsequently de-metalated by free Ph_3P molecules, leading to the monovacant polytungstate ligand, $[P_2W_{20}O_{70}(OH_2)_2]^{10-}$, and Au-$PPh_3$ coordination complexes. Exchange of free and Au(I)-bound Ph_3P is more rapid than the ^{31}P NMR timescale and gives rise to peaks for the Au-PPh_3 coordination complexes whose chemical shifts (30 - 40 ppm)[33] vary with the ratio of Ph_3P to initial **5**. No free Ph_3P peak appears when even 5 equivalents of Ph_3P are added to the solution of **5** in $CH_3CN/CDCl_3$. Based on the ^{31}P and ^{17}O NMR results, an oxo transfer reaction followed by a competing demetalation of Au(I) is illustrated in **Figure 7.4** (balanced reaction in Equation 7.1). Control experiments involving addition of Ph_3P to a solution of $Au^I(Ph_3P)Br$ (Alfa Aesar) in $CH_3CN/CDCl_3$ give the same behavior as in the presence of **5** (no free Ph_3P peak was detected), and independently, Ph_3P and $\mathbf{P_2W_{21}}$, an all-tungsten compound isostructural to **5**, were shown to give no reaction. In addition, ^{31}P NMR indicates that reaction of $(NH_4)AuCl_4 + Ph_3P$ under identical conditions to the

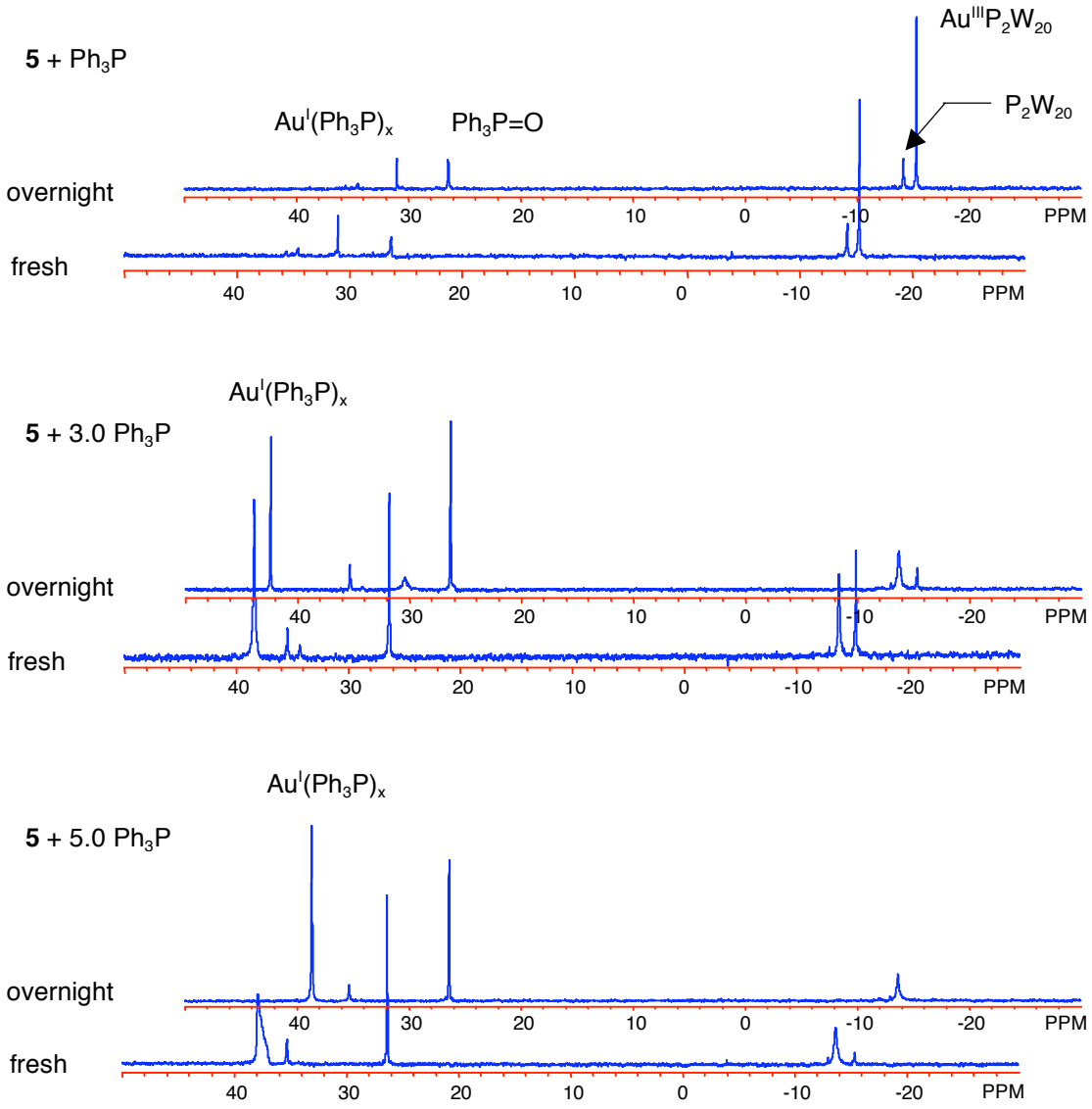

Figure 7.2 ^{31}P NMR spectroscopy studies of oxo transfer from Au-oxo complex **5** (K⊂*cis*-dicyclohexano-18-crown-6 salt) to Ph_3P in 50:50 (v:v) CH_3CN:$CDCl_3$ solution.

reactions of **5** (same solvent and temperature under an argon atmosphere) produces Ph_3PCl_2 but no Ph_3P=O (detectable limit < 1%). The reactions of Au(III) with Ph_3P are well established in the literature (Equation 7.2).[34] In conclusion, these experiments

suggest two lines of evidence that the terminal oxo oxygen on the Au center of **5** transfers to an oxo acceptor, Ph_3P. First, the reaction of **5** + Ph_3P leads to Ph_3P=O and Au(I) complex, while the all-tungsten complex isostructural to **5** does not react with Ph_3P under the same conditions. Second, although regular Au(III) complexes oxidize Ph_3P, the oxidized product is not Ph_3P=O but Ph_3PX_2 (X = Cl or Br).

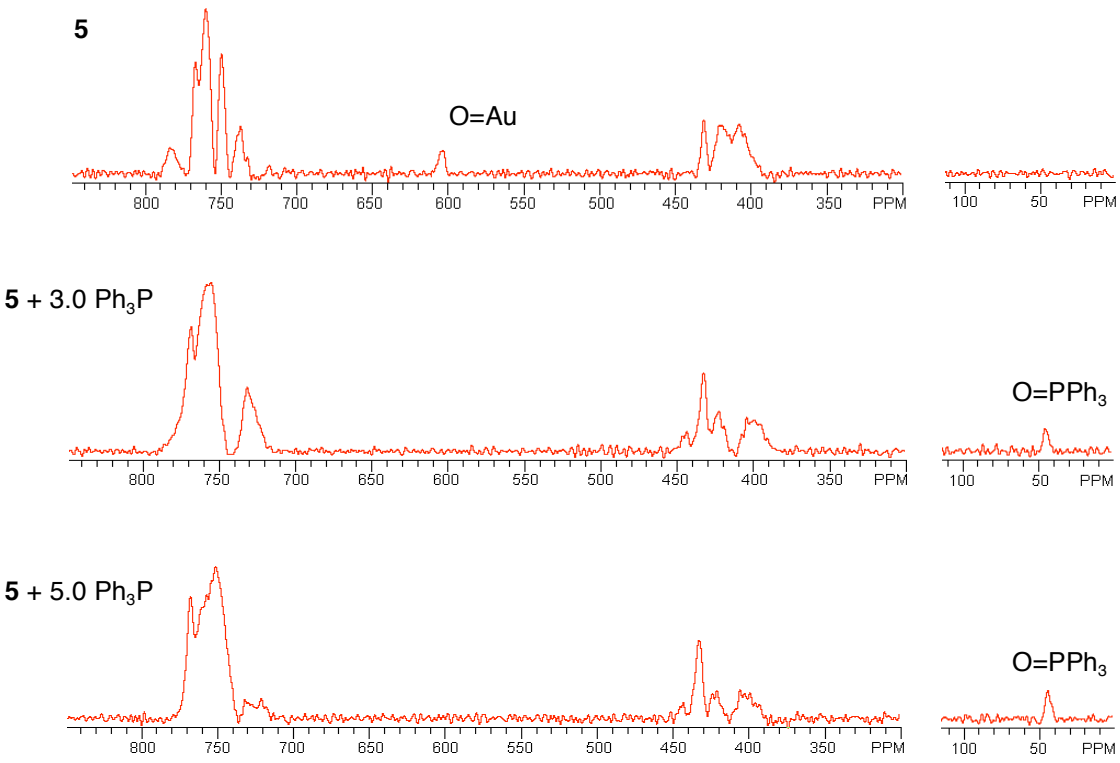

Figure 7.3 ^{17}O NMR spectroscopy studies of oxo transfer from Au-oxo complex **5** (K⊂*cis*-dicyclohexano-18-crown-6 salt) to Ph_3P in 50:50 (v:v) CH_3CN:$CDCl_3$ solution, showing the selective disappearance of the terminal Au(III)=O peak at 605 ppm and the appearance of the Ph_3P=O peak at 45 ppm.

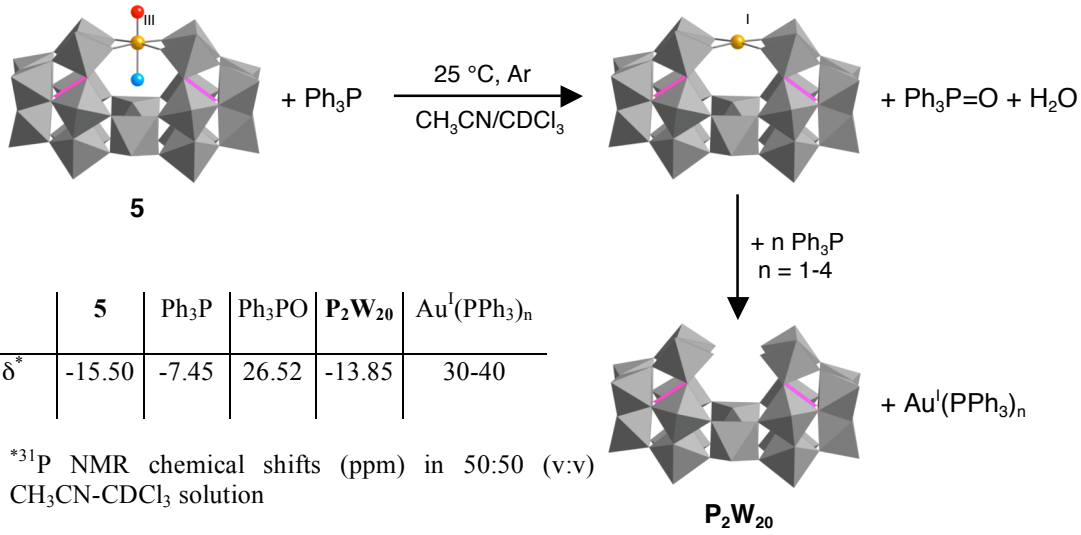

	5	Ph_3P	Ph_3PO	P_2W_{20}	$Au^I(PPh_3)_n$
δ^*	-15.50	-7.45	26.52	-13.85	30-40

*^{31}P NMR chemical shifts (ppm) in 50:50 (v:v) CH_3CN-$CDCl_3$ solution

$$[Au^{III}(O)(OH_2)P_2W_{20}O_{70}(OH_2)_2]^{9-} + (n+1)\ Ph_3P$$

$$\rightarrow [P_2W_{20}O_{70}(OH_2)_2]^{10-} + Ph_3PO + Au^I(PPh_3)_n + H_2O \quad \text{(Equation 7.1)}$$

$$[Au^{III}Cl_4]^- + 2\ Ph_3P \rightarrow [Au^I(PPh_3)Cl] + Ph_3PCl_2 + Cl^- \quad \text{(Equation 7.2)}$$

Figure 7.4 Illustration of oxo transfer reaction from Au-oxo complex **5** to Ph_3P competed with a demetalation of the resulted Au(I) by free unreacted Ph_3P molecules.

Stoichiometric Oxo Transfer of Pd-oxo Complex 4

An organic soluble form, the tetra-*n*-butylammonium (TBA) salt of **4**, is made by extraction of **4** in aqueous solution, with a dichloromethane solution of eight equivalents of TBABr followed by removal of the dichloromethane solvent. ^{31}P NMR confirmed that there was no decomposition of the polyanion in this ion exchange process (one peak at -13.28 ppm, in 50:50 CH_3CN:$CDCl_3$ solvent). Oxo oxygen transfer of the terminal Pd-

oxo unit of **4** (TBA salt) is documented by the reaction with triphenylphosphine (Ph_3P) under argon (many other phosphor and sulfur based molecules can be oxo acceptors). Addition of Ph_3P to the CH_3CN:$CDCl_3$ solution of **4** causes immediate color change from brown to yellow. The oxidized product Ph_3P=O is confirmed by its characteristic ^{31}P NMR chemical shift at 26.52 ppm, and the other new peak at -12.45 ppm (**Figure 7.5**) is assigned to the deoxygenated **4**. As shown in **Figure 7.5**A, 20% of **4** still remains with addition of only 0.80 equivalents of Ph_3P. Importantly, as shown in **Figure 7.5**B, addition of three equivalents of Ph_3P causes the disappearance of **4**, and the extra two equivalents of Ph_3P remain as free molecule in solution (the peak at -7.45 ppm is assigned to free Ph_3P). Furthermore, the peak integration of Ph_3P=O and free Ph_3P gives a ratio of 1:2, a result consistent to the stoichiometric oxo transfer from Pd(IV)=O to Ph_3P. These results strongly suggest that only the terminal Pd-oxo transfers stoichiometricly to Ph_3P and W-oxo is inactive in this reaction.

The oxo transfer process is further confirmed by ^{17}O NMR spectroscopy. The terminal Pd-oxo oxygen peak of the ^{17}O-enriched **4** is assigned at 545 ppm, based on the well-established correlation between downfield chemical shift and oxygen π-bond order[35-39] (terminal W=O (triple bond) have peaks in the range of 705-765 ppm; bridging W-O-W (single bond) are between 400-450 ppm). Reaction of terminal Pd-oxo complex **4** with Ph_3P causes selective disappearance of the Pd-oxo oxygen peak, and the formation of Ph_3P=O is confirmed by its characteristic peak showing up at 45 ppm (**Figure 7.6**). Addition of extra Ph_3P does not change the ^{17}O NMR spectrum. These findings from ^{17}O NMR studies, (1) the stoichiometric oxo transfer, (2) the high stability of the reduced

Pd(II) in polytungstate ligand environment and (3) the inactivity of W=O oxygens in oxo transfers, are all in good agreement with the ^{31}P NMR results.

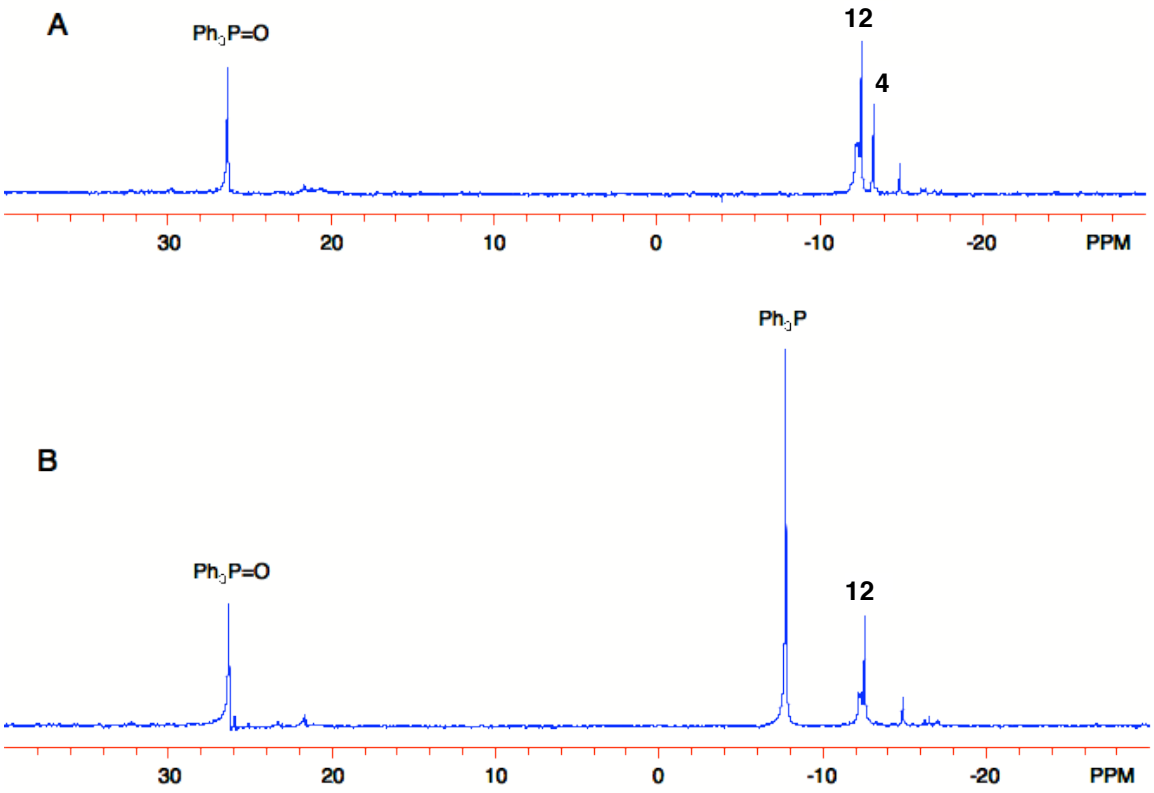

Figure 7.5 ^{31}P NMR spectroscopy studies of oxo transfer from Pd-oxo complex **4** (tetra-*n*-butylammonium (TBA) salt) to Ph_3P in 50:50 (v:v) CH_3CN:$CDCl_3$ solution. (A) **4** + 0.8 Ph_3P; (B) **4** + 3.0 Ph_3P. The deoxygenated product, $[Pd(II)P_2W_{20}O_{70}(OH_2)_2]^{8-}$ (**12**), is stable in the presence of extra Ph_3P molecules and confirms the stoichiometric oxo transfer from the terminal Pd(IV)=O unit to Ph_3P.

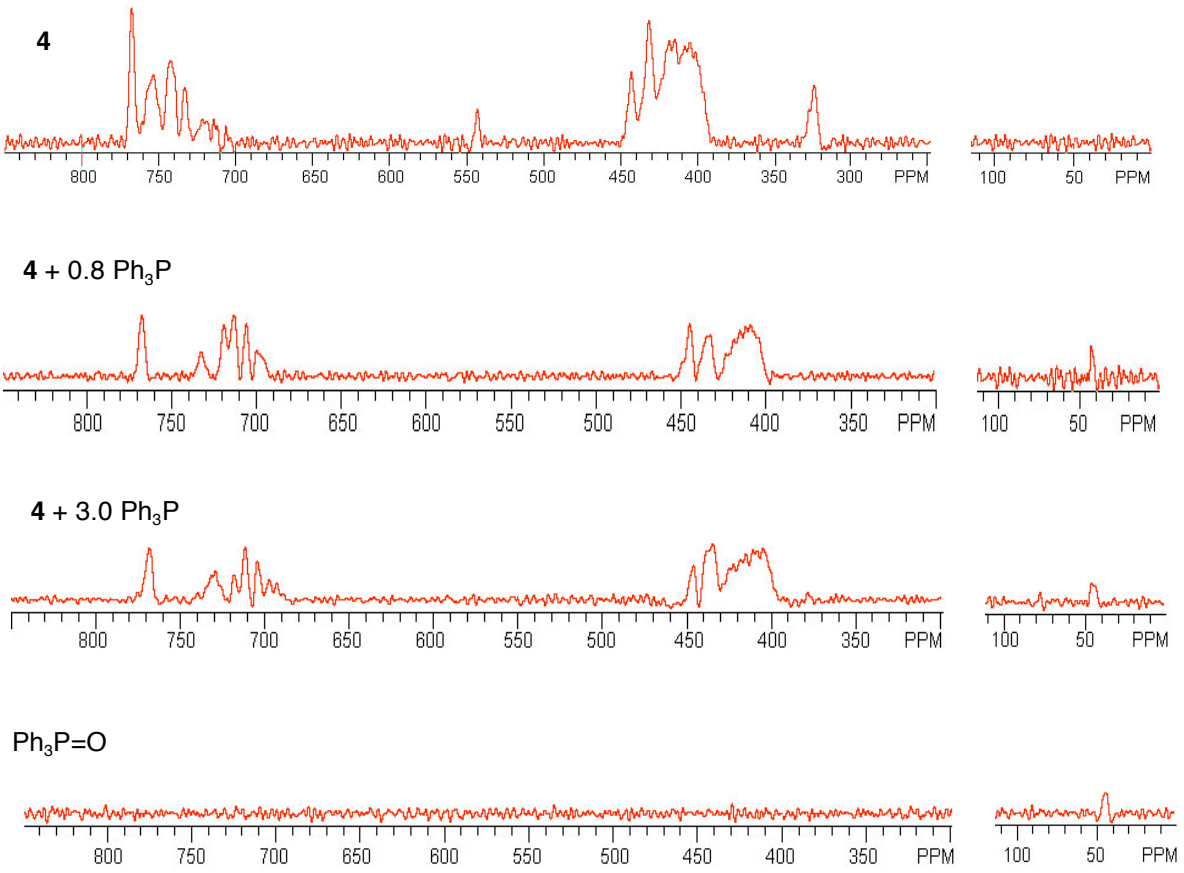

Figure 7.6 ^{17}O NMR spectroscopy studies of oxo transfer from Pd-oxo complex **4** (tetra-*n*-butylammonium (TBA) salt) to Ph_3P in 50:50 (v:v) CH_3CN:$CDCl_3$ solution, showing the selective disappearance of the terminal Pd(IV)=O peak at 545 ppm and the appearance of the Ph_3P=O peak at 45 ppm.

Crystallography Studies of 12

Unlike the Au(I) polytungstate, $[Au^{I}P_2W_{20}O_{70}(OH_2)_2]^{9-}$, which is not stable and loses the Au(I) center in the presence of free Ph_3P molecules to give Au(I)-PPh_3 coordination complexes, the stability of the deoxygenated product,

$[Pd^{II}P_2W_{20}O_{70}(OH_2)_2]^{8-}$ (**12**), under inert atmosphere, renders the possibility for its isolation. Metathesis of **12** (TBA salt) in $CHCl_3$ by dimethylammonium hydrochloride (DMA^+Cl^-) in water results in a yellow aqueous layer, which is separated and filtered using a fine filter paper. Addition of appropriate amount of KCl to the filtrate precipitates crystalline yellow-brown plates of **12**.

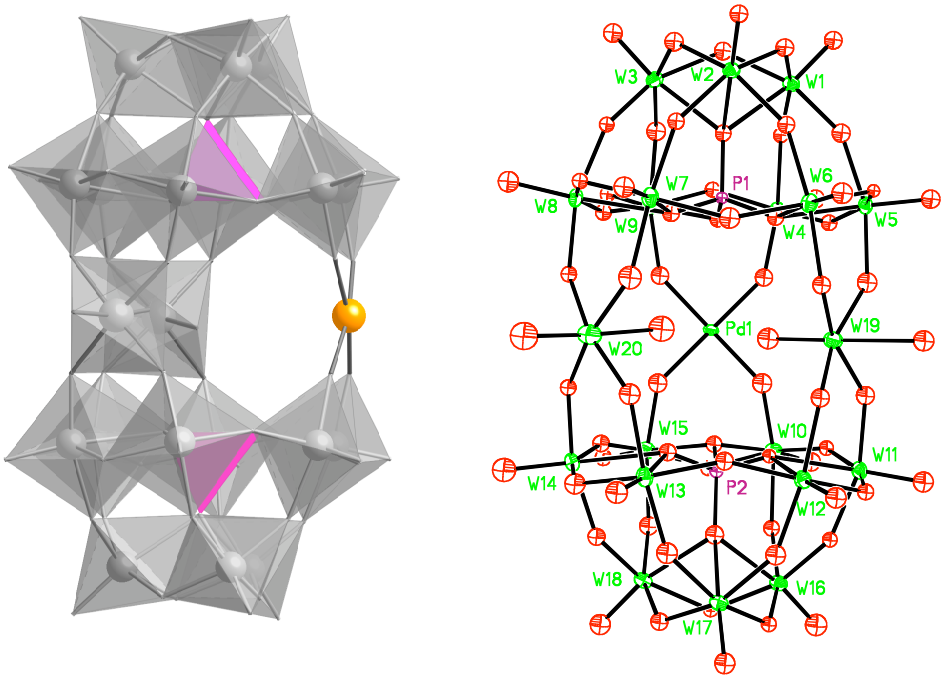

Figure 7.7 Combination polyhedral/ball-and-stick representation (left) and thermal ellipsoid plots and numbering scheme (right) for polyanion **12**. The WO_6 (or W atom) and PO_4 polyhedra are shown in gray and pink, respectively. The Pd atom is shown in yellow.

X-ray crystallography studies of **12** confirm the existence of a square-planar Pd center flanked by the monovacant polytungstate ligand $[P_2W_{20}O_{70}(OH_2)_2]^{10-}$ through four oxygens (**Figure 7.7**). The polyanion structure is disorder-free; thus, we take the structural analysis to be unambiguous. The coordination geometry of the Pd atom, including the Pd-$(O\text{-}W)_{eq}$ bond lengths (1.950(15)-1.979(15) Å) and the O-Pd-O bond angles (89.2(6)°-91.1(6)°, 175.5(6)° and 176.6(6)°), suggests the d^8 Pd(II) oxidation state, a result consistent with the deoxygenation of a Pd(IV)=O unit. All the countercations (7 DMA^+ and 1 K^+) can be located in X-ray crystallography and found by elemental analysis, and the formula of **12** is established as $(DMA)_7K[Pd^{II}P_2W_{20}O_{70}(OH_2)_2]$. Crystal data and refinement parameters for the X-ray diffraction studies are summarized in **Table 7.1**.

Reoxygenation of Pd(II) Complex 12

A well-characterized oxo transfer from terminal Pd(IV)=O to substrates (e.g. Ph_3P) is only half of the O_2-based catalytic oxidation cycle. Importantly, our subsequent studies show that the deoxygenated form, **12**, can be reoxidized in the presence of O_2. As shown in **Figure 7.8**, the oxo transfer (to Ph_3P) and reoxygenation (by O_2) processes of **4** are followed by ^{31}P NMR spectroscopy. In the first four spectra, where the reaction of **4** and Ph_3P are protected under argon, the reaction products, Ph_3P=O and **12** (peaks at 26.52 and -12.45 ppm, respectively), accumulate, while simultaneously the oxo donor (**4**, -13.28 ppm) and acceptor (Ph_3P, -7.45 ppm) decrease/disappear. The reaction stops when all Ph_3P is converted.

Table 7.1 Crystal data and structural refinement for the X-ray structures of $(C_2H_6NH_2)_7K[PdP_2W_{20}O_{70}(OH_2)_2]\bullet 18H_2O$ (**12**)

complex	**12**
molecular formula	$H_{96}C_{14}N_7KO_{90}P_2PdW_{20}$
formula wt. (g mol^{-1})	5687.38
temperature (K)	173(2)
radiation (λ, Å)	0.71073
crystal system	Monoclinic
space group	*P2(1)/c* (#14)
a (Å)	11.7359(4)
b (Å)	32.7975(14)
c (Å)	22.1673(8)
β (º)	98.168(2)
Volume (Å^3)	8445.8(6)
Z	4
ρ_{calcd} (g cm^{-3})	4.271
μ (mm^{-1})	27.523
F(000)	9392
crystal size (mm^3)	0.18 × 0.06 × 0.03
reflections collected	62779
independent reflections	17176 [R(int) = 0.1201]
absorption correction	SADABS and face index
refinement method	full-matrix least-squares on F^2
goodness-of-fit on F^2	1.003
final R indices	R1[a] = 0.0672
[R > 2σ (I)]	wR2[b] = 0.1415
R indices (all data)	R1[a] = 0.1329
	wR2[b] = 0.1736
largest diff. peak and hole (e Å^{-3})	7.260 and -5.542

[a] $R_1 = \Sigma||F_o| - |F_c|| / |F_o|$

[b] $wR_2 = \{\Sigma[w(F_o^2 - F_c^2)^2] / \Sigma[w(F_o^2)^2]\}^{0.5}$

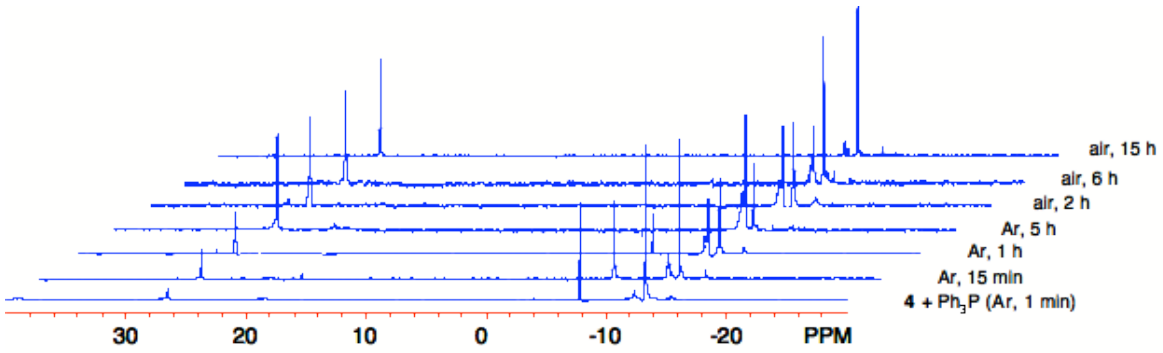

Figure 7.8 ^{31}P NMR spectroscopy studies of oxo transfer from Pd-oxo complex **4** (tetra-*n*-butylammonium (TBA) salt) to Ph_3P under argon as well as followed reoxygenation of the reduced form **12** under air in 50:50 (v:v) CH_3CN:$CDCl_3$ solution.

The resulted solution in the NMR tube is then exposed to air at room temperature, and the reoxygenation is shown in the last three spectra in **Figure 7.8**. These spectra confirm that the deoxygenated form, **12**, can react with O_2 to regenerate the Pd-oxo complex **4**. This result is consistent with the finding in the synthesis of **4** that the terminal Pd(IV)=O complex **4** can be obtained by the reaction of the starting Pd(II) material with the polytungstate ligand under air, but the identical protocol under inert atmosphere gives no product. The reoxygenation process of **12** by air is also studied by electronic absorption spectroscopy (**Figure 7.9**). Addition of Ph_3P to the acetonitrile solution of **4** under argon causes a significant increase of the absorption coefficient in the higher energy range (< 465 nm), a result consistent with the reduction of a Pd(IV)-oxo unit to a square-planar Pd(II) center. Exposure of the resulted solution to air leads to the

gradual recovering of the original spectrum of **4**, indicating the deoxygenated form does react with O_2 to afford the Pd-oxo complex.

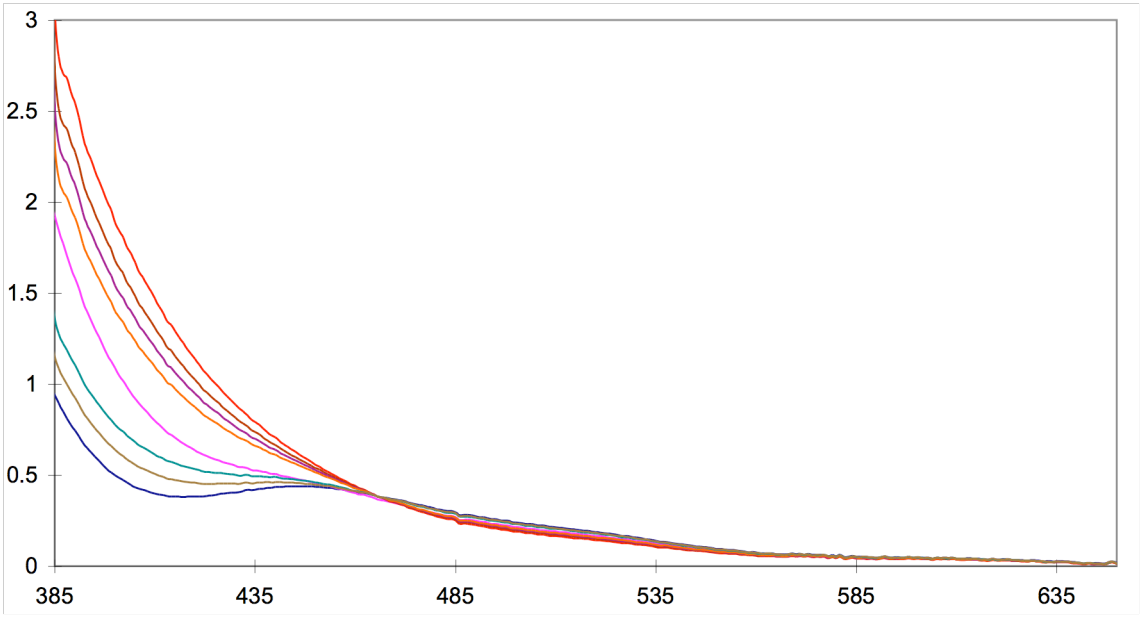

Figure 7.9 Electronic absorption spectroscopy studies of oxo transfer from Pd-oxo complex **4** (tetra-*n*-butylammonium (TBA) salt) to Ph_3P under argon as well as followed reoxygenation of the reduced form **12** under air in 50:50 (v:v) CH_3CN:$CDCl_3$ solution.

The most direct evidence for the O_2 activation on a Pd center is documented by ^{17}O labeling experiments. A 0.1 g organic soluble sample of **4** is dissolved in the freshly dried $CH_3CN/CDCl_3$ solvent and is first treated with an oxo acceptor (like Ph_3P). After the complete conversion of **4** to its deoxygenated form **12**, the resulted solution is sealed in the presence of an atmosphere of 10%-atom enriched $^{17}O_2$. The ^{17}O NMR spectrum of this solution is acquired after 5 hours when most of **4** is recovered monitored by ^{31}P NMR

spectroscopy. As shown in **Figure 7.10**, the terminal Pd-oxo oxygen peak at 545 ppm (established in previous ^{17}O NMR studies) selectively shows up. The ^{17}O labeling experiments confirm that the deoxygenated form, $[Pd^{II}P_2W_{20}O_{70}(OH_2)_2]^{8-}$ (**12**), can be reoxidized and the terminal oxo oxygen on the Pd center comes from O_2.

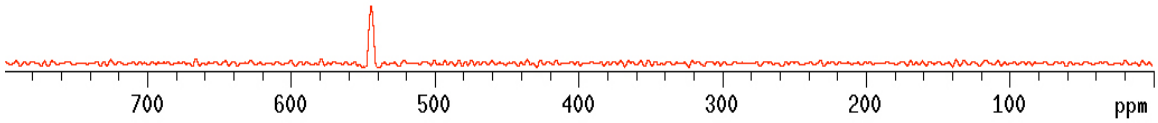

Figure 7.10 ^{17}O NMR spectrum of the reoxygenation of the reduced form **12** with ^{17}O-enriched dioxygen ($^{17}O_2$) in 50:50 (v:v) CH_3CN:$CDCl_3$ solution, showing the selective building up of the terminal Pd(IV)=O peak at 545 ppm.

Catalytic Oxidation by Pd-oxo Complex 4

By incorporating Pd atom in appropriate polytungstate ligand environments, which resemble the geometric and electronic structures of redox metal-oxides supported palladium catalysts, we have shown that the terminal Pd-oxo complex **4** can stoichiometricly transfer its terminal oxo oxygen to other substrates; and more importantly, the deoxygenated Pd(II) product **12** can be oxidized by dioxygen to reform the Pd(IV)=O species. Both the stoichiometric oxo transfer and the reoxygenation processes are carefully studied by ^{31}P and ^{17}O NMR as well as electronic absorption spectroscopy. The synthesis of terminal Pd-oxo complex **4** and its reactivity (oxo transfer and reoxygenation) are summarized in **Figure 7.11**. As shown in this figure, the Pd-

centered catalytic O_2 activation cycle is completed, and this renders the possibility for Pd-oxo complex **4** to catalyze the green O_2-based oxidation.

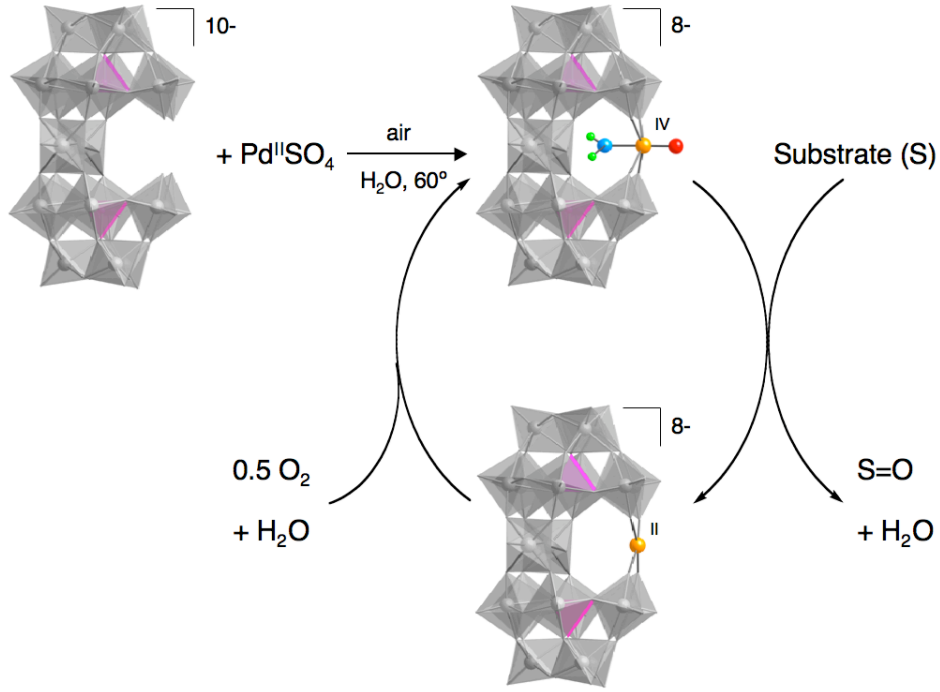

Figure 7.11 Schematic representation of the synthesis and reactivity (oxo transfer and reoxygenation by O_2) of the terminal Pd-oxo complex **4**. The polyanion structures of the monovacant polytungstate ligand $K_{10}[P_2W_{20}O_{70}(OH_2)_2]$ (top left), **4** (top right) and the deoxygenated product **12** (bottom) are shown as combined polyhedral/ball-and-stick representations. The WO_6 and PO_4 polyhedra are shown in gray and pink. The Pd, O atoms, and aqua (H_2O) ligand are shown in yellow, red, and blue, respectively.

An exemplary O_2-based catalytic oxidation by the terminal Pd-oxo complex **4** is addressed below to support the above statement. In the presence of **4**, trimethylphosphite

reacts with O_2 to selectively form trimethylphosphate (**Figure 7.12**). Two important features of this reaction suggest that **4** is the catalyst. First, the absence of an induction period argues that **1** is a precatalyst. Second, a turnover number (TON) larger than 200 is obtained with a 60% yield of $(MeO)_3P=O$, and no detectable decomposition of **4** is found in the ^{31}P NMR spectroscopy. Moreover, control experiments without **4** or with regular Pd(II) complexes show no reaction, which also indicate the catalytic properties of **4** in the O_2-based oxidation.

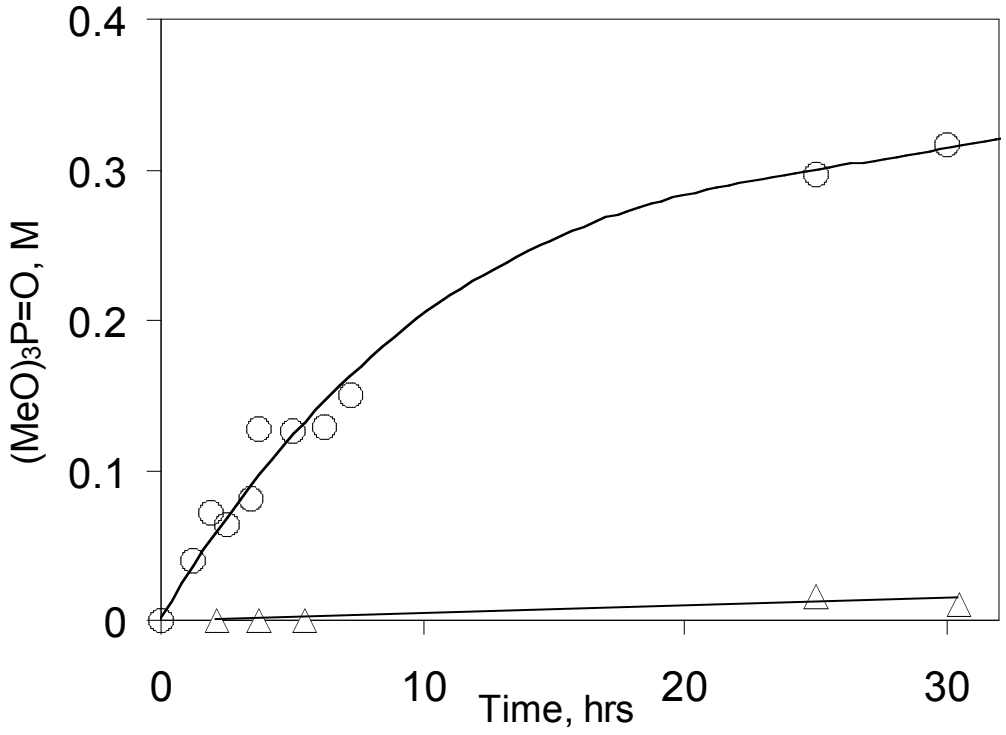

Figure 7.12 Oxidation of $(MeO)_3P$ (0.55 M) to $(MeO)_3P=O$ catalyzed by **4** (1.3 mM) in acetonitrile at 80° C with 1.0 atm of air (open circle). A control reaction (Δ) was carried out in the absence of POM. Important numbers: a yield of $(MeO)_3P=O$ (based on initial $(MeO)_3P$) after 30 hrs is ~ 60%; TON = $[(MeO)_3P=O]/[\mathbf{4}] \geq 2x10^2$; initial TOF ~ 20 h^{-1}.

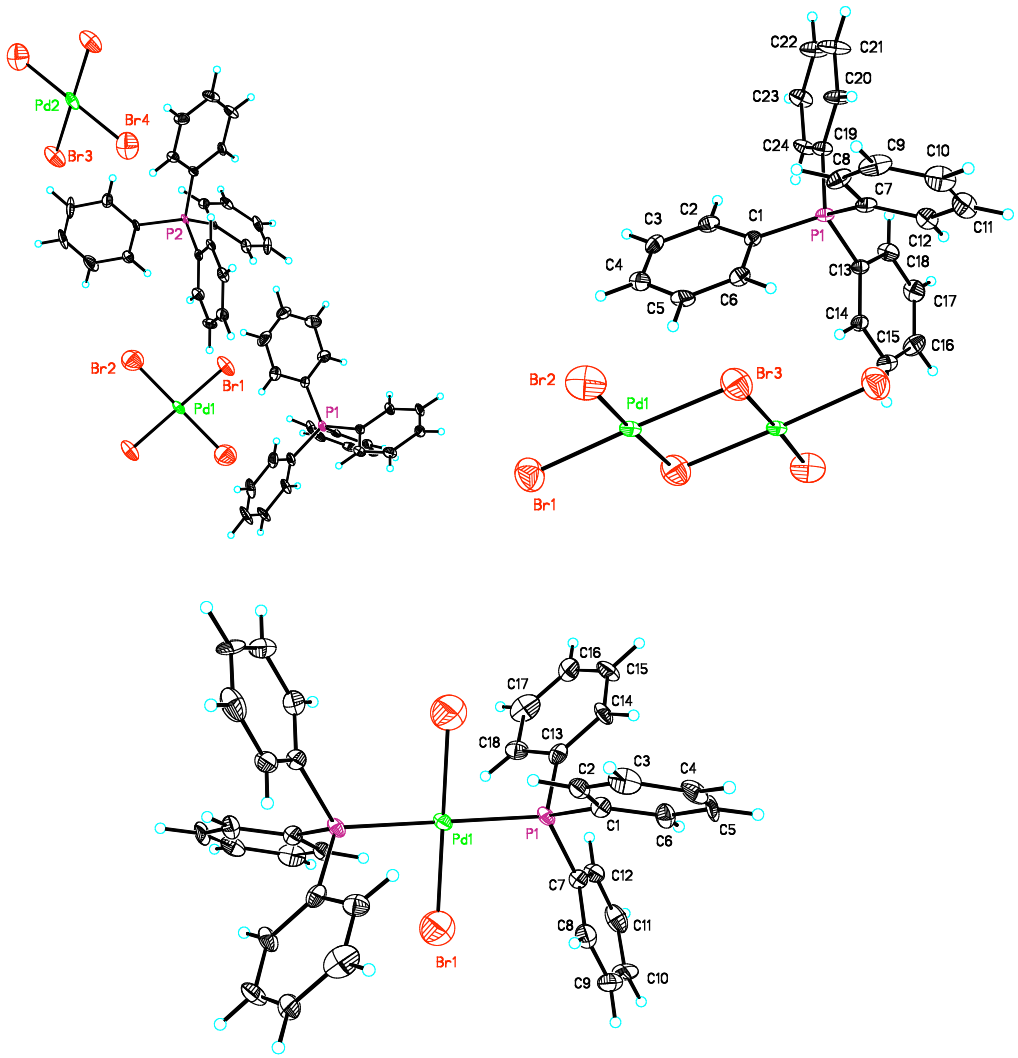

Figure 7.13 Thermal ellipsoid plots and numbering scheme for $(Ph_4P)_2PdBr_4$ (top left), $(Ph_4P)_2Pd_2Br_6$ (top right) and *trans*-$(Ph_3P)_2PdBr_2$ (bottom).

Table 7.2 Crystal data and structural refinement for the X-ray structures of $[(C_6H_5)_4P]_2[PdBr_4]$, $[(C_6H_5)_4P]_2[Pd_2Br_6]$ and $[(C_6H_5)_3P]_2PdBr_2 \bullet 2CH_2Cl_2$

complex	$[(C_6H_5)_4P]_2[PdBr_4]$	$[(C_6H_5)_4P]_2[Pd_2Br_6]$
molecular formula	$H_{40}C_{48}Br_4P_2Pd$	$H_{40}C_{48}Br_6P_2Pd_2$
formula wt. (g mol^{-1})	1104.83	1371.00
temperature (K)	173(2)	173(2)
radiation (λ, Å)	0.71073	0.71073
crystal system	Triclinic	Triclinic
space group	*P-1* (#2)	*P-1* (#2)
a (Å)	10.2535(2)	10.4233(2)
b (Å)	14.0879(3)	10.8755(3)
c (Å)	14.9256(2)	10.8775(2)
α (º)	91.370(1)	79.5320(10)
β (º)	92.176(1)	79.0840(10)
γ (º)	102.071(1)	71.3080(10)
Volume ($Å^3$)	2105.70(7)	1137.14(4)
Z	2	1
ρ_{calcd} (g cm^{-3})	1.742	2.002
μ (mm^{-1})	4.346	6.166
F(000)	1088	660
crystal size (mm^3)	0.54 × 0.28 × 0.15	0.25 × 0.12 × 0.03
reflections collected	14332	10474
independent reflections	8190 [R(int) = 0.0252]	4634 [R(int) = 0.0387]
absorption correction	SADABS and face index	SADABS and face index
refinement method	full-matrix least-squares on F^2	full-matrix least-squares on F^2
goodness-of-fit on F^2	1.066	1.079
final R indices	$R1^a$ = 0.0714	$R1^a$ = 0.0788
[R > 2σ (I)]	$wR2^b$ = 0.2248	$wR2^b$ = 0.2454
R indices (all data)	$R1^a$ = 0.0825	$R1^a$ = 0.1015
	$wR2^b$ = 0.2360	$wR2^b$ = 0.2681
largest diff. peak and hole (e $Å^{-3}$)	2.820 and -3.557	3.194 and -3.181

$^a R_1 = \Sigma||F_o| - |F_c|| / |F_o|$

$^b wR_2 = \{\Sigma[w(F_o^2 - F_c^2)^2] / \Sigma[w(F_o^2)^2]\}^{0.5}$

Table 7.2 Continued: Crystal data and structural refinement for the X-ray structures of $[(C_6H_5)_4P]_2[PdBr_4]$, $[(C_6H_5)_4P]_2[Pd_2Br_6]$ and $[(C_6H_5)_3P]_2PdBr_2 \bullet 2CH_2Cl_2$

complex	$[(C_6H_5)_3P]_2PdBr_2 \bullet 2CH_2Cl_2$
molecular formula	$H_{34}C_{38}Br_2Cl_4P_2Pd$
formula wt. (g mol^{-1})	960.61
temperature (K)	173(2)
radiation (λ, Å)	0.71073
crystal system	Orthorhombic
space group	*Pbca* (#61)
a (Å)	20.160(3)
b (Å)	8.0369(12)
c (Å)	23.100(4)
Volume ($Å^3$)	3742.7(10)
Z	4
ρ_{calcd} (g cm^{-3})	1.705
μ (mm^{-1})	3.030
F(000)	1904
crystal size (mm^3)	0.28 × 0.05 × 0.02
reflections collected	15560
independent reflections	3588 [R(int) = 0.1195]
absorption correction	SADABS and face index
refinement method	full-matrix least-squares on F^2
goodness-of-fit on F^2	1.034
final R indices	$R1^a$ = 0.0964
[R > 2σ (I)]	$wR2^b$ = 0.2723
R indices (all data)	$R1^a$ = 0.1838
	$wR2^b$ = 0.3338
largest diff. peak and hole (e $Å^{-3}$)	2.747 and -3.077

$^a R_1 = \Sigma||F_o| - |F_c|| / |F_o|$

$^b wR_2 = \{\Sigma[w(F_o^2 - F_c^2)^2] / \Sigma[w(F_o^2)^2]\}^{0.5}$

Comparative Reactions

In order to show different reactivities of the terminal Pd(IV)=O species and regular Pd(II) complexes, comparative reactions of $PdBr_4^{2-}$ (or $Pd_2Br_6^{2-}$) with Ph_3P are also conducted under the same condition (organic solvent and argon protection). The tetraphenylphosphonium (Ph_4P^+) salt of $PdBr_4^{2-}$ is made by suspension of $PdCl_2$ in the dichloromethane solution of Ph_4PBr overnight. The mixture is filtered and the dark-brown crystals of $(Ph_4P)_2PdBr_4$ grow from a CH_2Cl_2-CH_3CN mixture solvent (if ethanol-acetone mixture is used for crystal growth, $(Ph_4P)_2Pd_2Br_6$ is obtained; both structures are studied by X-ray diffraction). Reaction of $PdBr_4^{2-}$ (or $Pd_2Br_6^{2-}$) with Ph_3P only leads to ligand exchanged product: two bromides are replaced by two Ph_3P molecules, giving a *trans*-$Pd^{II}(Ph_3P)_2Br_2$ (**Figure 7.13**, crystal data and refinement parameters for the X-ray structures of $PdBr_4^{2-}$, $Pd_2Br_6^{2-}$ and *trans*-$Pd^{II}(Ph_3P)_2Br_2$ are summarized in **Table 7.2**). Spectroscopy studies (^{31}P and ^1H NMR) also confirm that no Ph_3P=O is formed during this reaction. The different behaviors of Pd-oxo complex **4** with Ph_3P compared to this control experiment support the assignment of a terminal Pd(IV)=O unit in the molecule of **4** and its ability to transfer the terminal oxo oxygen to other substrates, such as Ph_3P.

References

(1) Appleby, A. J.; Foulkes, F. R. *Fuel cell handbook*; Krieger Publising Company, Malabar, Florida, 1993.

(2) Somorjai, G. A. *Introduction to surface chemistry and catalysis*; Wiley: New York, 1994.

(3) Malleron, J. L.; Fiaud, J. C.; Legros, J. Y. *Handbook of Palladium-Catalyzed Organic Reactions: Synthetic Aspects and Catalytic Cycles*; Academic Press: San Diego, CA., 1997.

(4) Singh, A.; Sharp, P. R. *Dalton Trans.* **2005**, 2080-2081.

(5) Luyben, M. L.; Tyreus, B. D. *Computers & Chem. Eng.* **1998**, *22(7-8)*, 867-877.

(6) Macleod, N.; Keel, J. M.; Lambert, R. M. *Appl. Catal. A:* **2004**, *261*, 37-46.

(7) Valden, M.; Lai, X.; Goodman, D. W. *Science* **1998**, *281*, 1647-1650.

(8) Chen, M. S.; Goodman, D. W. *Science* **2004**, *306*, 252-255.

(9) Arrii, S.; Morfin, F.; Renouprez, A. J.; Rousset, J. L. *J. Am. Chem. Soc.* **2004**, *126*, 1199-1205.

(10) Kim, W. B.; Voitl, T.; Rodriguez-Rivera, G. J.; Dumesic, J. A. *Science* **2004**, *305*, 1280-1283.

(11) *Catalysis by Gold*; Hutchings, G. J.; Haruta, M., Eds.; Elsevier: New York, 2005; Vol. 291.

(12) Barteau, M. A. *Topics in Catalysis* **2003**, *22*.

(13) Linic, S.; Piao, H.; Adib, K.; Barteau, M. A. *Angew. Chem. Int. Ed.* **2004**, *43*, 2918-2921.

(14) Linic, S.; Barteau, M. A. *J. Am. Chem. Soc.* **2004**, *126*, 8086-8087.

(15) Bond, G. C.; Thompson, D. T. *Gold Bulletin* **2000**, *33*, 41-51.

(16) Cinellu, M. A.; Minghetti, G.; Stoccoro, S.; Zucca, A.; Manassero, M. *Chem. Comm.* **2004**, 1618-1619.

(17) Cinellu, M. A.; Minghetti, G.; Cocco, F.; Stoccoro, S.; Zucca, A.; Manassero, M. *Angew. Chem. Int. Ed.* **2005**, *44*, 6892-6895.

(18) Sharp, P. R. *Dalton Trans.* **2000**, *16*, 2647-2657.

(19) Anderson, T. M.; Neiwert, W. A.; Kirk, M. L.; Piccoli, P. M. B.; Schultz, A. J.; Koetzle, T., F.; Musaev, D. G.; Morokuma, K.; Cao, R.; Hill, C. L. *Science* **2004**, *306*, 2074-2077.

(20) Anderson, T. M.; Cao, R.; Slonkina, E.; Hedman, B.; Hodgson, K. O.; Hardcastle, K. I.; Neiwert, W. A.; Wu, S.; Kirk, M. L.; Knottenbelt, S.; Depperman, E. C.; Keita, B.; Nadjo, L.; Musaev, D. G.; Morokuma, K.; Hill, C. L. *J. Am. Chem. Soc.* **2005**, *127*, 11948-11949.

(21) Cao, R.; Anderson, T. M.; Piccoli, P. M. B.; Schultz, A. J.; Koetzle, T. F.; Geletii, Y. V.; Slonkina, E.; Hedman, B.; Hodgson, K. O.; Hardcastle, K. I.; Fang, X.; Kirk, M. L.; Knottenbelt, S.; Kogerler, P.; Musaev, D. G.; Morokuma, K.; Takahashi, M.; Hill, C. L. *J. Am. Chem. Soc.* **2007**, *129*, 11118-11133.

(22) *Polyoxometalate Chemistry From Topology via Self-Assembly to Applications*; Pope, M. T.; Müller, A., Eds.; Kluwer Academic Publishers: Dordrecht, 2001.

(23) *Polyoxometalate Chemistry for Nano-Composite Design*; Yamase, T.; Pope, M. T., Eds.; Kluwer Academic/Plenum Publishers: New York, 2002; Vol. 2.

(24) Pope, M. T. In *Comprehensive Coordination Chemistry II: From Biology to Nanotechnology*; Wedd, A. G., Ed.; Elsevier Ltd.: Oxford, UK, 2004; Vol. 4, p 635-678.

(25) Hill, C. L. In *Comprehensive Coordination Chemistry-II: From Biology to Nanotechnology*; Wedd, A. G., Ed.; Elsevier Ltd.: Oxford, UK, 2004; Vol. 4, p 679-759.

(26) Kozhevnikov, I. V. *Catalysis by Polyoxometalates*; Wiley: Chichester, England, 2002; Vol. 2.

(27) Hay-Motherwell, R. S.; Wilkinson, G.; Hussain-Bates, B.; Hursthouse, M. B. *Polyhedron* **1993**, *12*, 2009-2012.

(28) Jacobi, B. G.; Laitar, D. S.; Pu, L.; Wargocki, M. F.; DiPasquale, A. G.; Fortner, K. C.; Schuck, S. M.; Brown, S. N. *Inorg. Chem.* **2002**, *41*, 4815-4823.

(29) SMART; Bruker AXS; 5.628 ed.; Analytical X-ray Systems: Madison, WI, 2003.

(30) SAINT; Bruker AXS, I.; 6.28 ed.; Analytical X-ray Systems: Madison, WI, 2003.

(31) SHELXTL; 6.14 ed.; Bruker AXS, Inc.: Madison, WI, 2003.

(32) SADABS; Sheldrick, G.; 2.10 ed. 2003.

(33) Parish, R. V.; Rush, J. D. *Chem. Phys. Lett.* **1979**, *63*, 37-39.

(34) Laguna, A. In *Gold: Progress in Chemistry, Biochemistry and Technology*; Schmidbaur, H., Ed.; John Wiley & Sons: Chichester, UK, 1999, p 350-427.

(35) Filowitz, M.; Ho, R. K. C.; Klemperer, W. G.; Shum, W. *Inorg. Chem.* **1979**, *18*, 93-103.

(36) *^{17}O NMR Spectroscopy in Organic Chemistry*; Boykin, D. W., Ed.; CRC Press, Inc.: Boca Raton, 1991.

(37) Besecker, C. J.; Klemperer, W. G.; Maltbie, D. J.; Wright, D. A. *Inorg. Chem.* **1985**, *24*, 1027-1032.

(38) Butler, L. G. In *^{17}O NMR Spectroscopy in Organic Chemistry*; Boykin, D. W., Ed.; CRC Press: Boca Raton, 1991; Vol. 1, p Ch. 1.

(39) Klemperer, W. G. *Angew. Chem., Int. Ed.* **1978**, *17*, 246-254.